

ENHANCEMENT OF GRAPHENE BIOCOMPATIBILITY
AS A POTENTIAL NANO-CARRIER FOR DRUG
DELIVERY APPLICATIONS USING NATURAL DEEP
EUTECTIC SOLVENT

MOHAMAD HAMDY BIN ZAINAL ABIDIN

FACULTY OF ENGINEERING
UNIVERSITY OF MALAYA
KUALA LUMPUR

2020

**ENHANCEMENT OF GRAPHENE
BIOCOMPATIBILITY AS A POTENTIAL NANO-
CARRIER FOR DRUG DELIVERY APPLICATIONS
USING NATURAL DEEP EUTECTIC SOLVENT**

MOHAMAD HAMDI BIN ZAINAL ABIDIN

**THESIS SUBMITTED IN FULFILMENT OF THE
REQUIREMENTS FOR THE DEGREE OF DOCTOR OF
PHILOSOPHY**

**FACULTY OF ENGINEERING
UNIVERSITY OF MALAYA
KUALA LUMPUR**

2020

UNIVERSITY OF MALAYA
ORIGINAL LITERARY WORK DECLARATION

Name of Candidate: Mohamad Hamdi Bin Zainal Abidin
Matric No: KHA160028

Name of Degree: Doctor of Philosophy (Ph.D.)

Title of Thesis ("this Work"):

ENHANCEMENT OF GRAPHENE BIOCOMPATIBILITY AS A
POTENTIAL NANO-CARRIER FOR DRUG DELIVERY APPLICATIONS
USING NATURAL DEEP EUTECTIC SOLVENT

Field of Study: Chemical Engineering

I do solemnly and sincerely declare that:

- (1) I am the sole author/writer of this Work;
- (2) This Work is original;
- (3) Any use of any work in which copyright exists was done by way of fair dealing and for permitted purposes and any excerpt or extract from, or reference to or reproduction of any copyright work has been disclosed expressly and sufficiently and the title of the Work and its authorship have been acknowledged in this Work;
- (4) I do not have any actual knowledge nor ought I reasonably to know that the making of this work constitutes an infringement of any copyright work;
- (5) I hereby assign all and every rights in the copyright to this Work to the University of Malaya ("UM"), who henceforth shall be owner of the copyright in this Work and that any reproduction or use in any form or by any means whatsoever is prohibited without the written consent of UM having been first had and obtained;
- (6) I am fully aware that if in the course of making this Work I have infringed any copyright whether intentionally or otherwise, I may be subject to legal action or any other action as may be determined by UM.

Candidate's Signature

Date:

Subscribed and solemnly declared before,

Witness's Signature

Date:

Name:

Designation:

ABSTRACT

Graphene has attracted massive interest in numerous biomedical applications such as anti-cancer therapy, drug delivery, bio-imaging and gene delivery. Therefore, it is important to ensure that graphene is nontoxic, and that its cellular biological behavior is safe and biocompatible. Herein, a new route was used to enhance the biocompatibility of graphene as a nano-carrier for potential drug delivery applications, using different compositions of natural deep eutectic solvents (DESs) as functionalizing agents, owing to their capability to introduce various functional groups and surface modifications. To meet this end, eight different combinations of binary and ternary DESs were synthesized using choline chloride salt with several hydrogen bond donors (i.e., urea, glucose, fructose, sucrose, glycerol and malonic acid). Characterizations of the physicochemical changes in DES-functionalized graphene were conducted by FE-SEM, EDX, FTIR, XRD, BET and Raman spectroscopy. The cytotoxicity profile of DES-functionalized graphenes on human breast adenocarcinoma (MCF-7), human gastric adenocarcinoma (AGS) and macrophage cell line (RAW264.7) was significantly improved compared to pristine graphene and oxidized graphene, as demonstrated by cell viability, cell cycle progression, and reactive oxygen species evaluation assays. This work also studied the association between cellular toxicity of DES-functionalized graphene and their physicochemical properties. The application of DESs as functionalizing agents, especially for DES choline chloride (ChCl):malonic acid (1:1), ChCl:glucose:water (5:2:5) and ChCl:glycerol:water (1:2:1), significantly reduced the cytotoxicity level of graphenes. Next, it was selected doxorubicin and tamoxifen, as representatives of common anti-cancer drugs, to load on the DES-functional graphene samples. Subsequently, the drug loading capacity and entrapment efficiency were determined. The DES ChCl:malonic acid (1:1) and

ChCl:glucose:water (5:2:5) functionalized graphenes demonstrated higher tamoxifen and doxorubicin entrapment efficiency and loading capacity in comparison to the other DES-functionalized graphenes. The drug-loaded on the DES-functionalized graphene possessed higher toxicity level against MCF-7 and AGS cell lines in comparison to unloaded graphenes. The drug-loaded DES-functionalized graphene also had destructive effects against cancerous cells through the generation of intracellular ROS and cell cycle disruption phenomena. The anti-cancer activity of drug-loaded graphene was confirmed by real-time cell growth analysis. Across all tested cellular kinetic models, the most significant reduction in the growth rate constant of cancerous cells was obtained using graphene functionalized with DES ChCl:glucose:water (5:2:5) and ChCl:fructose:water (5:2:5). Overall, DES-functionalized graphene demonstrated improved anti-cancer activity compared to non-functionalized graphene. This study supports DESs as potential green functionalizing agents for nano drug carriers, owing to their lower cytotoxicity, higher drug loading capacity and better anti-cancer activity.

ABSTRAK

Grafyn telah mendapat perhatian yang luas dalam pelbagai aplikasi bioperubatan seperti terapi bagi anti-kanser, penghantaran ubat, bio-pengimejan dan penghantaran gen. Oleh itu, adalah penting untuk memastikan bahawa grafyn tidak toksik, dan kelakuan biologi selularnya adalah selamat dan kesesuaian alami. Dalam kajian ini, satu kaedah baru digunakan untuk meningkatkan kesesuaian alami grafyn, dengan menggunakan beberapa pelarut eutektik (DES) semula jadi sebagai ejen pemungsaan, kerana berkemampuan untuk memperkenalkan pelbagai kumpulan berfungsi dan pengubahsuaian pada permukaan grafyn. Oleh itu, lapan kombinasi berbeza bagi binari dan ternari DESs telah disintesis menggunakan garam klorin klorida dengan beberapa penderma ikatan hidrogen (i.e., urea, glukosa, fruktosa, sukrosa, gliserol dan asid malonat). Pencirian perubahan fizikokimia dalam pemungsaan-DES grafyn telah dilakukan melalui kaedah spektroskopi FE-SEM, EDX, FTIR, XRD, BET dan Raman. Terdapat banyak penambahbaikan dalam profil sitotoksiti pemungsaan-DES grafyn berbanding grafyn tulen dan grafyn teroksida, seperti yang ditunjukkan dalam ujian-ujian seperti daya maju sel, perkembangan kitaran sel, dan reaksi bagi spesies oksigen reaktif (ROS). Kajian ini juga melihat persamaan antara sifat ketoksikan selular bagi pemungsaan-DES grafyn dan juga sifat fizikokimia mereka. Kajian ini merupakan kajian yang pertama mengenai penambahbaikan profil sitotoksik grafyn menggunakan DES sebagai agen pemungsaan, dan kelakuan biologi selularnya. Penggunaan DES sebagai agen pemungsaan, terutamanya untuk DES klorin klorida (ChCl):asid malonat (1:1), ChCl:glukosa:air (5:2:5) dan ChCl:gliserol:air (1:2:1), dapat mengurangkan tahap sitotoksiti grafyn dengan ketara. Kemudian, doxorubicin and tamoxifen, ubat anti-cancer yang popular, digunakan untuk mengkaji kapasiti kecekapan pemuatan ubat ke atas pemungsaan-DES grafyn. Dalam kapasiti kecekapan pemuatan ubat, DES ChCl:asid malonat (1:1) dan

ChCl:glukosa:air (5:2:5) juga menunjukkan kapasitas kecekapan penambahan dan pemuatan tamoxifen dan doxorubicin yang tinggi berbanding dengan pelarut DES yang lain. Ubat yang dimuatkan pada pemungisian-DES grafin mempunyai tahap ketoksikan yang lebih tinggi terhadap sel-sel MCF-7 dan AGS berbanding dengan sampel grafin yang tidak dimuatkan ubat. Grafin yang dimuatkan oleh ubat juga mempunyai kesan kerosakan terhadap sel-sel kanser melalui penjanaan ROS intraselular dan fenomena gangguan kitaran sel. Aktiviti anti-kanser bagi grafin yang telah dimuatkan ubat telah disahkan melalui analisis pertumbuhan sel masa nyata. Di antara semua model kinetik sel yang diuji, pengurangan yang paling ketara dalam kadar pertumbuhan sel kanser diperoleh dengan menggunakan grafin yang telah difungsikan dengan DES ChCl:glukosa:air (5:2:5) dan ChCl:fruktosa:air (5:2:5). Secara keseluruhannya, grafin yang telah difungsikan dengan DES menunjukkan peningkatan aktiviti anti-kanser berbanding dengan grafin yang tidak difungsikan. Kajian ini mengesahkan DES sebagai ejen pemungisian hijau yang berpotensi untuk pembawa ubat nano, disebabkan oleh sitotoksiti yang lebih rendah, keupayaan muatan ubat yang lebih tinggi dan aktiviti anti-kanser yang lebih baik.

ACKNOWLEDGEMENTS

In the name of Allah, the Most Gracious and the Most Merciful.

First and foremost, I would like to extend my sincere gratitude to my supervisors, Associate Prof. Dr. Ngoh Gek Cheng, Dr. Maan Hayyan, and Dr. Wong Won Fen for their guidance, assistance, encouragement, patience, and support throughout this journey. Without their knowledge and assistance this study would not have been successful. My sincere gratitude also goes to Dr Adeeb Hayyan for his guidance and assistance throughout my PhD study and related researches.

I would like to acknowledge University of Malaya, Centre for Ionic Liquid (UMCIL) for the facilities and Malaysia Toray Science Foundation grant for the financial support. My genuine appreciation to Prof Dr Mohd Ali Hashim, who gave access to the laboratory and research facilities under UMCIL.

Special thanks to my family especially to my parents, Zainal Abidin Hamzah and Fatimah Noordin, and other family members (Wan, Haiqal, Hasnidah) for their unending love, encouragement and strong support to complete this project. As well as to all my friends, especially the crazy bunch of my colleagues from UMCIL (Ainul, Anis, Ein, Killa, Seela, Shira, Syiqin, Zul) and medical microbiology (Chalysta, Chin Yap, Dr Looi, Grace, Heng Choon, Hui Jing, Shin yan, Ting Fang, Yee Teng, Yi Ying) for their favor, support, encouragement, and happiness throughout my study. I owe every one of you all for so many things. Thank you so much and may Allah bless all of you.

Sincerely,

Mohamad Hamdi Zainal-Abidin

TABLE OF CONTENTS

ABSTRACT	iii
ABSTRAK	v
ACKNOWLEDGEMENT	vii
TABLE OF CONTENTS	viii
LIST OF FIGURES	xi
LIST OF SCHEMES	xiv
LIST OF TABLES	xv
LIST OF SYMBOLS AND ABBREVIATIONS	xvii
LIST OF APPENDICES	xxiv
CHAPTER 1: INTRODUCTION	1
1.1 OVERVIEW	1
1.2 PROBLEM STATEMENT AND SIGNIFICANCE OF STUDY	4
1.3 RESEARCH OBJECTIVES	5
1.4 RESEARCH SCOPE	5
1.5 OUTLINE OF THE THESIS	8
CHAPTER 2: LITERATURE REVIEW	10
2.1 DEEP EUTECTIC SOLVENTS	10
2.2 DESS AS A DRUG SOLUBILIZATION VEHICLE	14
2.3 THEDESs	23
2.3.1 Drug dissolution enhancement via THEDESs	25
2.3.2 Drug permeation	26
2.3.2.1 Ibuprofen-based THEDESs	26
2.3.2.2 THEDESs from other drugs	28
2.3.2.3 Polymerized drug-based DESs	30
2.3.3 Potential biomedical and pharmaceutical applications of DESs	33
2.3.1 Anti-bacterial activity	33
2.3.2 Anti-fungal activity	44
2.3.3 Anti-viral activity	45
2.3.4 Anti-cancer activity	47
2.4 BIOSAFETY ASPECTS OF DESS	51
2.5 NANOTECHNOLOGY IN DRUG DELIVERY	54
2.5.1 Conventional functionalization of graphene	56

2.5.2	Functionalization of carbon nanomaterials using DES	57
CHAPTER 3: RESEARCH METHODOLOGY		59
3.1	PREPARATION OF BINARY AND TERTIARY DESs	60
3.2	PREPARATION OF OXIDIZED GRAPHENE AND DES-FUNCTIONALIZED GRAPHENE	62
3.3	PHYSICOCHEMICAL CHARACTERIZATION	63
3.4	CELL CULTURE	63
3.5	CELL VIABILITY ASSAY	64
3.6	CELL CYCLE ASSAY	64
3.7	REACTIVE OXYGEN SPECIES (ROS) ASSAY	65
3.8	DRUG LOADING	65
3.9	CELLULAR KINETIC RESPONSES	67
CHAPTER 4: RESULTS AND DISCUSSIONS		68
4.1	CHARACTERIZATION OF DES-FUNCTIONALIZED GRAPHENE	68
4.1.1	Morphological changes and surface elements of the graphenes (FE-SEM and EDX analysis)	68
4.1.2	XRD analysis	72
4.1.3	Raman spectroscopy	75
4.1.4	BET surface area analysis	77
4.1.5	FTIR study	79
4.2	BIOLOGICAL BEHAVIOR OF DES-FUNCTIONALIZED GRAPHENE	86
4.2.1	MTT cell viability assay	86
4.2.2	Reactive oxygen species (ROS) assay	90
4.2.3	Cell cycle analysis	96
4.3	DRUG LOADING ON THE DES-FUNCTIONALIZED GRAPHENE	100
4.3.1	TAMOXIFEN LOADING PROFILE	101
4.3.2	DOXORUBICIN LOADING PROFILE	105
4.4	ANTI-CANCER ACTIVITIES OF DRUG LOADED- DES-FUNCTIONALIZED GRAPHENE	110
4.4.1	Cytotoxicity analysis	110
4.4.1.1	TAM-loaded graphene	111
4.4.1.2	DOX-loaded graphene	116
4.4.2	Reactive oxygen species generation	121
4.4.2.1	TAM-loaded graphene	121
4.4.2.2	DOX-loaded graphene	125
4.4.3	Cell cycle disruption	129

4.4.3.1 TAM-loaded graphene	129
4.4.3.2 DOX-loaded graphene	133
4.4.4 Cellular kinetic responses	138
4.4.4.1 TAM-loaded graphene	138
4.4.4.2 DOX-loaded graphene	146
CHAPTER 5: CONCLUSIONS AND FUTURE WORKS	153
5.1 CONCLUSIONS	153
5.2 NOVELTIES AND IMPLICATIONS OF THE STUDY	155
5.3 FUTURE RECOMMENDATIONS	156
REFERENCES	158
LIST OF PUBLICATIONS AND AWARDS	186
APPENDIX A	188
APPENDIX B	206
APPENDIX C	211
APPENDIX D	217
APPENDIX E	221
APPENDIX F	225

LIST OF FIGURES

Figure 1.1: The scopes of study based on the reseach objectives.	8
Figure 2.1: Biopharmaceutical characterization system of drugs	28
Figure 2.2: Promising biomedical and pharmaceutical activities of DESs.	33
Figure 2.3: HSV-1 and HSV-2 were neutralized by CAGE (Zakrewsky et al., 2016).	46
Figure 2.4: Number of publications dedicated to nanotechnology, nanoscience, and nanomedicine.	55
Figure 3.1: The research methodology sequences.	59
Figure 4.1: FE-SEM images of (a) PrGr, (b) OxGr, (c) GrG, (d) GrU, (e) GrF, (f) GrMa, (g) GrGW, (h) GrFW, (i) GrSW, and (j) GrGlyW.	70
Figure 4.2: XRD patterns of PrGr and GrMa.	73
Figure 4.3: Raman spectra of PrGr with identified peaks of 2D, G and D bands.	76
Figure 4.4: FTIR spectra for (a) PrGr and (b) OxGr at wavenumbers 400 to 4000 cm^{-1} .	81
Figure 4.5: FTIR spectra for (a) GrGW and (b) GrFW at wavenumbers 400 to 4000 cm^{-1} .	82
Figure 4.6: FTIR spectra for (a) GrGlyW, (b) GrSW, and (c) GrMa at wavenumbers 400 to 4000 cm^{-1} .	84
Figure 4.7: IC_{50} values of PrGr, OxGr and DES-functionalized Grs on MCF-7, AGS and RAW264.7 cell lines.	89
Figure 4.8: ROS generation of (a) untreated AGS cells, and with AGS cells treated with (b) PrGr, (c) OxGr, (d) GrU, (e) GrG, (f) GrF, (g) GrMa and (h) GrGlyW. Values indicates the percentages of cells generated ROS (by the fluorescence intensity) in the gated area. Shown are representative data of three independent experiments.	94
Figure 4.9: ROS generation of (a) untreated RAW264.7 cells, and with RAW264.7 cells treated with (b) PrGr, (c) OxGr, and (d) GrU. Values indicates the percentages of cells generated ROS (by the fluorescence intensity) in the gated area. Shown are representative data of three independent experiments.	95
Figure 4.10: ROS generation of (a) untreated MCF-7 cells, and with MCF-7 cells treated with (b) PrGr, (c) OxGr, and (d) GrG. Values indicates the percentages of cells generated ROS (by the fluorescence intensity) in the gated area. Shown are representative data of three independent experiments.	96
Figure 4.11: Cell cycle comparison of the (a) untreated AGS cells with the (b) PrGr- and (c) OxGr- treated AGS cells. Cells were harvested after 24 h, fixed and stained with PI to detect DNA contents. Values represent the percentages of viable cells at G0/G1, S or G2/M phases. Shown are representative data of three independent experiments.	99
Figure 4.12: Cell cycle comparison of the (a) untreated AGS cells with (b) GrF-treated AGS cells. Cells were harvested after 24 h, fixed and stained with PI to detect DNA	

contents. Values represent the percentages of viable cells at G0/G1, S or G2/M phases. Shown are representative data of three independent experiments. 99

Figure 4.13: Cell cycle comparison of the (a) untreated RAW 264.7 cells with (b) GrMa-treated RAW 264.7 cells. Cells were harvested after 24 h, fixed and stained with PI to detect DNA contents. Values represent the percentages of viable cells at G0/G1, S or G2/M phases. Shown are representative data of three independent experiments. 100

Figure 4.14: Amount of unloaded TAM in the mixture of TAM (50 $\mu\text{g}/\text{mL}$)+DES-functionalized Grs (100 $\mu\text{g}/\text{mL}$) at absorbance peak 290 nm. Standard TAM solution (50 $\mu\text{g}/\text{mL}$) was used as a control. 102

Figure 4.15: Amount of unloaded DOX in the mixture of DOX (50 $\mu\text{g}/\text{mL}$)+DES-functionalized Grs (100 $\mu\text{g}/\text{mL}$) at absorbance peak 480 nm. Standard DOX solution (50 $\mu\text{g}/\text{mL}$) was used as a control. 105

Figure 4.16: IC_{50} values of TAM-loaded PrGr, OxGr and DES-functionalized Grs on MCF-7, AGS and RAW264.7 cell lines. 111

Figure 4.17: IC_{50} values of DOX-loaded PrGr, OxGr and DES-functionalized Grs on MCF-7, AGS and RAW264.7 cell lines. 118

Figure 4.18: ROS generation of (a) untreated MCF-7 cells and MCF-7 cells treated with TAM-loaded (b) GrF, (c) GrMa, (d) OxGr, and (e) GrGW. Values indicates the percentages of cells generated ROS (by the fluorescence intensity) in the gated area. Shown are representative data of three independent experiments. 123

Figure 4.19: ROS generation of (a) untreated AGS cells and AGS cells treated with TAM-loaded (b) GrG, (c) GrU, (d) OxGr, and (e) GrGW. Values indicates the percentages of cells generated ROS (by the fluorescence intensity) in the gated area. Shown are representative data of three independent experiments. 124

Figure 4.20: ROS generation of (a) untreated MCF-7 cells and MCF-7 treated with DOX-loaded (b) PrGr, (c) OxGr, (d) GrSW, (e) GrGlyW, and (f) GrF. Values indicates the percentages of cells generated ROS (by the fluorescence intensity) in the gated area. Shown are representative data of three independent experiments. 128

Figure 4.21: ROS generation of (a) untreated AGS cells and AGS cells treated with DOX-loaded (b) GrU, (c) GrG, (d) GrGW, (e) GrF and (f) GrFW. Values indicates the percentages of cells generated ROS (by the fluorescence intensity) in the gated area. Shown are representative data of three independent experiments. 129

Figure 4.22: Cell cycle comparison of the (a) untreated MCF-7 cell line and MCF-7 cells treated with TAM-loaded (b) GrU, (c) GrG, (d) GrF, and (e) GrGW. Cells were harvested after 24 h, fixed and stained with PI to detect DNA contents. Values represent the percentages of viable cells at G0/G1, S or G2/M phases. Shown are representative data of three independent experiments. 131

Figure 4.23: Cell cycle comparison of the (a) untreated AGS cell line and AGS cells treated with TAM-loaded (b) GrU, (c) GrG, (d) GrF, and (e) GrGW. Cells were harvested after 24 h, fixed and stained with PI to detect DNA contents. Values represent the percentages of viable cells at G0/G1, S or G2/M phases. Shown are representative data of three independent experiments. 132

Figure 4.24: Cell cycle comparison of the (a) untreated MCF-7 cells and MCF-7 cells treated with DOX-loaded (b) PrGr, (c) OxGr, (d) GrSW, (e) GrGlyW, and (f) GrGW.

Cells were harvested after 24 h, fixed and stained with PI to detect DNA contents. Values represent the percentages of viable cells at G0/G1, S or G2/M phases. Shown are representative data of three independent experiments. 136

Figure 4.25: Cell cycle comparison of the (a) untreated AGS cell line and AGS cells treated with DOX-loaded (b) GrG, (c) GrGW, (d) GrF and (e) GrFW. Cells were harvested after 24 h, fixed and stained with PI to detect DNA contents. Values represent the percentages of viable cells at G0/G1, S or G2/M phases. Shown are representative data of three independent experiments. 137

Figure 4.26: Diagrammatic of cell cycle phases 137

Figure 4.27: Cellular kinetic responses of TAM-loaded PrGr, OxGr and DES-functionalized Grs on MCF-7 cells. All graphene samples were tested at concentration 100 $\mu\text{g/ml}$ and TAM was tested at 25 $\mu\text{g/ml}$ on MCF-7 cell line. 139

Figure 4.28: Cellular kinetic responses of TAM-loaded PrGr, OxGr and DES-functionalized Grs on AGS cells. All graphene samples were tested at concentration 100 $\mu\text{g/ml}$ and TAM was tested at 25 $\mu\text{g/ml}$ on AGS cell line. 139

Figure 4.29: Cellular kinetic responses of DOX-loaded PrGr, OxGr and DES-functionalized Grs on MCF-7 cells. All graphene samples were tested at concentration 100 $\mu\text{g/ml}$ and DOX was tested at 25 $\mu\text{g/ml}$ on MCF-7 cell line. 147

Figure 4.30: Cellular kinetic responses of DOX-loaded PrGr, OxGr and DES-functionalized Grs on AGS cells. All graphene samples were tested at concentration 100 $\mu\text{g/ml}$ and DOX was tested at 25 $\mu\text{g/ml}$ on AGS cell line. 147

LIST OF SCHEMES

Scheme 2.1: Some examples of phenolic compounds extracted using DESs	12
Scheme 2.2: Antimalarial agent, artemisinin extracted from <i>Artemisia annua</i> leaves using MTAC:1-butanol (1:4).	13
Scheme 2.3: Illustration for the synthesis of DNA-incorporated AgCl material and its antimicrobial action	18
Scheme 2.4: Anti-bacterial curcumin solubilized in NADES maleic acid: ChCl (1:3) inhibits bacteria growth.	21
Scheme 2.5: Components used for the preparation of the THEDESs	29
Scheme 3.1: Molecular structures of the starting components of the DESs prepared in this work.	61

LIST OF TABLES

Table 2.1: List of solubility of bioactive compounds in DESs	15
Table 2.2: List of therapeutic deep eutectic solvent (THEDES) and their potential applications.	24
Table 2.3: Permeability of API and THEDES systems (Duarte et al., 2017).	27
Table 2.4: Solubility of API and THEDES systems in PBS solution pH 7.4. (Duarte et al., 2017)	30
Table 2.5: Anti-bacterial activities of DESs/NADESs against various bacteria strains.	36
Table 2.6: Main categories of DESs (Smith et al., 2014).	45
Table 2.7: Selectivity index of ammonium-based DESs for cancer cells compared to human oral keratinocyte cell line (Hayyan et al., 2015b).	48
Table 2.8: Comparison between DES and conventional functionalization agents	57
Table 3.1: List of abbreviations for DES-functionalized Gr	60
Table 3.2: List of abbreviations for drug loaded-Gr.	66
Table 4.1: EDX surface elements analysis of PrGr, OxGr and DES-functionalized Gr	71
Table 4.2: Diffraction speaks obtained from XRD for PrGr, OxGr and DES-functionalized Grs	74
Table 4.3: Raman spectra of PrGr, OxGr and DES-functionalized Grs.	76
Table 4.4: BET surface area of PrGr, OxGr and DES-functionalized Grs.	78
Table 4.5: Summary of the physicochemical characterization analyses.	85
Table 4.6: IC ₅₀ values of PrGr, OxGr and DES-functionalized Grs on MCF-7, AGS and RAW264.7 cell lines. Values are expressed as the mean ± standard deviation of three different experiments.	87
Table 4.7: Effect of tamoxifen loading on entrapment efficiency and drug loading capacity for PrGr, OxGr and DES-functionalized Grs.	103
Table 4.8: Effect of doxorubicin loading on entrapment efficiency and drug loading capacity for PrGr, OxGr and DES-functionalized Gr samples.	106
Table 4.9: List of various nanocarrier systems with their EE% and DL%.	109
Table 4.10: IC ₅₀ values of TAM-loaded PrGr, OxGr, and DES-functionalized Gr samples on MCF-7 and RAW264.7 cell lines, and also their selectivity index. Values are expressed as the mean ± standard deviation of three different experiments.	112
Table 4.11: IC ₅₀ values of PrGr, OxGr, and TAM-loaded DES-functionalized Gr samples on AGS and RAW264.7 cell lines, and also their selectivity index. Values are expressed as the mean ± standard deviation of three different experiments.	113

Table 4.12: IC ₅₀ values of DOX-loaded PrGr, OxGr and DES-functionalized Gr samples on MCF-7 and RAW264.7 cell lines, and also their selectivity index. Values are expressed as the mean ± standard deviation of three different experiments.	119
Table 4.13: IC ₅₀ values of DOX-loaded PrGr, OxGr and DES-functionalized Gr samples on AGS and RAW264.7 cell lines, and also their selectivity index. Values are expressed as the mean ± standard deviation of three different experiments.	120
Table 4.14: Growth rate constant of the untreated MCF-7 cells and MCF-7 cells treated with TAM-loaded Gr.	144
Table 4.15: Growth rate constant of the untreated AGS cells and AGS cells treated with TAM-loaded Gr.	145
Table 4.16: Growth rate constant of the untreated MCF-7 cells and MCF-7 cells treated with DOX-loaded Gr.	151
Table 4.17: Growth rate constant of the untreated AGS cells and AGS cells treated with DOX-loaded Gr.	152

LIST OF SYMBOLS AND ABBREVIATIONS

%	Percentage
[C₈mim][Cl]	1-Octyl-3-methyl-limidazolium chloride
2-D	Two-dimensional
A375	Human malignant melanoma cell line
AC	Acrylic acid
ACP	Acetaminophen
AgCl	Silver chloride
AGS	Human gastric cancer cell line
ALT	Alanine aminotransferase
API	Active pharmaceutical ingredient
AST	Aspartate transaminase
ATCC	American Type Cell Collection
BA	Benzoic acid
BET	Brunauer–Emmett–Teller

BSA	Bovine serum albumin
CAGE	Choline bicarbonate and geranic acid
CD	Cannabidiol drug
Ch⁺	Cholinium
ChAc	Choline acetate
ChCl	Choline chloride
Cl	chlorine
cm	centimetre
CM	ChCl:maleic acid
CNM	Carbon nanomaterial
CNT	Carbon nanotube
CO₂	Carbon dioxide
COSMO-RS	Conductor-like screening model for real solvent
DAC	Diethylethanolammonium chloride
DESD	Deep eutectic solvent derivative
DESs	Deep eutectic solvents
DL	Drug loading capacity

DMEM	Dulbecco's Modified Eagle's Medium
DNA	Deoxyribonucleic acid
EAC	<i>N,N</i> -diethylethanolammonium chloride
EC₅₀	Effective concentration at 50%
EDX	Energy dispersive X-ray
EE	Entrapment efficiency
F	Fructose
FBS	Fetal bovine serum
FE-SEM	Field emission scanning electron microscope
FTIR	Fourier-transform infrared spectroscopy
G	Glucose
g	Gram
Gly	Glycerol
Gr	Graphene
GS	Glucose:sucrose
h	Hour
H₂SO₄	Sulfuric acid

H413	Human oral keratinocyte cells
HBA	Hydrogen bond acceptor
HBD	Hydrogen bond donor
HEK293	human embryo kidney cells
HEK-293	Human embryonic kidney cells
HelaS3	Human cervical cancer cell line
HepG2	Human liver hepatocellular cell line
HPLC	High performance liquid chromatography
HSV-1	Herpes simplex virus type-1
HSV-2	Herpes simplex virus type-2
HT-29	Human colon adenocarcinoma cell line
ILs	Ionic liquids
ITR	Itraconazole
K⁺	Potassium ion
KMnO₄	Potassium permanganate
LC₅₀	Lethal concentration at 50%
LD₅₀	Median lethal dose

LDH	Lactate dehydrogenase
LidHCl	Lidocaine hydrochloride
m	Metre
Ma	Malonic acid
MAA	Methacrylic acid
MCF-7	Human breast cancer cell line
MIC	Minimum inhibitory concentration
min	Minute
Mn	Manganese
MTPPB	Methyltriphenylphosphonium bromide
MTT	3-(4,5-Dimethylthiazol-2-yl)-2,5-diphenyltetrazolium bromide)
N	nitrogen
n	Nano
NADES	Natural deep eutectic solvent
NMR	Nuclear magnetic resonance
°C	Degree celcius
OKF6	Human oral keratinocyte cell

OxGr	Oxidized graphene
PA	Phenylacetic acid
PAC	Poly(acrylic acid)
PBS	Phosphate-buffered saline
PC3	Human prostate cancer cell line
pH	Potential hydrogen
POS	Poly(octanediol- <i>co</i> -citrate) elastomers
PrGr	Pristine graphene
PV	Poly(vinyl alcohol)
R^2	Coefficient of determination
RAW264.7	Macrophage line
ROS	Reactive oxygen species
RPMI	Roswell Park Memorial Institute
S	Sucrose
SPCL	Starch:poly- ϵ -caprolactone
TB	<i>Mycobacterium tuberculosis</i>
TEG	Triethylene glycol

T_g	Glass transition temperature
TH	Tetrahydrocannabinol
THA	Tetrahydrocannabinolic acid
THEDES	Therapeutic deep eutectic solvent
T_m	Melting point
U	Urea
UV-Vis	Ultraviolet-visible
Vero	African green monkey kidney cells
W	Water
XRD	X-Ray diffraction

LIST OF APPENDICES

APPENDIX A: Physicochemical characterization results	188
APPENDIX B: ROS generation of cells treated with Gr	206
APPENDIX C: Cell cycle of cells treated with Gr	211
APPENDIX D: ROS generation of cells treated with drug-loaded Gr	217
APPENDIX E: Cell cycle of cells treated with drug-loaded Gr	221
APPENDIX F: Cell kinetic response of drug-loaded Gr	225

Universiti Malaya

CHAPTER 1: INTRODUCTION

1.1 Overview

Graphene is a two-dimensional (2-D) material consisting of sp^2 hybridized carbon atoms, which is considered a basic building block for other graphitic components (Chen et al., 2016; Liu et al., 2013). It has a 2-D planar structure with delocalized π electrons on its plane, a large surface area and high intrinsic mobility (Chen et al., 2016). These features have prompted graphene research in various fields including biomedicine, electronics, sensors, chemical, and industrial processes (Bitounis et al., 2013; Chen et al., 2016; Zhu et al., 2010). Furthermore, graphene was introduced as a potential nano-carrier for drug loading via π - π stacking and hydrophobic or electrostatic interactions (Goenka et al., 2014). It has high drug loading capacity which is significantly higher than other drug nano-carriers (Liu et al., 2013). Therefore, graphene has been implemented as a nano-carrier for numerous bioactive compounds and drugs namely ellagic acid, doxorubicin, ibuprofen and camptothecin (Bitounis et al., 2013; Yang et al., 2013a). However, it has been speculated that graphene is potentially toxic to humans and the environment (Chen et al., 2016). Aggregation or flocculation of graphene on cell membranes is presumed to play a major role in its cellular toxicity (McCallion et al., 2016; Zhang et al., 2010). Therefore, it is important to modify the surface chemistry of graphene, which may improve the biocompatibility of graphene with cells and biological macromolecules.

The toxicology level of a nanomaterial is highly dependent on its shape, size and surface chemistry (Liu et al., 2013; Yang et al., 2013b). These features could be controlled by surface modification or functionalization of the targeted nanomaterial, including graphene (Biswas et al., 2013; Goenka et al., 2014). The functionalization process involves the attachment of new functional groups to the surface of carbon nanomaterials (CNMs) through either chemical or physical means, thereby modulating the dispersibility of CNMs under given conditions (Bitounis et al., 2013; Bottari et al., 2017). Enhanced dispersibility of graphene may significantly reduce the level of toxicity and thus improve biocompatibility (Sun et al., 2016; Sun et al., 2008).

In chemical functionalization process, many alternative chemical methods which exert less adverse effects on the environment are being used to replace the conventional chemical methods. One example is the use of green solvents to replace the traditional hazardous solvents that have been used extensively in industry (Tang et al., 2015). In this context, ionic liquids (ILs) have gained considerable attention due to their unique physical and chemical characteristics (Jin et al., 2016; Smith et al., 2014). ILs are molten salts that are liquids at temperatures below 100 °C, and they usually consist of bulky and asymmetric organic cations and organic or inorganic anions (Egorova et al., 2017; Ventura et al., 2017). Despite their attractive attributes such as non-flammability, high thermal stability, chemical stability, and low volatility (Hayyan et al., 2016b), there are concerns about the use of ILs that might have related to the toxicity of these compounds, their potential effects on health and the environment, and the high cost associated with their synthesis and purification requirements (Gorke et al., 2010; Hayyan et al., 2015b; Juneidi et al., 2015; Mbous et al., 2017a). To address the stated drawbacks, focus has been shifted to the applications of deep eutectic solvents (DESSs) that are viewed as being

analogous to ILs. DESs are also biodegradable, less toxic, and have lower costs as compared to ILs and other conventional solvents (Hayyan et al., 2013b; Hayyan et al., 2015b; Li & Lee, 2016).

DESs was introduced by Abbott et al. (2004) as a system which formed from a mixture of two or more Lewis acids and bases or Brønsted-Lowry acids and bases that has the lowest freezing point compared with its starting constituents. The physical structure of some DESs might be similar to that of the ILs. However, DESs, are different from ILs in terms of the source of the starting ingredients and the preparation process (Carriazo et al., 2012; Smith et al., 2014). The formation of DES results from the complexation of a halide salt, which acts as a hydrogen-bond acceptor, and a hydrogen-bond donor (HBD) (Mbous et al., 2017a). Unlike ILs, DESs normally are prepared from non-ionic starting materials, such as molecular compounds and salts (Zhang et al., 2012a). Recently, DESs that have been prepared from the combination of primary metabolites and bio-renewable starting materials, e.g., sugar alcohols, sugars, amino acids, and organic acids (Choi, 2011; Dai et al., 2016) are referred to as “natural deep eutectic solvents” (NADESs). Interestingly, the NADESs formation could explain some previously-inconceivable phenomena, such as the biosynthesis of intermediate-polarity compounds that are insoluble in both water and the lipid phase (Choi, 2011; Dai et al., 2013a). Attributing to their potentiality, DESs and NADESs have been used in numerous chemical and biochemical applications (Aroso et al., 2016; Jhong et al., 2009; Morrison et al., 2009; Nkuku & LeSuer, 2007; Smith et al., 2014). One of which is their use as functionalizing agents for carbon nanomaterials (CNMs) (Abo-Hamad et al., 2017; Hayyan et al., 2015a).

1.2 Problem Statement and Significance of Study

Similar to other nanoparticles, pure graphene is deemed to be potentially toxic to human health which hinders its application (Chen et al., 2016). Aggregation or flocculation of graphene on cell membranes is presumed to play a primary role in its cellular toxicity (McCallion et al., 2016; Zhang et al., 2010). The sharpened edges of graphene may act like blades, severely cutting or inserting into the cell membrane (Akhavan & Ghaderi, 2010; Dallavalle et al., 2015). Subsequently, graphene may lead to cell death through cell membrane destruction, oxidative stress, inflammatory response, necrosis, DNA damage, or apoptosis (Ou et al., 2016). Therefore, the functionalization of graphene may significantly reduce the level of toxicity, and thus improve biocompatibility of the nanoparticle (Liu et al., 2013). However, there are issues associated with the available functionalizing agents that deserve further consideration, such as tedious and complicated procedures, high temperature requirements (i.e., above 100 °C), use of highly corrosive solutions (e.g., H₂SO₄), and high process cost. In view of the issues, exploring novel 'green' functionalizing agents is highly desirable.

The DES proved promising surface modifications and introduced new functional groups on the CNMs. However, there has been no study of the cellular biological behavior of the DES-functionalized CNMs. Therefore, in depth study is needed to elucidate the applicability of DES-functionalized CNMs to act as nano-carriers in drug delivery applications.

1.3 Research Objectives

The objectives of this study are as follows:

1. To functionalize graphene with different NADES systems and to characterize their physicochemical and morphological changes.
2. To evaluate cytotoxicity profiles of unfunctionalized graphene and DES-functionalized graphene against normal cells (macrophage cells, RAW264.7) and cancerous cells (human breast cancer cells, MCF-7 and human gastric cancer cells, AGS).
3. To perform loading capacity and entrapment efficiency of doxorubicin and tamoxifen, as representatives of common anti-cancer drugs, on the DES-functionalized graphene samples.
4. To assess the anti-cancer activity of drug-loaded DES-functionalized graphene on the selected human cancer cells MCF-7 and AGS.
5. To identify the kinetic cellular phenotypic profiling of drug-loaded DES-functionalized graphene against the selected cancer cells.

1.4 Research Scope

This research aims to introduce new biocompatible nanocarriers to be used in cancer therapy. The surface modification caused by the functionalization with DES provides remarkable improvement in the cytotoxicity profiles of the graphene. New functional

groups are anticipated to be added along with other possible structural changes. The improved cytotoxicity profile of the DES-functionalized graphene confers higher drug loading capacity which hence, enhance the anti-cancer activity of the drug-loaded DES-functionalized graphene. This research could open a door for a new research field by the possibility of using the DES formulations to functionalize nanomaterials for drug delivery. This indeed give a high flexibility for researchers to enhance the performance of nanocarriers and to boost drug release. Therefore, this study is divided into five different sections based on the reseach objectives: DES functionalization of graphene, cytotoxicity profiles of graphene (unfunctionalized and DES-functionalized graphene), drug loading capacity of graphene, anti-cancer activity of drug-loaded graphene and kinetic cellular phenotypic profile of drug-loaded graphene. The scopes of research are described in Figure 1.1.

Objective 1

- Preparation of eight different combinations of binary and ternary NADESs using choline chloride salt with several hydrogen bond donors (i.e., urea, glucose, fructose, sucrose, glycerol and malonic acid)
- Pretreatment and oxidation of graphene using potassium permanganate.
- Functionalization of graphene using the prepared DESs.
- Physicochemical characterization of pristine, oxidized, and DES-functionalized graphene samples using FE-SEM, EDX, FTIR, XRD, BET, and Raman spectroscopy analyses.

Objective 2

- Evaluate the effect of pristine-, oxidized- and DES-functionalized graphene on the cell viability of normal cells (macrophage cells, RAW264.7) and cancerous cells (human breast cancer cells, MCF-7 and human gastric cancer cells, AGS).
- Investigate the impact of pristine-, oxidized-, and DES-functionalized graphene on cell cycle progression.
- Measure the level of intracellular reactive oxygen species induced by pristine-, oxidized-, and DES-functionalized graphene.

Objective 3

- To load doxorubicin and tamoxifen, as representatives of common anti-cancer drugs, on pristine-, oxidized-, and DES-functionalized graphene samples.
- Determine the drug loading capacity and entrapment efficiency of pristine, oxidized-, and DES-functionalized graphene.

Objective 4

- Assess the anti-cancer activity of tamoxifen- and doxorubicin-loaded graphene against cancerous cells through cell viability, reactive oxygen species, and cell cycle progression assays.

Objective 5

- Identify the kinetic cellular phenotypic profile of tamoxifen- and doxorubicin-loaded graphene against cancerous cells.
- Kinetics analysis is carried out on both MCF-7 and AGS cells by fitting their cell growth data to zero order, 1st order, and 2nd order models.
- The growth rate constants are determined for each drug-loaded graphene samples.

Figure 1.1: The scopes of study based on the reseach objectives.

1.5 Outline of the thesis

This thesis comprises of five chapters. The content of each chapter is described as follows:

Chapter 1 introduces the background and problem statement of the study. The research objectives and a brief description of the research methodology are also detailed.

Chapter 2 covers a review of the relevant scientific literature on DESs, including the previous studies done in relation to drug discovery and drug delivery applications. The potential biomedical and pharmaceutical applications, as well as the biosafety aspects of DESs are reviewed. In addition, the current application of DESs as green functionalizing agents for CNMs is also being discussed.

Chapter 3 provides the detailed research methodology of this project. All the materials, chemicals, instruments, and equipments employed in this research are also described in this chapter.

Chapter 4 presents the results and discussions, which covers the physicochemical characterization of the DES-functionalized graphene, the cytotoxicity profile of the DES-functionalized graphene, the anti-cancer drug loading capacity of the DES-functionalized graphene, and also the anti-cancer activities of drug-loaded DES-functionalized graphene.

Chapter 5 provides conclusion and recommendations for future studies. The novelty and significance of the study are also emphasized in this chapter.

CHAPTER 2: LITERATURE REVIEW

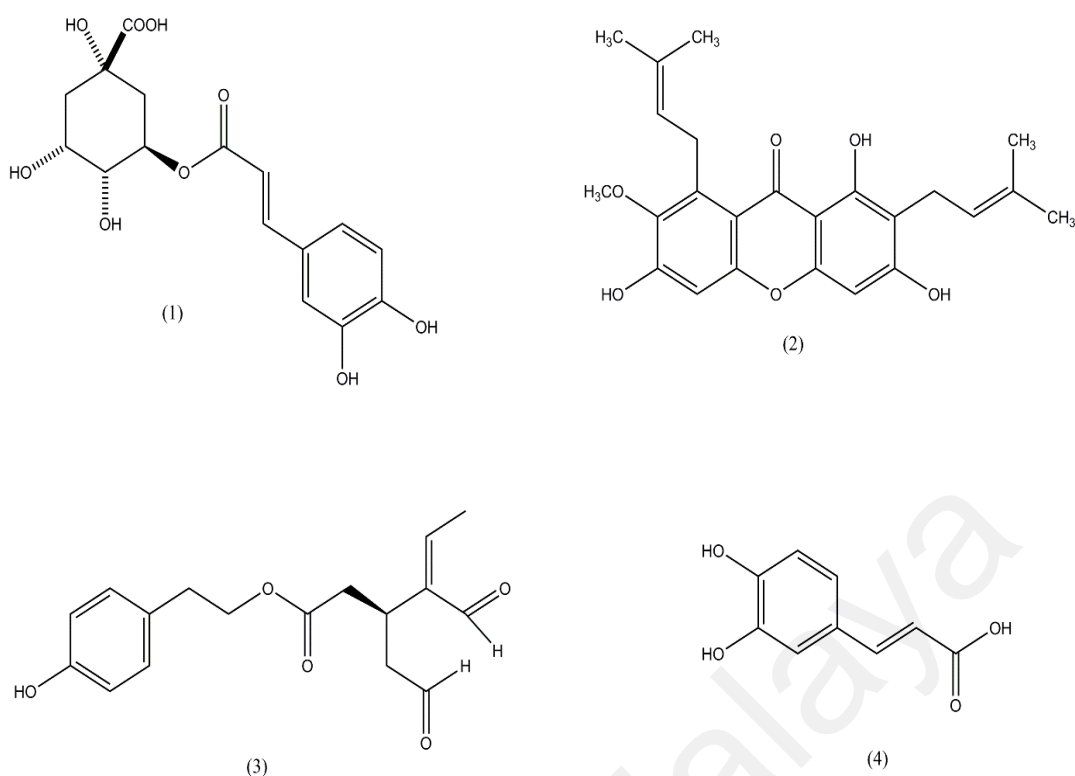
2.1 Deep eutectic solvents

Deep eutectic solvents (DESS) are a new generation of eutectic mixtures which have gained widespread scientific and technological attention as low-cost alternatives for organic solvents and ionic liquids (ILs). The mixture is a complexation of two or more components which at a specific molar ratio becomes liquid at room temperature. These neoteric, green solvents achieve lower melting points than do their single components because of the charge delocalization resulting from hydrogen bonding between the hydrogen bond donor and the halide anion (Abbott et al., 2004; Carriazo et al., 2012; Smith et al., 2014). Compared to ILs and other conventional solvents, DESS are recognized as less volatile, thermally stable, highly tunable, biodegradable, less toxic, and lower in cost (Juneidi et al., 2015; Mbous et al., 2017a; van Osch et al., 2015). To that end, DESS have become essential players in various fields of the chemical, biotechnology, and electrochemical industries (Chakrabarti et al., 2015; Wang et al., 2018; Xing et al., 2018; Yao et al., 2017; Zhang et al., 2017).

A new class of DESS has been synthesized from complexations of primary metabolites or bio-renewable ingredients such as amino acids, sugar alcohols, sugars, and organic acids (Choi, 2011; Dai et al., 2016; Hayyan et al., 2016b). This novel category is termed “natural deep eutectic solvents (NADES),” which has been linked to some previously incomprehensible natural phenomena such as the solubility and biosynthesis of semi-polar components that are neither soluble in water nor a lipid phase (Dai et al., 2013a; Liu

et al., 2018; Markham et al., 2000; Pisano et al., 2018). NADESs have also been associated with several biological mechanisms for drought resistance, dehydration, germination, and cryoprotection (Gertrudes et al., 2017; Hayyan et al., 2016b). In particular, the emerging push for green practices among the scientific community has led to a huge demand for the application of NADES in the nutraceutical and pharmaceutical fields. NADESs are touted as great alternatives to hazardous organic solvents in the separation, extraction, and purification of natural bioactive substances. They have been employed for the extraction of numerous bioactive compounds, such as phenolic acid, polyphenols, flavonoids, polysaccharide, and proteins, from diverse natural sources (García et al., 2016; Li & Lee, 2016; Liu et al., 2017; Wei et al., 2015a; Zhang & Wang, 2017).

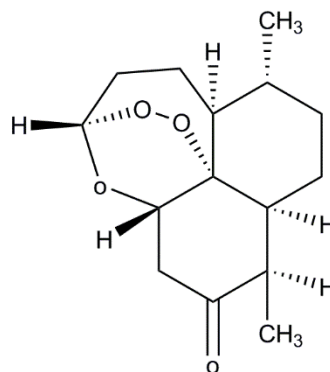
One of the most gained attention bioactive compounds was phenolic compounds (Scheme 2.1). Phenolics have been widely studied as anti-inflammatory, anti-cancer, anti-oxidant and neuro-protective agents (Mayakrishnan et al., 2013; Phan et al., 2015; Rahman et al., 2016). As reported previously (Bakirtzi et al., 2016; Dai et al., 2013b; Hayes et al., 2011; Mayakrishnan et al., 2013; Orhan & Üstün, 2011), numerous extraction techniques were applied to extract phenolic compounds from diverse group of natural sources. Recently, DESs have gained huge consideration as potential substitution to the typical media/solvents in the extraction of phenolic compounds (Bakirtzi et al., 2016; Dai et al., 2013b; García et al., 2016; Wei et al., 2015a; Wei et al., 2015b).



Scheme 2.1: Some examples of phenolic compounds extracted using DESs (1) chlorogenic acid, (2) α -mangostin, (3) oleocanthal and (4) caffeic acid.

Although most of the bioactive compounds extracted using DESs have hydrophilic characteristic, there were some previous studies (Abdul Hadi et al., 2015; Cao et al., 2018; Cao et al., 2017a; Wang et al., 2016a) reporting the potential use of DESs to extract hydrophobic compounds from natural sources. One example is in the extraction of antimalarial agent, artemisinin (Scheme 2.2) from *Artemisia annua* leaves (Cao et al., 2017b). A tailor-made hydrophobic DES methyltrioctylammonium chloride (MTAC):1-butanol (1:4) was the most efficient solvent for the extraction of artemisinin in comparison to other MTAC-based DESs. Under the optimum condition, this DES exhibited extraction yield of 7.99 mg/g, in which significantly higher than that of volatile

organic solvent petroleum ether (6.18 mg/g). DES MTAC:1-butanol (1:4) also had high recovery yield (i.e., 85.65%) and can be reused for minimum two cycles.



Scheme 2.2: Antimalarial agent, artemisinin extracted from *Artemisia annua* leaves using MTAC:1-butanol (1:4).

In addition, certain types of recently-introduced DESs possess medicinal or pharmaceutical activities in their own right, e.g. anti-fungal, anti-bacterial, anti-viral, and anti-cancer activities. To the extent that, a term therapeutic deep eutectic solvent (THEDES) was coined for DESs that contain active pharmaceutical ingredients (APIs) (Aroso et al., 2015; Aroso et al., 2016).

Another recently-developed type of DES is the deep eutectic solvent derivative (DESD) (Li & Lee, 2016). This is a DES-like, room temperature liquid that is similar to but distinct from eutectic systems; it is also referred to as a low transition temperature mixture, eutectic mixture, and low melting mixture (Francisco et al., 2013; Ru & Konig, 2012; Wang et al., 2016b). DESD encompasses an extensive range of DES-like derivatives, especially those derived from ternary systems, for which the eutectic point is difficult to

determine. Examples of DESDs reported to date include DESD ChCl:glycolic acid (1:2), DESD ChCl:glycolic acid:oxalic acid (1:1.6:0.4), and DESD ChCl:glycolic acid:oxalic acid (1:1.7:0.3) (Li & Lee, 2016; Zahedifard et al., 2015).

Presently, DESs are attracting significant interest as drug delivery systems, owing to their high tunability and lower toxicology profiles. In addition, certain types of the DESs that have been recently introduced possess some medicinal or pharmaceutical activities (e.g., anti-fungal, anti-bacterial, anti-viral and anti-cancer activities). Therefore, increased attention has been focused on the applications of DESs in the field of biomedical and the pharmaceutical industry.

2.2 DESs as a drug solubilization vehicle

Low solubility and dissolution issues are frequently encountered in the formulation of drugs, and numerous drug candidates failed in preclinical and clinical trials because of bioavailability and formulation problems. Thus, there is a high demand for a universal and safe drug dissolver with which to overcome these drawbacks. There is great potential in implementing DESs for this purpose due to their adjustable physicochemical properties. Table 2.1 shows available information on the solubility of various types of drugs/APIs in DES systems. In short, DESs are capable of dissolving a wide range of drugs/APIs, including itraconazole, lidocaine, piroxicam, benzoic acid, salvianolic acid, curcumin, danazol, and posaconazole.

Table 2.1: List of solubility of bioactive compounds in DESs

DES	Ratio	Bioactive compounds	Solubility (mg/mL)	Reference	
ChCl:ethylene glycol	1:2	DNA	N.A	(Mondal et al., 2013)	
ChCl:ethylene glycol	1:2	AgCl-DNA	N.A		
ChCl:glycerol	1:2	DNA	N.A	(Chen et al., 2017)	
ChCl:glycerol	1:2	Salvianolic acid B	N.A		
ChCl:glycolic acid	1:2	Itraconazole	6.70	(Lin et al., 2016)	
ChCl:glycolic acid	1:2	Piroxicam	9.90		
ChCl:glycolic acid	1:2	Lidocaine	100.60		
ChCl:glycolic acid	1:2	Posaconazole	76.80		
ChCl:glycolic acid	1:1.7:0.3	Piroxicam	3.10		
ChCl:glycolic acid	1:1.7:0.3	Lidocaine	295.40		
ChCl:glycolic acid	1:1.7:0.3	Posaconazole	88.40		
ChCl:glycolic acid:oxalic acid	1:1.7:0.3	Itraconazole	46.40		
ChCl:maleic acid	3:1	Curcumin	0.0667		(Wikene et al., 2015)
ChCl:malonic acid	1:3	Benzoic acid	18.0		(Morrison et al., 2009)
ChCl:malonic acid	1:3	Griseofulvin	0.0044		
ChCl:malonic acid	1:3	Danazol	0.1007		
ChCl:malonic acid	1:3	AMG517	0.014		
ChCl:malonic acid	1:3	Itraconazole	6.60		
ChCl:malonic acid	1:1	Benzoic acid	11.00		

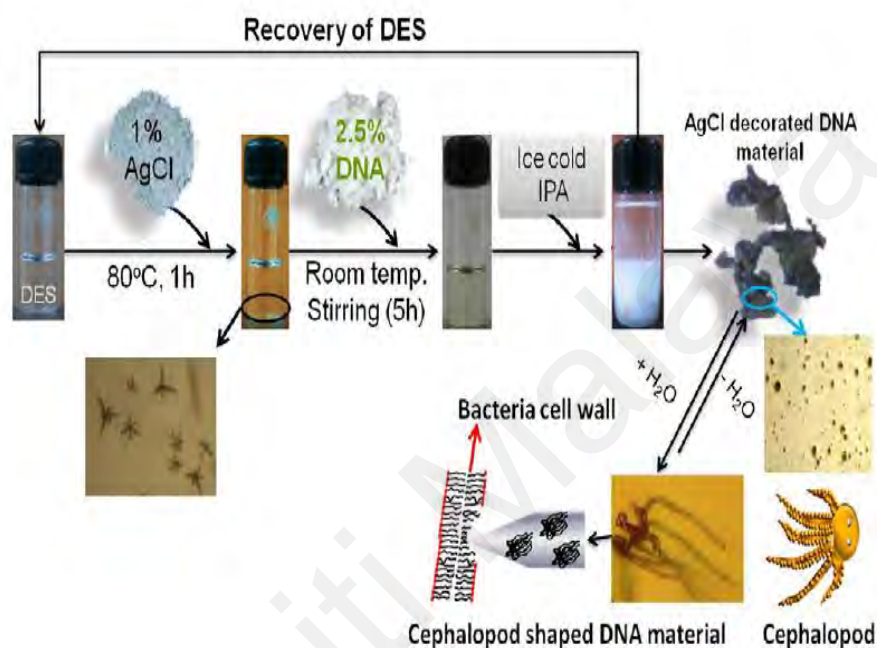
DES	Ratio	Bioactive compounds	Solubility (mg/mL)	Reference
ChCl:malonic acid	1:1	Griseofulvin	0.002	
ChCl:malonic acid	1:1	Danazol	0.043	
ChCl:malonic acid	1:1	AMG517	0.002	
ChCl:malonic acid	1:1	Itraconazole	1.20	
ChCl:urea	1:3	Benzoic acid	23.00	
ChCl:urea	1:3	Griseofulvin	0.0061	(Morrison et al., 2009)
ChCl:urea	1:3	Danazol	0.016	
ChCl:urea	1:3	AMG517	0.00022	
ChCl:urea	1:3	Itraconazole	< 0.001	
ChCl: urea	1:1	Benzoic acid	14.00	
ChCl: urea	1:1	Griseofulvin	0.002	
ChCl: urea	1:1	Danazol	0.015	
ChCl: urea	1:1	AMG517	< 0.0001	
ChCl: urea	1:1	Itraconazole	< 0.001	
ChCl:1,2-propanediol	1:2	Aspirin	202.00	(Lu et al., 2016)
ChCl:1,2-propanediol	1:2	Acetaminophen	324.00	
ChCl:1,2-propanediol	1:2	Naproxen	45.26	
ChCl:levulinic acid	1:2	Ketoprofen	329.10	
ChCl:proline	3:1	Rutin	2.79	(Phaechamud et al., 2016)
Camphor:menthol	1:1	Ibuprofen	282.11	(Faggian et al., 2016)
Glucose:sucrose	1:1	Curcumin	0.05211	(Wikene et al., 2015)

One of the most intriguing applications of DESs as drug solubilizing vehicles is their capability to dissolve poorly water-soluble drugs/APIs. For instance, ChCl:urea (1:3) and ChCl:malonic acid (1:1) have been shown to increase the solubility of low-soluble drugs such as benzoic acid, itraconazole, griseofulvin, and also synthesized drug AMG517 by 5- to 22,000-fold over water solution (Morrison et al., 2009). Furthermore, the solubility of benzoic acid, itraconazole, griseofulvin, and AMG517 in the DES binary mixture was considerably superior to the corresponding solubilities in individual aqueous solutions of eutectic mixture components. The study also concluded that DESs, especially ChCl:urea (1:3) and ChCl:malonic acid (1:1), are pharmaceutically acceptable for use as drug carriers in pharmacokinetic *in vivo* studies (Morrison et al., 2009).

DNA dissolution capacity also was explored for new combinations of DESs. For instance, ChCl:ethylene glycol (1:2) and ChCl:glycerol (1:2) were the most efficient in dissolving DNA (Lannan et al., 2012; Mamajanov et al., 2010). These DESs also can be recycled over three consecutive reuses, indicating the sustainability of DES mixtures as promising multi-purpose agents.

In the study of food-borne pathogens and wound treatment (Bhatt et al., 2015), 2.5% w/w salmon sperm DNA was incorporated with silver chloride (AgCl) to form a poorly water-soluble anti-microbial agent. This AgCl-coated DNA was successfully solubilized in a DES ChCl:ethylene glycol (1:2). Further addition of 2.5% w/w DNA led to the AgCl-coated DNA taking on cephalopod- or bullet-like morphology, as shown in Scheme 2.3. This unique morphology improved the bacteriostatic and bactericidal activity of the DNA-incorporated AgCl material against different Gram-negative bacterial species i.e.,

Escherichia coli, *Shigella boydii*, *Shigella flexineri*, *Pseudomonas fluorescens*, *Salmonella enterica*, *Vibrio cholerae* N16961 and Gram-positive bacterial species i.e., *Bacillus licheniformis* and *Bacillus subtilism*.



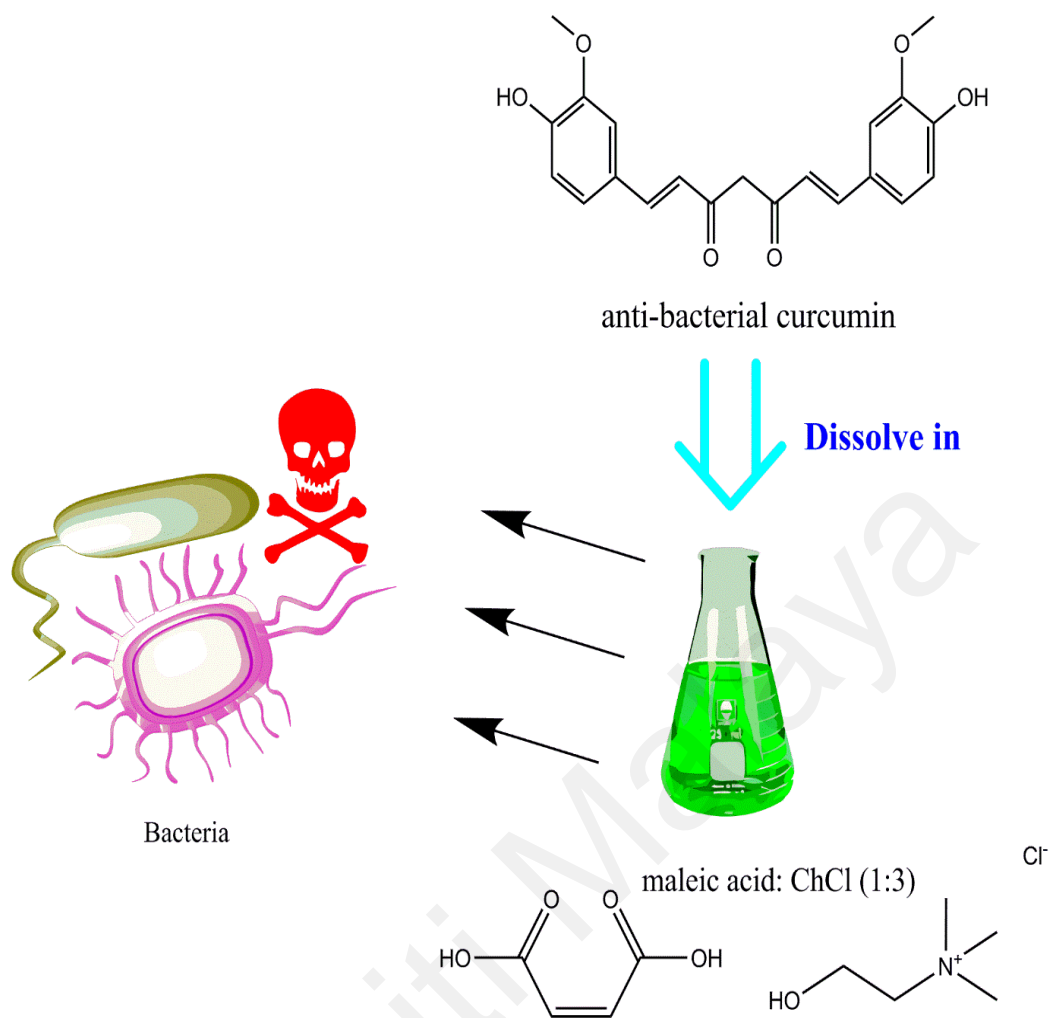
Scheme 2.3: Illustration for the synthesis of DNA-incorporated AgCl material and its antimicrobial action (Bhatt et al., 2015).

The occurrence of strong solvent-solute interactions between DESs and acetaminophen (ACP) was confirmed by its solubilization of in various ChCl-based DESs (Shekaari et al., 2017). The solubility of ACP in DESs increased in a dose-dependent manner positively correlated with DES concentration and temperature. This implies that the interaction between ACP and the DES was strengthened by increased DES concentration. Similar improvement of the solubility of ACP in DESs was also observed by Lu et al.

(2016). Specifically, DESs based on ChCl, tetrapropylammonium bromide, betaine, choline bitartrate, and ethylammonium chloride all demonstrated higher solubility of ACP (i.e. 89.07–352.7 mg/mL) than water. However, the solubility of ACP was lessened as the HBD ratio increased, especially in the case of ChCl:1,2-propanediol and betaine:levulinic acid. In contrast, the solubility of naproxen increased with increasing HBD ratio in ChCl:levulinic acid, but decreased with increasing HBD ratio in ChCl:1,2-propanediol. It is apparent that changes in the HBD molar ratio may affect the solubility of drugs, and not all in the same way. Different drugs may interact differently with different DESs, hence influencing their solubility levels.

In work on curcumin compounds as photosensitizers in antimicrobial photodynamic therapy, maximum solubilization values were obtained with NADES mixtures of glucose:sucrose (1:1) (GS) and ChCl:maleic acid (3:1) (CM), at 0.05211 mg/mL and 0.0667 mg/mL, respectively (Wikene et al., 2015). Both NADESs were determined to develop no degradation side-products, as confirmed by HPLC. NADESs are known to feature intermolecular hydrogen bonding, which is implicated in the improvement of curcumin solubilization (Dai et al., 2013a; Liu et al., 2018; Wikene et al., 2015). The differences in solubilization between NADESs primarily arise from distinct H-bonds accepting and donating, and also the steric arrangement of the liquid crystals. In terms of solubility efficiency, the NADESs were equivalent to other solubilizers such as cyclodextrins, surfactants, and aqueous solutions containing alginate or gelatin (Tonnesen, 2006; Wikene et al., 2015). However, the GS and CM NADES exhibited better hydrolytic stability, at up to 2–10 times greater than a cyclodextrin solution and also >1300 times greater than a pH 8 solution buffer (Tonnesen, 2006; Tønnesen, 2002; Tønnesen et al., 2002). In addition, the GS NADES featured better photolytic stability

than the cyclodextrin solution. This result is very promising, as curcumin is susceptible to hydrolysis under alkaline conditions and photochemical reactions (Tønnesen & Karlsen, 1985; Tønnesen et al., 1986; Tønnesen et al., 2002). NADES of GS, GS with curcumin, and photo-assisted GS, are all considered non-toxic to *E. coli*. However, the CM NADES was toxic to the bacteria, especially at 50-fold dilution; in addition, CM with curcumin showed photo inactivation capability towards *E. coli* at a curcumin concentration of 1.25 μM (Wikene et al., 2015). The curcumin dissolved in CM possessed a higher phototoxic effect on *E. coli* than reported in previous studies (Haukvik et al., 2010; Hegge et al., 2013; Wikene et al., 2015). These might be due to synergistic effects between the curcumin and CM (or NADES in general) that increase the phototoxicity (Scheme 2.4). Specifically, photodegradation of curcumin in CM played a vital role in stimulating the production of bacteria-toxic molecules such as free radicals and reactive oxygen species. This shows that NADES has great potential for use as a photosensitizer in antimicrobial photodynamic therapy.



Scheme 2.4: Anti-bacterial curcumin solubilized in NADES maleic acid: ChCl (1:3)

inhibits bacteria growth.

Another study evaluated various combinations of natural components such as sugars, amino acids and organic acids for their effects on NADESs-solubilized berberine (Sut et al., 2017). However, among the thirty-eight types of NADESs tested, the majority showed lower berberine solubility at 22 °C compared to ethanol (2.75 mg/mL) or water (2.10 mg/mL). For instance, proline:ChCl in various ratios (i.e. 1:1, 2:1, and 1:2) was inefficient at dissolving berberine, demonstrating low solubility and stability. In contrast,

a tailor-made NADES of proline:malic acid:lactic acid:water (1:0.2:0.3:0.50) exhibited the highest berberine solubility, at 25.0 mg/mL. An earlier study (Sato et al., 1992) reported that malic acid had a good interaction with berberine, resulting in the formation of soluble berberine malate. This explains the enhancement of berberine solubility in a NADES of proline:malic acid:lactic acid:water (1:0.2:0.3:0.50) (Dai et al., 2015). Sut et al. (2017) concluded that a NADES tailor-made for the solubilization of berberine must incorporate a combination of amino acids, organic acids (malic or lactic), and water. The addition of an appropriate proportion of water to DESs or NADESs may significantly change their physicochemical properties, which subsequently influence drug solubility.

In a work on drug solubility enhancement using DESD, the solubility of itraconazole in a ternary DESD ChCl:glycolic acid:oxalic acid (1:1.6:0.4) was markedly higher than in aqueous solution (5.36 mg/mL, a 53,600-fold increase) (Li & Lee, 2016). The solubilities of other tested drugs lidocaine, posaconazole, piroxicam, and itraconazole were also increased by 28-, 640-, 430-, and 6700-fold relative to the corresponding solubility in aqueous solution. Furthermore, itraconazole, lidocaine, and posaconazole displayed higher solubility in the ternary DESD system of ChCl:glycolic acid:oxalic acid (1: 1.7: 0.3) than in the binary DESD ChCl:glycolic acid (1:2) (Table 2.1). This improved drug solubilization is mainly ascribed to polarity alteration of the basic drug in the acidic DESD through a protonating mechanism. For instance, the carboxylic acids used in a DESD can provide an adequate source of free-flowing protons to cause polarity alteration of the basic drug, hence increasing the drug's solubility (Li & Lee, 2016). The outstanding improvement in drug solubility observed with DESDs has proven the applicability of DESs and their derivatives in improving drug delivery efficiency. Therefore, it is essential

to look for tangible and intangible means for maximizing the usefulness of drugs and their delivery.

2.3 THEDESs

The development of drug-based or active pharmaceutical ingredient (API)-based DESs that boost the pharmacological performance of the API has attracted increasing interest (Pedro et al., 2019; Sánchez-Leija et al., 2014). As introduced in Section 1.0, the term THEDES is widely used for DESs that contain an API as part of their compositions (Aroso et al., 2016). Notably, the thermal properties of THEDES have been found to be different from those of their starting constituents (Aroso et al., 2015). In a recent study (Duarte et al., 2017), NMR analysis has confirmed the formation of a THEDES through hydrogen bonding between menthol and the API (benzoic acid, ibuprofen, and phenylacetic acid). Pulsed-field gradient NMR analysis indicated that the diffusion mechanism of each component of the THEDESs was similar to that observed in ILs and ChCl-based NADESs, in which a species migrates by jumping between holes or voids in the mixture generated via punctual thermal fluctuations (D'Agostino et al., 2011; Duarte et al., 2017).

THEDESs development has drawn intense attention from researchers, especially in the fields of biomedicine and pharmacy. The use of THEDESs in drug delivery applications has been reported to boost efficacy in terms of drug solubility, bioavailability, and skin permeation (Aroso et al., 2015; Aroso et al., 2016; Duarte et al., 2017). A list of THEDESs and their applications in drug delivery is shown in Table 2.2. The application of

THEDESs to drug dissolution enhancement and drug permeation will be further discussed in the following Sections 2.3.1 and 2.3.2.

Table 2.2: List of therapeutic deep eutectic solvent (THEDES) and their potential applications.

THEDES	Ratio	Application	References
Cannabidiol:phosphotidylcholine	N.A	<ul style="list-style-type: none"> • Enhance transdermal delivery • Better accumulation in muscle and skin • Ameliorate edema and inflammation 	(Lodzki et al., 2003)
Ibuprofen:1,8-cineole	2:3	<ul style="list-style-type: none"> • Enhance transdermal delivery 	(Stott et al., 1998)
Ibuprofen:LD-menthol	1:3	<ul style="list-style-type: none"> • Enhance transdermal delivery 	
Ibuprofen:L-menthol	3:7	<ul style="list-style-type: none"> • Enhance transdermal delivery 	
Ibuprofen:L-menthol	1:1	<ul style="list-style-type: none"> • Enhance transdermal delivery 	
Ibuprofen:thymol	2:3	<ul style="list-style-type: none"> • Enhance transdermal delivery 	

THEDES	Ratio	Application	References
Lidocaine:prilocaine	3:7	<ul style="list-style-type: none"> Enhance transdermal delivery 	(Fiala et al., 2010)
Menthol:phenylacetic acid	2:1	<ul style="list-style-type: none"> Anti-microbial agent 	(Aroso et al., 2015; Aroso et al., 2016)
Menthol:phenylacetic acid	3:1	<ul style="list-style-type: none"> Anti-microbial agent 	
Menthol:benzoic acid	3:1	<ul style="list-style-type: none"> Anti-microbial agent 	
Methyl nicotinate:ibuprofen	1:1	<ul style="list-style-type: none"> Enhance transdermal delivery 	(Woolfson et al., 2000)
Capric acid:menthol	4:1, 1:1, 1:4	<ul style="list-style-type: none"> Enhance drug solubility 	(Al-Akayleh et al., 2019)

2.3.1 Drug dissolution enhancement via THEDESs

API-containing THEDES have different dissolutions than does the API alone, because they are in a different form. For example, an ibuprofen-based THEDES exists in liquid form while isolated ibuprofen exists in powder form. As mentioned previously (Williams et al., 2013), the physicochemical properties of the API may influence its dissolution. A more recent study reported that the dissolution of ibuprofen from ibuprofen:menthol (1:3) THEDES was up to 12-fold greater than that of ibuprofen alone (Duarte et al., 2017). The release of ibuprofen by the THEDES was speculated to result from disruption in the interaction between ibuprofen and menthol when the THEDES was dissolved in phosphate-buffered saline (PBS) solution (Aroso et al., 2015).

THEDESs incorporating menthol and one of three different anti-microbial APIs, namely phenylacetic acid (PA), benzoic acid (BA), and acetylsalicylic acid, all showed higher solubility in PBS solution than the corresponding API in powder form. The final THEDESs of menthol:PA (3:1), menthol:PA (2:1), and menthol:BA (3:1) all demonstrated high dissolution efficiency (i.e. 81%, 78%, and 87%), and were observed to be liquid at room temperature (Aroso et al., 2016). It is worth noting that ratio is influential on the stability of the THEDES. THEDES menthol:BA at ratios of 1:1 and 2:1 and menthol:PA at a ratio of 1:1 all formed crystals at room temperature, as observed by polarized optical microscopy analysis. However, as the ratio of menthol in either mixture increased to 3:1, the resulting THEDES was less crystallized. The homogenous THEDESs (with no crystal formation) were stable for at least two months. This level of stability is paramount for the development and design of a safe and effective drug carrier/medium.

2.3.2 Drug permeation

2.3.2.1 Ibuprofen-based THEDESs

Most reported THEDESs were used to enhance transdermal drug delivery (Table 2.3). Among the drugs evaluated in THEDESs applications, ibuprofen was the most-studied; other types of drugs remain poorly explored. A recent study by Duarte et al. (2017) investigated the relationship between ibuprofen solubility in THEDES and its permeability through a membrane, and found that ibuprofen permeability increased proportionately with ibuprofen solubility. A THEDES of menthol:ibuprofen (3:1) showed three-fold increment in permeability through a polyethersulphone membrane (14×10^{-5}

cm s⁻¹), relative to ibuprofen alone (4.6 x 10⁻⁵ cm s⁻¹) (Table 2.3). A drug with permeability greater than 6 x 10⁻⁶ cm s⁻¹ is considered highly permeable according to Duarte et al. (Duarte et al., 2017). Powder ibuprofen was originally categorized as Class II in the biopharmaceutical classification system (Trzenschiok et al., 2019); THEDES menthol:ibuprofen (3:1) could be counted as Class I due to the improvements in solubility and permeability (Figure 2.1). However, existing studies used a synthetic membrane, and it is recommended to use a mammalian skin membrane for a better and more realistic understanding of the interactions and conditions involved in the transdermal delivery system.

Table 2.3: Permeability of API and THEDES systems (Duarte et al., 2017).

APIs/THEDESs	Permeability (10 ⁻⁵ cm s ⁻¹)
Ibuprofen	4.6±0.14
Ibuprofen: menthol (1:3)	14.0±1.53
Benzoic acid	0.9±0.01
Benzoic acid: menthol (1:3)	6.8±0.63
Phenylacetic acid	16.0±2.30
Phenylacetic acid: menthol (1:2)	18.0±0.38
phenylacetic acid: menthol (1:3)	13.0±0.59

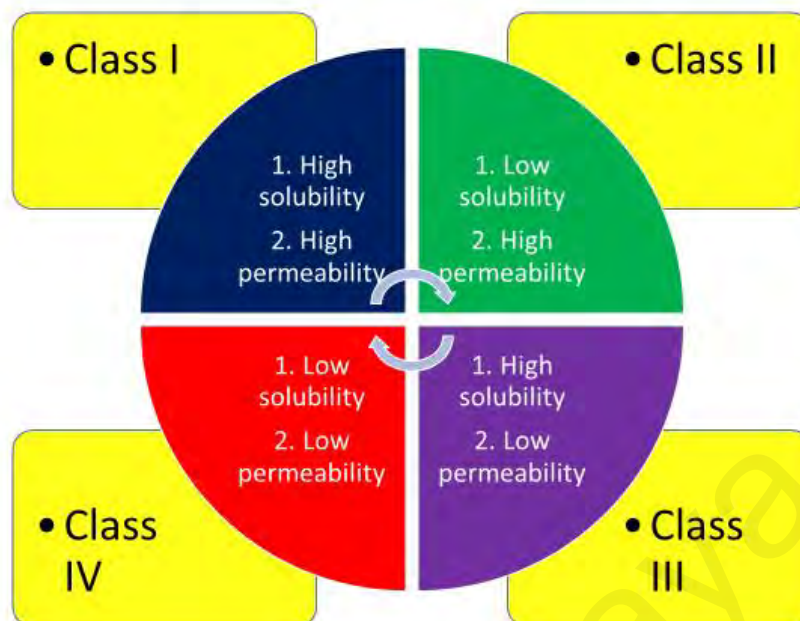
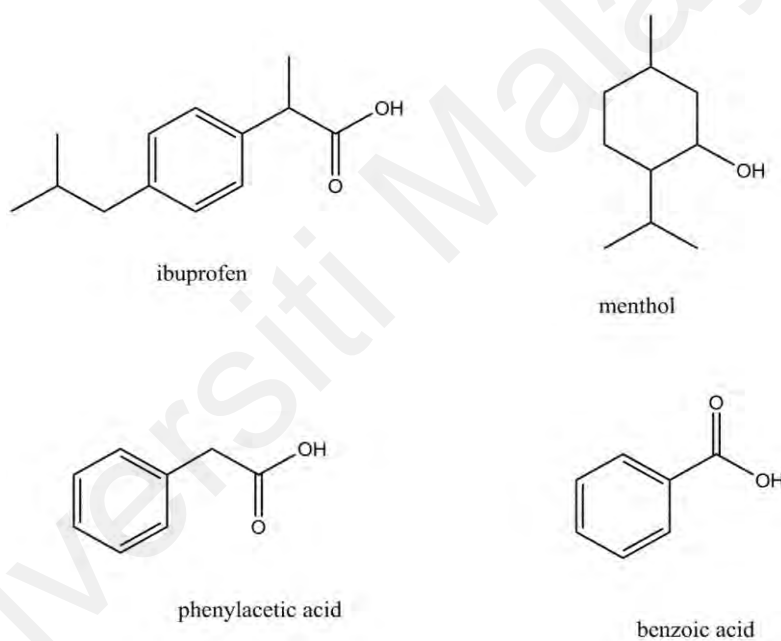


Figure 2.1: Biopharmaceutical characterization system of drugs

2.3.2.2 THEDESs from other drugs

Phenolic acids such as phenylacetic acid and benzoic acid have anti-microbial activities against a wide range of microbial strains (Aroso et al., 2015; Aroso et al., 2016; Papadopoulou et al., 2005; Proestos et al., 2006). Duarte et al. (2017) has investigated the permeability enhancement of these APIs using THEDES formulations (Scheme 2.5). Of tested THEDES, phenylacetic acid:menthol (1:2) presented the highest rate of permeability ($18 \times 10^{-5} \text{ cm s}^{-1}$), surpassing both THEDES benzoic acid:menthol (1:3) and THEDES ibuprofen:menthol (1:3). However, this result was not significantly different from that of individual phenylacetic acid (Table 2.4). Meanwhile, significant improvement of API permeability was found for THEDES benzoic acid:menthol (1:3), at an increment of 7.5-fold increment (i.e. $6.8 \times 10^{-5} \text{ cm s}^{-1}$ compared to $0.9 \times 10^{-5} \text{ cm s}^{-1}$ for benzoic acid alone).

In terms of solubility, THEDES benzoic acid:menthol (1:3) demonstrated higher solubility (218.7 mg/mL) in PBS solution than did the other THEDESs and APIs tested (all <110 mg/mL) (Table 2.4). This greater solubility could be the reason for the higher driving force and penetration into the membrane observed for this formulation. Benzoic acid is categorized as a Class III drug; in this THEDES formulation, it could be promoted to Class I (Figure 2.1).



Scheme 2.5: Components used for the preparation of the THEDESs done by Duarte et al. (2017).

Table 2.4: Solubility of API and THEDES systems in PBS solution pH 7.4. (Duarte et al., 2017)

Systems	Solubility (mg/mL)
Ibuprofen	2.1±0.23
Ibuprofen:menthol (1:3)	26.8±2.62
Benzoic acid	105.0±11.85
Benzoic acid:menthol (1:3)	218.7±21.71
Phenylacetic acid	18.4±2.13
Phenylacetic acid:menthol (1:2)	22.5±2.38
Phenylacetic acid:menthol (1:3)	16.1±1.90

2.3.2.3 Polymerized drug-based DESs

After polymeric eutectic mixture was introduced, polymerized drug-based DESs began to emerge as an alternative to and expansion of efforts in the development of drug transdermal delivery systems. Frontal polymerization of DES systems has been introduced as a way to improve drug transdermal permeation (Mota-Morales et al., 2013; Pedro et al., 2019; Sánchez-Leija et al., 2014). One study prepared two DESs consisting of 3:1 mixtures of methacrylic acid (MAA) or acrylic acid (AC) (acting as HBDs) with lidocaine hydrochloride (LidHCl) (as ammonium salt). These ready-to-polymerize mixtures were then polymerized via free-radical frontal polymerization. During this process, hydrogen bonding between the DES components plays a vital role in maintaining API stability against high-temperature denaturation (Serrano et al., 2012).

Both polymer-based DES systems confer the possibility of a controlled, stimuli-responsive release of LidHCl (e.g. through pH and temperature). LidHCl is an API whose degree of dissolution, ionization, and delivery are pH dependent; an increase of the medium pH leads to the alteration of positively-charged molecules to electrically-neutral species. At every pH and ionic strength condition tested, the kinetics of LidHCl release from poly(methacrylic acid) (PMAA) and poly(acrylic acid) (PAC) DES systems were in the maximum theoretical range (Sánchez-Leija et al., 2014). Proton nuclear magnetic resonance (^1H NMR) spectra attested that LidHCl was the only compound released from the system, and its structure was maintained (not denatured). Therefore, the chance of losing LidHCl efficiency in these DES systems is expected to be low.

The optimum temperature for the frontal polymerization of DESs was at 80–120 °C, with complete conversion of monomers to polymers (i.e. from MAA and AC to PMAA and PAC) (Mota-Morales et al., 2013). In the context of frontal polymerization, this temperature range is considered mild (Pedro et al., 2019). Complete polymerization at a mild temperature is paramount in order to easily control the drug's release and also to avoid the release of potentially toxic by-products.

Another study utilized a DES as a synthesis medium, with it providing essential ingredients for API synthesis. In this work, the lidocaine drug carrier poly(octanediol-*co*-citrate) elastomers (POS) was synthesized using DESs comprised of 1,8-octanediol and lidocaine (Serrano et al., 2012). As the synthesis medium, DES played a vital role in solubilizing citric acid at temperatures below 100 °C and also assisted in incorporating lidocaine with POS constituents. The optimized POS (1,8-octanediol:lidocaine at ratio

1:3) possessed high loading of lidocaine and was able to maintain the lidocaine structure, as validated by ^1H NMR analysis.

In another work (Mano et al., 2017), a gelatin-based THEDES was tested for the development of a fast-dissolving delivery system. The THEDES of ChCl:mandelic acid (1:2) encapsulated in a gelatin membrane was observed to rapidly dissolve in PBS solution and also showed no cytotoxicity effects on a mammalian cell line. This system was found to retain the antibacterial properties of mandelic acid against both Gram-negative bacteria (*E. coli*) and Gram-positive bacteria (*S. aureus*).

Overall, the use of polymerized drug-based DESs for drug delivery applications employs three modalities of action—namely, acting as an essential monomer for the preparation of an elastomer, acting as synthesis media for polymerization, and enhancing drug release efficiency. The polymerized drug-based DESs have great potential for the development of novel drug delivery systems.

2.3.3 Potential biomedical and pharmaceutical applications of DESs

Recently, DESs have been implicated as potential candidates for active anti-bacterial, anti-fungal, anti-viral, and anti-cancer agents. Some positive results are highlighted with an emphasis on their current progress (Figure 2.2).

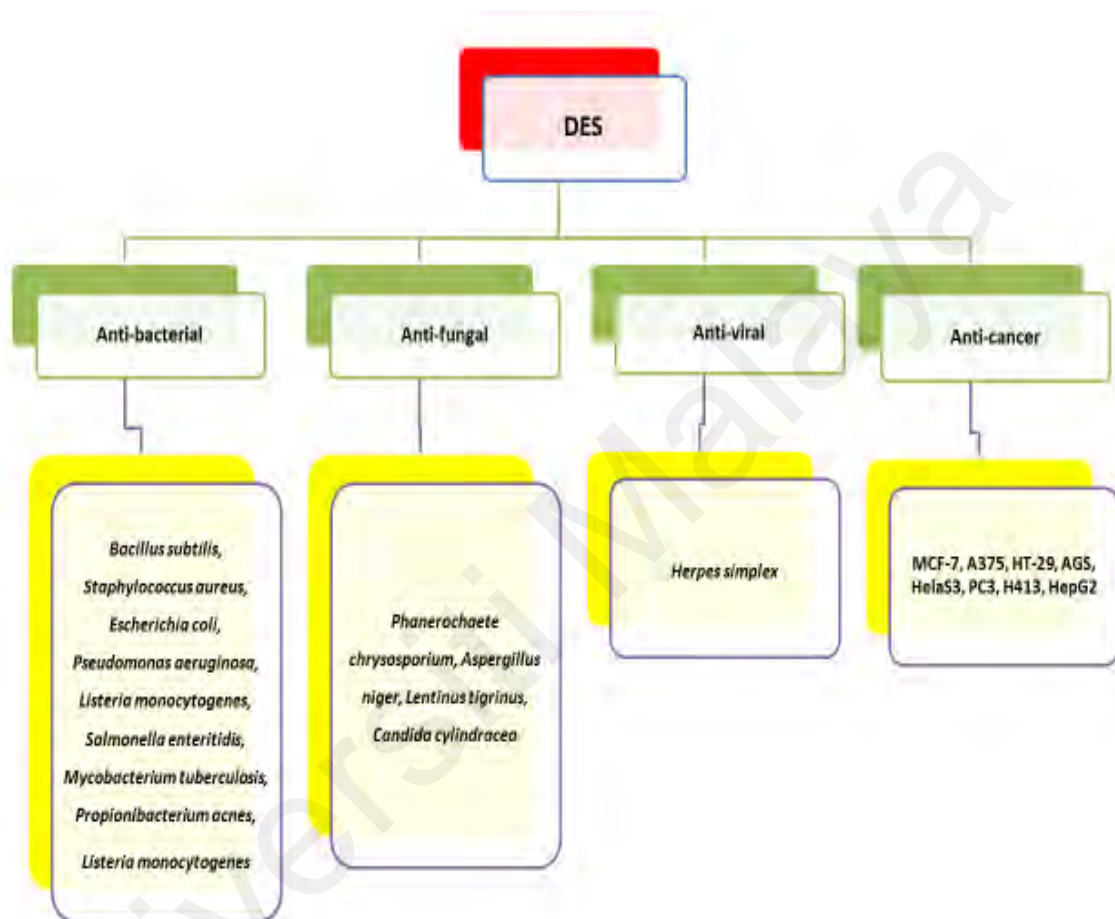


Figure 2.2: Promising biomedical and pharmaceutical activities of DESs.

2.3.1 Anti-bacterial activity

Initial reports of DES anti-bacterial activity were made by Hayyan's group (Hayyan et al., 2013b; Hayyan et al., 2013c) and involved two sets of DESs, namely cholinium- and phosphonium-based, that were evaluated for activity against diverse

bacteria species. Of the two, phosphonium-based DESs showed higher inhibition of both Gram-positive and Gram-negative bacteria (Gram-positive: *Staphylococcus aureus*, *Bacillus subtilis*; Gram-negative: *Pseudomonas aeruginosa*, *Escherichia coli*). Notably, both sets of DESs also showed higher anti-bacterial activities than their corresponding individual components. Since similar types of HBDs (i.e. triethylene glycol, glycerine, and ethylene glycol) were used in these two experiments, the results proved that the type of salt plays an important role in determining the anti-bacterial activity of a DES. Other researchers have commented that DESs at lower concentrations are non-toxic to bacteria, but at higher concentrations, their anti-bacterial activities are significantly more acute than those of their individual components (Wen et al., 2015).

In another evaluation of DES anti-bacterial activities, a number of DESs were tested against *Staphylococcus aureus*, *Listeria monocytogenes*, *Escherichia coli*, and *Salmonella enteritidis* (Zhao et al., 2015). Inhibition of bacterial growth was observed for organic acid-based DESs including ChCl:*p*-toluenesulfonic acid, ChCl:oxalic acid (1:1), ChCl:levulinic acid (1:2), ChCl:malonic acid (1:1), ChCl:malic acid (1:1), ChCl:citric acid (1:1) and ChCl:tartaric acid (2:1) (Table 2.5). In contrast, alcohol-based, sugar-based, and amine-based DESs exhibited no inhibition of the same bacterial species. Similar trend was reported by Hayyan et al. (2013c) for ammonium-based DESs on the same species of bacteria. When using NADES, again, the organic acid-based DESs demonstrated a considerable anti-bacterial effect, while alcohol-based, sugar-based, and amine-based mixtures showed no inhibition of bacterial growth (Table 2.5).

The interaction between DESs with bacterial membrane components is another important factor that influence their anti-bacterial activities. Different types of DESs can have different membrane's interaction to the different types of bacteria. For instance, a series of ChCl-based DESs (i.e., ChCl:urea, 1:1; ChCl:acetamide, 1:1; ChCl:glycerol, 1:1; ChCl:ethylene glycol, 1:1) exhibited acute anti-bacterial activities against *E. coli* with 72.8–93.8% inhibition at concentration 0.75 M (Wen et al., 2015). This was speculated due to the role of choline anion and cholinium cation from DES that may interact with bacteria peptidoglycan (i.e., polysaccharide backbone) and other polysaccharide chains through electrostatic interaction or hydrogen bonding, which eventually cause cell membrane disruption. Such anti-bacterial activity interactions were also observed in previous studies on other choline-based salts or compounds against a wide range of bacteria (Hou et al., 2013; Pernak & Chwała, 2003; Petkovic et al., 2010; Ventura et al., 2014). On the other hand, in comparison between Gram-negative and Gram-positive bacteria, ChCl:oxalic acid (1:1) demonstrated less inhibition towards Gram-negative bacteria such as *P. mirabilis* (49 mm), *S. typhimurium* (45 mm), *P. aeruginosa* (50 mm) and *E. coli* (47 mm) compared to Gram-positive bacteria, *S. aureus* (73 mm) (Radošević et al., 2018). This is because the presence of additional lipopolysaccharide membrane on the Gram-negative bacteria cell wall may hinder the interaction and permeability of ChCl:oxalic acid (1:1). This again proved that the DES composition and types of HBD are also highly responsible in determining the anti-bacterial properties of DESs towards different types of bacteria.

Table 2.5: Anti-bacterial activities of DESs/NADESs against various bacteria strains.

DESs/NADEs	Bacterial inhibition (in cm)								References
	<i>L. monocytogenes</i>	<i>S. aureus</i>	<i>S. enteritidis</i>	<i>E. coli</i>	<i>P. aeruginosa</i>	<i>B. subtilis</i>	<i>P. mirabilis</i>	<i>S. typhimurium</i>	
Betaine:malic acid:proline (1:1:1)	–	4.90, 4.50, 4.40	–	4.40, 2.20	4.50, 3.80, 3.00	–	6.20, 4.50, 4.70	2.40, 2.70	(Radošević et al., 2018)
Betaine:malic acid:glucose (1:1:1)	–	5.10, 4.70, 4.40	–	2.80, 2.30	5.00, 4.50, 2.80	–	7.30, 6.50, 4.40	3.00, 2.80, 3.40	(Radošević et al., 2018)
Citric acid:proline (1:1)	–	5.00, 4.60, 4.40, 4.80	–	4.90, 4.40, 3.30, 4.60	4.40, 4.50, 2.40, 5.00	–	4.70, 5.60, 4.40, 6.80	3.30, 3.70, 2.60, 4.40	(Radošević et al., 2018)

DESs/NADEs	Bacterial inhibition (in cm)								References
	<i>L. monocytogenes</i>	<i>S. aureus</i>	<i>S. enteritidis</i>	<i>E. coli</i>	<i>P. aeruginosa</i>	<i>B. subtilis</i>	<i>P. mirabilis</i>	<i>S. typhimurium</i>	
Citric acid:glucose:glycerol (1:1:1)	–	4.60, 4.40	–	3.40, 2.20	4.70, 4.40	–	8.30, 4.90	5.10, 5.70	(Radošević et al., 2018)
Citric acid:fructose:glycerol (1:1:1)	–	5.10, 4.80, 4.30	–	5.00, 4.50, 3.80	5.10, 4.30, 2.80	–	8.10, 7.60, 5.00	5.50, 4.20, 3.70	(Radošević et al., 2018)
ChCl: <i>p</i> -toluenesulfonic acid (1:1)	0.70	1.12	1.20	1.71	–	–	–	–	(Zhao et al., 2015)
ChCl:oxalic acid (1:1)	1.50	1.97, 5.00, 5.50, 5.00	1.93	2.48	5.00, 4.90, 4.90	–	4.90	4.50	(Radošević et al., 2018)

DESs/NADEs	Bacterial inhibition (in cm)								References
	<i>L. monocytogenes</i>	<i>S. aureus</i>	<i>S. enteritidis</i>	<i>E. coli</i>	<i>P. aeruginosa</i>	<i>B. subtilis</i>	<i>P. mirabilis</i>	<i>S. typhimurium</i>	
ChCl:levulinic acid (1:1)	0.97	1.00	1.60	1.65	–	–	–	–	(Zhao et al., 2015)
ChCl:malonic acid (1:1)	0.93	1.32	1.17	1.53	–	–	–	–	(Zhao et al., 2015)
ChCl:malic acid (1:1)	1.10	1.50	1.22	1.92	–	–	–	–	(Zhao et al., 2015)
ChCl:citric acid (1:1)	1.30	1.58	1.77	1.93	–	–	–	–	(Zhao et al., 2015)
ChCl:tartaric acid (1:1)	1.10	1.50	1.50	1.76	–	–	–	–	(Zhao et al., 2015)

DESs/NADEs	Bacterial inhibition (in cm)								References
	<i>L. monocytogenes</i>	<i>S. aureus</i>	<i>S. enteritidis</i>	<i>E. coli</i>	<i>P. aeruginosa</i>	<i>B. subtilis</i>	<i>P. mirabilis</i>	<i>S. typhimurium</i>	
MTPPB:glycerol (1:3)	–	NI*	–	NI	0.70	NI	–	–	(Hayyan et al., 2013b)
MTPPB:ethylene glycol (1:3)	–	0.15	–	0.70	0.45	0.75	–	–	(Hayyan et al., 2013b)
MTPPB:triethylene glycol (1:3)	–	0.30	–	0.50	0.35	NI	–	–	(Hayyan et al., 2013b)
ChCl:urea (1:2)	NI	NI	NI	3.70	–	NI	NI	NI	(Hayyan et al., 2013c; Zhao et al., 2015)

DESs/NADEs	Bacterial inhibition (in cm)								References
	<i>L. monocytogenes</i>	<i>S. aureus</i>	<i>S. enteritidis</i>	<i>E. coli</i>	<i>P. aeruginosa</i>	<i>B. subtilis</i>	<i>P. mirabilis</i>	<i>S. typhimurium</i>	
ChCl:acetamide (1:2)	NI	NI	NI	NI	–	–	–	–	(Zhao et al., 2015)
ChCl:ethylene glycol (1:2)	NI	NI	NI	NI	–	–	–	–	(Hayyan et al., 2013c)
ChCl:glycerol (1:2)	NI	NI	NI	NI	–	–	–	–	(Zhao et al., 2015)
ChCl:1,4-butanediol (1:4)	NI	NI	NI	NI	–	–	–	–	(Zhao et al., 2015)
ChCl:triethylene glycol (1:4)	NI	NI	NI	NI	–	–	–	–	(Hayyan et al., 2013c)

DESs/NADEs	Bacterial inhibition (in cm)								References
	<i>L. monocytogenes</i>	<i>S. aureus</i>	<i>S. enteritidis</i>	<i>E. coli</i>	<i>P. aeruginosa</i>	<i>B. subtilis</i>	<i>P. mirabilis</i>	<i>S. typhimurium</i>	
ChCl:xylitol (1:1)	NI	NI	NI	NI	–	–	NI	NI	(Zhao et al., 2015)
ChCl:D-sorbitol (1:1)	NI	NI	NI	NI	–	–	NI	NI	(Zhao et al., 2015)
ChCl: <i>p</i> -toluenesulfonic acid (1:1)	0.70	1.12	1.20	1.71	–	–	–	–	(Zhao et al., 2015)
ChCl:oxalic acid (1:1)	1.50	1.97	1.93	2.48	–	–	–	–	(Zhao et al., 2015)
ChCl:levulinic acid (1:2)	0.97	1.00	1.60	1.65	–	–	–	–	(Zhao et al., 2015)

DESs/NADEs	Bacterial inhibition (in cm)								References
	<i>L. monocytogenes</i>	<i>S. aureus</i>	<i>S. enteritidis</i>	<i>E. coli</i>	<i>P. aeruginosa</i>	<i>B. subtilis</i>	<i>P. mirabilis</i>	<i>S. typhimurium</i>	
ChCl:malonic acid (1:1)	0.93	1.32	1.17	1.53	–	–	–	–	(Zhao et al., 2015)
ChCl:malic acid (1:1)	1.10	1.50	1.22	1.92	–	–	–	–	(Zhao et al., 2015)
ChCl:citric acid (1:1)	1.30	1.58	1.77	1.93	–	–	–	–	(Zhao et al., 2015)
ChCl:tartaric acid (2:1)	1.10	1.50	1.50	1.76	–	–	–	–	(Zhao et al., 2015)
ChCl:xylose:water (1:1:1)	NI	NI	NI	NI	–	–	–	–	(Zhao et al., 2015)

DESs/NADEs	Bacterial inhibition (in cm)								References
	<i>L. monocytogenes</i>	<i>S. aureus</i>	<i>S. enteritidis</i>	<i>E. coli</i>	<i>P. aeruginosa</i>	<i>B. subtilis</i>	<i>P. mirabilis</i>	<i>S. typhimurium</i>	
ChCl:sucrose:water (5:2:5)	NI	NI	NI	NI	–	–	–	–	(Zhao et al., 2015)
ChCl:fructose:water (5:2:5)	NI	NI	NI	NI	–	–	–	–	(Zhao et al., 2015)
ChCl:glucose:water (5:2:5)	NI	NI	NI	NI	–	–	–	–	(Zhao et al., 2015)
ChCl:maltose:water (5:2:5)	NI	NI	NI	NI	–	–	–	–	(Zhao et al., 2015)

Abbreviation: ChCl (choline chloride), no inhibition (NI), methyltriphenylphosphonium bromide (MTPPB)

2.3.2 Anti-fungal activity

The screening of DES anti-fungal activity has been paid less attention in comparison to their anti-bacterial spectrum. Juneidi et al. (2016) evaluated the ChCl-based DESs for activity against various fungi such as *Lentinus tigrinus*, *Phanerochaete chrysosporium*, *Candida cylindracea*, and *Aspergillus niger*, revealed the highest anti-fungal activity for ChCl:zinc chloride (1:2) followed by ChCl:malonic acid and (1:1) and DES ChCl:*p*-toluenesulfonic acid (1:3). Additionally, the DESs had higher anti-fungal activities than did their respective starting materials. This finding is consistent with a previous work by the same group (Juneidi et al., 2015), where ChCl:ethylene glycol (1:2) showed higher anti-fungal activity against *Aspergillus niger* than its individual starting materials. The differences in anti-fungal activity between DESs and their individual components are probably due to the synergistic effects resulting from DES formation (Hayyan et al., 2013b). Another possible factor is hydrogen bonding between the salt anion and HBD, which may change the physicochemical properties of the mixture (Hayyan et al., 2015b). Specifically, the charge delocalization that develops through hydrogen bonding is expected to cause the mixture to be more toxic (Modica-Napolitano & Aprille, 2001).

A comparison of ChCl-based and *N,N*-diethylethanolammonium chloride (EAC)-based DESs revealed higher anti-fungal activity for the latter against *Aspergillus niger* (Juneidi et al., 2015). The highest anti-fungal activities ascribed that DES types I, II, and IV, which contain metal salts that interact ionically, have higher anti-fungal activities than do type III DESs, which contain amides and polyols such as urea, glycerol, and ethylene glycol. Details on the classification of all types of DES can be obtained from Table 2.6. The ionic

interaction between metal and salt contributes in the anti-fungal attributes of DESs types I, II, and IV. Meanwhile, a mild anti-fungal effect was observed for ChCl:urea (1:2), with MIC 138.5 mg/mL (Juneidi et al., 2015). This is because the urea is not toxic to the fungi and might even be used as a fertilizer and nitrogen source for fungal growth (Abreu et al., 2010; Azizullah et al., 2011). The mechanism of DES toxicity towards fungi is speculated to involve stimulating dehydrating effects, similar to those induced by CaCl₂ (a dehydrating agent) (Cardellini et al., 2015; Cardellini et al., 2014).

Table 2.6: Main categories of DESs (Smith et al., 2014).

Type	DES mixtures
I	Organic salts + metal
II	Organic salt + hydrate metal salt
III	Organic salt + HBD
IV	Metal salt + HBD

2.3.3 Anti-viral activity

A recent study (Zakrewsky et al., 2016) has shown that DES CAGE possesses anti-viral activities against two types of viruses, namely herpes simplex virus type-1 (HSV-1) and herpes simplex virus type-2 (HSV-2), via a neutralization mechanism. Specifically, HSV-1 and HSV-2 were completely neutralized from infecting the cells at <1.0% CAGE, as confirmed by the absence of viral plaques after incubation (Figure 2.3). However, this finding was not discussed further, which leaves unanswered many questions pertaining to the anti-viral activity of CAGE. For instance, virus neutralization

mechanisms normally involve the specific binding of antibody to the virus receptor (He et al., 2015; Klasse & Sattentau, 2001; Mandel, 1984; O'Shea et al., 2016); how does the neutralization of HSV-1 and HSV-2 by CAGE occur? Is there any specific binding to the HSV-1 and HSV-2 receptors? Therefore, there is still need for additional assessment and verification of the mechanism of action for CAGE, along with elucidating the interactions between CAGE and the viruses. It is important that the anti-viral DESs be well-characterized, including their biological activities on other, non-pathogenic microorganisms. Although only one study has reported on the anti-viral activity of a DES, its promising results may prompt the scientific community to continue the effort and pursue all stages of anti-viral validation, including *in vitro*, *in vivo*, and pre-clinical.

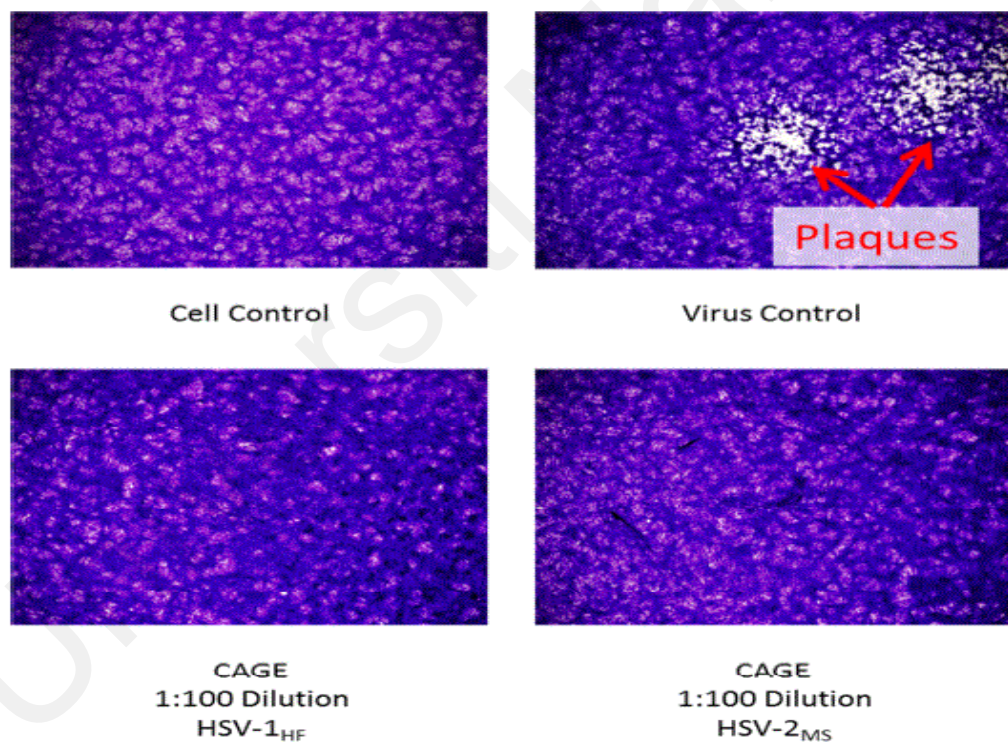


Figure 2.3: HSV-1 and HSV-2 were neutralized by CAGE (Zakrewsky et al., 2016).

2.3.4 Anti-cancer activity

Although research is still in its preliminary stages, the reported anti-cancer behavior of DESs is promising (Hayyan et al., 2015b; Hayyan et al., 2016b; Mbous et al., 2017b). It has been agreed that the complexation of two or more components in DESs could produce more acute destructive impacts on cancer cells, compared to the individual components alone (Mbous et al., 2017a). Ammonium-based DESs have been evaluated for selectivity towards cancer cell lines and a normal cell line (OKF6, human oral keratinocytes) (Hayyan et al., 2015b). The selectivity index values of the ammonium-based DESs varied across the range of > 2 or ≤ 2 (Table 2.7). ChCl:glycerine (1:3) was found to be selective against a human malignant melanoma cell line (A375) and a human breast cancer cell line (MCF-7); ChCl:ethylene glycol (1:3) was selective against a human colon adenocarcinoma cell line (HT-29), a human prostate cancer cell line (PC3), a human liver hepatocellular cell line (HepG2), and MCF-7 cells; ChCl:urea (1:3) was selective against HT29, PC3, HepG2 and MCF-7 cells; and ChCl:triethylene glycol (1:3) was selective against A375 and MCF-7 cells (Table 2.7). All DESs displayed low selectivity indexes for the carcinoma-derived human oral keratinocyte cells (H413). Other synthetic anti-cancer drugs, such as alisiaquinol, 4-hydroxy tamoxifen and piperidinyl-diethylstilbestrol, have shown lower selectivity indexes (i.e. < 2) (Badisa et al., 2009). Based on the aforementioned results, the existence of DESs with acute toxicity against cancerous cells while being harmless to non-cancerous cells is not implausible. Better understanding of the mechanism of DES toxicity against cancer cells may generate new ideas for developing a DES tailor-made for anti-cancer applications.

Table 2.7: Selectivity index of ammonium-based DESs for cancer cells compared to human oral keratinocyte cell line (Hayyan et al., 2015b).

DES	Selectivity Index					
	MCF-7	PC3	A374	HepG2	HT29	H413
ChCl:glycerine	2.162	1.542	2.615	1.309	1.662	0.864
ChCl:ethylene glycol	2.579	2.120	1.979	2.812	2.282	1.232
ChCl:urea	2.789	2.949	1.374	2.172	2.263	1.204
ChCl:triethylene glycol	2.137	1.692	2.797	1.902	1.974	1.782

It has been implied that one mechanism by which DESs induce cancer cell death is through disruption of the cell membrane. Cell membrane disruption was observed in three different cancer cell lines (MCF-7, a human gastric cancer cell line [AGS], and a human cervical cancer cell line [HelaS3]) when the permeability dye stained-cells were treated with ChCl:fructose (2:1), ChCl:glucose (2:1), and DAC:TEG (1:3). In another study on ammonium-based DESs, the cell membranes of MCF-7 cells were disrupted, as evidenced by increased release of lactate dehydrogenase (LDH).

As a result of the cell membrane disruption in MCF-7 cells, reactive oxygen species (ROS) generation is increased, stimulating apoptosis (Hayyan et al., 2015b). Increased ROS generation was also observed in other cancer cells, such as WRL-68, HelaS3, and AGS, when they were treated with ChCl:glucose (2:1), ChCl:fructose (2:1), and

diethylethanolammonium chloride:triethylene glycol (1:3) (DAC:TEG) (Mbous et al., 2017b). When comparing the anti-cancer effects of NADESs and DESs, cells treated with DES DAC:TEG (1:3) exhibited more acute redox stress than those treated with NADES ChCl:fructose (2:1) and ChCl:glucose (2:1). Based on the MTT cell viability analysis, DES DAC:TEG (1:3) also exhibited higher anti-cancer activity compared to NADES ChCl:fructose (2:1) and ChCl:glucose (2:1) (Hayyan et al., 2016b; Mbous et al., 2017b). When tested on a variety of cancer cells such as PC3, HeLaS3, AGS, A375, and MCF-7 cells, the IC_{50} of DESs was in the range of $34 \leq IC_{50} \leq 120$ mM, which is more toxic than those of NADESs (range $98 \leq IC_{50} \leq 516$ mM).

DESs may also initiate cancer cell destruction through changing the cell morphology. Cancer cells treated with ChCl:fructose (2:1), ChCl:glucose (2:1), and DAC:TEG (1:3) display lethal impacts to their morphology (Mbous et al., 2017b), with the cells being shrunk significantly and the field filled with many dead cells. DES DAC:TEG (1:3) demonstrated more pronounced destructive effects than did NADES ChCl:glucose (2:1) and ChCl:fructose (2:1).

The weaker anti-cancer effects of NADESs are expected due to their natural-origin starting materials, for which cellular tolerances are high. For example, glucose and fructose are utilized as sources of energy and carbon for cell proliferation. Glucose is basically metabolized through glycolysis to produce energy, and also provides metabolic intermediates for other cellular pathways such as the pentose phosphate pathway and tricarboxylic acid pathway (Butler, 2004). Cancer cells require more nutrients (e.g. sugars, salts, and amino acids) due to higher energy demands for their cell growth. This

is probably the key reason for the greater cellular tolerance of ChCl:fructose (2:1) and ChCl:glucose (2:1) by cancer cells in comparison to DAC-TEG (1:3).

A computational simulation approach using the conductor-like screening model for real solvent (COSMO-RS) analysis has been applied to understand the interaction between NADESs and cancer cell membranes (Hayyan et al., 2016b). From this analysis, the hypothetical thermodynamic behavior of an individual compound in a solvent and its affinity towards other materials/compounds could be derived. The analysis of NADESs proposed that mixtures such as ChCl:glucose:water (5:2:5), ChCl:fructose:water (5:2:5), and ChCl:sucrose:water (4:1:4) have strong interactions with cell membrane surfaces, and their aggregation or accumulation on the cell membrane may possibly destroy the cancer cells. However, another two NADESs, ChCl:malonic acid (1:1) and ChCl:glycerol:water (1:2:1), showed only mild interaction with the cell membrane. Their anti-cancer effects are perhaps not mainly attributable to aggregation at the cell surface, but instead through other mechanisms such as ROS generation or DNA degradation.

The anti-cancer activities of DESs are highly correlated with their starting materials, the combination of hydrogen bond acceptor (HBA) and HBD, and the cell type used. For example, organic acid-based NADESs exhibited higher anti-cancer activities against two cancer cell lines (HeLa and MCF-7 cells) than did non-organic acid-based NADESs (Radošević et al., 2018). This finding is in accordance with the results obtained by Hayyan et al. (2016b), in which higher anti-cancer activities were observed for organic acid-based NADES (i.e. malonic acid) than sugar-based NADESs. Nevertheless, the anti-cancer activity of NADES betaine:malic acid:proline (1:1:1) was lower than other NADESs.

This is probably due to suppression of the toxic potential of malic acid by betaine and proline, highlighting the tunability of DESs. The adjustable/tunable properties of DESs are their main feature in the context of creating therapeutic anti-cancer agents with selective destructive effects towards targeted cancerous cells.

2.4 Biosafety aspects of DESs

The most commonly applied method in the preparation of DESs is a combination of mixing and heating (El Achkar et al., 2019; Mbous et al., 2017a). In this method, DES formation results from the mixing of the salt/HBA and HBD compounds while heating at temperatures below 100 °C (Abbott et al., 2004; Smith et al., 2014). DESs also can be prepared using the grinding method, in which the DES's initial ingredients are ground using a mortar and a pestle at room temperature until a clear liquid is formed (Florindo et al., 2014). Freeze-drying is a method infrequently used for the preparation of DESs. In this method, aqueous solutions of the DES's initial ingredients are mixed and frozen, then freeze-dried to form a homogenous viscous liquid (Gutiérrez et al., 2009). Overall, DES preparation may only take 30 min to 6 h depending on the initial ingredients and composition of the DES (Choi, 2011; Hayyan et al., 2013a; Hayyan et al., 2014).

It has been attested that DESs are noticeably more easily synthesized than are ILs (Benvenuti et al., 2019); the preparation of DESs is also considered “greener” and low-cost. The starting materials for preparing DESs are inexpensive and also widely available. The preparation involves simple procedures, requires no purification process, and also requires no organic/volatile solvents.

Before implementing DESs in drug delivery applications, a complementary investigation of toxicology profiles is indispensable to ensure their biosafety and health impacts. The following paragraphs highlight prior reports that assessed the toxicological behaviors of DESs on different organisms and environments.

The first study of DES cytotoxicity (Hayyan et al., 2013c) revealed lethal effects for cholinium-based DESs against an aquatic organism, *Artemia salina* (brine shrimp). The DESs also showed higher toxicity against *Artemia salina* than did their individual ingredients. Similar findings were also observed for phosphonium-based DESs against the same aquatic organism (Hayyan et al., 2013b). In contrast, other reports (Juneidi et al., 2015; Juneidi et al., 2016; Wen et al., 2015) indicated that DESs were less toxic than their individual ingredients on the European carp, *Cyprinus carpio*, and also the freshwater organism *Hydra sinensis*. For example, the lethal concentration at 50% (LC₅₀) of DES ChCl:glycerine on *C. carpio* fish (>8,000 mg/L) was considerably higher than those of its aqueous individual ingredients (Juneidi et al., 2015). This indicates that the synergistic interaction between the salt and HBD during DES formation not only changes the physical properties of the individual ingredients but also their chemical properties towards different organisms.

In an investigation of DES toxicity towards plants (common wheat, *Triticum aestivum*), DES ChCl:glycerine and ChCl:glucose exhibited low phytotoxicity in all evaluated parameters, with an effective concentration 50% (EC₅₀) >20,000 mg/L; this is in contrast to the low EC₅₀ of DES ChCl:oxalic acid (i.e. EC₅₀ > 5,325.26 mg/L) (Radošević et al.,

2015). The toxicity of ChCl:oxalic acid can be attributed to its acidity (pH: 2.08). Interestingly, the results from all tested DESs showed no significant inhibition of seed germination.

Wen et al. (2015) provided an evidence that ChCl- and ChAc-based DESs may induce morphological distortion of garlic plants (*Allium sativum*). However, treatment with DESs resulted in a significant improvement in root growth as compared to their individual ingredients, especially for the case of DES ChCl:glycerol (1:1). This indicates that the hydrogen bonding interaction between ChCl and glycerol in DES form can ameliorate their toxicity towards *Allium sativum*.

An *in vitro* study on human embryonic kidney cells (HEK-293) revealed that DES formation resulted in increased toxicity level compared to the individual (IC₅₀ values: 3.52-75.46 mM) (Ahmadi et al., 2018). Nevertheless, DES toxicity was still significantly lower than that of the most extensively used IL, 1-octyl-3-methyl-limidazolium chloride ([C₈mim][Cl]), which has an IC₅₀ of 0.02 mM. This is in a good agreement with a previous report on the potential toxicity of ILs and DESs (Kudlak et al., 2015). As a closer representation of toxicity in therapeutic use, the *in vivo* toxicity of DESs on mice was investigated by Hayyan et al. (Hayyan et al., 2015b). Their results showed that ChCl-based DESs had more lethal effects on mice than did the corresponding individual ingredients. This study also highlighted that ChCl-based DESs considerably increased the level of aspartate transaminase (AST) (by 5.7- to 9.5-fold) while maintaining normal levels of alanine aminotransferase (ALT) and alkaline phosphatase in liver serum. This

alteration in the ratio of AST:ALT suggests that a hepatocellular form of liver injury occurred following DES treatment.

2.5 Nanotechnology in drug delivery

Drug delivery system using nanomaterials, has attracted significant interest from academia and industry. The ever-rising number of diseases, particularly malignant tumors have prompted scientific community to explore new and innovative routes for cancer therapy. Nanotechnology is no stranger in cancer therapeutics. There is a significant research dedicated to nanotechnology, nanoscience, and nano-medicine (Figure 2.4). The potential ability of nanotechnology to combat cancer diseases has led to numerous number of studies conducted on cancer nanotherapeutics (Shi et al., 2016). Despite numerous promising results, it may be a long journey before graphene can be implemented clinically. At the nanoscale, the drug loaded nano-carrier can penetrate tumors deeply with a high-level specificity.

Many drug nano-carriers were explored, they are either organic, such as CNT and graphene, or inorganic, such as iron oxide and gold. However, similar to other nano-carriers, pure graphene is deemed to be potentially toxic to humans and the environment (Chen et al., 2016). The agglomeration of graphenes on the cell membrane is presumed to play a profound role in their cellular toxicity (Zhang et al., 2010). The sharpened edges of graphene may act like blades, severely cutting or inserting into the cell membrane (Akhavan & Ghaderi, 2010; Dallavalle et al., 2015). Subsequently, graphene may lead to cell death through cell membrane destruction, oxidative stress, inflammatory response, necrosis, DNA damage, or apoptosis (Ou et al., 2016). It is therefore very vital to modify

its surface chemistry for better biocompatibility interactions with biological systems, thereby implementing graphene in nanomedicine.

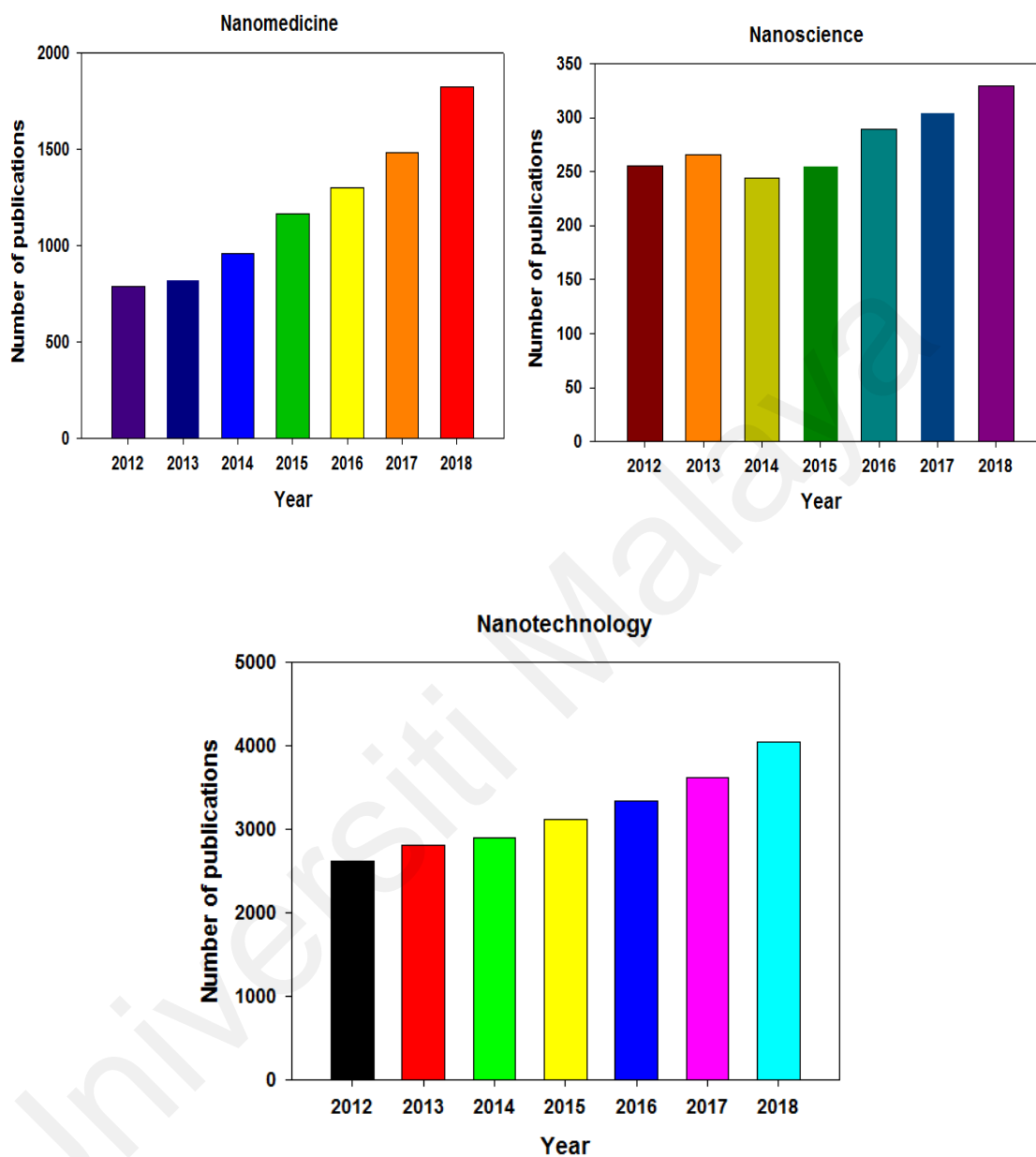


Figure 2.4: Number of publications dedicated to nanotechnology, nanoscience, and nanomedicine.

2.5.1 Conventional functionalization of graphene

Nanotoxicology is correlated to the shape, size, charge and surface chemistry of the nanoparticle (Bitounis et al., 2013). These features can be controlled by surface modification or functionalization of targeted nanoparticles. Functionalization is a process that includes the addition of new functional groups to the surface of the carbon through a chemical or physical attachment (Bottari et al., 2017). According to this connection, functionalization is classified into two types, i.e., covalent and non-covalent functionalization. With hydrophobic or hydrophilic functional groups on the surface of the carbon, dispersibility of graphene can be improved effectively. This is caused by reducing the strength of polar-polar interactions and/or the splitting of bulky structures. However, there are some adverse concerns regarding the conventional functionalization methods, such as involving a very long and complicated procedure, time consuming, requirement of high temperature (above 100 °C), use of highly corrosive solution, and as a result, highly cost protocols (Georgakilas et al., 2002; Georgakilas et al., 2012; Martínez et al., 2003). The preparation of most commonly used polymer-modified nanoparticles (e.g., polyethylene glycol (PEG) and poly(lactic-co-glycolic acid)) have been associated with several drawbacks such as a long preparation process, non-robust or insufficient surface binding of polymer, and a shortage of functional groups on the polymer's backbone (Liu et al., 2013; Liu et al., 2008; Moghimi & Szebeni, 2003; Park et al., 2009). Therefore, there is a high demand to seek for a new method of functionalization of graphene by using a safe and green functionalization agent which is none/low toxic, facil procedure, low cost, and applicable to synthesis with no highly corrosive or acidic solution.

2.5.2 Functionalization of carbon nanomaterials using DES

There is an escalation of attraction on the applications of DESs that arise as promising green multi-task mixtures. Recently, DESs have been introduced as novel functionalizing agents for CNMs (Hayyan et al., 2015a). The DESs conferred surface modifications and new functional groups on the DES-functionalized CNMs. Interestingly, there was a significant enhancement in the dispersion stability of the DES-functionalized CNMs in various organic solvents and also in aqueous solutions (Abou-Hamad et al., 2017; Hayyan et al., 2015a). Therefore, DESs are regarded as promising functionalization agents for carbonaceous nanomaterials. Table 2.8 shows the advantages of DES over the conventional functionalizing agents.

Table 2.8: Comparison between DES and conventional functionalization agents

	DES	Conventional functionalizing agents
Starting materials cost	Low	High
Procedure	Simple, easy, straightforward	Complicated and tedious, time-consuming, require professional skills
Volatility and flammability	None	Volatile and flammable
Handling temperature	< 100 °C	> 100 °C
Corrosivity and acidity	Under investigation	Corrosive and acidic

DES-functionalized CNMs have been studied for the electrochemical sensing application (Abo-Hamad et al., 2017). DES choline chloride (ChCl):urea (1:2) was the best functionalizing agent in the improvement of CNM-modified glassy carbon electrode performance. Generally, DES-functionalized graphene showed better performance in alkaline- and acidic-based electrolytes compared to DES-functionalized carbon nanotube (CNT). This is due to the higher surface area of graphene than that of CNT, in which possess greater enhancement effect on electrocatalytic activities in KOH- and H₂SO₄-based electrolytes.

Although several studies conducted have contributed to great achievement in the field, there are still many questions to unravel their answers. For instance, there are concerns about the application of DES-functionalized CNMs related to their toxicity and potential adverse effects on human health and natural environment. Up to now, there has been no study that investigate the cellular and biological behaviors of the DES-functionalized CNMs. There is also an urgent need to look for other potential avenues of DESs, especially as promising functionalizing agents for nano-carriers in drug delivery systems.

CHAPTER 3: RESEARCH METHODOLOGY

The research methodology consists of a multi-step procedure including DES preparation, graphene oxidation/functionalization and their characterization, drug loading, followed by the biological assays as illustrated in Figure 3.1.

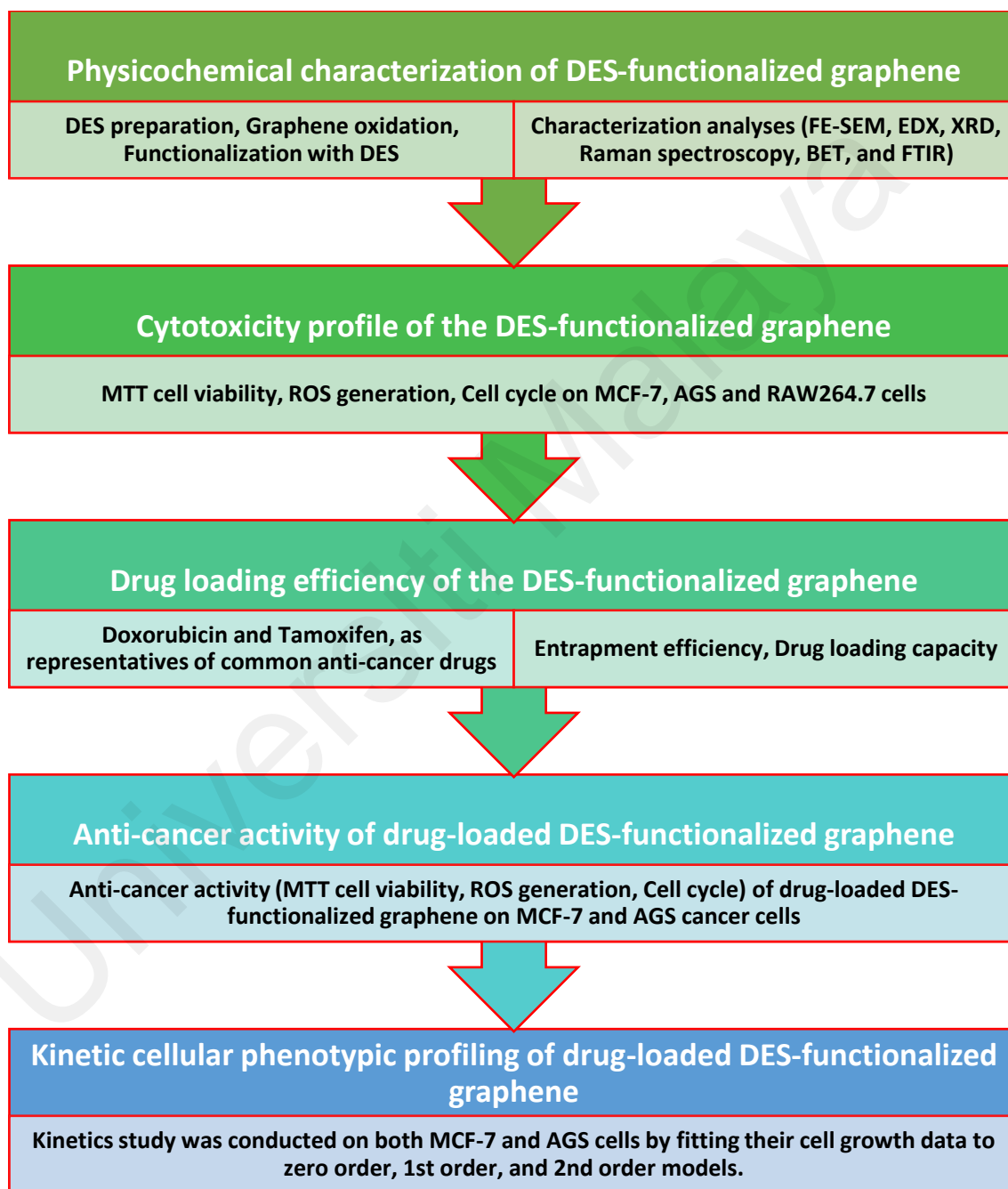


Figure 3.1: The research methodology sequences.

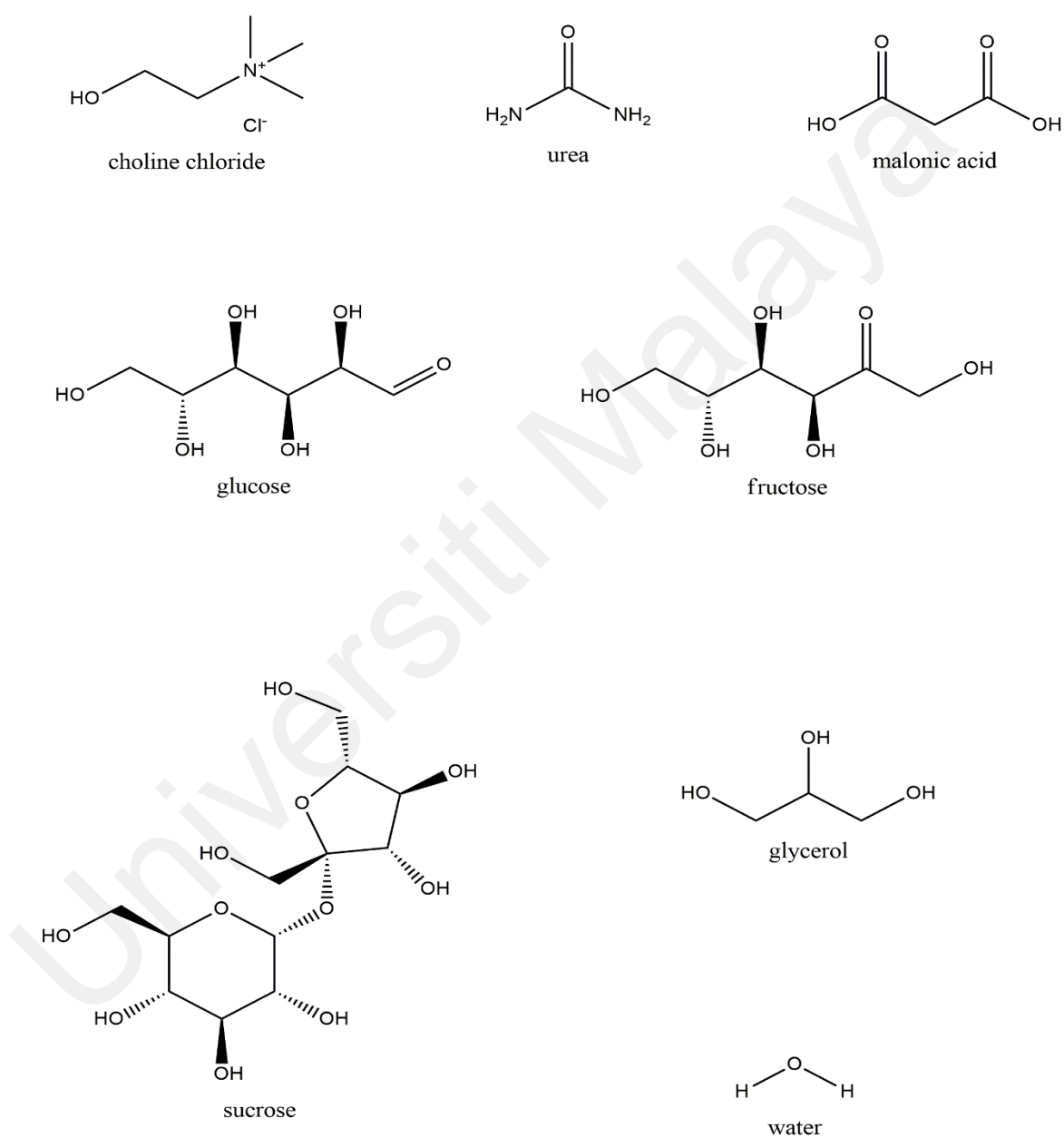
3.1 Preparation of binary and tertiary DESs

The chemicals used for the synthesis of DESs, such as choline chloride (ChCl) (purity $\geq 98\%$) and malonic acid (purity 99%), were purchased from Sigma-Aldrich. Anhydrous D(+)-glucose (purity $>98.0\%$), and D(-)-fructose (purity $>98.0\%$) were provided by R&M Chemicals. Urea and sucrose (purity $\sim 99.5\%$) were obtained from Merck (Darmstadt, Germany). Potassium permanganate (KMnO_4) with a purity of 99% was provided by UnivarSolutions (Ajax, Netherlands). Firstly, all solid chemicals listed in Table 3.1 were dried overnight in a vacuum oven (Mettler VO500, ThermoFisher, America) at 60 °C. Next, salts and HBDs were mixed according to the given molar ratio at 70 °C via magnetic stirring. The resulting homogenous mixtures were transferred to well-sealed and dark (covered with aluminium foil) bottle. The use of DESs as functionalizing agents for graphene was selected based on the cytotoxicity screening tests done by previous studies (Hayyan et al., 2015b; Hayyan et al., 2016b; Mbous et al., 2017a). Table 3.1 shows the composition, molar ratios and abbreviation of the selected binary and tertiary DESs.

Table 3.1: List of abbreviations for DES-functionalized Gr

Type of DESs				Abbreviations
Salt	HBD	Tertiary components	Molar ratio	
ChCl	Urea	-	1:2	GrU
ChCl	Glucose	-	2:1	GrG
ChCl	Fructose	-	2:1	GrF
ChCl	Malonic acid	-	1:1	GrMa

ChCl	Glucose	Water	5:2:5	GrGW
ChCl	Fructose	Water	5:2:5	GrFW
ChCl	Sucrose	Water	4:1:4	GrSW
ChCl	Glycerol	Water	1:2:1	GrGlyW



Scheme 3.1: Molecular structures of the starting components of the DESs prepared in this work.

3.2 Preparation of oxidized graphene and DES-functionalized graphene

Sixty-nanometer flakes of graphene nanoplatelets (Gr) were purchased from Graphene Supermarket (USA) with a purity of 98.5%, average thickness of 7 nm, lateral particle size ~ 3–7 microns, and specific surface area <math><15\text{ m}^2/\text{g}</math>. The oxidation and functionalization of graphene were followed the protocol of Hayyan et al. (2015a). Pristine graphene (PrGr) was dried overnight at 100 °C under vacuum in order to remove impurities (e.g., water) on carbon surface. Some of the dried PrGr were oxidized using a 1.0 M KMnO_4 solution by the following steps: (1) 200 mg of dried PrGr were mixed with 7 ml of the prepared KMnO_4 solution in a 20-ml glass vial; (2) the mixture was subjected to sonication using an ultrasonic bath (model JAC2010P, JAC, Korea) at 70 °C for for 3 h; (3) the oxidized graphene (OxGr) was washed with distilled water several times and filtered using a PTFE membrane (pore size: 0.45 μm) and a vacuum pump (Sartorius 220V, Germany) until the filtrate solution became transparent and neutral (pH=7); (4) the OxGr was collected and dried in the vacuum oven at 100 °C for 3 h; and (5) the OxGr was kept in a desiccator at room temperature.

In the functionalization procedure, the dried OxGr (200 mg) were mixed with 7 ml of DES in a 20-ml glass vial and sonicated using ultrasonic bath at 70 °C for for 3 h. Similar to the oxidation procedure, the DES-functionalized Gr was subsequently washed with distilled water and filtered until a clear and neutral solution was obtained. The collected DES-functionalized Gr was dried in the vacuum oven at 100 °C for 3 h. Then, the DES-functionalized Gr was stored in a desiccator at room temperature. Table 3.1 shows the abbreviation of each DES-functionalized Gr.

3.3 Physicochemical characterization

The samples including PrGr, OxGr and DES-functionalized Gr samples were analysed by FTIR using a Perkin Elmer 1600 FTIR spectrometer. The samples were measured in the range of 450–4000 wavenumbers for five times scanning repetition. Raman spectra were recorded using a Renishaw System 2000 Raman spectrometer under a wavelength of 514 nm. To detect morphology changes, graphene images were obtained using a Quant FEG 450 field emission scanning electron microscope (FE-SEM). An energy dispersive X-ray (EDX) analysis using an Oxford Inca 400 spectrometer was conducted to determine surface elements of the unfunctionalized Gr and DES-functionalized Gr. The surface area of the samples was analysed from the nitrogen adsorption-desorption isotherm at 77 K based on the Brunauer–Emmett–Teller (BET) method. This analysis was conducted using an automatic Micromeritics ASAP-2020, TRISTAR II 3020 Kr. X-Ray diffraction (XRD) analysis using a Panalytical Empyrean diffractometer was also performed to investigate the structural phases of the Gr samples.

3.4 Cell culture

Human breast adenocarcinoma MCF-7 was purchased from Cell Lines Service (Eppelheim, Germany, 3000273). Gastric adenocarcinoma AGS and macrophage cell line RAW264.7 were acquired from American Type Cell Collection (ATCC). MCF-7 was cultured in Roswell Park Memorial Institute (RPMI) medium supplemented with 10% heat inactivated fetal bovine serum (FBS), and 1% penicillin-streptomycin. AGS and RAW264.7 were grown in Dulbecco's Modified Eagle's Medium (DMEM) supplemented with 10% FBS, and 1% penicillin-streptomycin. Cells were incubated at 37 °C in a 5% CO₂ humidified incubator and subcultured every 2-3 days.

3.5 Cell viability assay

The 3-(4,5-dimethylthiazol-2-yl)-2,5-diphenyltetrazolium bromide (MTT) (Sigma-Aldrich, USA) cell viability assay was performed. The cells (1.5×10^4 /well) were seeded in 96-well plates (Corning, USA) for 24 h incubation at 37 °C in a 5% CO₂ humidified incubator. The Gr samples were added the next day, and the cells were again incubated for 24 h. Subsequently, the supernatant was replaced with fresh medium (to avoid sample interference in the reaction) followed by the addition of 2 mg/mL of MTT reagent. After a 2 h incubation, the MTT reagent was discarded and 100% DMSO was added. The absorbance was then read at 570 nm. The cell viability percentage was calculated relative to untreated cells (Eq. 3.1), and the 50% inhibitory concentration (IC₅₀) was determined by using Graph Pad Prism 5 software.

$$\text{Cell viability (\%)} = \left(\frac{a}{b}\right) \times 100 \quad (3.1)$$

Where *a* is the absorbance of treated cells and *b* is the absorbance of untreated cells.

3.6 Cell cycle assay

Cell cycle analysis of MCF-7, AGS and RAW264.7 cells was performed using a flow cytometer. After 24 h of treatment with the Gr samples, the cells were harvested and fixed with 1 mL of 70% cold ethanol, then incubated overnight at –80 °C. Next, the cells were washed and suspended in phosphate-buffered saline (PBS). Cells were stained with 200 µL of propidium iodide/ribonuclease A (RNase A) for 1 h at 37 °C before the DNA content was analyzed using a flow cytometer (BD FACSCanto™II).

3.7 Reactive oxygen species (ROS) assay

ROS were measured using the modified method of Hajrezaie et al. (2015). After the cells were treated with Gr samples for 24 h, dihydroethidium dye was loaded into the live culture for 30 min. Next, the cells were harvested, fixed and washed with wash buffer (i.e., PBS solution). The cells suspended in PBS solution was transferred and filtered into the flow cytometry tube. The dihydroethidium probe is oxidized into a red fluorescent product (i.e., ethidium) in the occurrence of ROS. The percentage of cells with ROS was determined using a BD FACSCanto II flow cytometer (BD Biosciences).

3.8 Drug loading

Graphene samples that included PrGr, OxGr and DES-functionalized Grs were dissolved in DMSO (100 µg/mL) and vortexed for complete dispersion. 50 µg/mL of the drug (Tamoxifen (TAM) or Doxorubicin (DOX)) was also dissolved in DMSO and vortexed. The two solutions were mixed and sonicated in a Branson 2800 ultrasonic bath for 15 min, and then shaken in orbital shaker ES-20 (Grant-Bio, UK) at 28 °C overnight (i.e., 12 h). The mixture was then centrifuged in an ultracentrifuge (Hermle Z233 MK-2, Lausanne) at 14,000 rpm for 30 min. The pellet was collected and stored at –20 °C. The supernatant was measured at a wavelength of 290 nm using a Synergy HTX multimode reader (Biotek, US). The entrapment efficiency % (EE) and drug loading capacity % (DL) were calculated by measuring the unbound drug in the supernatant at absorbance peak 290 nm (TAM) or 480 nm (DOX), and using Eqs 3.2 and 3.3, as reported previously (How et al., 2013).

$$EE (\%) = (W_{\text{drug added}} - W_{\text{unbound drug}}) / W_{\text{initial drug}} \times 100 \quad (3.2)$$

$$DL (\%) = (W_{\text{drug added}} - W_{\text{unbound drug}}) / W_{\text{graphene}} \times 100 \quad (3.3)$$

Where EE is the entrapment efficiency, DL is the drug loading capacity, and W is the weight. Drug-loaded Gr samples were labelled as shown in Table 3.2.

Table 3.2: List of abbreviations for drug loaded-Gr.

Drugs	Gr	Drug-loaded Gr
TAM	PrGr	TAM-PrGr
	OxGr	TAM-OxGr
	GrU	TAM-GrU
	GrG	TAM-GrG
	GrF	TAM-GrF
	GrMa	TAM-GrMa
	GrGW	TAM-GrGW
	GrFW	TAM-GrFW
	GrSW	TAM-GrSW
	GrGlyW	TAM-GrGlyW
DOX	PrGr	DOX-PrGr
	OxGr	DOX-OxGr
	GrU	DOX-GrU
	GrG	DOX-GrG
	GrF	DOX-GrF
	GrMa	DOX-GrMa
	GrGW	DOX-GrGW
	GrFW	DOX-GrFW
	GrSW	DOX-GrSW
	GrGlyW	DOX-GrGlyW

3.9 Cellular kinetic responses

Cell viability, cytotoxicity, and cell growth were evaluated in real time using the xCELLigence Real-Time Cell Analysis (RTCA) system (Roche Applied Science, ACEA Biosciences, USA). This instrument works by measuring the impedance of electron flow on a gold-coated electron plate induced by adherent cells (viable cells). Changes in electrical impedance reflect a combination of cell number, degree of cell viability, cell adhesion, and cell morphology. Briefly, 50 μL of cell culture medium was loaded in each well of a 96-well E-plate and background readings taken. Next, cells (5×10^3 /well) were seeded into the E-Plate. After 24 h, samples of each Gr (100 $\mu\text{g}/\text{mL}$) were added to the E-plate, and cellular impedances were continuously measured every 1 h for 96 h. Change in electrical impedance was converted to the unitless parameter cell index (CI). Wells containing Gr samples and-cell culture medium alone (without cells) were used as a baseline in order to avoid any possible interference with the samples.

CHAPTER 4: RESULTS AND DISCUSSIONS

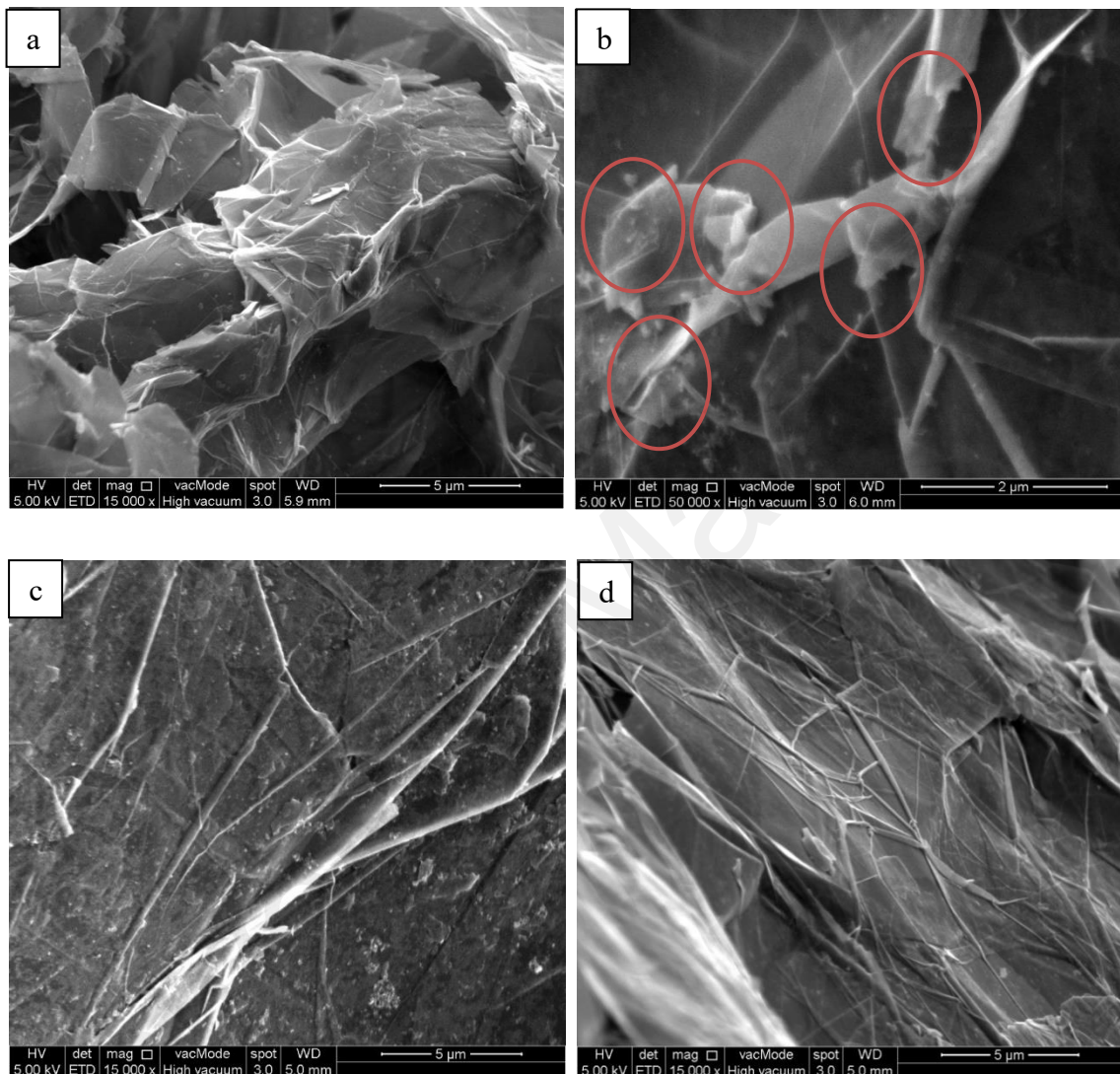
4.1 Characterization of DES-functionalized graphene

It is essential for any nano-based study to investigate the nanoscale properties and morphology changes on the nanoparticle prior and following oxidation and functionalization processes. Therefore, in this section FE-SEM, EDX, FTIR, XRD, Raman, and BET characterizations were conducted as illustrated in the next subsections.

4.1.1 Morphological changes and surface elements of the graphenes (FE-SEM and EDX analysis)

The morphology of all samples was visualized using FE-SEM to observe the DES functionalization effects on the structure of the functionalized Grs. Figure 4.1 shows FE-SEM images of (a) PrGr, (b) OxGr, (c) GrU, (d) GrG, (e) GrF, (f) GrMa, (g) GrGW, (h) GrFW, (i) GrSW, and (j) GrGlyW. As shown in Figure 4.1(b), after oxidation, there are several white spots on the surface of the OxGr, indicating the residual oxidants as a result of the oxidation process. Some significant deformation also occurred after oxidation of PrGr. These residual oxidants and deformed structures could enhance dispersibility, and can also be targeted by DES molecules during functionalization (Hayyan et al., 2015a). After DES functionalization, the deformed structures disappeared, especially in the case of GrG, GrU, GrF, and GrGW (Figure 4.1). This is likely due to the induction of restoration or healing effects by the DES molecules. In contrast, the structure of GrMa displayed a significant deformation, implying destruction by the DES ChCl:malonic acid (1:1) (Figure 4.1f). These occurrences (i.e. the deformation and the restoration of the

graphene structure) are in agreement with a previous study reported the functionalization of carbon nanotubes (CNTs) using DESs (Abo-Hamad et al., 2015).



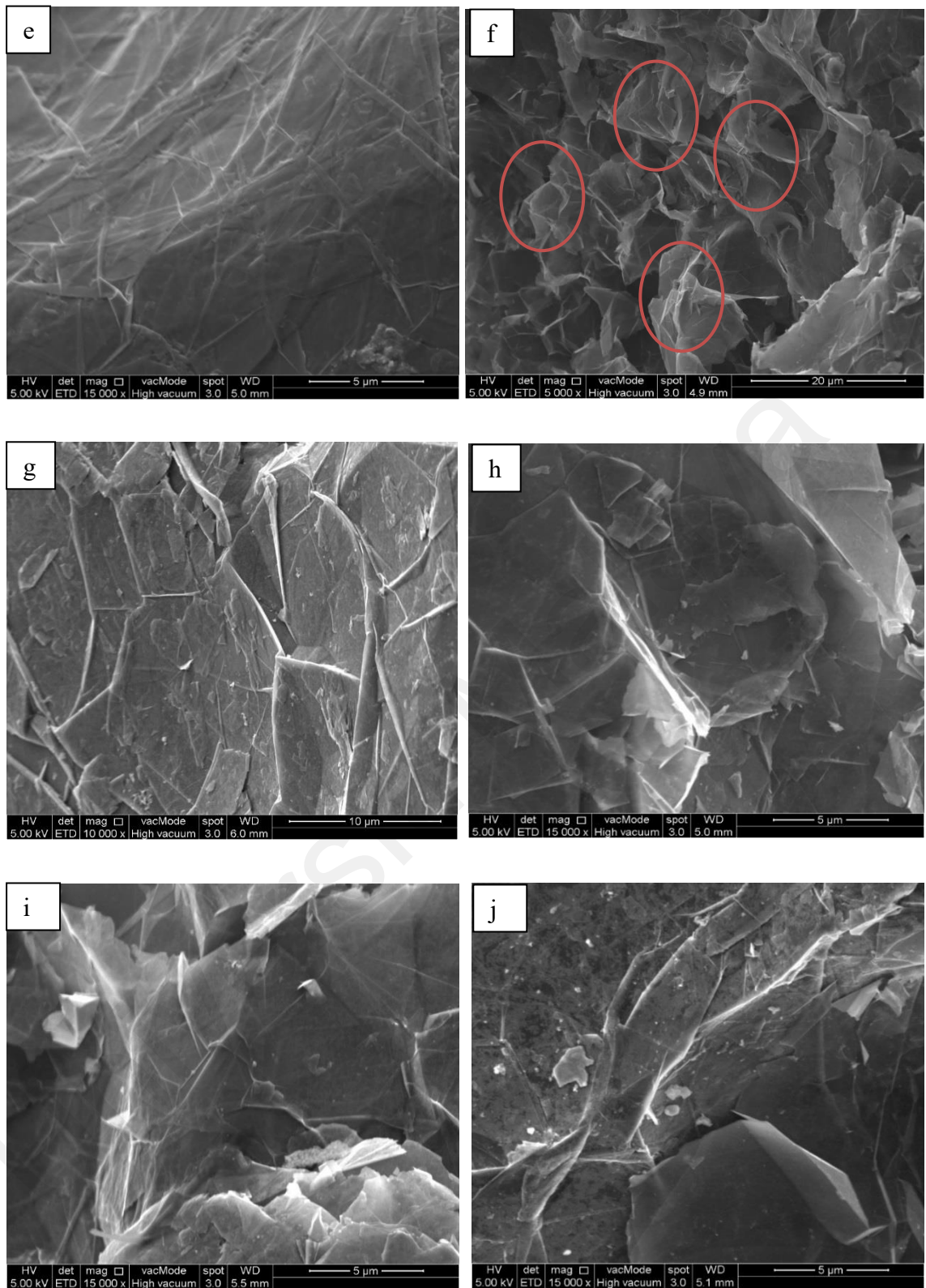


Figure 4.1: FE-SEM images of (a) PrGr, (b) OxGr, (c) GrG, (d) GrU, (e) GrF, (f) GrMa, (g) GrGW, (h) GrFW, (i) GrSW, and (j) GrGlyW.

As expected, carbon was the only one surface element identified for PrGr in the EDX analysis (Table 4.1). Mild oxidation by the KMnO_4 solution introduced new elements onto the surface of the Gr, including 4.73% oxygen (O), 0.46% potassium (K), and 2.99% manganese (Mn). Additional new surface elements appeared following the DES functionalization (i.e., chlorine (Cl) and nitrogen (N)) which were not observed for unfunctionalized Gr samples (Table 4.1). Functionalization using ammonium-based DESs led to the addition of Cl and N elements. In comparison to PrGr, the presence of these additional surface elements (i.e., O, K, Mn, Cl and N) corroborated completion of the oxidation and DES functionalization processes. Hence, this also confirmed the presence of DES-functional groups on the surface of Gr.

Table 4.1: EDX surface elements analysis of PrGr, OxGr and DES-functionalized Gr

Samples	Surface elements, weight %					
	C	O	K	Mn	Cl	N
PrGr	100.00	-	-	-	-	-
OxGr	91.84	4.73	0.46	2.99	-	-
GrU	95.11	2.96	0.12	1.00	0.10	0.71
GrG	95.11	3.24	0.03	1.21	0.07	0.34
GrF	96.08	3.32	0.04	0.15	0.03	0.38
GrMa	94.39	4.34	0.21	0.18	0.08	0.79
GrGW	94.00	2.75	0.40	1.72	0.88	0.24
GrFW	95.37	3.58	0.06	0.49	0.04	0.46
GrSW	95.79	3.79	0.07	0.21	0.07	0.07
GrGlyW	92.64	4.00	0.18	2.52	0.19	0.48

4.1.2 XRD analysis

The details of the XRD patterns are provided in Table 4.2 and Appendix A: Figure 1A. As shown in Table 4.2, the peaks displayed at $2\theta = 26.33, 42.07, 44.62, 49.14, 54.19,$ and 72.69° in PrGr represent the crystalline planes (002), (100), (101), (012), (004) and (014). These crystalline planes were also identified in OxGr and DES-functionalized Gr. This indicates that the structural integrity of Gr was maintained after the oxidation and functionalization process. The most prominent peak was observed at $2\theta = 26.33$, which represented the π - π stacking in graphene (Sun et al., 2016). After the oxidation process, a noticeable diffraction peak that occurred in the crystalline planes (002) at $2\theta = 26.33^\circ$ shifted to 26.59° . The peak intensity of crystalline plane (100), (101), (012), and (014) decreased significantly after the oxidation process. The restacking and exfoliation level of DES-functionalized Gr was greater than that of PrGr, as confirmed by the shift in diffraction peaks to lower or higher 2θ values.

The peak intensities of crystalline plane (002) remained unchanged for all samples. However, the peak intensities of other crystalline planes (i.e., (100), (101), (012), (004) and (014)) either increased or decreased, indicating the effect of the DES functionalization process (Figure 4.2). It is interesting to note that most of the peak intensities of DES-functionalized Gr were lower than those of PrGr. This occurrence has been regularly reported as a result of functionalization for carbon-based nanomaterials such as CNT and graphene (Hamwi et al., 1997; Talaemashhadi et al., 2013; Wang et al., 2013). In a comparison of all Gr samples, GrMa possessed the lowest stacking form (lower 2θ values) and largest interlayered spacing (Table 4.2). This was likely due to the addition of hydrophilic functional groups that substituted the oxygen groups and hence

led to lower stacking levels than the other Gr samples. In contrast, GrU, GrG, GrF and GrSW showed higher stacking levels (higher 2θ values) for overall crystalline planes, implying a lower interlayered spacing (Table 4.2). This was probably due to the addition of hydrophobic functional groups that resulted in a higher level of π - π stacking between the layers.

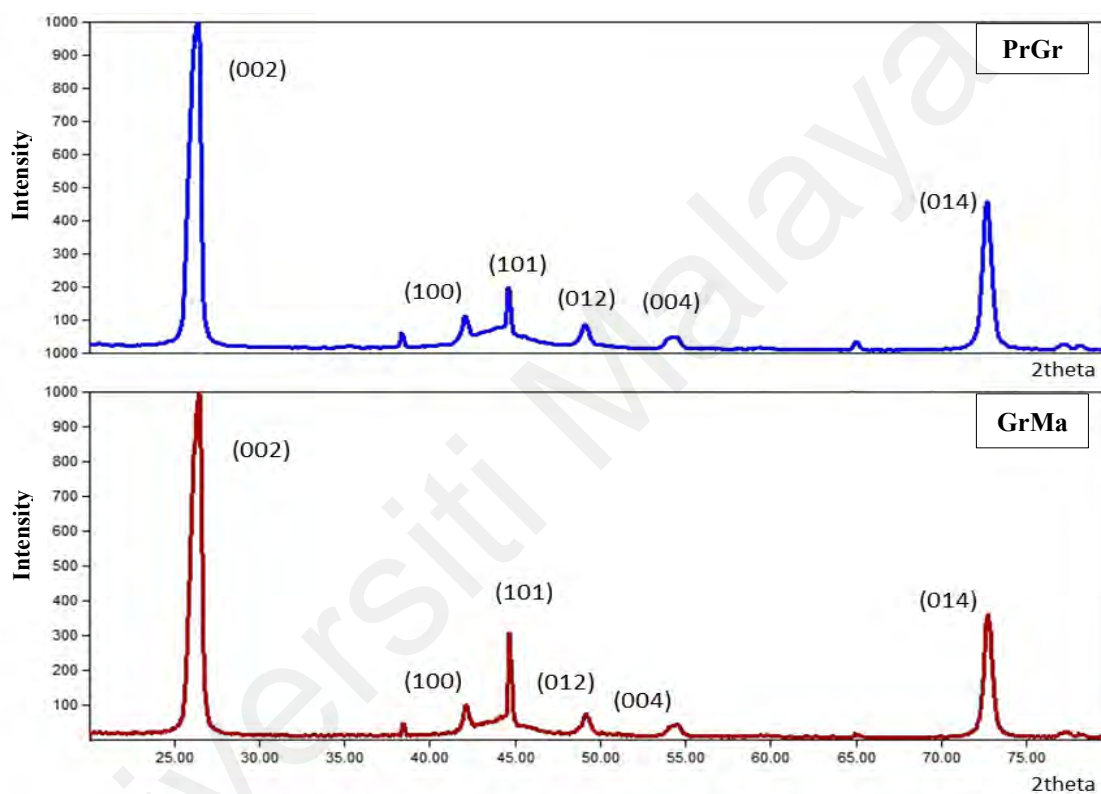


Figure 4.2: XRD patterns of PrGr and GrMa.

Table 4.2: Diffraction speaks obtained from XRD for PrGr, OxGr and DES-functionalized Grs

Sample	Diffraction peak of (002)		Diffraction peak of (100)		Diffraction peak of (101)		Diffraction peak of (012)		Diffraction peak of (004)		Diffraction peak of (014)	
	2 θ (degree)	Intensity										
PrGr	26.33	1000.0	42.07	94.9	44.62	172.8	49.14	65.4	54.19	35.7	72.69	459.7
OxGr	26.59	1000.0	42.23	40.3	44.78	124.1	49.10	24.8	54.32	34.9	72.80	356.4
GrU	26.57	1000.0	42.25	53.0	44.79	346.6	49.33	41.1	54.28	28.2	72.84	440.3
GrG	26.55	1000.0	42.20	48.9	44.74	125.1	49.24	39.2	54.25	30.7	72.80	403.1
GrF	26.57	1000.0	42.21	40.1	44.74	210.0	49.23	30.0	54.35	27.8	72.79	221.3
GrMa	26.47	1000.0	42.14	81.2	44.70	251.7	49.19	56.8	54.10	27.6	72.73	356.2
GrGW	26.56	1000.0	42.13	37.0	44.71	95.2	49.21	32.1	54.47	32.9	72.79	263.8
GrFW	26.59	1000.0	42.22	48.9	44.71	91.2	49.29	42.9	54.30	31.2	72.83	329.6
GrSW	26.63	1000.0	42.31	39.4	44.79	265.0	49.15	23.4	54.31	20.5	72.84	285.0
GrGlyW	26.61	1000.0	42.20	47.7	44.76	102.8	49.19	35.8	54.39	28.6	72.73	301.2

4.1.3 Raman spectroscopy

Raman spectroscopy was used to examine the structural changes in the Gr samples after oxidation and functionalization with DES. As observed in Figure 4.3 for the case of Raman spectra of PrGr: the prominent peaks at approximately 2700 cm^{-1} , 1580 cm^{-1} , and 1350 cm^{-1} indicate 2D, G and D bands, respectively, which is in accordance with previous reports (Hayyan et al., 2015a; Ramirez & Osendi, 2013). The most intense peak was for the G band, which is in good agreement with the previous studies (Ni et al., 2008; Prolongo et al., 2013). Generally, the G band is associated with sp^2 hybridization of the graphitic hexagonal lattice structure, while the D band is related to the carbon lattice defects or disorder caused by sp^3 -bonded hybridized carbon. On the other hand, the 2D band is linked to the structure and number of layers in the stacks (Ferrari et al., 2006).

The intensity ratio of I_D/I_G indicates the degree of oxidation and functionalization (Georgakilas et al., 2012). OxGr exhibited the highest I_D/I_G ratio, which can be ascribed to the destructive effect of the $KMnO_4$. After oxidation, the hybridization of carbon rearranged from sp^2 to sp^3 which hence, resulting in the presence of negatively charged oxygenated functional groups on the graphene's surface structure (Yan et al., 2012b). After functionalization with DES, the intensity ratio of I_D/I_G decreased. This was likely due to the healing effects that occurred from the restoration of sp^2 double bonds in the Gr-structure, implying that the graphene reduction reaction was accompanied by the addition of functional groups. The I_D/I_G ratio of DES-functionalized Gr was also higher than that of PrGR (i.e., > 0.04) (Table 4.3). A significant lattice distortion for the G band and D band was observed on the Gr samples for GrMa, GrGW, GrFW, GrSW, and GrGlyW. The I_D/I_G ratio for GrGlyW was the highest (i.e., 0.07) among the other DES-

functionalized Grs. After the oxidation process, GrU, GrG and GrF were expected to have higher exfoliation or graphene reduction effects, as indicated by the the 2D band shift to lower frequencies compared to OxGr (Ramirez & Osendi, 2013).

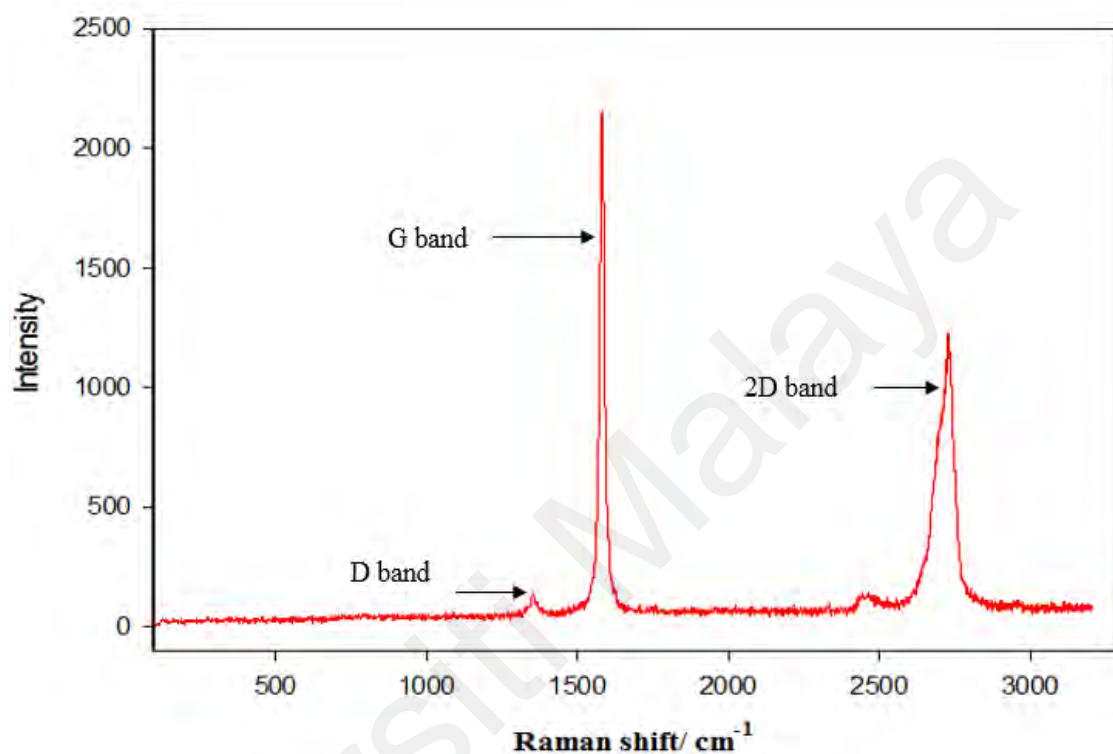


Figure 4.3: Raman spectra of PrGr with identified peaks of 2D, G and D bands.

Table 4.3: Raman spectra of PrGr, OxGr and DES-functionalized Grs.

Sample	G band		D band		2D band		I_D/I_G
	P (cm ⁻¹) ^a	I ^b	P (cm ⁻¹) ^a	I ^b	P (cm ⁻¹) ^a	I ^b	
PrGr	1581.18	2687.46	1355.63	115.22	2726.07	1220.23	0.04
OxGr	1581.09	1846.96	1356.92	254.20	2726.09	1077.98	0.14
GrU	1581.55	1820.98	1357.08	91.25	2724.80	1000.26	0.05

Sample	G band		D band		2D band		I_D/I_G
	P (cm ⁻¹) ^a	I ^b	P (cm ⁻¹) ^a	I ^b	P (cm ⁻¹) ^a	I ^b	
GrG	1580.93	2205.71	1354.01	114.02	2724.80	1215.43	0.05
GrF	1580.85	2266.18	1352.69	122.86	2723.51	1393.53	0.05
GrMa	1579.83	701.52	1365.26	39.14	2726.09	409.49	0.06
GrGW	1579.60	817.00	1356.88	45.63	2724.80	430.34	0.06
GrFW	1579.18	900.16	1361.68	41.99	2723.60	525.24	0.05
GrSW	1579.85	850.98	1367.90	47.44	2724.80	505.94	0.06
GrGlyW	1579.68	845.44	1358.91	62.26	2727.38	478.97	0.07

a: Position of Raman peak and b: Intensity of Raman peak

4.1.4 BET surface area analysis

BET analysis was conducted for PrGr, OxGr and DES-functionalized Grs to elucidate the effect of DES functionalization on the surface area of the Gr-structure. Table 4.4 demonstrates the increase trend in the surface area of Grs following oxidation by KMnO₄, from 14.65 m²/g to 15.06 m²/g. This is in accordance with the previous studies conducted on the oxidation of various carbon-based nanomaterials by different oxidizing agents (Dongil et al., 2011; Pifferi et al., 2014). GrMa exhibited the highest surface area that is attributed to the deformation effect caused by the acidic DES ChCl:Ma (1:1). However, except GrMa, smaller BET surface areas were observed after DES functionalization. This can be ascribed to the healing or recovering effects on the deformed structure of OxGr through the addition of functional groups such as oxygen- and amine-containing functional groups (Abo-Hamad et al., 2017). It is also in good

agreement with the Raman analysis that confirmed the recovery effects that occurred from the restoration of sp^2 double bonds in the structure of graphene.

Table 4.4: BET surface area of PrGr, OxGr and DES-functionalized Grs.

Sample	Surface area (BET) m^2/g
PrGr	14.65
OxGr	15.06
GrU	14.09
GrG	12.83
GrF	12.96
GrMa	39.05
GrGW	11.47
GrFW	11.98
GrSW	6.58
GrGlyW	8.09

4.1.5 FTIR study

The FTIR spectra of the Grs pre- and post-functionalization were performed to characterize the samples (Appendix A: Figure 2A). Several changes in the FTIR spectra were identified after treating with KMnO_4 (Figure 4.4). The spectrum was identified as having several peaks of oxygen-containing functional groups, such as a C=O stretching band at 1742 cm^{-1} , a C-O stretching band at 1165 cm^{-1} , and aldehyde -CH stretching bands at 2923 and 2852 cm^{-1} . In contrast, in the PrGr spectrum, there were hydrophobic functional groups detected in the PrGr including a C-H stretching band at 2312 cm^{-1} , C=C stretching bands at 2106 cm^{-1} and 1611 cm^{-1} , an in-plane C-H bending band at 1061 cm^{-1} , C-H out-of-plane bending bands at 711 cm^{-1} and 870 cm^{-1} , and a =C-H bending band at 646 cm^{-1} (Figure 4.4). This hydrophobic property was responsible for the low dispersion stability of pristine graphene in aqueous solutions (Hayyan et al., 2015a; Wang et al., 2009).

Following DES functionalization, several new functional groups were identified on the DES-functionalized Gr, including oxygen-based functional groups (Figure 4.5). In comparison to other DES-functionalized Gr, GrGW displayed new oxygen-based functional groups namely NO_2 asymmetric stretching band at 1561 cm^{-1} and nitrate NO_2 bending band at 709 cm^{-1} (Figure 4.5a), which were not present in other samples. Functionalization with DESs also introduced several peaks that represented amine-based functional groups, which were not identified in PrGr or in OxGr. For instance, Figure 4.6 shows that amine-based functional groups are detected in the GrGlyW (Figure 4.6a) and GrSW (Figure 4.6b), including aliphatic isonitrile $-\text{N}\equiv\text{C}$ stretching, aliphatic C-N stretching, aromatic isonitrile $-\text{N}\equiv\text{C}$ stretching, NH_2 wagging and twisting, and secondary

amide N-H wagging. Figure 4.6c illustrates the FTIR spectra of Gr after functionalization with DES ChCl:malonic acid (1:1). There are two new functional groups introduced by Gr's functionalization with ChCl:malonic acid, i.e., an aliphatic C=O stretching band at 1736 cm^{-1} and a phenol O-H stretching band at 3438 cm^{-1} , which were not identified in the other DES-functionalized Grs.

This is also in good agreement with the EDX analysis that confirmed additional surface elements, such as N and O, introduced following the DES functionalization. These results suggested that DES functionalization may enhance the hydrophilicity of Gr through the introduction of additional functional groups such as amine- and oxygen-based functional groups. This is supported by previous studies (Abo-Hamad et al., 2017; Hayyan et al., 2015a; Mondal et al., 2016) in which DES-functionalized carbon nanomaterials demonstrated better dispersion stability in an aqueous medium as compared to unfunctionalized Gr. Noteworthy, amine- and oxygen-based functional groups are important in increasing the hydrophilicity of drug carriers (Miao & Scott Obach, 2010; Yazdanian et al., 2004). Furthermore, they also may confer a good dispersion and decent biocompatibility in the cellular biological systems (Lin et al., 2015; Sun et al., 2016; Yan et al., 2012a). Overall, the characterization results advocate that DESs have good potential as functionalizing agents because they induce some surface modifications, including the introduction of new functional groups on the graphene's structure (Table 4.5).

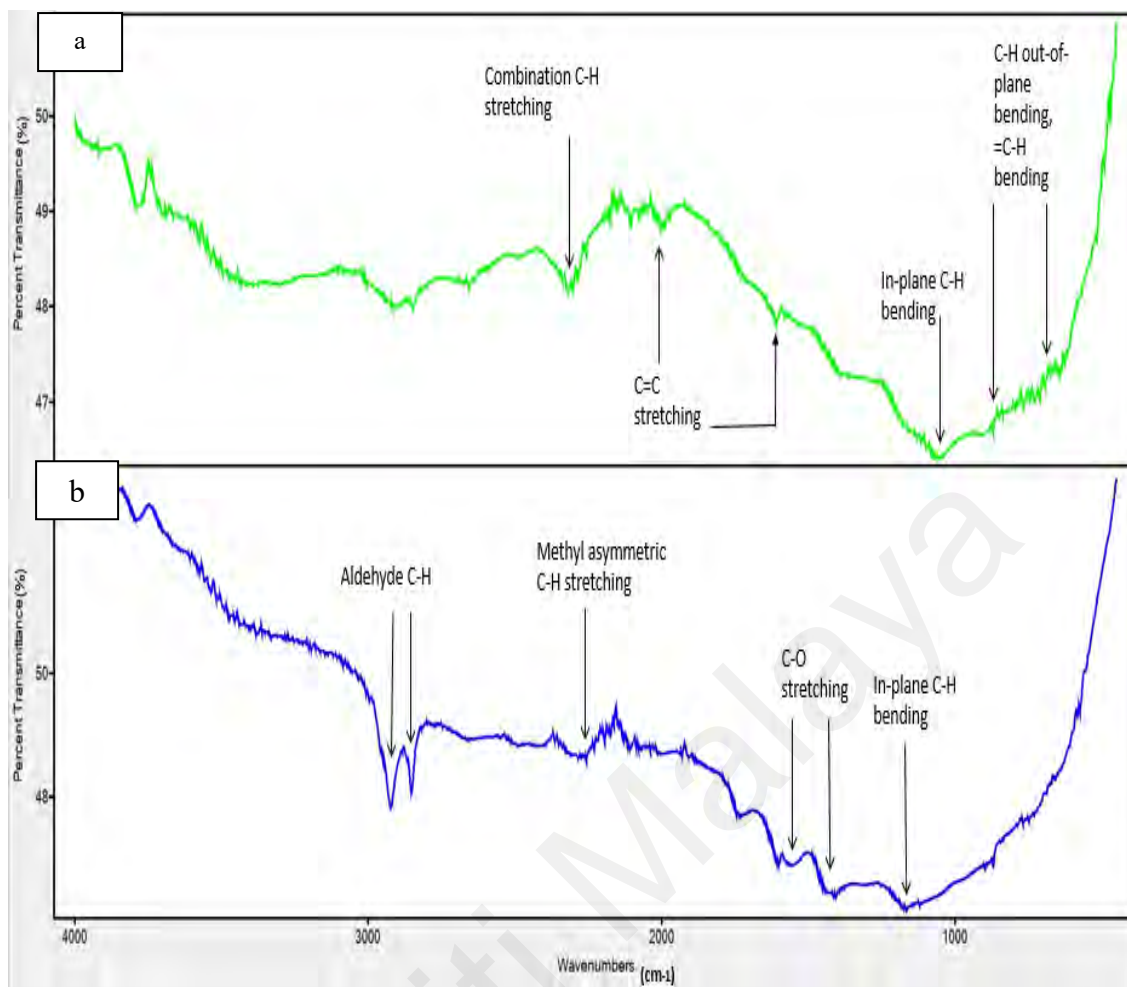


Figure 4.4: FTIR spectra for (a) PrGr and (b) OxGr at wavenumbers 400 to 4000 cm^{-1} .

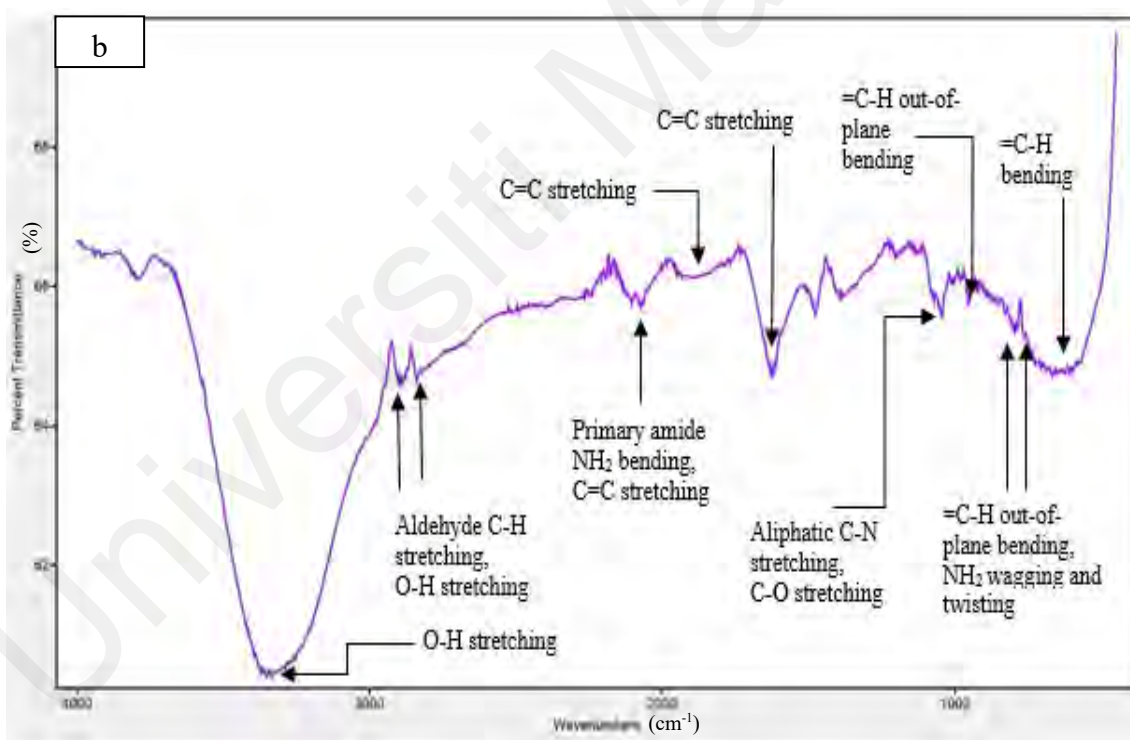
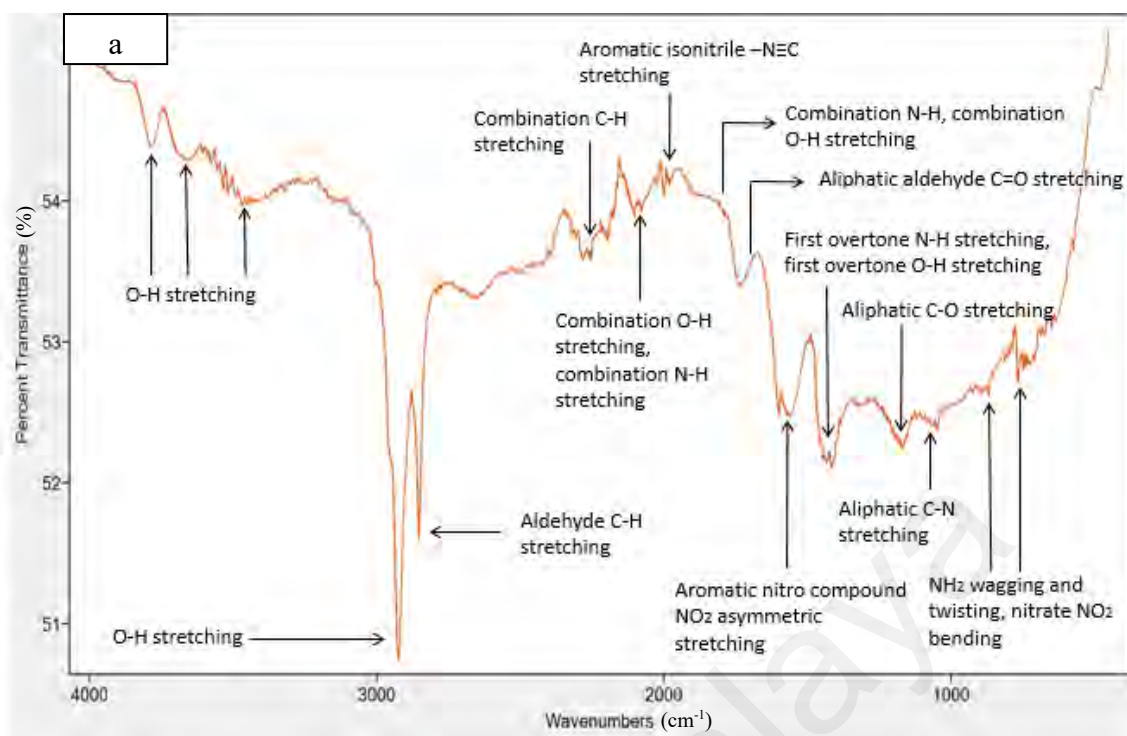
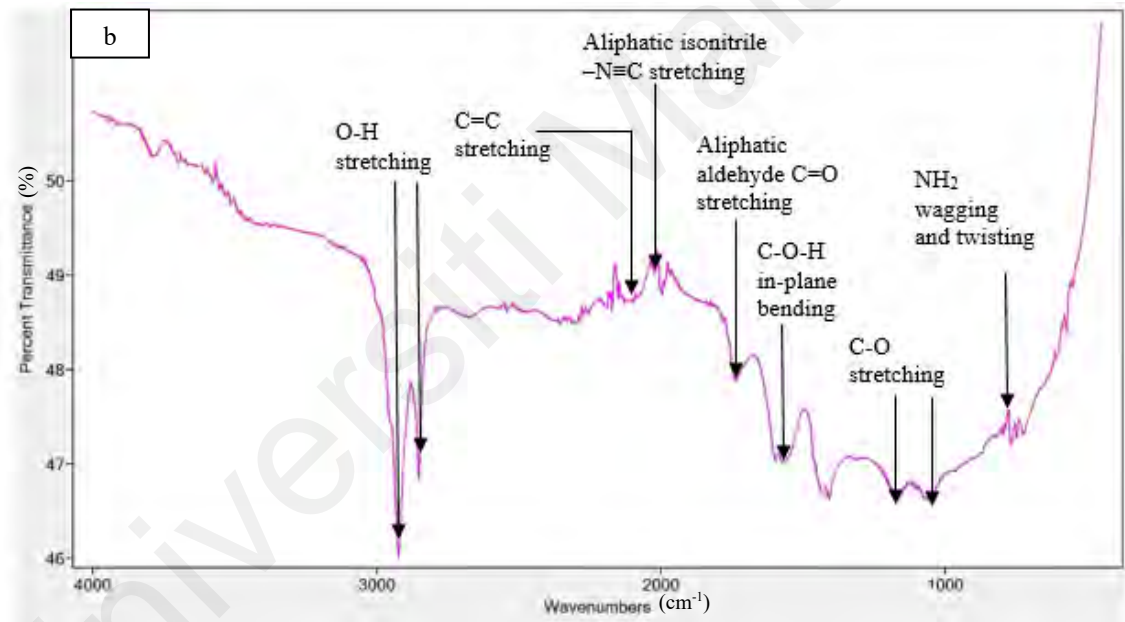
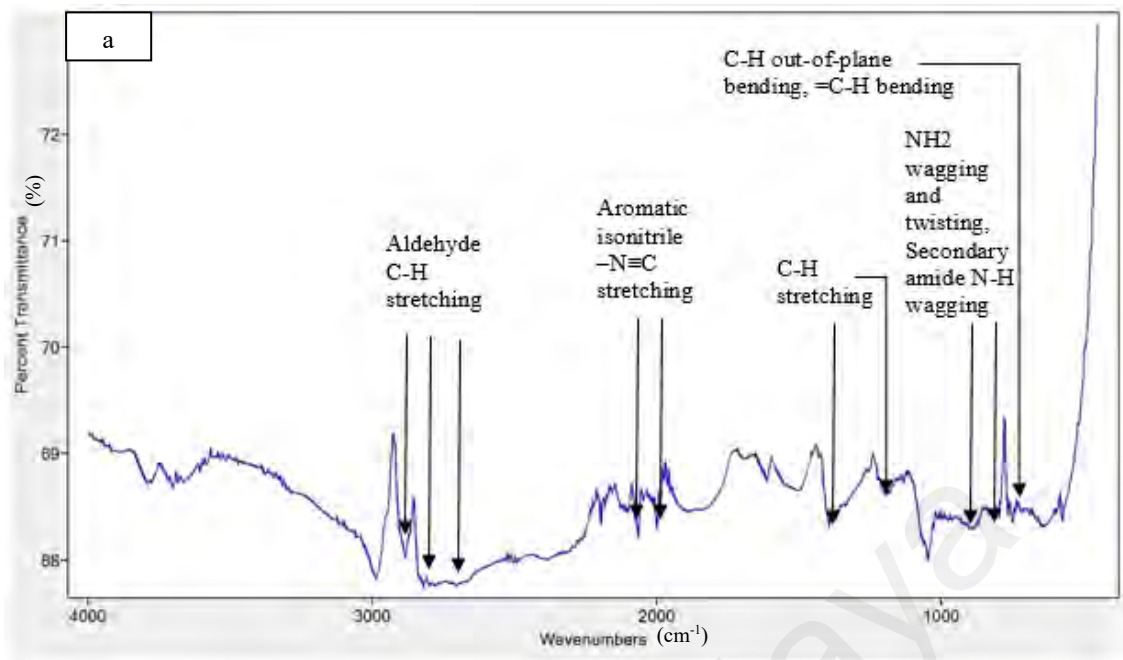


Figure 4.5: FTIR spectra for (a) GrGW and (b) GrFW at wavenumbers 400 to 4000 cm⁻¹.



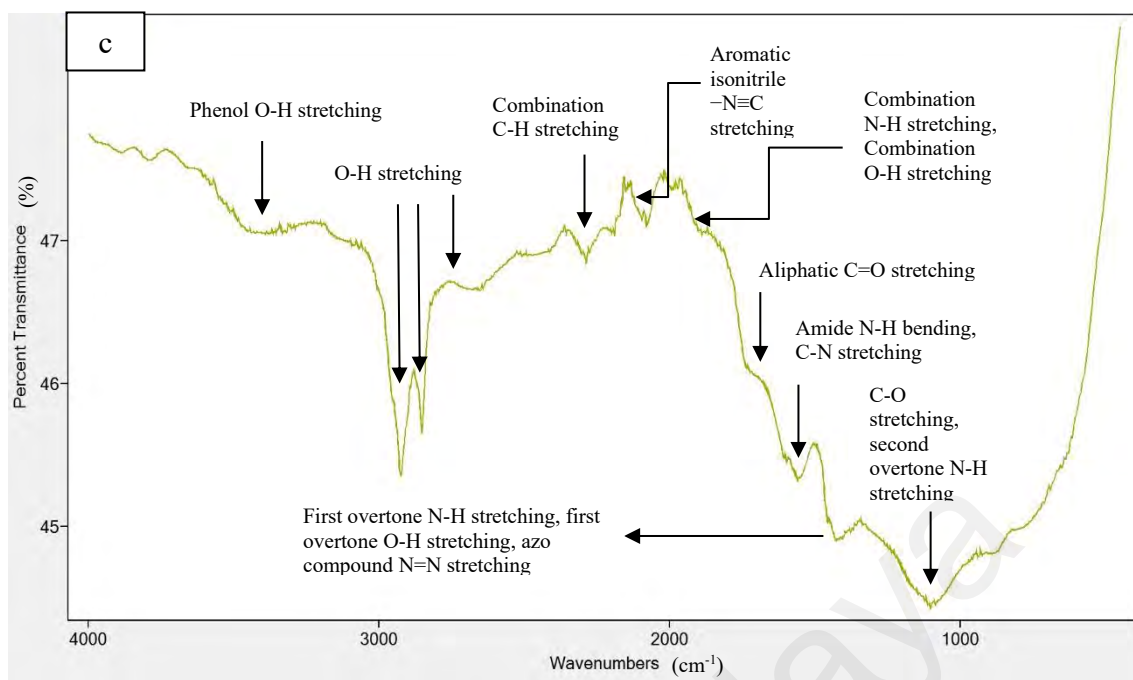


Figure 4.6: FTIR spectra for (a) GrGlyW, (b) GrSW, and (c) GrMa at wavenumbers 400 to 4000 cm^{-1} .

Table 4.5: Summary of the physicochemical characterization analyses.

Analysis	Significant findings
FE-SEM	Oxidation process caused deformation in the structure of graphene. However, after the functionalization with DES, the deformed structures were disappeared, which indicating to the healing effects by the DES molecules.
EDX	The presence of additional surface elements (i.e., O, K, Mn, Cl and N) which were not observed for unfunctionalized Gr samples, corroborated completion of the oxidation and DES functionalization processes. This also confirmed the presence of DES-functional groups on the surface of Gr.
XRD	The structural integrity of Gr was maintained after the oxidation and functionalization process. The restacking and exfoliation level of DES-functionalized Gr was greater than that of PrGr, as confirmed by the shift in diffraction peaks to lower or higher 2θ values.
Raman spectroscopy	Oxidation process increased the I_D/I_G ratio. Following the DES functionalization, the I_D/I_G ratio decreased, implying to the restoration of sp^2 double bonds in the Gr-structure by the addition of DES's functional groups.
BET surface area	OxGr and GrMa exhibited higher surface area due to the oxidation process and acidic property of the DES ChCl:Ma (1:1), respectively. After DES functionalization, smaller BET surface areas were identified, which signifying to the recovering effects on the deformed structure of the graphene.
FTIR	Some changes in the FTIR spectra were observed after DES functionalization. Several new functional groups were identified on the DES-functionalized Gr, including oxygen-based functional groups and amine-based functional groups. The addition of these functional groups induced the healing or restoration effects in the graphene structures.

4.2 Biological behavior of DES-functionalized graphene

4.2.1 MTT cell viability assay

The cytotoxic effect of the un-functionalized Gr and DES-functionalized Gr samples on MCF-7, AGS and RAW264.7 cell viability was studied using the MTT assay (Table 4.6). The results showed that PrGr possessed higher cytotoxicity towards MCF-7 (IC_{50} 161.70 $\mu\text{g/mL}$) and AGS (IC_{50} 177.85 $\mu\text{g/mL}$), but lower cytotoxicity towards RAW264.7 (IC_{50} 358.95 $\mu\text{g/mL}$). The graphene agglomeration effect on the cell membrane was anticipated to result in cell toxicity (Zhang et al., 2010). Lipid extraction mediated by graphene could occur due to the strong hydrophobic interaction between the sp^2 carbons on the 2D surface of graphene, and the phospholipid membrane of the cells (Tu et al., 2013). Therefore, it is critical to regulate the hydrophobicity of graphene to pacify its cytotoxic effects. After oxidation with $KMnO_4$, OxGr exhibited higher toxicity levels in comparison to PrGr for all cell lines tested, with an IC_{50} of 117.25 $\mu\text{g/mL}$, 88.25 $\mu\text{g/mL}$ and 278.10 $\mu\text{g/mL}$ for MCF-7, AGS and RAW264.7, respectively (Table 4.6). This result indicated that the changes in the structural morphology of the OxGr may modify its cellular biological behavior.

Table 4.6: IC₅₀ values of PrGr, OxGr and DES-functionalized Grs on MCF-7, AGS and RAW264.7 cell lines. Values are expressed as the mean ± standard deviation of three different experiments.

Sample	IC ₅₀ (µg/mL)		
	MCF-7	AGS	RAW264.7
PrGr	161.70±12.45	177.85±3.21	358.95±2.35
OxGr	117.25±11.95	88.25±9.62	278.10±2.00
GrU	87.16±8.80	167.10±10.45	356.20±2.30
GrG	76.64±8.00	135.10±7.80	346.45±4.95
GrF	76.29±8.16	161.80±2.33	373.10±6.24
GrMa	454.30±13.01	273.67±4.01	402.60±7.90
GrGW	442.40±7.93	218.15±4.96	620.65±4.15
GrFW	435.70±10.00	191.65±2.77	406.20±3.20
GrSW	284.20±7.27	206.77±11.07	363.03±9.95
GrGlyW	443.05±10.15	210.00±6.56	476.80±1.69

As shown in Table 4.6, there is a significant overall improvement in the cytotoxicity level of Gr samples after functionalization with DES, especially for AGS and RAW264.7 cells. The cytotoxicity level of Gr samples was the lowest following functionalization with ternary DES. In general, the ternary DES-functionalized Grs exhibited lower toxicity (i.e., IC₅₀ > 200 µg/mL for all cell lines) compared to binary DES-functionalized Grs, except for GrMa. The results also highlighted that GrMa exhibited lower toxicity (IC₅₀ > 250 µg/mL for all cell lines) compared to PrGr and OxGr. On the other hand, other binary DES-functionalized Grs (i.e., GrU, GrG and GrF) possessed higher toxicity for all cell

lines, especially MCF-7 cells ($IC_{50} < 100 \mu\text{g/mL}$). This can be attributed to the high exfoliation or graphene reduction effect that occurred on GrU, GrG and GrF, as previously discussed in Section 4.1.2. The high exfoliation and reduction effect of graphene is implicated in the increased generation of ROS (Fu et al., 2014; Nel et al., 2006). The ROS generation will be discussed with more details in Section 4.2.2.

With respect to the physicochemical characterization results, a number of similar functional groups were identified in GrMa, GrGlyW and GrGW that probably reduced the cytotoxicity level, such as O-H stretching (carboxylic acid, alcohol, and phenol groups), aliphatic C=O (carboxylic acid group), and N-H stretching (amine group). The presence of oxygenated functional groups in functionalized graphene may contribute to lower cytotoxicity and improved biocompatibility (Chang et al., 2011). The addition of negatively charged oxygen-based functional groups increases the stability of graphene through preventing them from aggregation in aqueous solution (Stankovich et al., 2006). The hydrophilicity of these functional groups is beneficial for the distribution and solubility of drugs in aqueous solution, and hence may hinder agglomeration (Lin et al., 2015; Miao & Scott Obach, 2010; Yan et al., 2012a; Yazdanian et al., 2004). This interpretation is supported by a previous study (Hayyan et al., 2015a), that showed a considerable improvement in the dispersion stability of graphene after functionalization with DES ChCl:Ma (1:1), ChCl:glycerol:water (1:2:1) and ChCl:glucose:water (5:2:5).

As discussed in Section 4.1.3, GrMa GrGW, and GrGlyW exhibited the highest I_D/I_G intensity ratio, indicating a higher degree of functionalization in comparison to the other DES-functionalized Grs (Table 4.3). This result is in good agreement with previous

studies on fullerene and single-walled carbon nanotubes (SWCNTs), which reported that a higher degree of functionalization may lead to reduced cytotoxicity level (Sayes et al., 2004; Sayes et al., 2006). The surface functionalization of the nanomaterial may enhance dispersion of the particles and improve their interaction with the lipid membrane.

Overall, the functionalization with DES ameliorated the cytotoxicity profile of the graphene in all types of cell lines (Figure 4.7). Noteworthy, the DES-functionalized Gr exhibited mild toxicity against RAW264.7 cells compared to MCF-7 and AGS cells, which indicating that DES-functionalized Gr had no lethal impacts on the normal cells or non-cancerous cells. The cell cycle and ROS analysis assays were also conducted at IC_{50} for all samples, to further elucidate the cell death mechanisms after exposure to the Gr samples. The use of IC_{50} in these studies was to provide insight into the cell death mechanisms, as 50% of the cells are killed at this concentration.

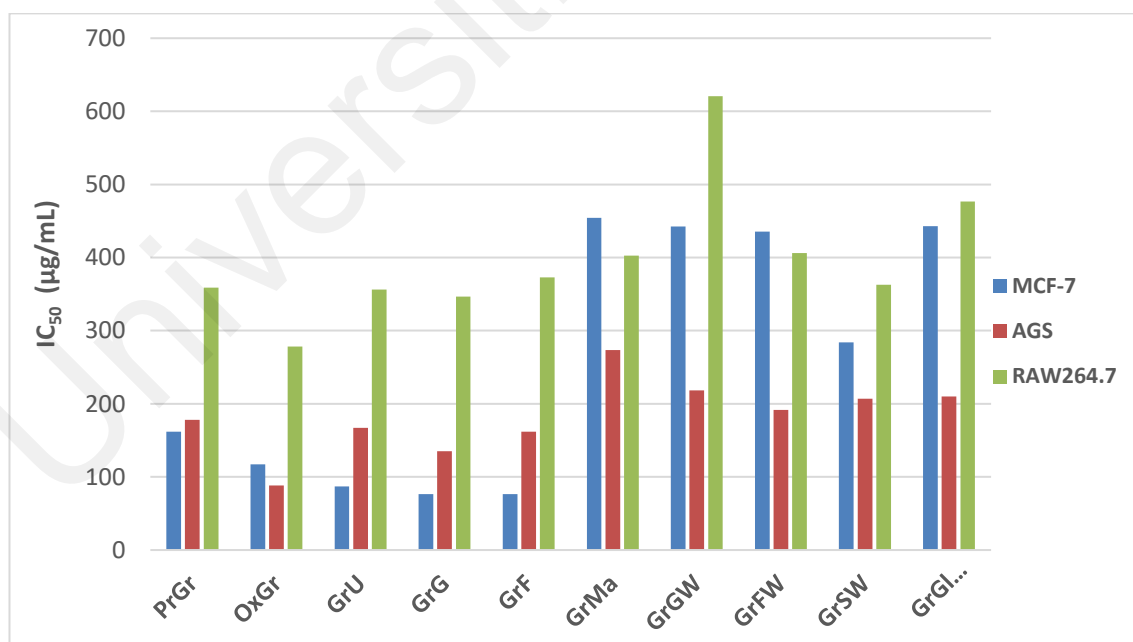


Figure 4.7: IC_{50} values of PrGr, OxGr and DES-functionalized Grs on MCF-7, AGS and RAW264.7 cell lines.

4.2.2 Reactive oxygen species (ROS) assay

The generation of ROS (i.e., superoxide, hydrogen peroxides, and hydroxyl radicals) disrupts the enzyme homeostasis system of ROS scavenging antioxidants. The resulting increase in the level of intracellular ROS leads to oxidative damage such as lipid peroxidation and protein denaturation, and hence causing cell death (Akhtar et al., 2017; Faraj et al., 2014; Hayyan et al., 2016a; Hegab et al., 2016; Kim et al., 2009; Sasidharan et al., 2012; Zahedifard et al., 2015). The generation of intracellular ROS occurs due to the hydrophobic-physical interaction between nanoparticles and the cell membrane (i.e., agglomeration on the cell membrane) (Chatterjee et al., 2014). The correlation between cytotoxicity of nanomaterials and ROS generation has been reported with high linear correlation, which signifies the importance of ROS generation as a primary cell death mechanism (Becker et al., 1996; Horev-Azaria et al., 2013; Jones & Grainger, 2009).

The level of intracellular ROS was determined in the AGS, MCF-7 and RAW 264.7 cells treated with the Gr samples. A 24 h of incubation with the Gr samples induced a significant generation of ROS (Appendix B: Figure 1B-3B). OxGr caused the highest ROS generation in all cell lines, with ROS level of 87.7%, 79.3% and 91.1% for AGS, MCF-7 and RAW 264.7 cells, respectively. The mechanism of cytotoxicity for the graphenes and graphene-based materials may begin with direct contact between the nanomaterial and the cell membrane, leading to stimulation of ROS (Bianco, 2013; Cheng et al., 2017; Zhang et al., 2012b). The generation of ROS by graphene stimulation is speculated to be due to the hydrophobic properties of graphene, where the cell-membrane-bound graphene flakes might impede the uptake of necessary proteins and other nutrients

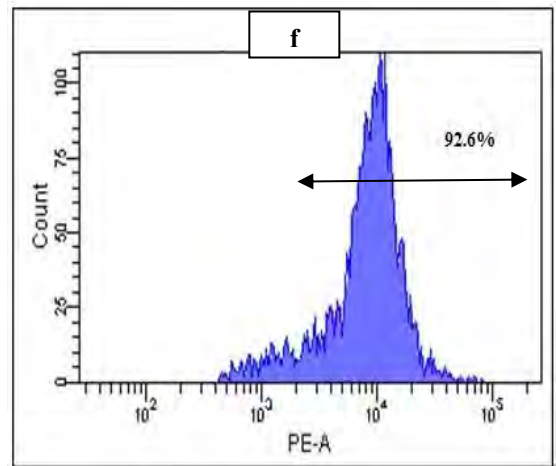
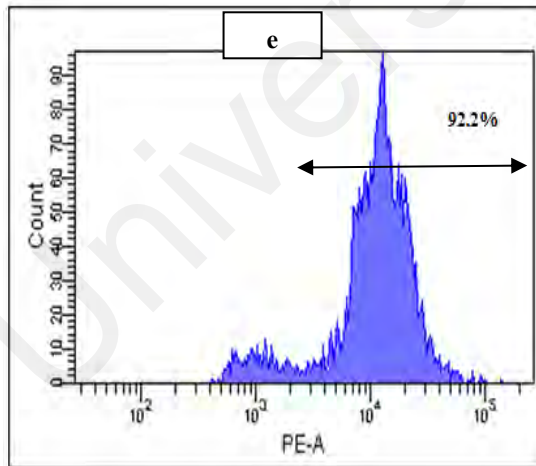
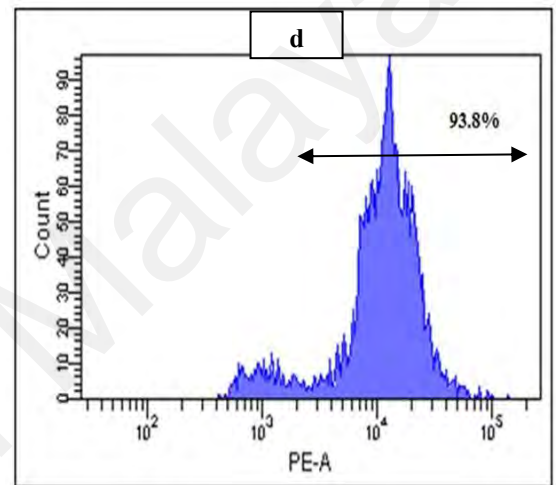
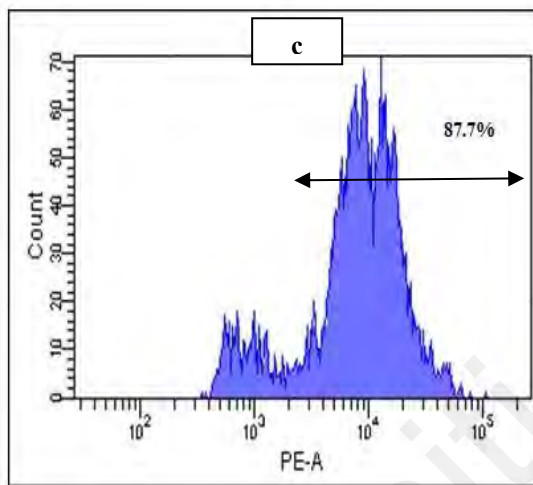
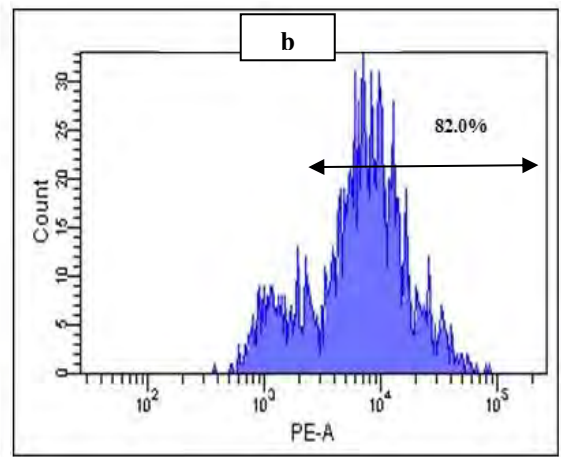
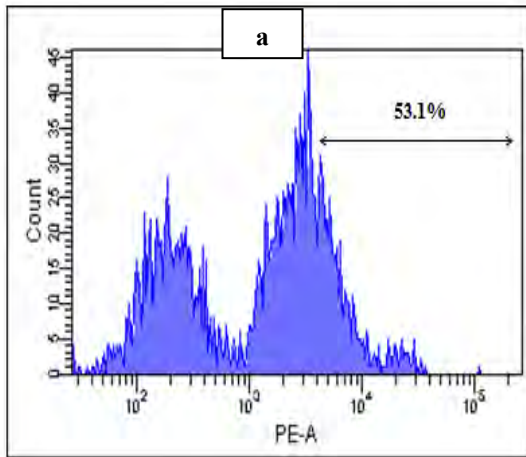
into the cell (Sasidharan et al., 2012). This aggregation of graphene on the plasma membrane also hinders critical ion channels, which increases ROS generation.

Among the DES-functionalized Grs, GrMa and GrGlyW were the most efficient in reducing ROS stimulation in all cell lines (Appendix B: Figure 1B-3B). Particularly, in the case of AGS cells, GrMa and GrGlyW exhibited lower ROS production (75.6% and 69.1%, respectively) in comparison to other Gr samples (> 82%) (Figure 4.8). The oxygen based-functional groups possessed by GrMa and GrGlyW are believed to play a primary role in reducing the generation of intracellular ROS. As reported in previous studies (Sasidharan et al., 2011; Sasidharan et al., 2012), the carboxyl-functionalized graphene with oxygenated functional groups exhibited a significant reduction of ROS generation in Vero and RAW264.7 cell lines.

GrU mediated the highest level of ROS in AGS and RAW264.7 cells, with 93.8% (Figure 4.8) and 90.6% (Figure 4.9), respectively. Meanwhile, GrG induced the highest ROS production in MCF-7, at 80.9% (Figure 4.10). As measured by Raman spectroscopy, both GrU and GrG exhibited a high level of exfoliation or graphene size reduction effect. It can be speculated that the high degree of exfoliation or reduction effect of graphene is associated with the increase in ROS production. As stated previously (Stankovich et al., 2007), a higher degree of exfoliation or reduction leads to an increase in surface area. Nanomaterials with a smaller size and larger surface area generate higher levels of ROS, resulting in genotoxicity and cytotoxicity (Fu et al., 2014; Nel et al., 2006). This is also complementary with previous studies (Das et al., 2013; Hussain et al., 2009; Stone et al., 1998) that observed consistent trend between oxidative stress of various cell lines (e.g.,

human umbilical vein endothelial cells, human bronchial epithelial cell line and human type II alveolar epithelial cells) and surface area of nanoparticles including graphene oxide, titanium dioxide, and ultrafine carbon black. These findings demonstrated that the higher surface area produced a higher level of ROS in the biological systems.

Universiti Malaya



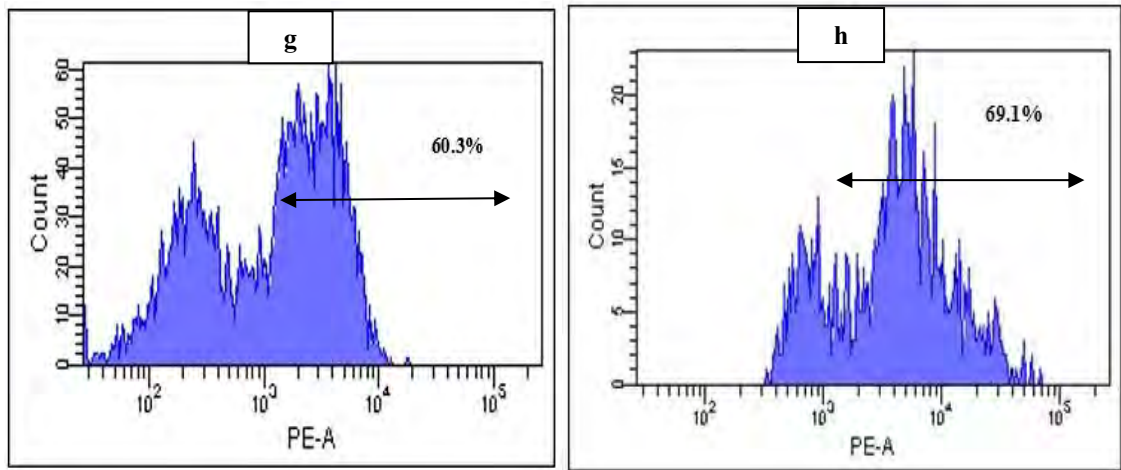
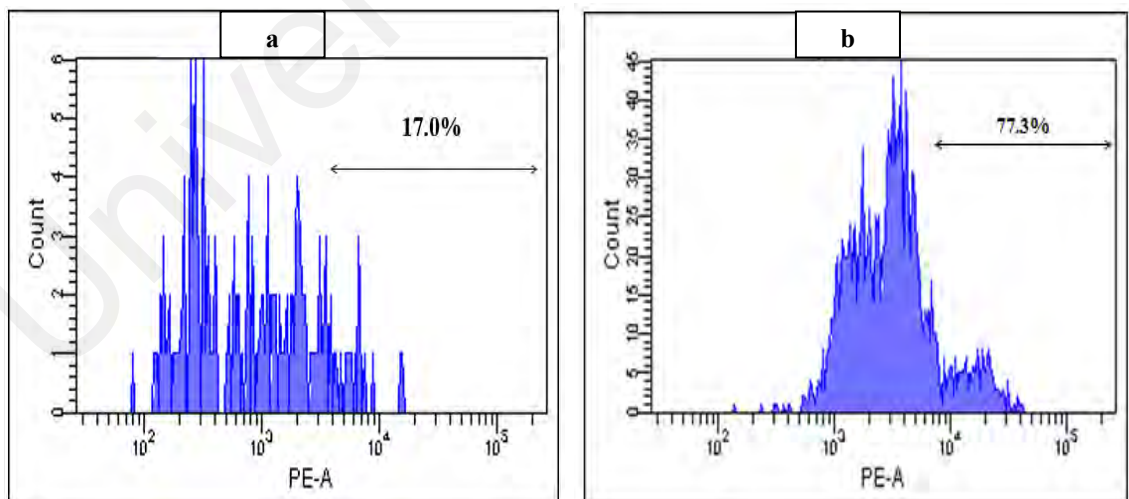


Figure 4.8: ROS generation of (a) untreated AGS cells, and with AGS cells treated with (b) PrGr, (c) OxGr, (d) GrU, (e) GrG, (f) GrF, (g) GrMa and (h) GrGlyW. Values indicates the percentages of cells generated ROS (by the fluorescence intensity) in the gated area. Shown are representative data of three independent experiments.



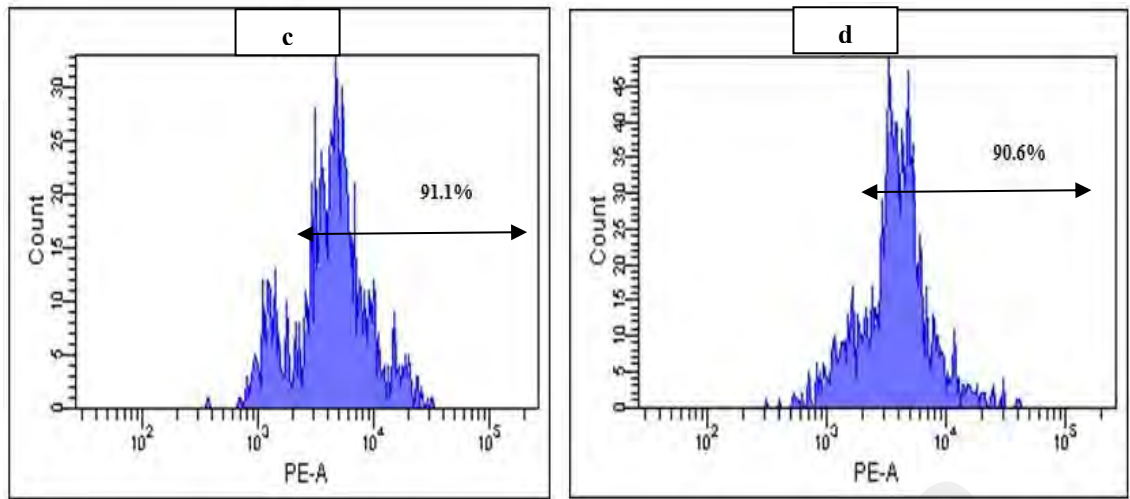
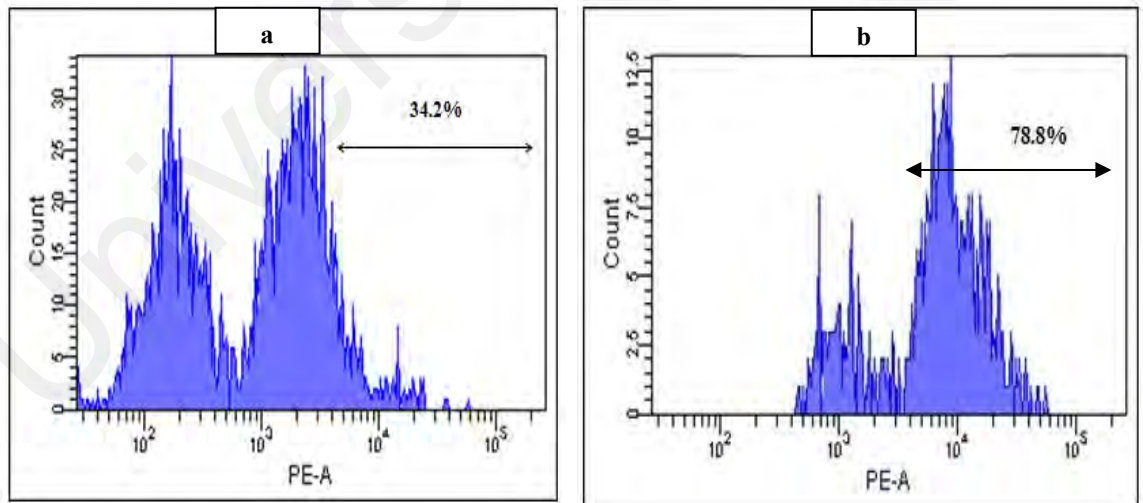


Figure 4.9: ROS generation of (a) untreated RAW264.7 cells, and with RAW264.7 cells treated with (b) PrGr, (c) OxGr, and (d) GrU. Values indicates the percentages of cells generated ROS (by the fluorescence intensity) in the gated area. Shown are representative data of three independent experiments.



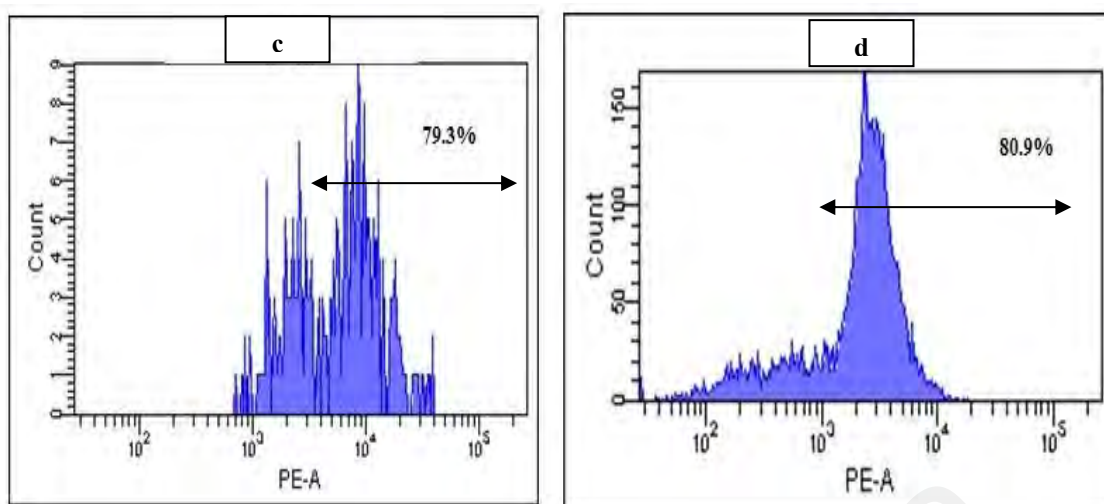


Figure 4.10: ROS generation of (a) untreated MCF-7 cells, and with MCF-7 cells treated with (b) PrGr, (c) OxGr, and (d) GrG. Values indicates the percentages of cells generated ROS (by the fluorescence intensity) in the gated area. Shown are representative data of three independent experiments.

4.2.3 Cell cycle analysis

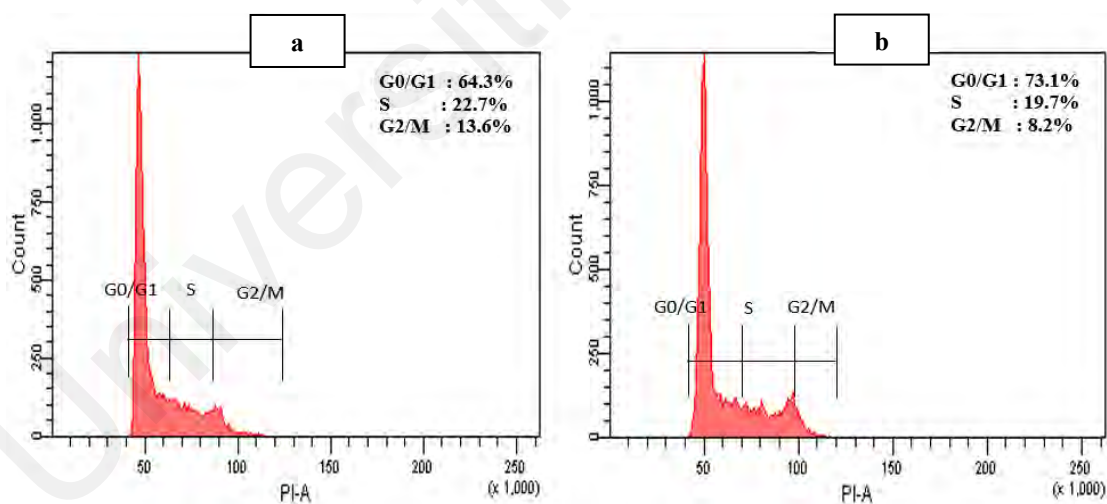
Given that cell death program is associated with DNA replication and cell cycle progression, propidium iodide staining and flow cytometry were used to analyze the treated MCF-7, AGS and RAW 264.7 cells to elucidate the impact of DES-functionalized Grs on cell cycle progression. Basically, cell cycle progression in eukaryotic cells is controlled by activation and inactivation of a sequence of cyclin-dependent kinases at specific phases in the cell cycle (Matesanz et al., 2013). The presence of toxicants may perturb the regulation of specific phases. Overall, PrGr and OxGr were shown to disrupt cell cycle progression regardless of cell type (Appendix C: Figures 1C-3C). Cell cycle progression was significantly arrested in G₀/G₁ phase, and consequently impeded the

progression of the cells into S or G2/M phase. The most severe cell cycle disruption by PrGr and OxGr was observed in the AGS cell line (Figure 4.11). Only 8.2% and 6.7% of the AGS cell population progressed into the G2/M phase when treated with PrGr and OxGr, respectively. The results also indicated that DES-functionalized Grs caused cell cycle disruption in all cell lines tested (Appendix C: Figures 1C-3C). Thus, it is proved that the cell cycle/ mitotic division disruption is one of the cell death mechanisms for the graphene-based nanomaterials. Similar finding was reported by a previous study (Matesanz et al., 2013) regarding the cell cycle progression phase arrest that was induced by graphene-based nanomaterials in several cell lines such as RAW264.7, osteoblasts (Saos-2), and preosteoblasts (MC3T3-E1).

In comparison with other CNMs, Cui et al. (2005) observed the same cell cycle arrest in G0/G1 phase by SWCNTs on the human embryo kidney cells (HEK293). The cell cycle disruption caused by SWCNT was ascribed to the down regulation of cyclin-dependent kinases and cyclins molecules. The same study also exhibited that 5.3% of HEK293 cells demonstrated apoptotic feature when tested with 25 $\mu\text{g/mL}$ of SWCNT. This suggested that cell cycle disruption by CNMs could lead to cell death through apoptosis mechanism.

In all cell lines tested, GrU produced the most acute disruption, where cells were significantly arrested in G0/G1 phase compared to untreated cells (Appendix C: Figures 1C-3C). GrF also resulted in acute cell cycle disruption, especially for AGS cells which had 72.0% of the cell population in G0/G1 phase, 13.0% in S phase and 9.9% in G2/M phase (Figure 4.12). In contrast, untreated AGS cells had 64.3% of the, cell population in

G0/G1 phase, 22.7% in S phase, and 13.6% in G2/M phase (Figure 4.12). The high exfoliation effect that occurred on GrU and GrF is implicated to this deterioration phenomenon. Meanwhile, GrMa demonstrated the least cell cycle disruption, particularly for RAW264.7 cells (Figure 4.13). Among the sugar based-DESs, graphene that functionalized using ChCl:G:W (i.e., GrGW) demonstrated the least cell cycle disruption with cell population in G2/M phase >11.2% for all cell lines. Again, this result is believed to be associated with the presence of hydrophilic functional groups in GrMa and GrGW as discussed in the Section 4.1. The surface modification of nanomaterials can prevent cell cycle disregulation (Mahmoudi et al., 2011). The addition of hydrophilic functional groups such as –OH and –COOH can prevent disruption of cell cycle progression by improving the solubility and distribution of the nanomaterials (Das et al., 2013; Mahmoudi et al., 2011; Sasidharan et al., 2011).



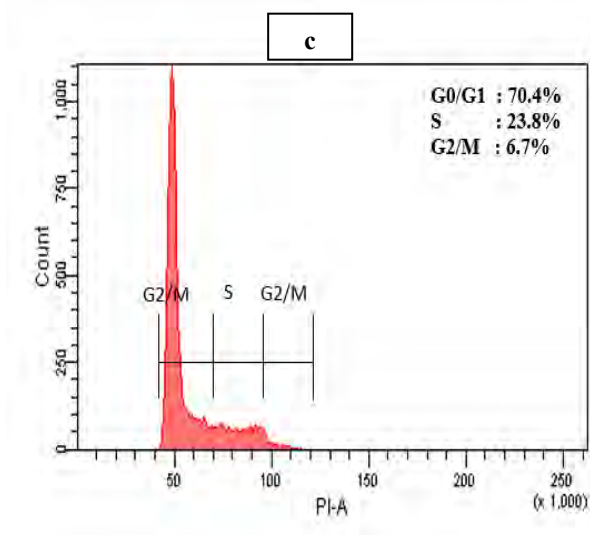


Figure 4.11: Cell cycle comparison of the (a) untreated AGS cells with the (b) PrGr- and (c) OxGr- treated AGS cells. Cells were harvested after 24 h, fixed and stained with PI to detect DNA contents. Values represent the percentages of viable cells at G0/G1, S or G2/M phases. Shown are representative data of three independent experiments.

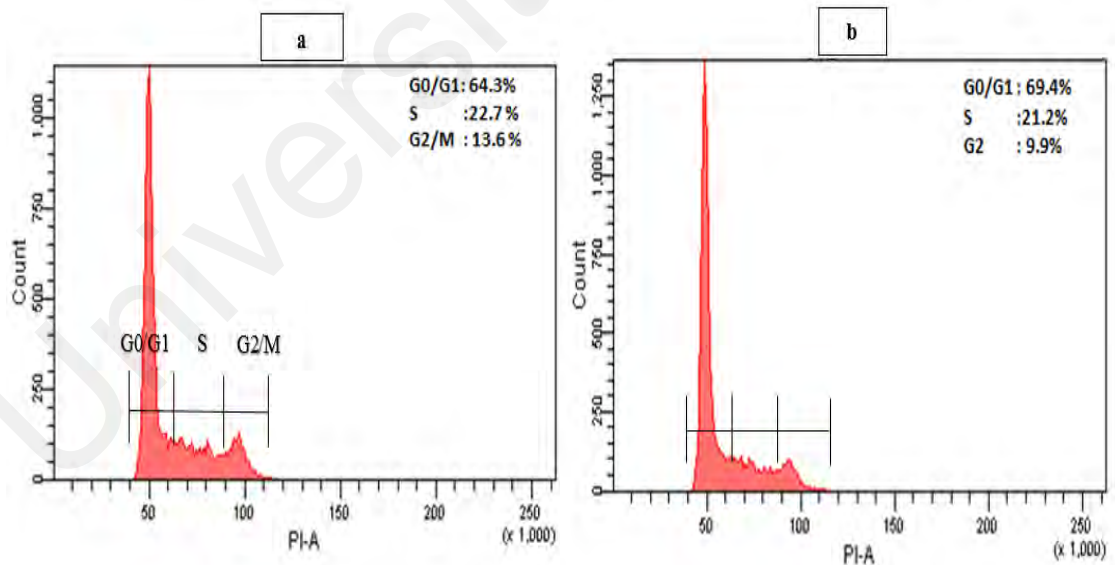


Figure 4.12: Cell cycle comparison of the (a) untreated AGS cells with (b) GrF-treated AGS cells. Cells were harvested after 24 h, fixed and stained with PI to detect DNA

contents. Values represent the percentages of viable cells at G0/G1, S or G2/M phases.

Shown are representative data of three independent experiments.

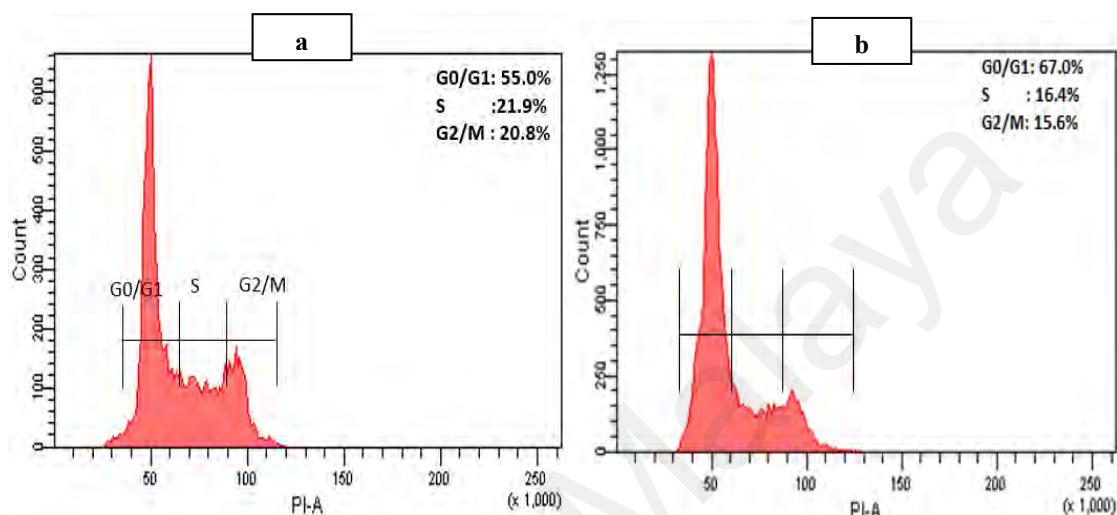


Figure 4.13: Cell cycle comparison of the (a) untreated RAW 264.7 cells with (b) GrMa-treated RAW 264.7 cells. Cells were harvested after 24 h, fixed and stained with PI to detect DNA contents. Values represent the percentages of viable cells at G0/G1, S or G2/M phases. Shown are representative data of three independent experiments.

4.3 Drug loading on the DES-functionalized Graphene

Two drugs tamoxifen (TAM) and doxorubicine (DOX) were selected to load on the DES-functionalized Grs. TAM and DOX are common anti-cancer drugs that are normally applied to treat breast cancer. TAM and DOX have been used in the treatment of various other cancers, including acute lymphocytic leukemia, Kaposi's sarcoma,

osteogenic sarcomas, bladder cancer, and lymphoma (Biswas et al., 2013; Chittasupho et al., 2014; Cortés-Funes & Coronado, 2007; How et al., 2013; Nawara et al., 2012; Shi et al., 2016). However, there is a need to improve conventional delivery of TAM and DOX, which lacks efficiency and selectivity against cancerous cells (Landeros-Martínez et al., 2016; Sultana et al., 2013; Zhao et al., 2018). Systemic delivery of TAM and DOX is highly critical in order to enhance the therapeutic application of TAM and DOX.

4.3.1 Tamoxifen loading profile

To confirm the feasibility of DES-functionalized Grs as promising nano-carriers for drug delivery applications, TAM loading on the DES-functionalized Grs was carried out. To determine the amount of TAM loaded on the PrGr, OxGr and DES-functionalized Grs, the amount of unbound TAM in the solution was measured at an absorbance peak of 290 nm. Overall, all samples (i.e., PrGr, OxGr, and DES-functionalized Grs) interacted with TAM as demonstrated by the decrease in the absorbance of TAM after 12 h of incubation (Figure 4.14). The most significant reduction in TAM was observed for GrMa, followed by GrGW. This indicates that TAM loading on GrMa and GrGW was higher than on the other Gr samples. The EE% and DL% were also determined, to further validate the drug loading capacity for each Gr sample.

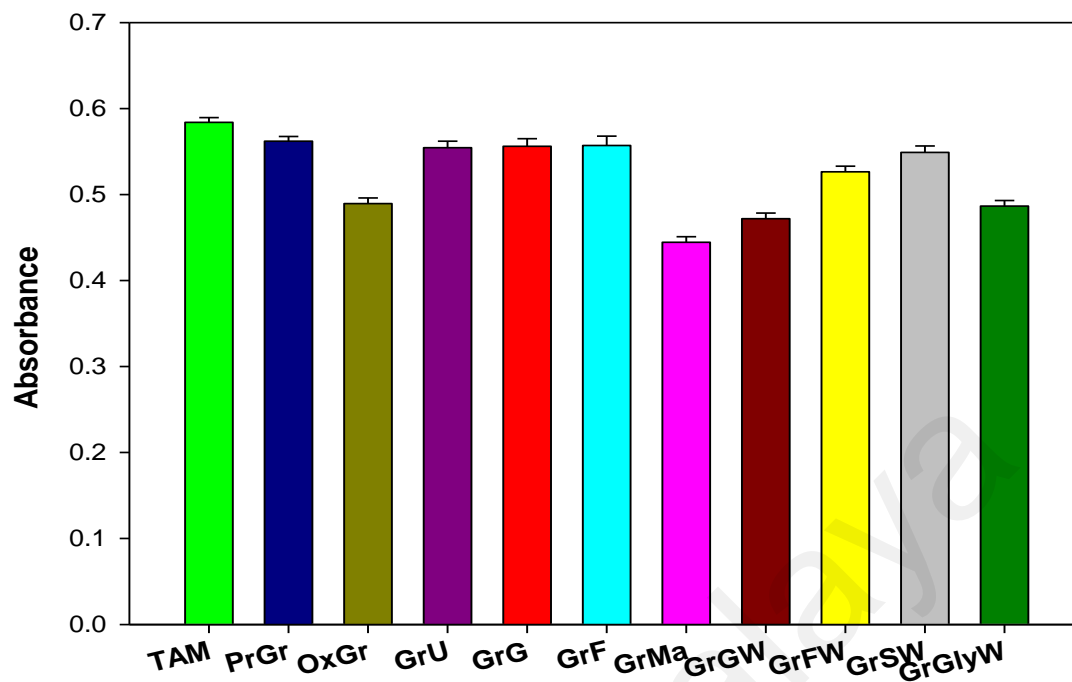


Figure 4.14: Amount of unloaded TAM in the mixture of TAM (50 $\mu\text{g/mL}$)+DES-functionalized Grs (100 $\mu\text{g/mL}$) at absorbance peak 290 nm. Standard TAM solution (50 $\mu\text{g/mL}$) was used as a control.

The EE% and DL% of PrGr, OxGr and DES-functionalized Grs are listed in Table 4.7. PrGr possessed an EE of 13.28% and DL of 6.64%. After oxidation and DES functionalization, an increase in both EE% and DL% was observed. GrMa showed the highest EE (42%) and DL (21.34%), followed by GrGW (EE 34.76% and DL 17.38%). GrGlyW was ranked the third highest tamoxifen loading capacity with EE 31.79% and DL 15.89%. In contrast, GrG exhibited the lowest EE (13%) and DL (6.64%), while the levels for GrF were intermediate (EE 15.81% and DL 7.91%). As discussed in Section 4.1.2 on XRD analysis, GrG and GrF possess a lower interlayered spacing, which implies

a higher level of π - π stacking between the layers. This was probably the reason for the lower EE% and DL% compared to GrMa.

Table 4.7: Effect of tamoxifen loading on entrapment efficiency and drug loading capacity for PrGr, OxGr and DES-functionalized Grs.

Sample	EE%	DL%
PrGr	13.28±0.80	6.64±0.46
OxGr	30.96±2.61	15.48±1.68
GrU	17.25±2.48	8.62±1.25
GrG	15.81±1.95	7.91±0.98
GrF	16.07±2.63	8.03±1.31
GrMa	42.67±1.15	21.34±0.67
GrGW	34.76±2.76	17.38±1.92
GrFW	21.98±2.29	10.99±1.39
GrSW	17.17±0.51	8.58±0.25
GrGlyW	31.79±2.46	15.89±1.42

Similar to what was done for PrGr, the crystalline plane (002) was identified in the DES-functionalized graphenes (Table 4.2), and directed to the π - π stacking in the graphene (Sun et al., 2016). When mixing the graphene with cancer drugs (typically aromatic), the drug molecules can easily adsorb onto the surface of graphene with stable chemical attachments, which is via π - π stacking interactions (Yan et al., 2012b). These π electrons on the plane may immobilize the tamoxifen via non-covalent interactions (Liu et al., 2013). In addition to the π - π stacking interactions, DES-functionalized Grs is believed to

have hydrogen bonding interactions with tamoxifen. This is because functional groups such as oxygen groups (e.g., -COOH and -OH) and lone-pair electrons from the amine groups (e.g., NH₂) may form strong hydrogen bonds with the drug (Depan et al., 2011; Yang et al., 2008). The involvement of these two interaction types, π - π stacking and hydrogen bonding interactions, may help the DES-functionalized Grs have a higher drug loading capacity than PrGr.

In comparison to the previous studies (Brigger et al., 2001; How et al., 2013; Khuroo et al., 2014), the tamoxifen loading capacity of GrMa, GrGW and GrGlyW exhibited lower EE% but higher DL%. For instance, Brigger et al. (2001) reported that tamoxifen-loaded poly(MePEGcyanoacrylate-co-hexadecylcyanoacrylate) nanospheres was as high as EE 73% and DL was as high as 0.46%. The DL of poly(MePEGcyanoacrylate-co-hexadecylcyanoacrylate) nanospheres increased dose dependently with increasing amount of tamoxifen that in the range of 0–25 μ g/mL. In contrast, the drug loading capacity for tamoxifen-loaded poly(lactic-co-glycolic acid) nanocarriers was significantly higher than poly(MePEGcyanoacrylate-co-hexadecylcyanoacrylate) nanospheres with EE% and DL% as high as 95.17% and 8.65%, respectively (Khuroo et al., 2014). Another study investigated various samples of tamoxifen-loaded nanostructured lipid carrier and showed EE% and DL% in the range of 97.39%–99.87% and 2.00%–5.84%, respectively (How et al., 2013). The highest tamoxifen loading capacity was demonstrated by the formulation of 300 mg tamoxifen in nanostructured lipid carrier solution with EE% and DL% as high as 97.39% and 5.84%, respectively.

4.3.2 Doxorubicin loading profile

To determine the amount of DOX loaded on the Gr samples, the amount of unbound DOX in the solution was measured by an absorbance peak 480 nm. Overall, all samples (i.e., PrGr, OxGr, and DES-functionalized Gr samples) interacted with DOX, as demonstrated by the decrease in the absorbance of DOX spectra after 12 h of incubation (Figure 4.15). A significant reduction in the spectra of absorption intensity of DOX was observed for DES-functionalized Gr samples, especially for the case of GrGW. This indicates that the loading of DOX onto the DES-functionalized Gr samples were higher than PrGr and OxGr.

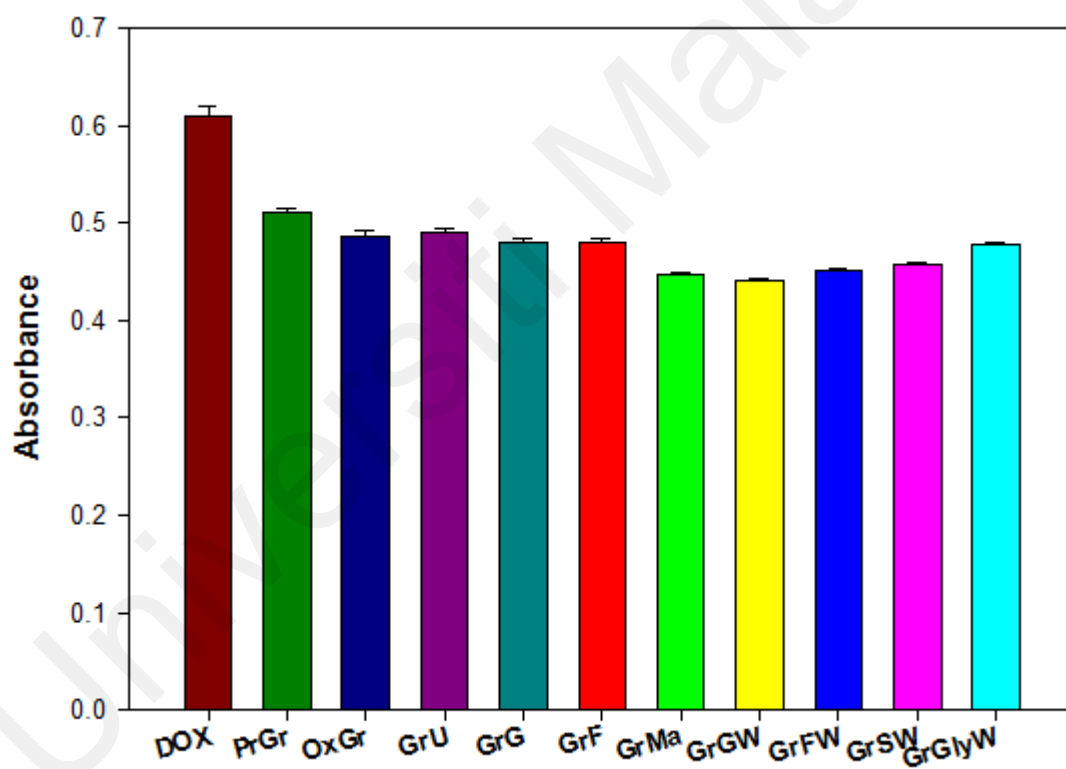


Figure 4.15: Amount of unloaded DOX in the mixture of DOX (50 µg/mL)+DES-functionalized Grs (100 µg/mL) at absorbance peak 480 nm. Standard DOX solution (50 µg/mL) was used as a control.

Table 4.8: Effect of doxorubicin loading on entrapment efficiency and drug loading capacity for PrGr, OxGr and DES-functionalized Gr samples.

Sample	EE%	DL%
PrGr	39.98±7.63	19.99±3.81
OxGr	39.68±5.71	19.84±2.85
GrU	41.65±5.45	20.83±2.72
GrG	48.25±2.35	24.13±1.17
GrF	48.50±4.04	24.25±2.01
GrMa	49.80±1.46	27.83±2.19
GrGW	56.57±7.63	28.28±3.81
GrFW	52.46±1.58	26.23±0.79
GrSW	51.84±2.94	25.92±1.47
GrGlyW	51.04±1.44	25.52±0.72

The EE% and DL% for PrGr, OxGr and DES-functionalized Gr were evaluated and are listed in Table 4.8. The OxGr showed an insignificant difference as compared to PrGr. The EE and DL for both samples were approximately equivalent. By contrast, DES functionalization of Gr influenced the amount of DOX loaded, based on the significant increase of EE% and DL% following both binary and ternary DESs functionalization as compared to unfunctionalized Gr (i.e., PrGr and OxGr) (Table 4.8). GrGW exhibited the highest EE (56.57%) and DL (28.28%), followed by GrMa (EE: 49.80% and DL: 27.83%). Notably, the EE% for both GrMa and GrGW was higher as compared to chitosan nanoparticle formulations; namely, Type B gelatin (EE: 8.4%), glucomannan

(EE: 9.3%), polyphosphoric acid (EE: 12.2%) and dextran sulfate incorporated chitosan nanoparticles (EE: 21.9%) (Janes et al., 2001). In addition, the DL of GrMa and GrGW was considerably higher in comparison to polymer micelle carrier systems such as poly(ethylene glycol)–poly(β -benzyl-L-aspartate) copolymer micelles that had a DL ranging from 15% to 20% (Kataoka et al., 2000). These DES-functionalized Gr systems also exhibited a higher DL as compared to other drug vehicles, such as biodegradable polymersomes vesicle of poly(trimethylene carbonate)-*b*-poly(L-glutamic acid) (i.e., DL: 4.7%) and glyceryl caprate-curdlan solid lipid nanoparticles (DL: 2.8%) (Sanson et al., 2010; Subedi et al., 2009).

Unlike other drug carriers, graphene is a superior nano-drug carrier, as both sides of a graphene sheet are accessible for drug loading/binding via a physical adsorption mechanism (Bao et al., 2011; Rana et al., 2011). The presence of π electrons on graphitic domains promote the formation of non-covalent binding via π - π stacking interactions with various compounds or substances, including DOX (Feng et al., 2013; Gonçalves et al., 2013; Wang et al., 2011; Yang et al., 2013a). These π electrons on the plane immobilize DOX via non-covalent physical adsorption (physisorption) (Liu et al., 2013). In addition to the π - π electron stacking interactions, DES-functionalized Gr may also form strong hydrogen bonds with DOX. This is because the presence of DES functional groups such as oxygen groups (e.g., -COOH and -OH) and lone-pair electrons from amine groups (e.g., NH₂) may promote hydrogen bonding interactions between DES-functionalized Gr and DOX (Depan et al., 2011; Yang et al., 2008). The combination effect of these two interactions (i.e., π - π stacking and hydrogen bonding) may impart GrMa and GrGW with a higher drug loading capacity as compared to unfunctionalized Gr. The drug release is

expected to be more effective as such non-covalent interactions are impermanent, which can easily release the drug from the carrier (de Sousa et al., 2018; Liu et al., 2013; Valentini et al., 2018). The comparison of anti-cancer activity between unloaded Gr and DOX-loaded Gr were discussed in the next sections.

In comparison to TAM loading capacity, DES-functionalized Gr had higher loading capacity towards DOX (EE: 41.65% - 56.57% and DL: 20.83% - 28.28%) than TAM (EE: 7.91% - 21.34% and DL: 15.81% - 42.67%). This is due to the presence of more hydrophilic functional groups, such as carboxyl group and hydroxyl group in DOX (Bagheri et al., 2011), in which have strong binding interactions with DES-functionalized Gr. This result is in agreement with Chanphai et al. (2017) where the DOX had higher loading capacity on nano-carrier dendrimer as compared to TAM with DOX loading efficiency was in the range of 40%-50%. The DOX also formed more stable binding interaction with dendrimer than that of TAM because of the existence of carboxyl and hydroxyl functional groups.

Overall, the drug loading capacity of graphene in both TAM and DOX significantly increased after the functionalization with DES rather than the unfunctionalized graphene. Drug-loaded DES-functionalized Gr also showed some promising results as compared to the previous studies (Table 4.9). For instance, although the EE% of DES-functionalized Gr on TAM was lower than the previous studies (Brigger et al., 2001; How et al., 2013; Khuroo et al., 2014), the DES-functionalized Gr exhibited significantly higher DL% than the other nanocarriers (e.g. poly(MePEGcyanoacrylate-co hexadecylcyanoacrylate), poly(lactic-co-glycolic acid, and nanostructured lipid carrier). Meanwhile, the DES-

functionalized Gr, especially GrGW and GrFW, possessed higher EE% (> 50%) and DL% (> 25%) on DOX in comparison to the other nanocarriers (Janes et al., 2001; Kataoka et al., 2000; Sanson et al., 2010; Subedi et al., 2009). Therefore, DES functionalization represented a promising green functionalizing agent for nano-drug carriers, owing to its easy to synthesize, less toxic, low cost, and relatively high drug loading capacity.

Table 4.9: List of various nanocarrier systems with their EE% and DL%.

Nanocarrier	Drug	EE%	DL%	Reference
Poly(MePEGcyanoacrylate-co hexadecylcyanoacrylate)	TAM	73.00	0.46	(Brigger et al., 2001)
Poly(lactic-co-glycolic acid)	TAM	95.17	8.65	(Khuroo et al., 2014)
Nanostructured lipid carrier	TAM	97.39	5.84	(How et al., 2013)
GrMa	TAM	42.67	21.34	This study
GrGW	TAM	34.76	17.38	This study
GrGlyW	TAM	31.79	15.89	This study
Chitosan-based Type B gelatin	DOX	8.40	–	(Janes et al., 2001)
Glucomannan	DOX	9.30	–	
Polyphosphoric acid	DOX	12.20	–	
Dextran sulfate incorporated chitosan	DOX	21.9	–	
Poly(ethylene glycol)–poly(β -benzyl-L-aspartate)	DOX	–	15.00 – 20.00	(Kataoka et al., 2000)
Poly(trimethylene carbonate)-b-poly(L-glutamic acid)	DOX	–	4.7	(Sanson et al., 2010)

Nanocarrier	Drug	EE%	DL%	Reference
Glyceryl caprate-curdlan solid lipid nanoparticles	DOX	–	2.8	(Subedi et al., 2009)
GrGW	DOX	56.57	28.28	This study
GrFW	DOX	52.46	26.23	This study

4.4 Anti-cancer activities of drug loaded- DES-functionalized graphene

In this section, the anti-cancer features of drug loaded-DES-functionalized graphene are addressed. The cell viability, reactive oxidative species (ROS), cell cycle progression, and real-time cell growth analysis was evaluated to elucidate their anti-cancer activities against cancerous cells (i.e., MCF-7 and AGS cells).

4.4.1 Cytotoxicity analysis

The cytotoxic effect of the TAM-loaded Gr and DOX-loaded Gr samples on the cell viability was studied in order to elucidate their anti-cancer activities against MCF-7 and AGS cell lines. The effect of TAM-loaded Gr and DOX-loaded Gr samples on non-targeted cells were tested to evaluate the selectivity of their activity against cancer cells through the selectivity index (SI) measurement. The RAW264.7 cell lines was used as non-targeted cells due to the significant role of macrophages cells in human immune defense system.

4.4.1.1 TAM-loaded graphene

After TAM loading, TAM-loaded Gr samples possessed acute toxicity against cancerous cells, especially for the case of TAM-loaded DES-functionalized Gr. As shown in Figure 4.16, the TAM-loaded Gr had higher toxicity against AGS compared to MCF-7 and RAW264.7 cells. TAM-GrF possessed the most acute toxicity against MCF-7 cells with an IC_{50} of 71.96 $\mu\text{g/mL}$, followed by TAM-GrG (IC_{50} of 74.49 $\mu\text{g/mL}$) and TAM-GrU (IC_{50} of 80.22 $\mu\text{g/mL}$) (Table 4.10). Against the AGS cell line, TAM-OxGr showed the highest toxicity with an IC_{50} of 75.31 $\mu\text{g/mL}$, followed by TAM-GrG (IC_{50} of 132.31 $\mu\text{g/mL}$) and TAM-GrF (IC_{50} of 157.58 $\mu\text{g/mL}$) (Table 4.11). In contrast, TAM-OxGr exhibited the lowest IC_{50} towards RAW264.7 cells (IC_{50} of 209.33 $\mu\text{g/mL}$), followed by the sequence of TAM-GrG (IC_{50} of 223.73 $\mu\text{g/mL}$) < TAMGrSW (IC_{50} of 253.07 $\mu\text{g/mL}$).

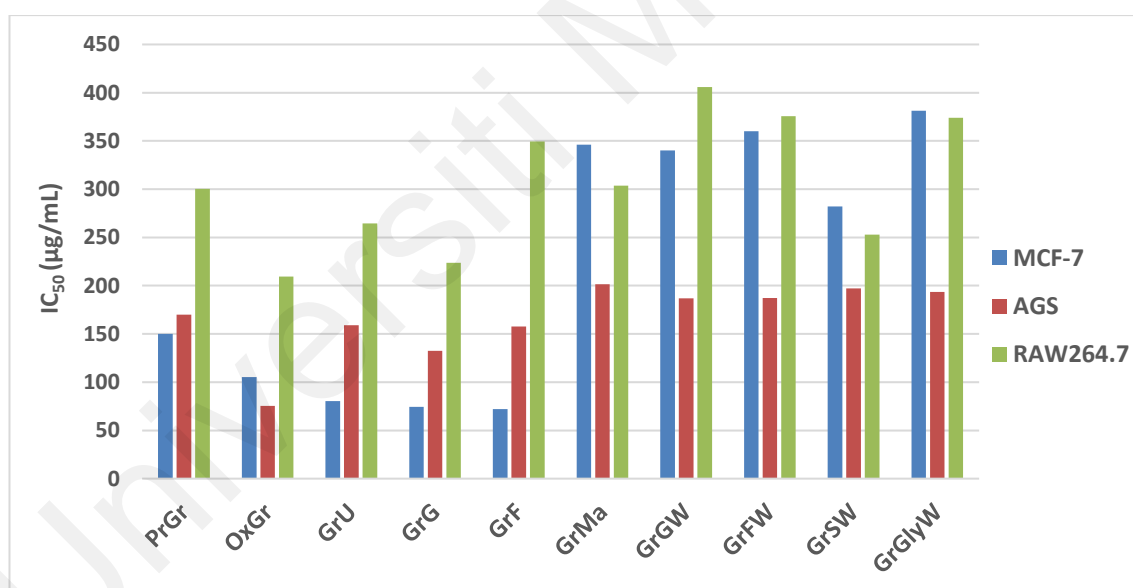


Figure 4.16: IC_{50} values of TAM-loaded PrGr, OxGr and DES-functionalized Grs on MCF-7, AGS and RAW264.7 cell lines.

Table 4.10: IC₅₀ values of TAM-loaded PrGr, OxGr, and DES-functionalized Gr samples on MCF-7 and RAW264.7 cell lines, and also their selectivity index. Values are expressed as the mean ± standard deviation of three different experiments.

Sample	IC ₅₀ (µg/mL)		SI
	RAW264.7	MCF-7	
TAM-PrGr	300.20±4.37	150.00±7.31	2.00
TAM-OxGr	209.33±7.10	105.20±6.55	1.99
TAM-GrU	264.63±5.80	80.22±6.52	3.30
TAM-GrG	223.73±4.40	74.49±4.17	3.00
TAM-GrF	349.50±4.90	71.96±1.20	4.86
TAM-GrMa	303.63±5.43	346.00±6.72	0.88
TAM-GrGW	405.70±8.03	340.10± 6.29	1.19
TAM-GrFW	375.73±4.79	360.10±7.15	1.04
TAM-GrSW	253.07±3.64	282.10±5.75	0.90
TAM-GrGlyW	374.00±5.23	381.20±4.41	0.98

Table 4.11: IC₅₀ values of PrGr, OxGr, and TAM-loaded DES-functionalized Gr samples on AGS and RAW264.7 cell lines, and also their selectivity index. Values are expressed as the mean ± standard deviation of three different experiments.

Sample	IC ₅₀ (µg/mL)		SI
	RAW264.7	AGS	
TAM-PrGr	300.20±4.37	170.01±6.91	1.77
TAM-OxGr	209.33±7.10	75.31±2.71	2.78
TAM-GrU	264.63±5.80	158.93±8.32	1.67
TAM-GrG	223.73±4.40	132.31±4.71	1.69
TAM-GrF	349.50±4.90	157.58±6.30	2.22
TAM-GrMa	303.63±5.43	201.47±7.11	1.51
TAM-GrGW	405.70±8.03	187.00±3.57	2.17
TAM-GrFW	375.73±4.79	187.37±5.12	2.01
TAM-GrSW	253.07±3.64	197.32±7.62	1.28
TAM-GrGlyW	374.00±5.23	193.66±3.79	1.93

Noteworthy, the toxicity of these TAM-loaded Gr samples was significantly higher in comparison to the drug-free DES-functionalized Gr. This indicates that the lethal interaction between graphene and cells significantly increased by loading TAM on the Gr. The toxicity level significantly increased after TAM loading on the GrGW, GrFW, GrGlyW and GrMa for both MCF-7 and AGS cell lines. Particularly, for the case of MCF-7 cells, TAM-GrGW and TAM-GrMa resulted in IC_{50} of 340.10 $\mu\text{g/mL}$ and 346.00 $\mu\text{g/mL}$, respectively (Table 4.10), which were more toxic than free-loaded GrGW (IC_{50} of 442.40 $\mu\text{g/mL}$) and free-loaded GrMa (IC_{50} of 454.30 $\mu\text{g/mL}$). The same trend was observed on the AGS cell line as TAM-GrGW and TAM-GrMa possessed lower IC_{50} (i.e., 187.00 $\mu\text{g/mL}$ and 201.47 $\mu\text{g/mL}$, respectively) compared to GrGW and GrMa (i.e., 218.15 $\mu\text{g/mL}$ and 273.67 $\mu\text{g/mL}$, respectively).

These results are in accordance with the previous studies (Abbasalipourkabir et al., 2016; Fontana et al., 2005; Li et al., 2012) where the toxicity of TAM-loaded nano-carrier, namely solid lipid nanoparticles and poly(amidoamine) dendrimers-based nano-carriers against cancerous cells significantly increased as compared to the drug free-nano-carriers. The TAM-loaded nano-carriers possessed more detrimental effect against MCF-7 cells in comparison to their toxicity effect on another human breast cancer cell line, MDA-MB231 cells. For example, TAM-loaded solid lipid nanoparticles exhibited IC_{50} of 11.78 $\mu\text{g/mL}$ on MCF-7 cells, while the IC_{50} for MDA-MB231 cells was 15.80 $\mu\text{g/mL}$ (Abbasalipourkabir et al., 2012). This implies that the toxicity of TAM-loaded nanoparticles was dependent on the type of cancerous cells tested. The increase in the toxicity of TAM was likely due to the enhanced drug release and drug internalization by

the nano-carriers in which upsurge the drug efficacy (Serpe et al., 2004; Yuan et al., 2008).

The SI of DES-functionalized Gr for MCF-7 was higher than that of PrGr (2.00) and OxGr (1.99). TAM-GrF was the most selective drug vehicle for MCF-7 cells, having a SI of 4.86, followed by TAM-GrU (3.30) and TAM-GrG (3.00). By contrast, in general, TAM-loaded DES-functionalized Grs exhibited lower selectivity for AGS cells than MCF-7 cells. With regard to AGS cells, TAM-GrF was the most selective DES-functionalized Gr, having SI value of 2.22, followed by TAM-GrG (1.69), TAM-GrU (1.67), and TAM-GrMa (1.51) (Table 4.9). Of all tested samples, TAM-OxGr exhibited the most selective activity against AGS, with a SI value of 2.78, followed by TAM-GrF (2.22). Although TAM-OxGr showed higher selectivity against AGS, its toxicity towards RAW264.7 cells is considerable. Such high toxicity against macrophages is undesirable for anti-cancer drugs, as it may cause deterioration of the patient's defense system. Therefore, TAM-GrF is the most appropriate potential carrier for TAM as it has only mild cytotoxicity against macrophages. Moreover, the SI values obtained for TAM-loaded DES-functionalized Gr were considerably higher than those of other synthetic anti-cancer drugs such as alisiaquinol, 4-hydroxy tamoxifen, piperidinyl-diethylstilbestrol, and pyrrolidinyl-diethylstilbestrol, which were all reported to have SI values < 2.00 (Badisa et al., 2009; Desoubzdanne et al., 2008).

To further elucidate the anti-cancer mechanisms of TAM-loaded Grs, ROS and cell cycle analyses were conducted at the IC₅₀ concentration to provide a better reflection on cell death mechanisms, as 50% of cells are inhibited at this concentration.

4.4.1.2 DOX-loaded graphene

Following DOX loading, DOX-loaded Gr samples exhibited lethal impact against all types of cancer cells. Unlike TAM-loaded Gr, the DOX-loaded Gr especially for DES-functionalized Gr samples, possessed higher toxicity against MCF-7 cells compared to AGS and RAW264.7 cells (Figure 4.17). DOX-GrF resulted in the lowest IC_{50} especially on MCF-7 cell line (i.e., IC_{50} of 24.44), followed by the sequence: DOX-GrG (IC_{50} of 26.14 $\mu\text{g/mL}$) < DOX-OxGr (IC_{50} of 26.49 $\mu\text{g/mL}$) < DOX-GrU (IC_{50} of 26.83 $\mu\text{g/mL}$) (Table 4.12). On the other hand, DOX-OxGr displayed the lowest IC_{50} towards AGS cells (IC_{50} of 71.19 $\mu\text{g/mL}$), followed by DOX-GrG (IC_{50} of 122.31 $\mu\text{g/mL}$) and DOX-GrGW (IC_{50} of 137.71 $\mu\text{g/mL}$) (Table 4.13). The same trend was observed on RAW264.7 cell line which DOX-OxGr (IC_{50} of 130.8 $\mu\text{g/mL}$) resulted in the lowest IC_{50} compared to DOX-GrG (IC_{50} of 156.57 $\mu\text{g/mL}$) < DOX-GrU (IC_{50} of 191.93 $\mu\text{g/mL}$) < DOX-GrSW (IC_{50} of 234.87 $\mu\text{g/mL}$). The combined cytotoxic effect of OxGr and DOX was highly toxic toward both cells. Unlike DOX loaded-DES functionalized Gr, the high cytotoxicity of DOX-OxGr against macrophages cells (i.e., RAW264.7 cells) is somehow unfavorable for the drug delivery system.

As compared to free-loaded Gr samples, the toxicity of DES-functionalized Gr for both cancerous cells (i.e., MCF-7 and AGS cells) significantly increased following the DOX loading onto the Gr, especially for the case of GrGW, GrMa, GrFW, and GrGlyW. For instance, DOX-GrGW exhibited IC_{50} of 92.35 $\mu\text{g/mL}$ and 137.17 $\mu\text{g/mL}$ on MCF-7 and AGS cells, respectively, which was more toxic than free-loaded GrGW (MCF-7: 442.40 $\mu\text{g/mL}$, AGS: 218.15 $\mu\text{g/mL}$). Conversely, DOX-GrMa resulted in IC_{50} of 124.27 $\mu\text{g/mL}$ and 159.36 $\mu\text{g/mL}$ against MCF-7 and AGS cells, respectively, while free-loaded GrMa

had IC_{50} of 454.30 $\mu\text{g/mL}$ and 273.67 $\mu\text{g/mL}$ on MCF-7 and AGS cells, respectively. In comparison with other graphene-based DOX carriers, multifunctional graphene oxide drug carriers named GO/PEI.Ac-FI-PEG-LA at various concentration (0.5 μM , 1 μM , 2 μM and 4 μM) exhibited higher cell inhibition than free-loaded Gr (i.e., approximately 50% inhibition) (Lv et al., 2016). This higher toxicity of DOX-loaded Gr as compared to free-loaded Gr indicates that the lethal interaction between graphene and cells was significantly increased when DOX was loaded onto graphene which is in accordance with previous studies with other nano-delivery systems (Ashley et al., 2011; Deepa et al., 2014; Hekmat et al., 2012; Oktay et al., 2013; Park et al., 2009). The toxicity of DOX-loaded nano-carriers, such as PEGylated poly(lactic-co-glycolic acid) nano-carrier, nanoporous silica particles, silver nanoparticles, and liposomes against cancerous cells considerably increased as compared to the drug free-nano-carriers (Ashley et al., 2011; Deepa et al., 2014; Hekmat et al., 2012; Oktay et al., 2013; Park et al., 2009). The DOX encapsulated within nano-carrier systems were efficiently released at the targeted cancer cells due to their distinctive tiny size (Oktay et al., 2013). However, DOX-loaded nanoparticles caused lower cytotoxicity against 9L gliosarcoma cells (GS-9L) as compared to other types of glioblastoma (i.e., F-98 and RG-2 cells) (Sanchez De Juan et al., 2006). This indicates that the DOX-loaded nanoparticles have different toxicity effects on different types of cancerous cells.

On the selectivity of the DOX-loaded Gr against cancer cells, DOX-GrF counted the highest selectivity index against MCF-7 cells with 11.01, followed by PrGr (7.81), GrU (7.15) and GrSW (6.88) (Table 4.12). As for the selectivity index against AGS cells, DOX-GrGW was the most selective with 2.86, followed by DOX-GrMa (2.16) and DOX-

GrGlyW (2.12) (Table 4.13). DOX-loaded DES-functionalized Gr exhibited lower SI against AGS cells as compared to their selectivity against MCF-7 cell line. Nevertheless, these levels of selectivity are considered to be significantly higher as compared to other synthetic anti-cancer drugs such as piperidinyl-diethylstilbestrol, pyrrolidinyl-diethylstilbestrol, alisiaquinol and 4-hydroxy tamoxifen, which were reported to possess a selectivity index < 2.00 (Badisa et al., 2009; Desoubzdanne et al., 2008).

The ROS and cell cycle analysis assays were conducted at the IC₅₀ of all Gr samples to further elucidate the anti-cancer mechanisms after exposure to the DOX-loaded Gr. The use of IC₅₀ concentration may give better reflection on the cell death mechanisms as 50% of the cells are inhibited at this concentration.

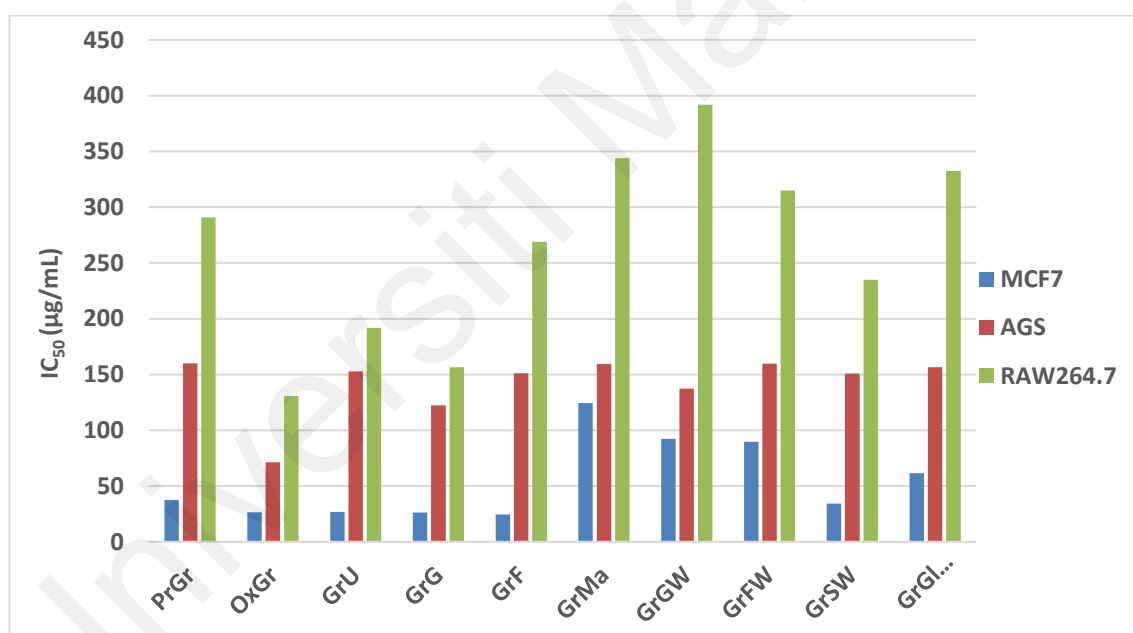


Figure 4.17: IC₅₀ values of DOX-loaded PrGr, OxGr and DES-functionalized Grs on MCF-7, AGS and RAW264.7 cell lines.

Table 4.12: IC₅₀ values of DOX-loaded PrGr, OxGr and DES-functionalized Gr samples on MCF-7 and RAW264.7 cell lines, and also their selectivity index. Values are expressed as the mean ± standard deviation of three different experiments.

Sample	IC ₅₀ (µg/mL)		SI
	RAW264.7	MCF-7	
DOX-PrGr	291.00±8.39	37.26±4.33	7.81
DOX-OxGr	130.8±4.81	26.49±4.29	4.94
DOX-GrU	191.93±3.55	26.83±5.34	7.15
DOX-GrG	156.57±4.86	26.14±5.52	5.99
DOX-GrF	269.13±4.91	24.44±3.93	11.01
DOX-GrMa	343.97±9.32	124.27±7.17	2.77
DOX-GrGW	391.9±3.43	92.35±6.93	4.24
DOX-GrFW	315.03±5.96	89.70±6.97	3.51
DOX-GrSW	234.87±10.34	34.15±4.82	6.88
DOX-GrGlyW	332.63±4.95	61.46±5.80	5.41

Table 4.13: IC₅₀ values of DOX-loaded PrGr, OxGr and DES-functionalized Gr samples on AGS and RAW264.7 cell lines, and also their selectivity index. Values are expressed as the mean ± standard deviation of three different experiments.

Sample	IC ₅₀ (µg/mL)		SI
	RAW264.7	AGS	
DOX-PrGr	291.00±8.39	159.97±7.10	1.82
DOX-OxGr	130.8±4.81	71.19±1.53	1.84
DOX-GrU	191.93±3.55	152.73±6.20	1.26
DOX-GrG	156.57±4.86	122.31±4.71	1.28
DOX-GrF	269.13±4.91	151.09±7.21	1.78
DOX-GrMa	343.97±9.32	159.36±6.32	2.16
DOX-GrGW	391.9±3.43	137.17±5.13	2.86
DOX-GrFW	315.03±5.96	159.57±3.39	1.97
DOX-GrSW	234.87±10.34	150.76±6.95	1.56
DOX-GrGlyW	332.63±4.95	156.57±2.13	2.12

4.4.2 Reactive oxygen species generation

4.4.2.1 TAM-loaded graphene

Cellular oxidative stress occurs due to excessive production of free radicals, especially reactive oxidative species (ROS), which leads to cellular macromolecular damage (Ray et al., 2012). Stimulating the generation of ROS has become one of the most promising strategies for exterminating cancerous cells in the human body. TAM has been reported to generate a gradual and sustained increase of intracellular ROS, thereby mediating the occurrence of apoptosis (Ferlini et al., 1998). TAM-stimulated ROS is generated through the increase of intracellular Ca^{+2} , which activates NAD(P)H oxidase (an oxidant enzyme) (Lee et al., 2000). Overall, TAM-loaded PrGr, OxGr, and DES-functionalized Grs increased ROS generation over that of untreated AGS and MCF-7 cells (Appendix D: Figure 1D-2D).

In particular, ROS generation increased significantly after treatment with TAM-loaded DES-functionalized Gr for both MCF-7 and AGS cells (Figures 4.18 and 4.19). This indicates that, as with PrGr and OxGr, TAM-loaded DES-functionalized Gr retained the capacity for TAM-induced ROS generation. This is in agreement with TAM-loaded chitosan-coated silver nano-carriers, which also retained the ROS generation behavior of TAM (Varadharajaperumal et al., 2017). Although the Gr samples did not significantly differ, TAM-GrGW, TAM-GrG, TAM-GrF, and TAM-GrU led to the highest ROS generation with more than 90% of cells containing ROS in both MCF-7 (Figure 4.18) and AGS cells (Figure 4.19). This is in a good agreement with the cell viability results where the same four samples resulted in the most acute toxicity against AGS and MCF-7 cells. In contrast with unloaded Gr, TAM-loaded Gr generated considerably more ROS than

the unloaded Gr, particularly for the case of PrGr and OxGr, which induced ROS in less than 88% of cells for both MCF-7 and AGS cells.

TAM-GrGW exhibited the highest level of ROS generation on both MCF-7 (99.2%) and also AGS cells (99.4%). In MCF-7 cells, the most significant increase in ROS generation was between TAM-GrGW (99.2%) and unloaded GrGW (74.1%). Meanwhile, in AGS cells, the greatest increase was for TAM-GrMa (79.0%) relative to unloaded GrMa (60.3%). The induction of ROS by TAM-Gr was also significantly higher than those of unloaded Gr from various graphene-based compounds such as graphene oxide, aggregated graphene, nitric oxide-functionalized graphene, and oxygenated graphene (Matesanz et al., 2013; Sasidharan et al., 2011; Sasidharan et al., 2012; Yang et al., 2013b). These results support that TAM loading has a major influence on intracellular ROS generation.

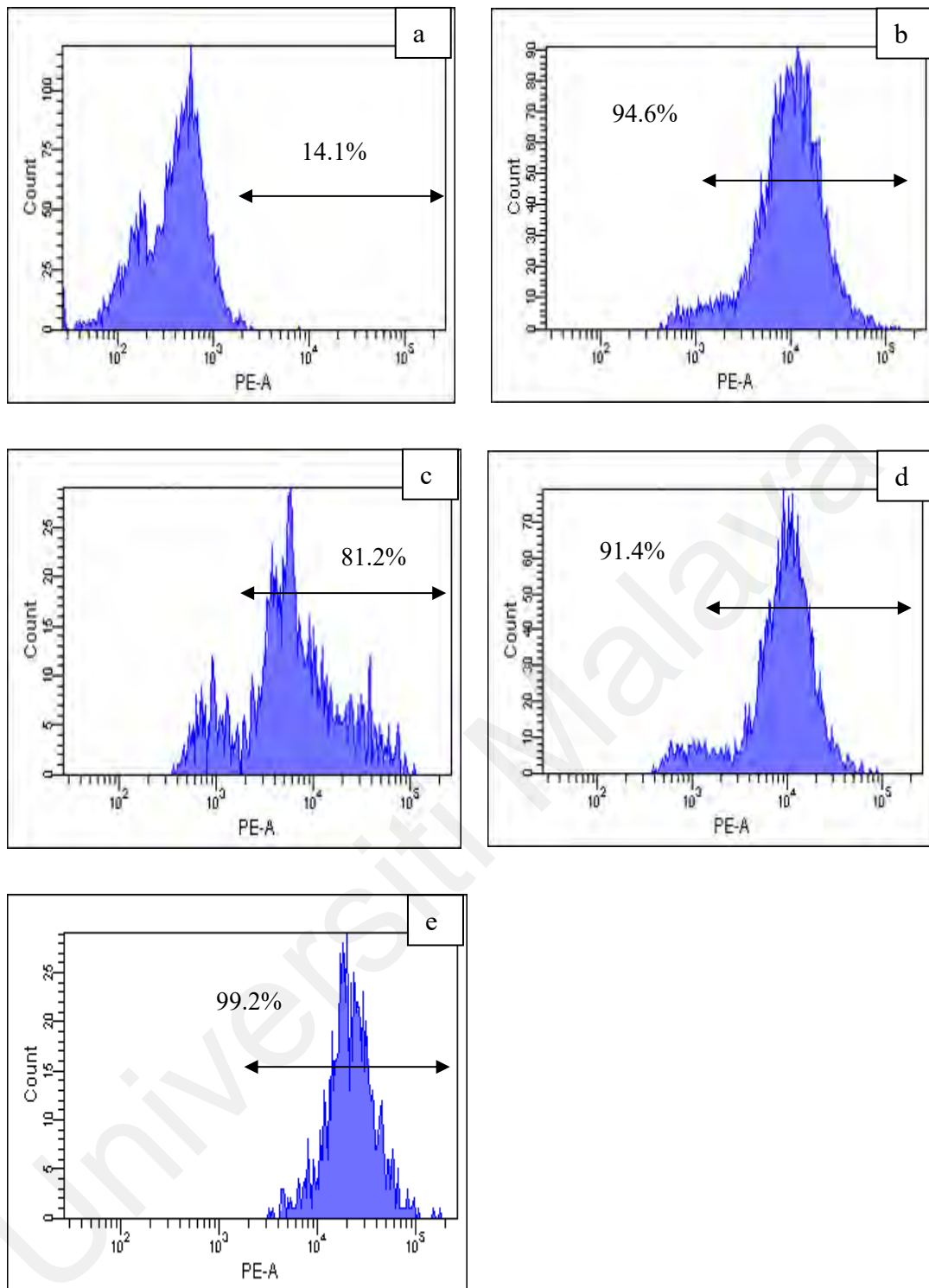


Figure 4.18: ROS generation of (a) untreated MCF-7 cells and MCF-7 cells treated with TAM-loaded (b) GrF, (c) GrMa, (d) OxGr, and (e) GrGW. Values indicates the percentages of cells generated ROS (by the fluorescence intensity) in the gated area. Shown are representative data of three independent experiments.

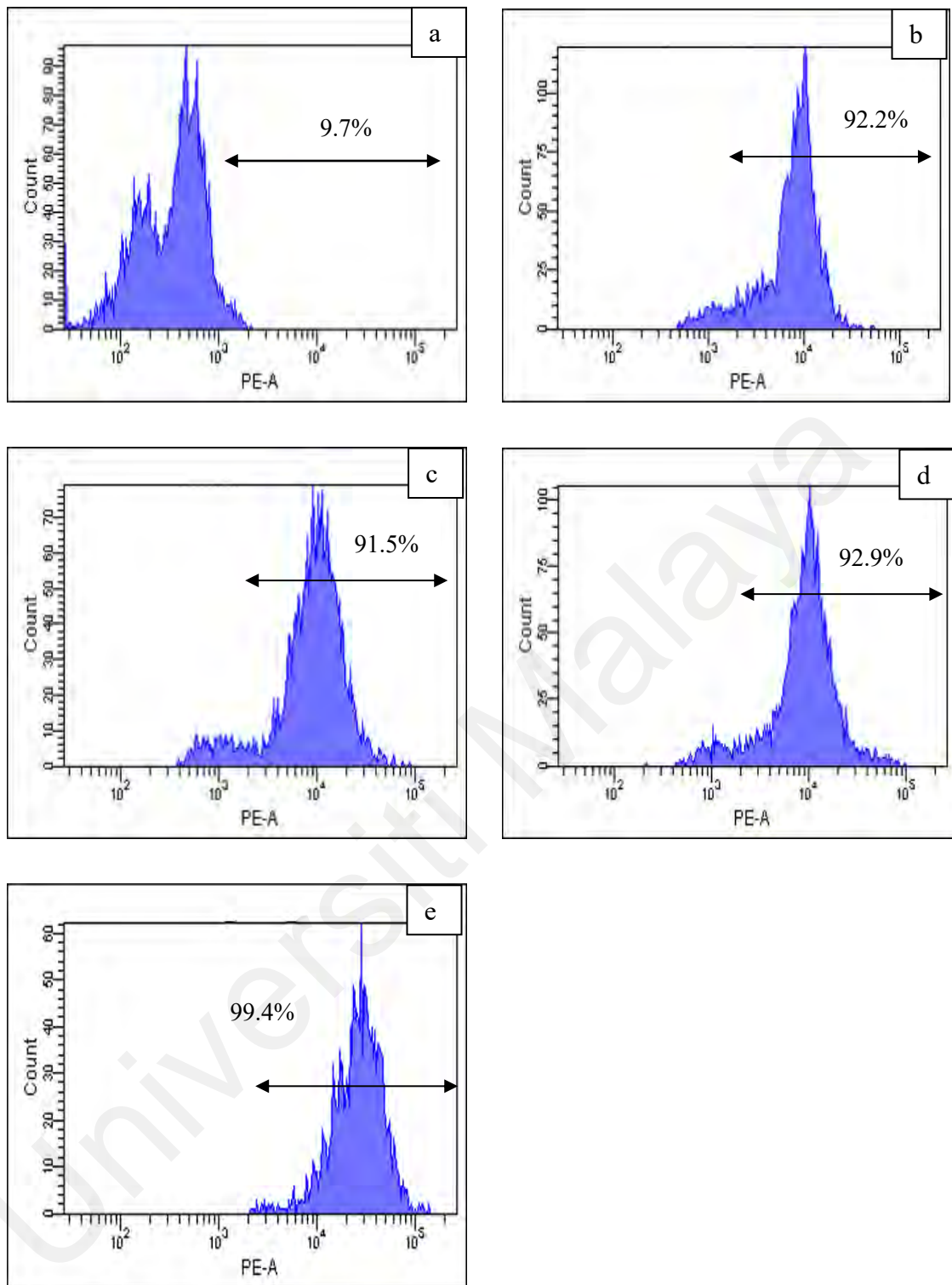


Figure 4.19: ROS generation of (a) untreated AGS cells and AGS cells treated with TAM- loaded (b) GrG, (c) GrU, (d) OxGr, and (e) GrGW. Values indicates the percentages of cells generated ROS (by the fluorescence intensity) in the gated area.

Shown are representative data of three independent experiments.

4.4.2.2 DOX-loaded graphene

One of the cell death mechanisms caused by DOX involves the generation of ROS, which may lead to cellular oxidative damage (Kim et al., 2006; Lau et al., 2008; Minotti et al., 2004). Previous studies (Gutierrez, 2000; Shadle et al., 2000) de-convoluted several mechanisms of DOX-mediated ROS stimulation, including one that involves an enzymatic pathway that is coupled with the mitochondrial respiratory chain and also a non-enzymatic mechanism that used iron. Several enzymes, namely NAD(P)H dehydrogenase, cytochrome p450 and nitric oxide synthase, have been speculated to initiate metabolic oxidation via the reductive effect of DOX (Childs et al., 2002; Doroshov & Davies, 1986). In addition, DOX also may induce release of calcium from internal stores, thereby stimulating the ROS and interrupting of cellular redox balance (Kim et al., 2006).

Figure 4.20 demonstrates that the peaks shift to the right (i.e., greater fluorescence intensity), indicating an increase of ROS generation by all DOX-loaded Gr samples as compared to untreated cells. However, there was insignificant difference among the DOX-loaded Gr samples in which the ROS generation was higher than 90% for both MCF-7 and AGS cells (Appendix D: Figure 3D-4D). This indicates that the Gr samples were able to retain one of the DOX anti-cancer properties (i.e., ROS generation). This is in accordance with poly(γ -benzyl-L-glutamate)-block-hyaluronan (PBLG-*b*-HYA)-based polymersomes and PEG-poly(lactic-co-glycolic acid)-based copolymeric nano-carrier, which also retained the ROS generation behavior of DOX (Li et al., 2017; Upadhyay et al., 2010).

DOX-GrF possessed the highest level of ROS generation (99.7%) on MCF-7 cells, followed by DOX-GrGlyW (99.5%), DOX-GrFW (99.5%), DOX-GrG (99.5%), and DOX-OxGr (99.5%) (Figure 4.20). In contrast, in AGS cells, DOX-GrGW and DOX-GrFW led to the highest ROS generation with 99.8%, followed by DOX-GrG (99.7%) and DOX-GrF (99.2%) (Figure 4.21). DOX-loaded Gr also exhibited higher ROS generation as compared to free-loaded Gr in which ROS level was averagely less than 90% for MCF-7 and also AGS cells. For instance, DOX-GrG showed significantly higher ROS production (i.e., >99.0%) as compared to unloaded GrG in both MCF-7 (74.1%) and AGS cells (71.0%). These levels of ROS generation were significantly higher as compared to unloaded graphene samples from various graphene-based compounds such as oxygenated graphene, aggregated graphene, graphene oxide, and nitric oxide-functionalized graphene (Matesanz et al., 2013; Sasidharan et al., 2011; Sasidharan et al., 2012; Yang et al., 2013b). This indicates that loading of DOX onto graphene increased intracellular ROS generation.

The ROS stimulation through DES-functionalized Grs is also aligned with the cell viability analysis, where DOX-loaded GrF led to the highest destructive impact on MCF-7 cells in comparison to other DOX-loaded Gr samples. This confirms the significant role of DOX-induced ROS generation in cancer cell death, which is in agreement with previous studies (Dietze et al., 2001; Matés & Sánchez-Jiménez, 2000; Minotti et al., 2004; Wiseman & Halliwell, 1996) regarding the critical role of ROS in anti-cancer activities toward various cancerous cells. For instance, Tsang et al. (2003) found that increased intracellular ROS generation, namely superoxide and hydrogen peroxide, resulted in cell death of the human osteosarcoma cell line (Saos-2).

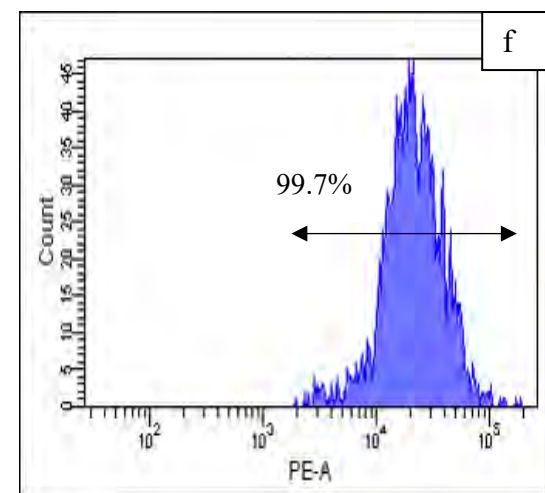
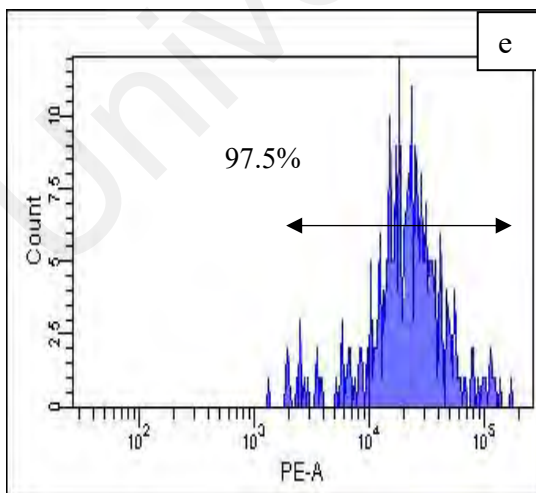
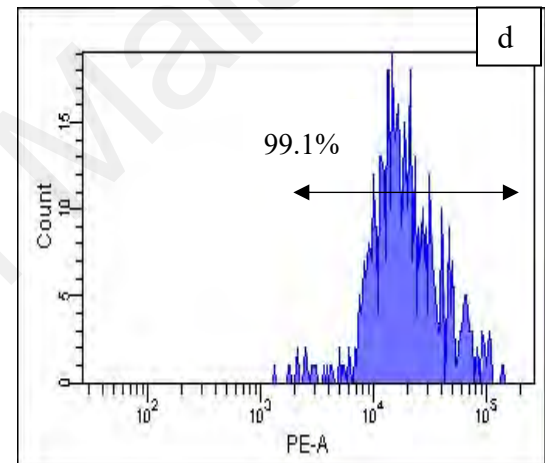
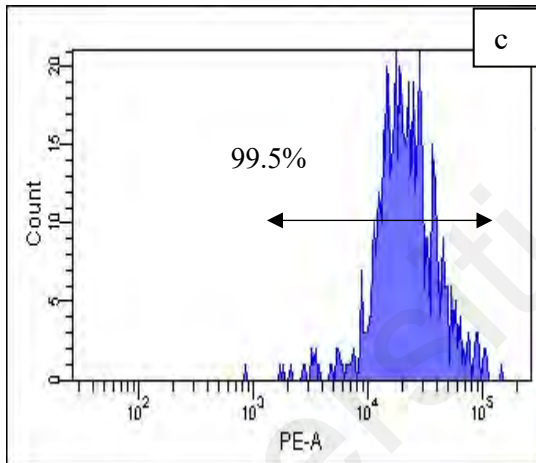
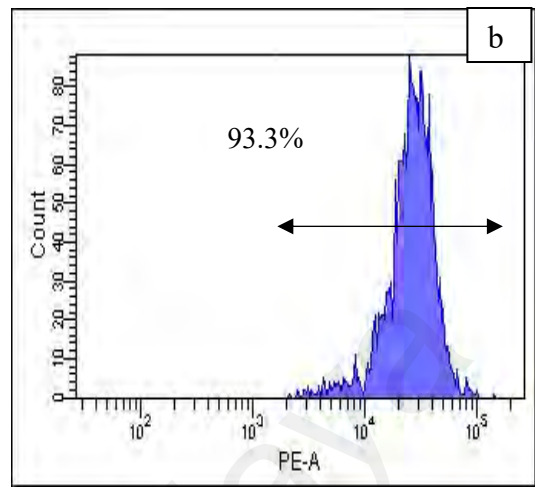
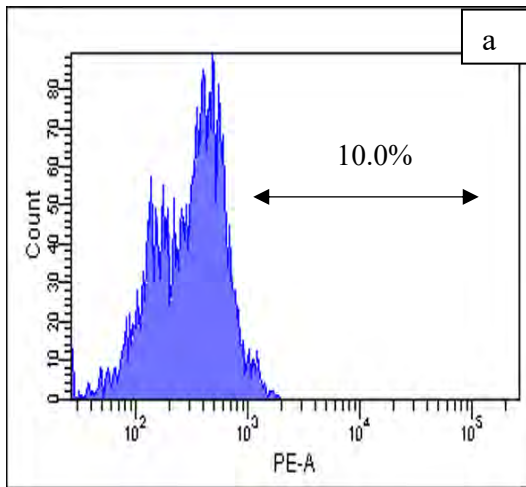
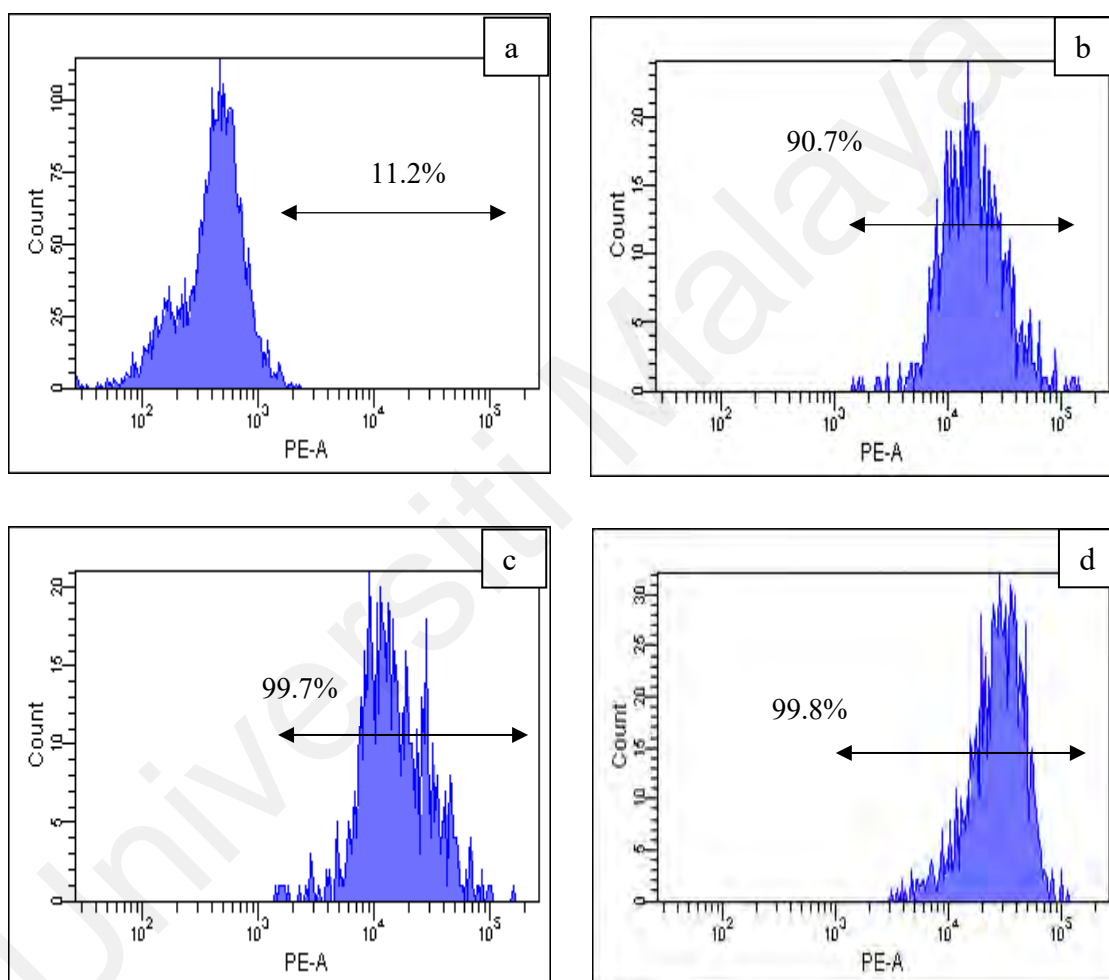


Figure 4.20: ROS generation of (a) untreated MCF-7 cells and MCF-7 treated with DOX-loaded (b) PrGr, (c) OxGr, (d) GrSW, (e) GrGlyW, and (f) GrF. Values indicates the percentages of cells generated ROS (by the fluorescence intensity) in the gated area.

Shown are representative data of three independent experiments.



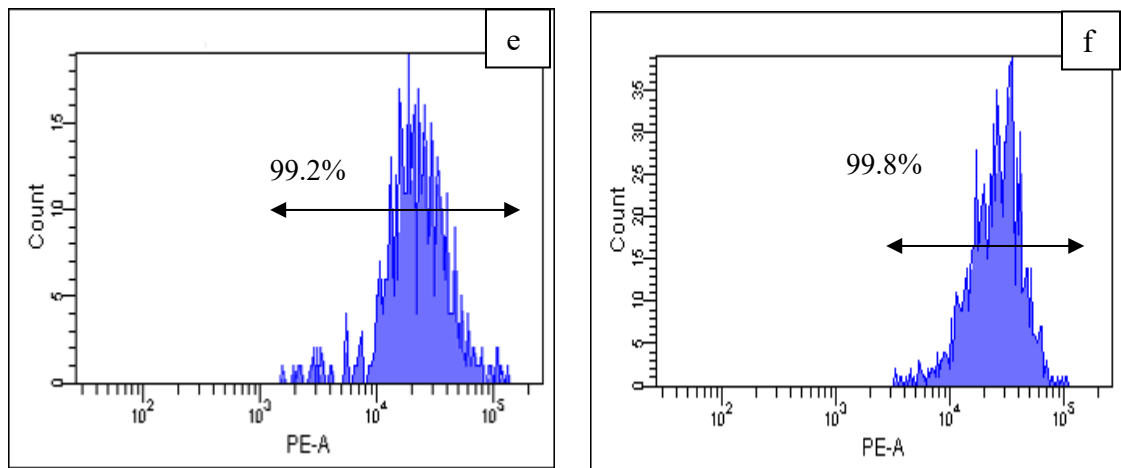


Figure 4.21: ROS generation of (a) untreated AGS cells and AGS cells treated with DOX-loaded (b) GrU, (c) GrG, (d) GrGW, (e) GrF and (f) GrFW. Values indicates the percentages of cells generated ROS (by the fluorescence intensity) in the gated area.

Shown are representative data of three independent experiments.

4.4.3 Cell cycle disruption

4.4.3.1 TAM-loaded graphene

One of the strategies used for developing anti-cancer agents is modulating progression of the cell cycle. Tamoxifen-induced cell cycle disruption is one of the most effective protocols to prevent the progression of cancer cells, as tamoxifen is able to acutely inhibit the proliferation of cancerous cells (Buzdar et al., 2006; Mao et al., 2009; Sutherland et al., 1983; Yaacob et al., 2015). The impact of TAM-loaded Gr on the cell cycle phases of cancerous cells was examined by flow cytometric analysis with propidium iodide staining. Overall, the results verified that TAM-loaded PrGr, OxGr, and DES-functionalized Gr disrupted cell cycle progression in both AGS and MCF-7 cell lines (Appendix E: Figure 1E-2E).

Untreated MCF-7 cells (a control) have cell population proportions of 46.8% at G0/G1 phase, 26.6% at S phase, and 26.6% at G2/M phase (Figure 4.22). After treatment with TAM-GrU, TAM-GrG, or TAM-GrF, MCF-7 cell progression was arrested at G0/G1 phase (> 68% of cells), which consequently impeded cell cycle progression. On the other hand, TAM-PrGr, TAM-OxGr, TAM-GrMa, and TAM-GrGW mildly disrupted the cell cycle progression at G0/G1 phase with >44% of the cell population. In AGS cells, untreated cells had a distribution of 52.1% of the cell population at G0/G1 phase, 26.9% at S phase, and 21.0% at G2/M phase (Figure 4.23). Unlike MCF-7, treatment with TAM-loaded GrU, GrG, GrF, and GrGW disrupted the cycle of AGS cells at the S and G2/M phases (Figure 4.23). For example, significant cell arrest at S phase and G2/M phase was observed with TAM-GrG, with 30.9% of the cell population at S phase and 28.2% at G2/M phase, and subsequently impeded cell cycle progression.

Drug-induced DNA damage is believed to predominantly occur at the G2/M phase (DiPaola, 2002); cell arrest at the G2/M checkpoint may cause cancer cells to undergo apoptosis, and subsequently increase the destructive effects. These findings are in accordance with previous studies (Ling et al., 1996; Potter et al., 2002; Wu et al., 2008) carried out in various types of cancer cell lines. The results also demonstrated a good relationship between ROS and cell cycle mechanisms, where the increase of intracellular ROS generation by TAM-loaded Gr led to the inhibition of cell cycle proliferation. As reported previously (Ferlini et al., 1999; Kumar et al., 2013; Lau et al., 2008), high levels of ROS can cause cell cycle disruption and apoptosis, especially in the case of TAM-mediated cell death.

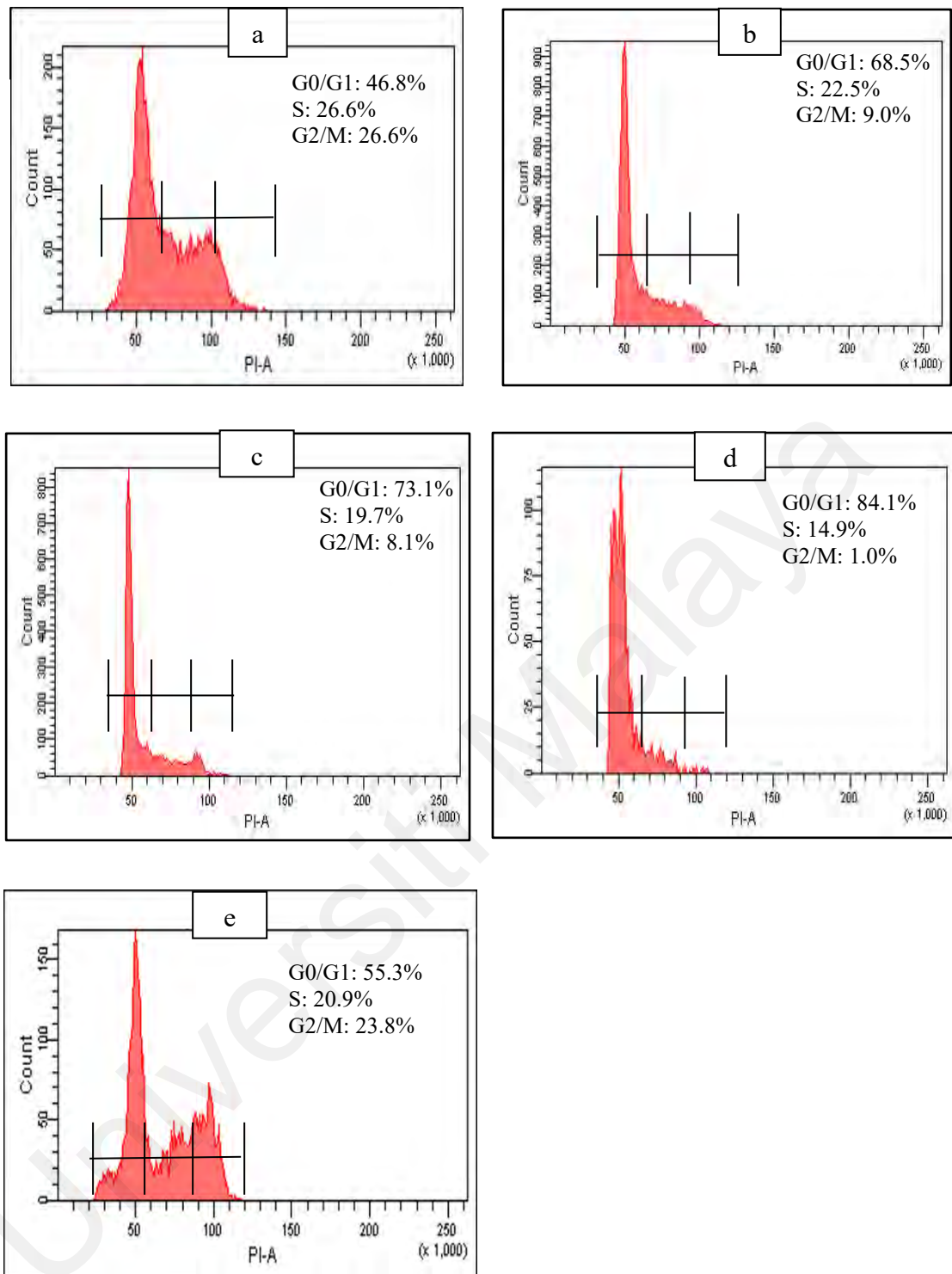


Figure 4.22: Cell cycle comparison of the (a) untreated MCF-7 cell line and MCF-7 cells treated with TAM-loaded (b) GrU, (c) GrG, (d) GrF, and (e) GrGW. Cells were harvested after 24 h, fixed and stained with PI to detect DNA contents. Values represent the percentages of viable cells at G0/G1, S or G2/M phases. Shown are representative data of three independent experiments.

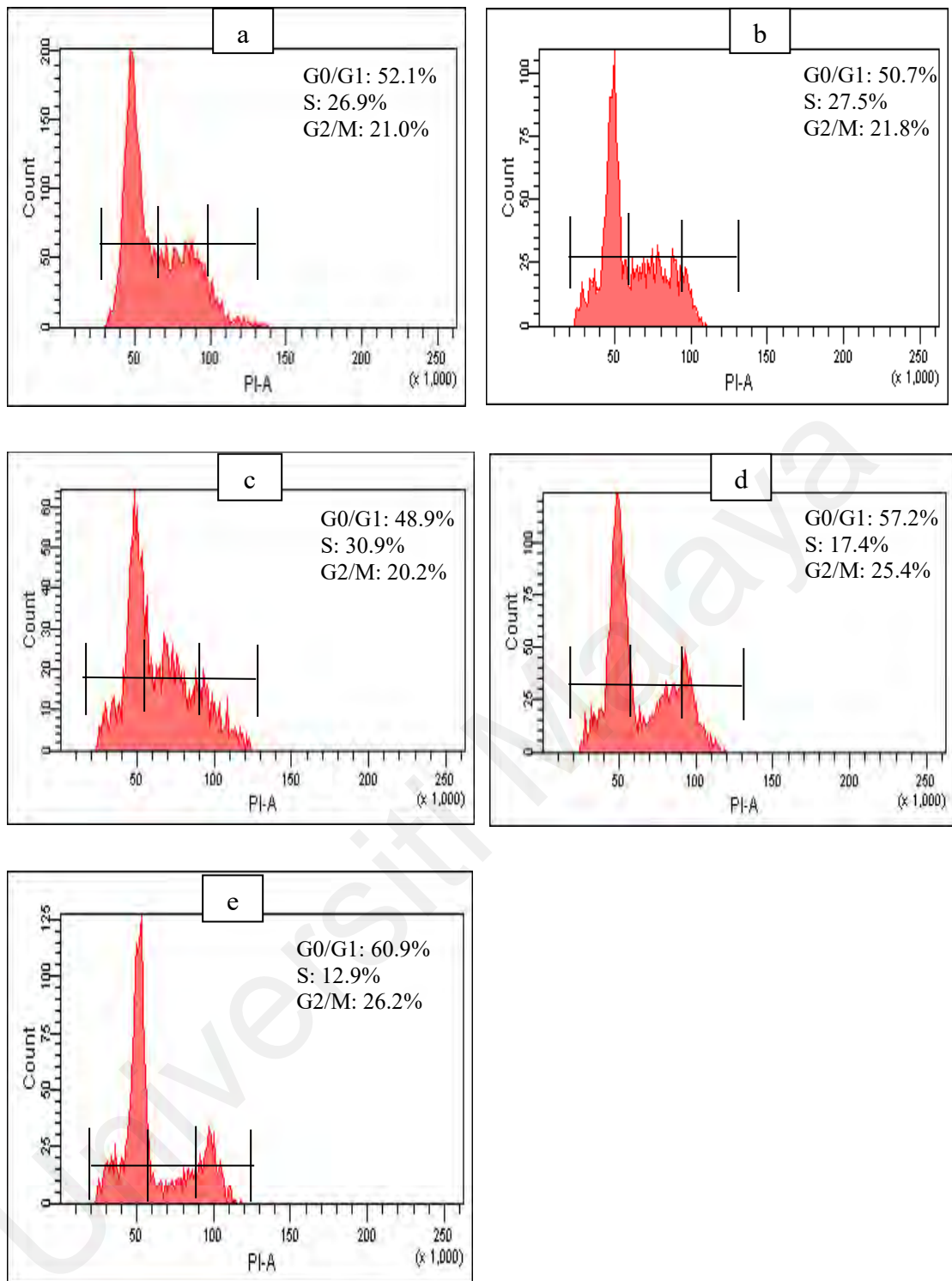


Figure 4.23: Cell cycle comparison of the (a) untreated AGS cell line and AGS cells treated with TAM-loaded (b) GrU, (c) GrG, (d) GrF, and (e) GrGW. Cells were harvested after 24 h, fixed and stained with PI to detect DNA contents. Values represent the percentages of viable cells at G0/G1, S or G2/M phases. Shown are representative data of three independent experiments.

4.4.3.2 DOX-loaded graphene

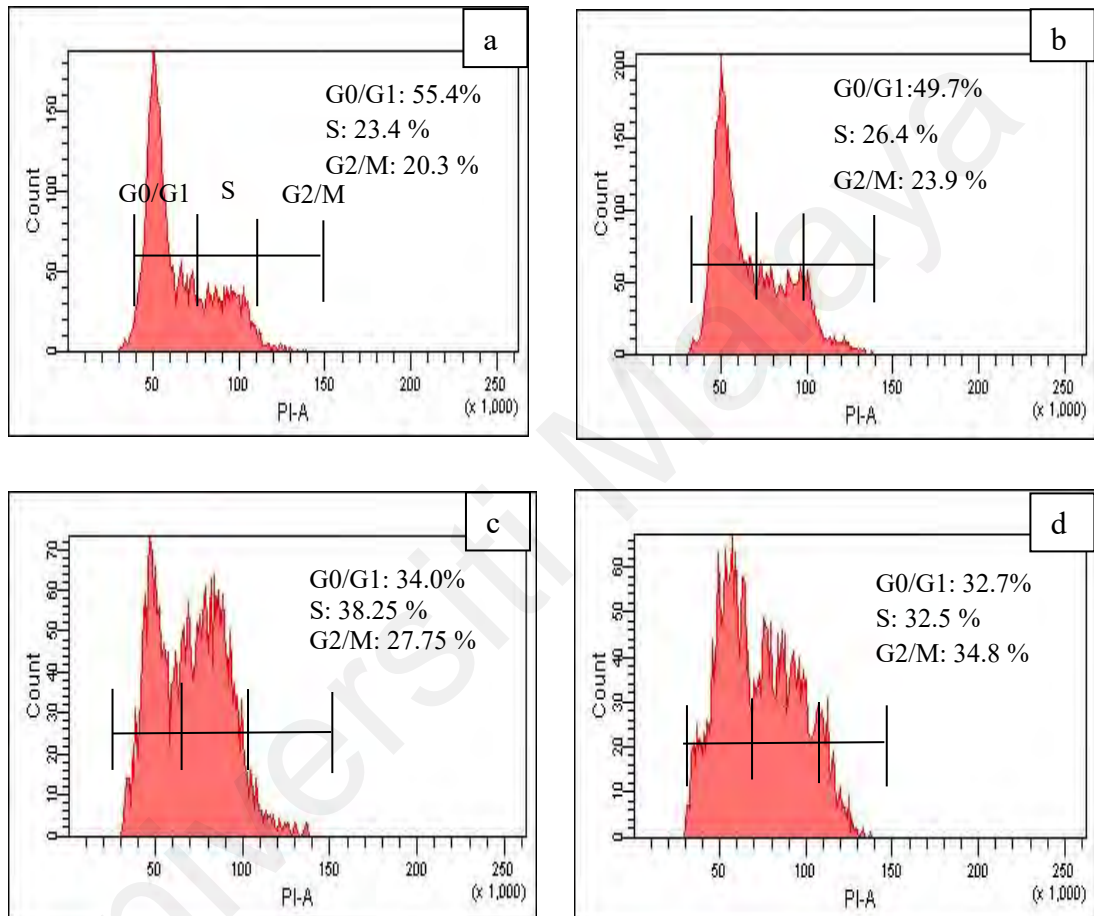
Doxorubicin-induced cell cycle disruption is one of the most effective ways to tackle the progression of cancer cells. Several studies highlighted that DOX may target multiple molecular mechanisms to disrupt cell cycle progression (Ashley & Poulton, 2009; Chen et al., 2011a; Hilmer et al., 2004; Oktay et al., 2013). One of the examples, DOX induces the activation of numerous molecular signals via activated protein kinase (AMPK), in which triggering a series of apoptosis pathways and disrupting cell cycle progression (Jones et al., 2005; Okoshi et al., 2008; Xiang et al., 2004). Therefore, propidium iodide staining and flow cytometry analysis of the treated MCF-7 and AGS cells were conducted to elucidate the impact of DOX-loaded Gr on cell cycle phases. The result exhibits that DOX-loaded Gr (i.e., PrGr, OxGr, and DOX-loaded DES-functionalized Gr) disrupted cell cycle progression in both MCF-7 and AGS cells (Appendix E: Figure 3E-4E).

Untreated MCF-7 cells (as a control) had 55.4% of its cell population at G0/G1 phase, 23.4% at S phase, and 20.3% at G2/M phase (Figure 4.24). On the other hand, untreated AGS cells have cell population proportions of 51.9% in G0/G1 phase, 23.9% in S phase, and 24.2% in G2/M phase (Figure 4.25). The DOX-loaded PrGr, OxGr, and DES-functionalized Gr led to the cells arrest at S phase and G2/M phase (i.e., increased the number of cells at S phase and G2/M phase), and consequently impeded cell cycle progression in both MCF-7 and AGS cells. This indicates that DOX-loaded Grs were effective in disrupting the cell cycle of cancerous cells and therefore eventually cause cell death.

In MCF-7 cell line, significant cell arrest at S phase and G2/M phase was observed with DOX-GrGlyW, with 40% of the cell population at S phase and 28.4% at G2/M phase, as compared to untreated MCF-7 cells (i.e., S phase: 23.4% and G2/M phase: 20.3% of the cell population). Meanwhile, DOX-GrFW considerably disrupted the cell cycle progression of AGS cells at S phase and G2/M phase, with 42.4% and 26.8% of the cell population at S phase and G2/M phase, respectively, as compared to untreated AGS cells (i.e., S phase: 23.9% and G2/M phase: 24.2% of the cell population). The increase in the number of cell population at S phase and G2/M phase hindered the progression of the cells into the G0/G1 phase. This led to a significant decrease in the number of cells at G0/G1 phase in both MCF-7 and AGS cells after treatment with DOX-GrGlyW and DOX-GrFW.

In comparison to unloaded DES-functionalized Gr samples, the impact of DOX-loaded DES-functionalized Grs on the cell cycle proliferation was more acute. The cell cycle proliferation of unloaded Gr was arrested at G0/G1 phase, while the cell cycle disruption by DOX-loaded Gr was significantly occurred at G2/M phase. As shown in Figure 4.26, the G2 checkpoint permits the cells to repair DNA damage before proceeding into the mitosis phase. The significant amount of DNA damage that occurs in the cells may lead to a higher number of cells arrested at G2/M phase. DOX-induced DNA damage is believed to predominantly occur at the G2/M phase (DiPaola, 2002). Cell arrest at the G2/M checkpoint may cause cancer cells to undergo apoptosis and subsequently increase the destructive effects. This incident is in accordance with previous studies (Ling et al., 1996; Potter et al., 2002) of various types of cancer cell lines. An obvious relationship between ROS and cell cycle mechanisms was observed in which the increase of

intracellular ROS by DOX-loaded Gr led to disruption of cell cycle progression. As studied previously (Kurz et al., 2004; Lau et al., 2008; Oktay et al., 2013), high level of ROS can cause cell cycle arrest and apoptosis, especially for DOX-mediated cell death.



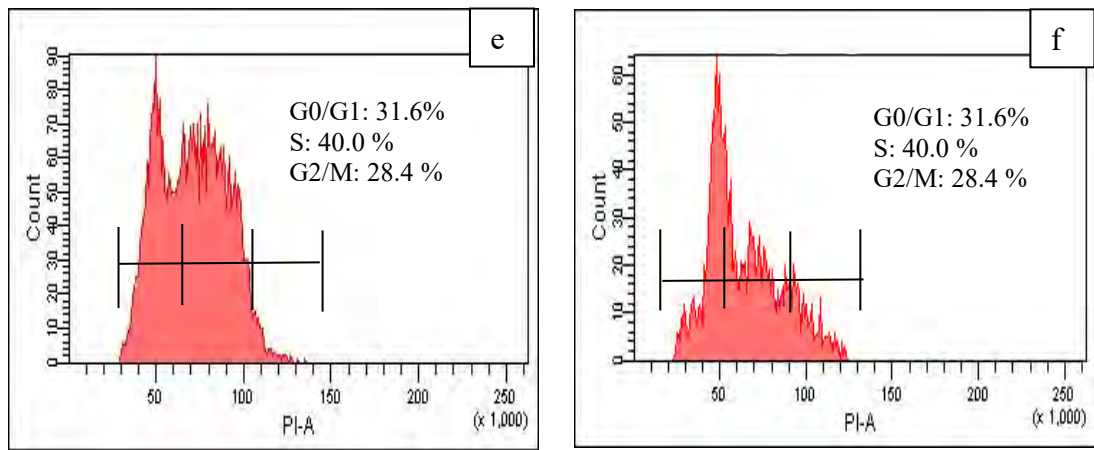
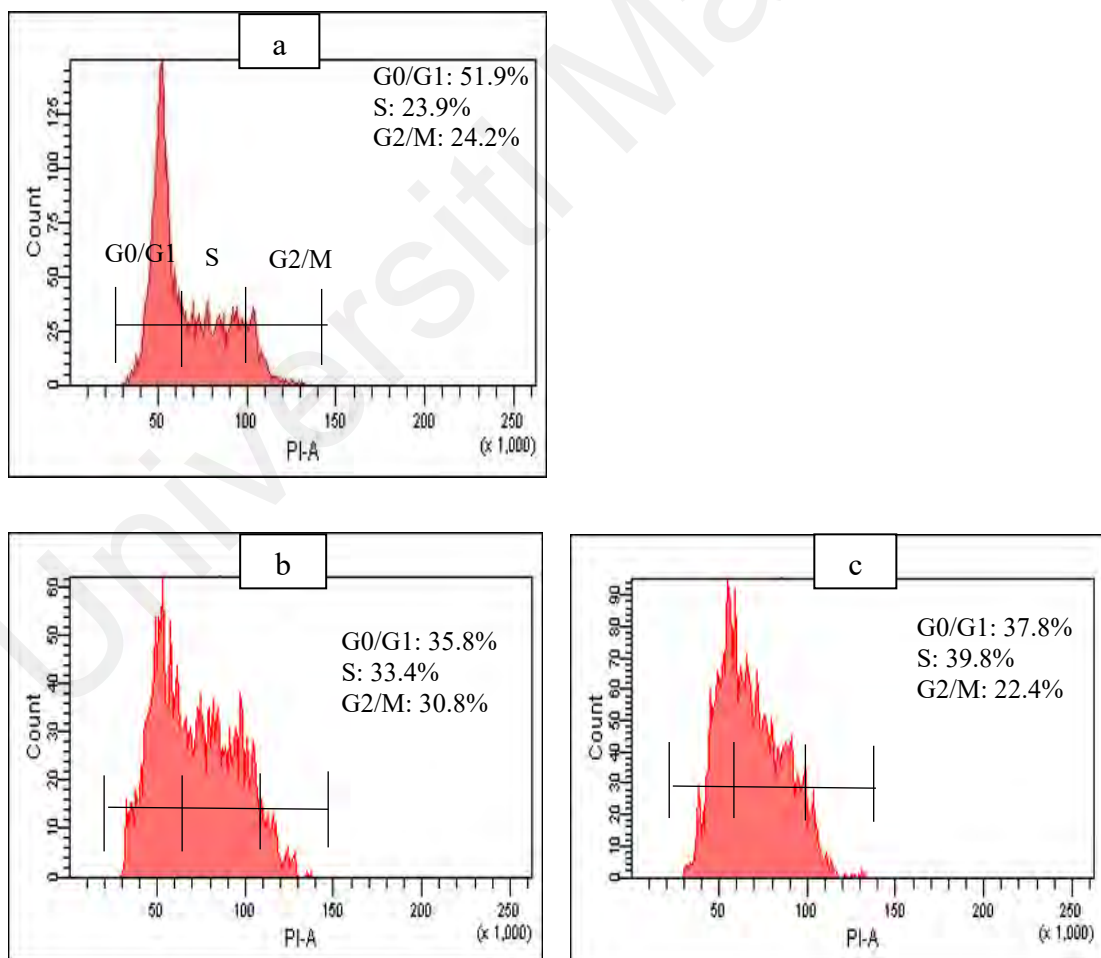


Figure 4.24: Cell cycle comparison of the (a) untreated MCF-7 cells and MCF-7 cells treated with DOX-loaded (b) PrGr, (c) OxGr, (d) GrSW, (e) GrGlyW, and (f) GrGW.

Cells were harvested after 24 h, fixed and stained with PI to detect DNA contents.

Values represent the percentages of viable cells at G0/G1, S or G2/M phases. Shown are representative data of three independent experiments.



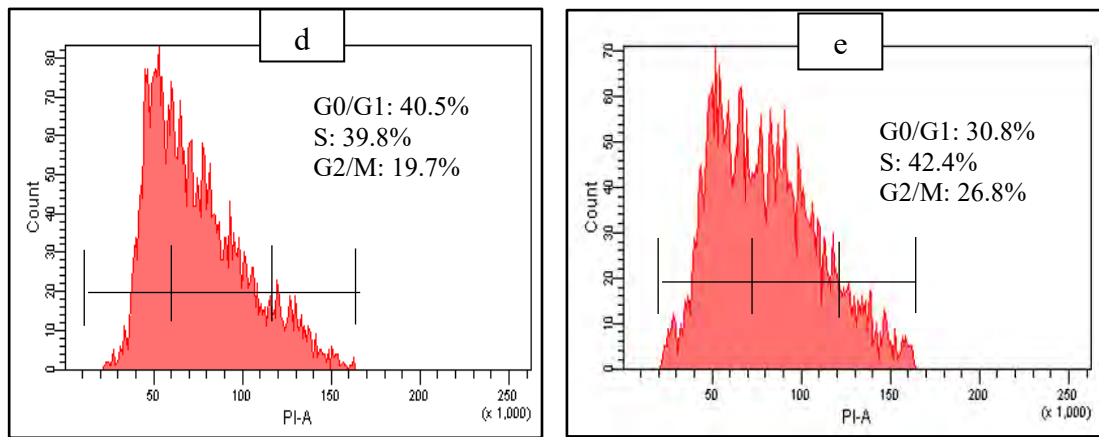


Figure 4.25: Cell cycle comparison of the (a) untreated AGS cell line and AGS cells treated with DOX-loaded (b) GrG, (c) GrGW, (d) GrF and (e) GrFW. Cells were harvested after 24 h, fixed and stained with PI to detect DNA contents. Values represent the percentages of viable cells at G0/G1, S or G2/M phases. Shown are representative data of three independent experiments.

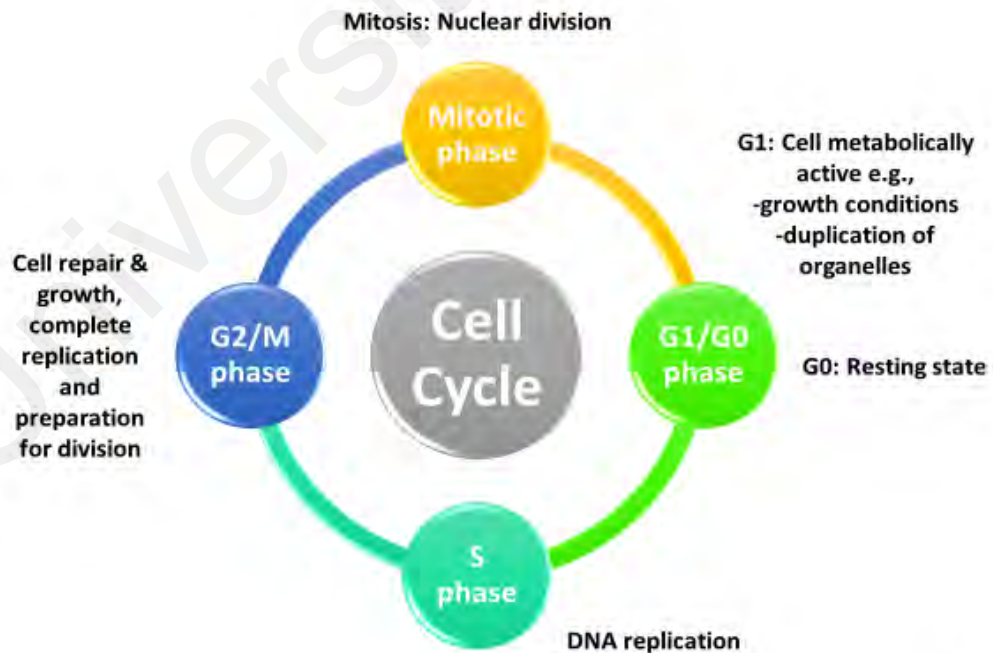


Figure 4.26: Diagrammatic of cell cycle phases

4.4.4 Cellular kinetic responses

4.4.4.1 TAM-loaded graphene

Changes in electrical impedance caused by viable cells were determined using xCELLigence RTCA. Impedance measurements were converted into the unitless parameter cell index (CI), which reflects the quantitative measurements of cell number, degree of cell adhesion, cell viability, and cell morphology. The changes in CI caused by TAM (25 $\mu\text{g}/\text{mL}$) and by TAM-loaded PrGr, OxGr, and DES-functionalized Gr (100 $\mu\text{g}/\text{mL}$) across 96 h are presented in Figure 4.27 and Figure 4.28. The TAM-loaded Gr had more lethal impact on AGS cells as compared to MCF-7 cells. The pure TAM (i.e., without loading) (25 $\mu\text{g}/\text{mL}$) exhibited the most acute inhibition of MCF-7 and AGS cell growth, with CI less than 4 and 1, respectively, for the entire 96 h. This response resembled the real-time cytotoxic profiles demonstrated by other chemotherapeutic drugs (e.g. methyl methanesulfonate and camptothecin) against various cancerous cells (Duerr et al., 2012; Xavier et al., 2018; Zhou et al., 2018). Such high toxicity in intracellular system is undesirable for chemotherapeutic drugs, as it may also cause detrimental impact on non-cancerous cells. It has been suggested that incorporation of TAM in nano-carriers could prevent or reduce such side effects due to that the destructive impact by TAM-loaded carriers is not sudden (i.e., gradual damage) (Khuroo et al., 2014; Tagne et al., 2008).

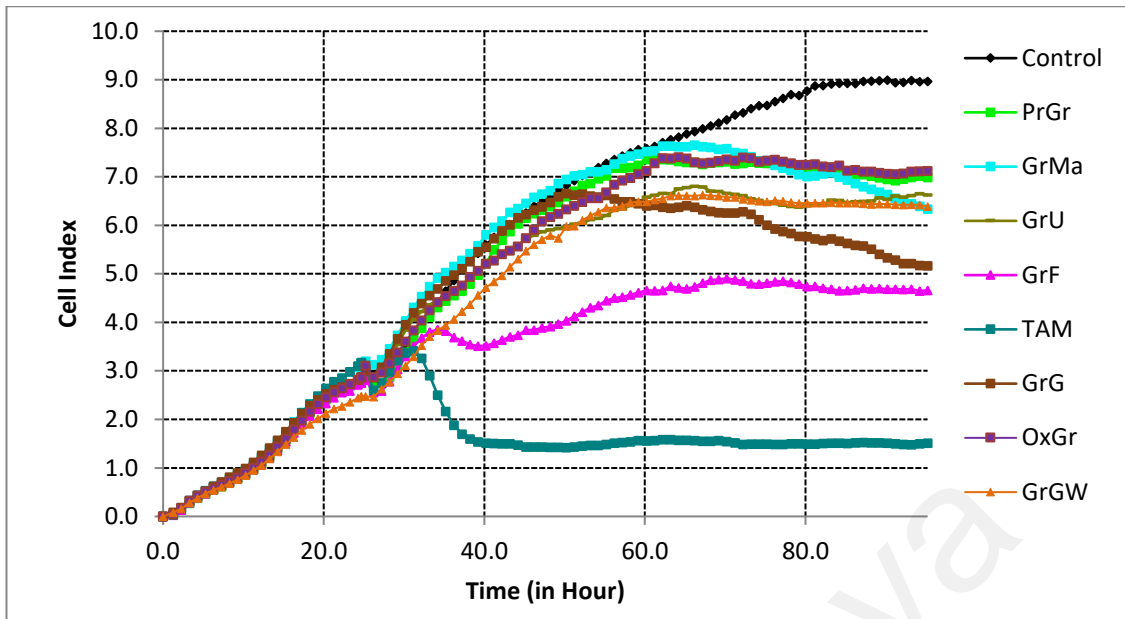


Figure 4.27: Cellular kinetic responses of TAM-loaded PrGr, OxGr and DES-functionalized Grs on MCF-7 cells. All graphene samples were tested at concentration 100 $\mu\text{g/ml}$ and TAM was tested at 25 $\mu\text{g/ml}$ on MCF-7 cell line.

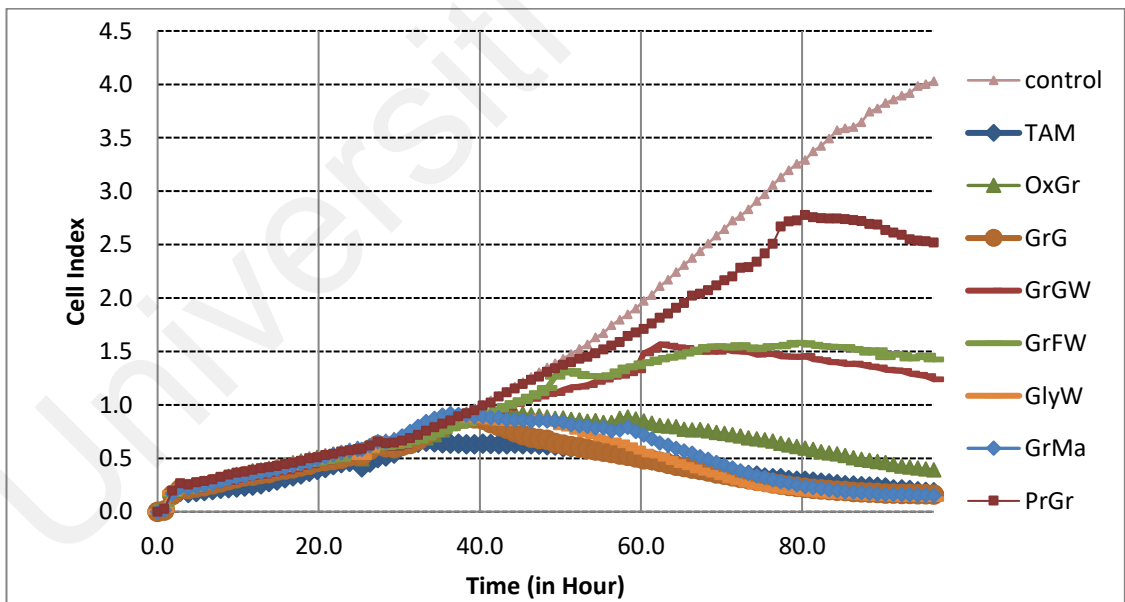


Figure 4.28: Cellular kinetic responses of TAM-loaded PrGr, OxGr and DES-functionalized Grs on AGS cells. All graphene samples were tested at concentration 100 $\mu\text{g/ml}$ and TAM was tested at 25 $\mu\text{g/ml}$ on AGS cell line.

All types of TAM-loaded Gr (i.e., TAM-PrGr, TAM-OxGr, and TAM-loaded DES-functionalized Gr) caused significant decrease in cell viability over time ($CI < 7.7$) relative to untreated MCF-7 cells ($CI > 8.5$). Likewise, a significant reduction was recorded for AGS cell viability over time after treating with TAM-loaded Gr ($CI < 3.0$), relative to untreated AGS cells ($CI > 4.0$). The significant toxicity for TAM-loaded Gr could be ascribed to the anti-cancer attribute of the TAM, resulting from either the efficient delivery of TAM or the synergistic cytotoxicity effect of TAM and graphene against cancerous cells. This is in accordance to the previous study on the effects of solid lipid nanoparticles (SPNs) and TAM-loaded SPNs towards MCF-7 and MDA-MB231 cells, in which the cytotoxic-combination of TAM and SPNs caused higher inhibition on the proliferation of cancerous cells (Abbasalipourkabir et al., 2016).

Inhibition of cell proliferation by TAM-loaded DES-functionalized Gr started at 24 h in both MCF-7 and AGS cells, and cell growth was continuously constrained through 96 h. However, in contrast with most types of TAM-loaded DES-functionalized Grs, significant cell inhibition was observed for TAM-GrMa only after 60 h of incubation, with consequent slowing of MCF-7 cell proliferation through the remaining period. Meanwhile, TAM-GrF caused the most significant reduction in CI (MCF-7: $CI < 5.0$ and AGS: $CI < 1.0$) out of all TAM-loaded Grs. This is in agreement with MTT cell viability results for MCF-7 and AGS cells, in which TAM-GrF exhibited the highest toxicity as compared to other TAM-loaded DES-functionalized Grs. As discussed previously in Section 4.4.2.1, TAM-GrF led to high ROS generation ($> 90.0\%$) in both MCF-7 and AGS cells, and also caused cell cycle disruption in the G0/G1 phase, which eventually encumbered the cell progression into S, G2/M, and mitosis phases (i.e., cytostatic effect).

This finding corresponded with those of previous studies (Chou et al., 2010; Tekin & Ozturk, 2017), which reported similar inhibition and cell cycle arrest of MCF-7 cells after treatment with the anti-oxidant drug quercetin. The high production of ROS and acute cell cycle disruption caused by TAM-GrF are likely primary reasons for the significant reduction in cell viability observed over 96 h.

A comparison between binary and ternary DES system, TAM-GrG and TAM-GrF indicated a higher inhibition of cell proliferation than their ternary TAM-GrGW and TAM-GrFW in both MCF-7 (Figure 4.27) and AGS cells (Figure 4.28). Although TAM-GrGW and TAM-GrFW had acute inhibition at 24 h however, after 30 h, the cell growth recovered back to normal cell proliferation. This is in agreement with MTT cell viability results, in which TAM-GrG and TAM-GrF exhibited higher toxicity (i.e., lower IC_{50}) as compared to TAM-GrGW and TAM-GrFW in both MCF-7 and AGS cells. For instance, in the case of MCF-7 cells, TAM-GrG and TAM-GrF showed significantly lower IC_{50} with 74.49 $\mu\text{g/mL}$ and 71.96 $\mu\text{g/mL}$, respectively, as compared to TAM-GrGW (340.10 $\mu\text{g/mL}$) and TAM-GrFW (360.10 $\mu\text{g/mL}$). Likewise, TAM-GrG (132.31 $\mu\text{g/mL}$) and TAM-GrF (157.58 $\mu\text{g/mL}$) possessed lower IC_{50} than TAM-GrGW (187.00 $\mu\text{g/mL}$) and TAM-GrFW (187.37 $\mu\text{g/mL}$) on AGS cell line.

Kinetics study was carried out on both MCF-7 and AGS cells by fitting their cell growth data to zero order, 1st order, and 2nd order models. As shown in Table 4.14, the untreated MCF-7 cells (i.e., control) fitted well to zero-order model ($R^2=0.948$) followed by 1st order model ($R^2=0.705$), and 2nd order model ($R^2=0.134$). In the case of AGS cells (Table 4.15), the untreated cells fitted well in both zero-order model ($R^2=0.954$) and 1st order

model ($R^2=0.946$), while it was not fitted in the 2nd order model ($R^2=0.321$). This trend is typically a mammalian cell growth profile (Lobo & Balthasar, 2002; Sukumaran et al., 2015). However, the fitting for cells treated with TAM was very low for all kinetic models, with R^2 values less than 0.026 in both MCF-7 and AGS cells. This indicates the acute toxicity of TAM towards cancerous cells, which considerably disrupted the zero and 1st order kinetic growth models.

Notably, the highest growth rate constants were obtained for untreated MCF-7 cells using zero and 1st order models, with values of 1.052×10^{-1} CI h⁻¹ and 0.302×10^{-1} h⁻¹, respectively (Table 4.14). Meanwhile, untreated AGS cells demonstrated the highest growth rate constants with values of 0.435×10^{-1} CI h⁻¹ (zero-order model) and 0.326×10^{-1} h⁻¹ (1st order model) in comparison to treated AGS cells (Table 4.15). These constants decreased after treatment with TAM-loaded Gr due to the inhibition of MCF-7 and AGS cells by TAM, which altered the cell growth curve and subsequently caused deceleration of the growth rate over time. This result clearly proved that the loading of TAM on Gr had a major inhibitory influence on the growth rate of cancerous cells.

In the zero-order model, the lowest growth rate constant of MCF-7 cells was obtained for TAM-GrF (0.478 CI h⁻¹), followed by TAM-GrG (0.599 CI h⁻¹) and TAM-GrU (0.731 CI h⁻¹). A similar trend was observed for the 1st order model, where TAM-GrF exhibited the lowest growth rate constant (0.228 h⁻¹), followed by TAM-GrG (0.230 h⁻¹) and TAM-GrU (0.258 h⁻¹). On the other hand, TAM-GrG possessed the lowest growth rate constant of AGS cells (0.011 CI h⁻¹) in the zero-order model, followed by TAM-GrMa (0.017 CI h⁻¹), and TAM-GrSW (0.022 CI h⁻¹). Similar finding was also obtained for the 1st order

model with the following sequence: TAM-GrG (0.010 h^{-1}) < TAM-GrMa (0.040 h^{-1}) < TAM-GrSW (0.052 h^{-1}). Severe disruption of the cell cycle triggered by a cell-cycle-specific anti-cancer drug may cause deviation in the cell growth kinetics, hence reducing the growth rate constant (Keefe et al., 1982; Panetta, 1997). These results attest that TAM-loaded DES-functionalized Gr possess acute toxicity against MCF-7 and AGS cells, and their effect on the growth rate was likely due to significant disruption of cell cycle progression.

Universiti Malaya

Table 4.14: Growth rate constant of the untreated MCF-7 cells and MCF-7 cells treated with TAM-loaded Gr.

Samples	Zero order	First order	Second order
	Rate constant x 10 ⁻¹ (CI h ⁻¹)	Rate constant x 10 ⁻¹ (h ⁻¹)	Rate constant x 10 ⁻¹ (CI ⁻¹ h ⁻¹)
Control	1.052	0.302	0.263
TAM-PrGr	0.837	0.286	0.324
TAM-OxGr	0.839	0.280	0.298
TAM-GrU	0.731	0.258	0.225
TAM-GrG	0.599	0.230	0.204
TAM-GrF	0.478	0.228	0.385
TAM-GrMa	0.786	0.266	0.301
TAM-GrGW	0.759	0.274	0.235
TAM-GrFW	0.869	0.303	0.319
TAM-GrSW	1.008	0.314	0.340
TAM-GrGlyW	0.899	0.272	0.215
TAM	0.024	0.041	0.232

Table 4.15: Growth rate constant of the untreated AGS cells and AGS cells treated with TAM-loaded Gr.

Samples	Zero order	First order	Second order
	Rate constant x 10 ⁻¹ (CI h ⁻¹)	Rate constant x 10 ⁻¹ (h ⁻¹)	Rate constant x 10 ⁻¹ (CI ⁻¹ h ⁻¹)
Control	0.435	0.326	0.469
TAM-PrGr	0.314	0.288	0.563
TAM-OxGr	0.025	0.070	0.381
TAM-GrU	0.075	0.154	0.662
TAM-GrG	0.011	0.010	0.156
TAM-GrF	0.024	0.549	0.040
TAM-GrMa	0.017	0.040	0.392
TAM-GrGW	0.158	0.225	0.573
TAM-GrFW	0.173	0.229	0.480
TAM-GrSW	0.022	0.052	0.070
TAM-GrGlyW	0.030	0.089	0.059
TAM	0.010	0.005	0.377

4.4.4.2 DOX-loaded graphene

In this experiment, the increase in the electrical impedance caused by the viable cells (untreated and treated cancerous cells) was determined using RTCA. The changes in CI caused by DOX (25 $\mu\text{g}/\text{mL}$) and DOX-loaded PrGr, OxGr and DES-functionalized Gr (100 $\mu\text{g}/\text{mL}$) throughout 96 h are presented in Figure 4.29 and Figure 4.30. The results revealed that, at concentration 25 $\mu\text{g}/\text{ml}$, DOX exhibited the most acute inhibition on the growth of MCF-7 and AGS cells with CI less than 0.9 over 96 h. The same trend was observed in TAM (25 $\mu\text{g}/\text{mL}$), and also in previous studies (Duerr et al., 2012; Xavier et al., 2018; Zhou et al., 2018) against various cancerous cells through other chemotherapeutic drugs (e.g., camptothecin and methyl methanesulfonate). Such common detrimental side effect of chemotherapeutic drugs is undesirable as it might also cause damage on non-targeted normal cells. Therefore, the availability of DOX incorporated in nano-carriers holds the potential of a substantial improvement for targeted chemotherapy (Chen et al., 2011b; Yoo et al., 2000; Yu et al., 2015). This is due to that the damaging effect of DOX-loaded nano-carriers is non-excessive and not sudden (Mitra et al., 2001; Wang et al., 2010).

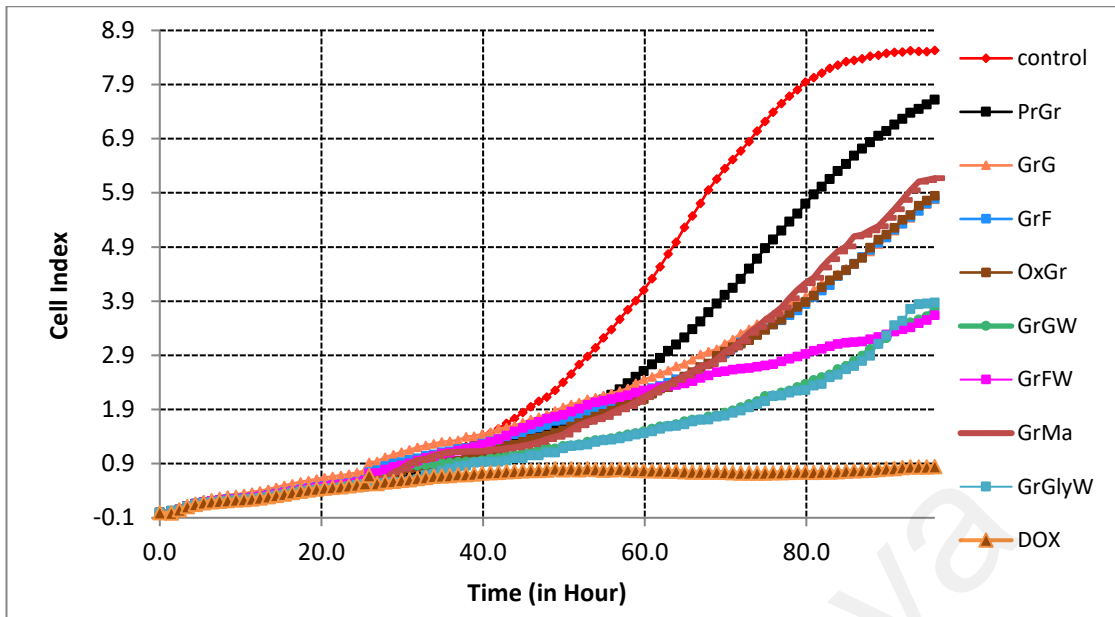


Figure 4.29: Cellular kinetic responses of DOX-loaded PrGr, OxGr and DES-functionalized Grs on MCF-7 cells. All graphene samples were tested at concentration 100 $\mu\text{g/ml}$ and DOX was tested at 25 $\mu\text{g/ml}$ on MCF-7 cell line.

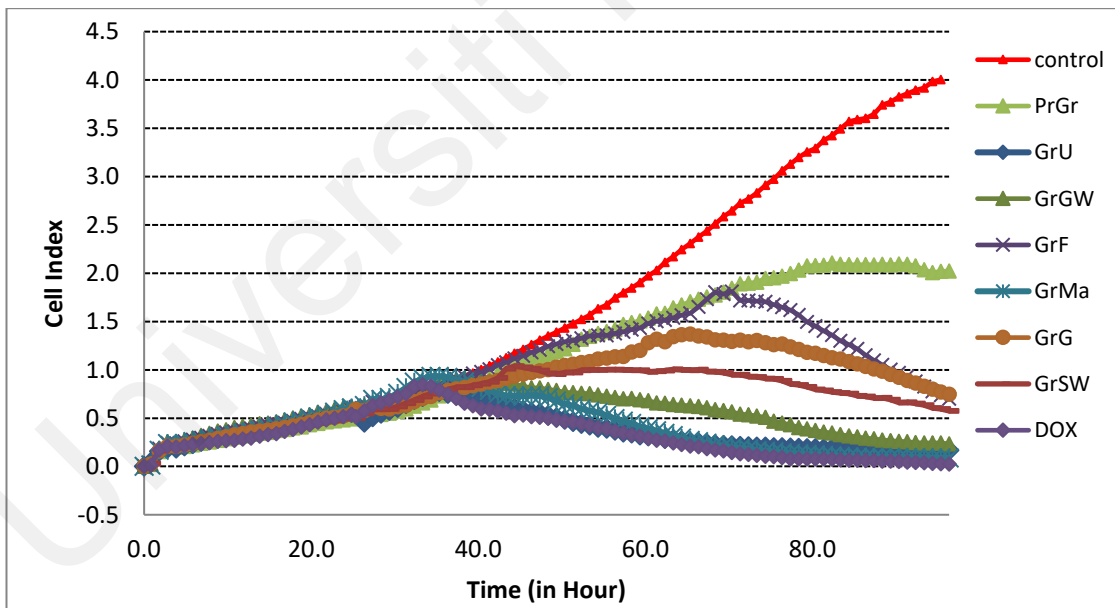


Figure 4.30: Cellular kinetic responses of DOX-loaded PrGr, OxGr and DES-functionalized Grs on AGS cells. All graphene samples were tested at concentration 100 $\mu\text{g/ml}$ and DOX was tested at 25 $\mu\text{g/ml}$ on AGS cell line.

DOX-GrGW, DOX-GrFW, and DOX-GrGlyW demonstrated a significant decrease in cell viability of MCF-7 ($CI < 4$) (Figure 4.29) and AGS cells ($CI < 1$) (Figure 4.30) over time as compared to other DOX-loaded Gr samples. The reduction in CI by DOX-GrGW and DOX-GrFW also was higher than that of the binary systems (DOX-GrG and DOX-GrF) on MCF-7 (Figure 4.29) and AGS cells (Figure 4.30). As discussed in the cell cycle results, DOX-GrGW, DOX-GrFW, and DOX-GrGlyW had cell cycle arrest at S and G2/M phases on MCF-7 and AGS cells, which may be linked to the observed inhibition of the cell growth (i.e. cytostatic response). This finding corresponded with previous studies (Chou et al., 2010; Tekin & Ozturk, 2017), reported the similar inhibition and cell cycle arrest of cancerous cells proliferation after treatment with anti-oxidant drug quercetin.

In both MCF-7 and AGS cell lines, the value of CI started to considerably decrease at 40 h incubation when exposed to DOX-loaded DES-functionalized Gr, while the cell inhibition was observed after 40 h of exposure to DOX-PrGr and DOX-OxGr. The acute toxicity for DOX-loaded Gr could be ascribed to the co-cytotoxic effects of graphene plus DOX on MCF-7 and AGS cells. This is in accordance to a previous study on the effects of superparamagnetic iron oxide nanoparticles (SPION) and mitoxantrone-loaded SPION towards cancerous cells, in which the cytotoxic-combination of mitoxantrone and SPION caused higher inhibition on the proliferation of cells (Duerr et al., 2012). This study also proved that DOX-GrGW and DOX-GrFW showed higher inhibition of cell growth in both MCF-7 and AGS cells (i.e., MCF-7: $CI < 4$, AGS: $CI < 1$) as compared to DOX-GrG and DOX-GrF (i.e., MCF-7: $CI < 6.5$, AGS: $CI < 2$). This is in accordance with the drug loading results where the ternary-DES-functionalized Gr had higher DOX loading

capacity compared to the binary-DES-functionalized Gr, in which led to the higher destructive effects against MCF-7 and AGS cells.

Kinetics was carried out on the effect of DOX-loaded Gr towards MCF-7 and AGS cells by fitting their cell growth data to zero order, 1st order and 2nd order models. Table 4.16 shows that the untreated MCF-7 (i.e. control) followed zero and 1st order model with correlation coefficient (R^2) 0.926 and 0.956, respectively. The untreated MCF-7 cells showed weak correlation in the 2nd order model ($R^2=0.394$). On the other hand, the untreated AGS exhibited strong correlation in the zero order model ($R^2=0.954$) and in the 1st order model ($R^2=0.946$) (Table 4.17). Similar to MCF-7 cells, AGS cells also exhibited weak correlation in the the 2nd order model ($R^2=0.321$). All DOX-loaded Gr samples also exhibited strong correlation on zero and 1st order models, but weak correlation with the 2nd order model, especially on MCF-7 cells. This is typically expected from such mammalian's cell growth profile as reported in previous studies (Lobo & Balthasar, 2002; Sukumaran et al., 2015). However, for the case of DOX, it showed weak correlation on every kinetic order model with R^2 value of 0.699, 0.556 and 0.257 for zero, 1st and 2nd order models, respectively. This infers to the acute toxicity of DOX towards MCF-7 and AGS cells which considerably disrupted the zero and 1st order kinetic growth models.

Table 4.16 also indicates that the untreated MCF-7 cells had the highest growth rate constant in both zero ($1.105 \times 10^{-1} \text{ CI h}^{-1}$) and 1st ($0.468 \times 10^{-1} \text{ h}^{-1}$) order models. Meanwhile, among AGS cells, the untreated AGS cells exhibited the highest growth rate constant in zero and 1st order models with 0.435 CI h^{-1} and 0.327 h^{-1} , respectively (Table 4.17). However, it can be observed that the growth rate constant of MCF-7 and AGS cells

was significantly decreased after treatment with DOX-loaded Gr. This is due to the inhibition effects of the DOX against cancerous cells, which altered the cell growth curve and subsequently, caused a deceleration in the growth rate over time. This clearly proved that the DOX loading onto Gr had a major influence in inhibiting the growth rate of cancerous cells.

In MCF-7 cells, DOX-GrGW displayed the lowest growth rate constants in the zero order model (i.e., 0.343 CI h^{-1}) and the 1st order model (i.e., 0.317 CI h^{-1}), respectively, followed by DOX-GrFW (zero order: 0.396 CI h^{-1} , 1st order: 0.325 h^{-1}) and DOX-GrGlyW (zero order: 0.396 CI h^{-1} , 1st order: 0.325 h^{-1}). The same trend was also observed in AGS cells, in which DOX-GrGW exhibited the lowest growth rate constant (zero order: 0.010 CI h^{-1} , 1st order: 0.010 h^{-1}), followed by the following sequence DOX-GrFW (zero order: 0.031 CI h^{-1} , 1st order: 0.089 h^{-1}) < DOX-GrGlyW (zero order: 0.029 CI h^{-1} , 1st order: 0.067 h^{-1}). The severe disruption of the cell cycle triggered by cell-cycle-specific anti-cancer drug may cause a deviation on the cell growth kinetic and hence, reduce the growth rate constant (Keefe et al., 1982; Panetta, 1997). This attested that the lethal impact of DOX-GrGW, DOX-GrFW and DOX-GrGlyW on the growth rate of MCF-7 and AGS cells was likely due to their significant disruption on the cell cycle progression.

Table 4.16: Growth rate constant of the untreated MCF-7 cells and MCF-7 cells treated

DOX-loaded Gr.

Samples	Zero order	First order	Second order
	Rate constant x 10 ⁻¹ (CI h ⁻¹)	Rate constant x 10 ⁻¹ (h ⁻¹)	Rate constant x 10 ⁻¹ (CI ⁻¹ h ⁻¹)
Control	1.105	0.468	0.546
DOX-PrGr	0.825	0.448	0.768
DOX-OxGr	0.588	0.389	0.564
DOX-GrU	0.729	0.414	0.593
DOX-GrG	0.566	0.353	0.666
DOX-GrF	0.569	0.383	0.765
DOX-GrMa	0.626	0.398	0.610
DOX-GrGW	0.343	0.317	0.568
DOX-GrFW	0.396	0.325	0.510
DOX-GrSW	0.755	0.461	0.107
DOX-GrGlyW	0.349	0.324	0.580
DOX	0.063	0.014	0.043

Table 4.17: Growth rate constant of the untreated AGS cells and AGS cells treated with DOX-loaded Gr.

Samples	Zero order	First order	Second order
	Rate constant x 10 ⁻¹ (CI h ⁻¹)	Rate constant x 10 ⁻¹ (h ⁻¹)	Rate constant x 10 ⁻¹ (CI ⁻¹ h ⁻¹)
Control	0.435	0.327	0.469
DOX-PrGr	0.248	0.284	0.683
DOX-OxGr	0.011	0.186	0.162
DOX-GrU	0.031	0.087	0.222
DOX-GrG	0.110	0.181	0.534
DOX-GrF	0.135	0.188	0.559
DOX-GrMa	0.045	0.154	0.437
DOX-GrGW	0.010	0.010	0.156
DOX-GrFW	0.031	0.089	0.131
DOX-GrSW	0.065	0.139	0.491
DOX-GrGlyW	0.029	0.067	0.074
DOX	0.044	0.212	0.135

CHAPTER 5: CONCLUSIONS AND FUTURE WORKS

5.1 Conclusions

Deep eutectic solvents (DESs) are new generation of eutectic mixtures currently gaining widespread scientific and technological attention as low-cost alternatives for organic solvents and ILs. These neoteric, green solvents are recognized as less volatile, thermally stable, highly tunable, biodegradable, less toxic, and lower in preparation cost as compared to ILs and other conventional solvents. In this study, natural-based DESs comprises of binary and tertiary DESs, were synthesized and used as functionalizing agents. The conclusions from the research findings are as follows:

1. Physicochemical characterization analyses indicated the changes on Gr surface chemistry after DES functionalization as compared to prior functionalization (i.e., PrGr and OxGr). In FE-SEM, the morphological and textural changes after DES functionalization were observed, especially in the induction of deformation or restoration effects by the DES molecules. EDX analysis identified additional surface elements (i.e., O, K, Mn, Cl and N) that corroborated completion of the oxidation and DES functionalization processes. FTIR results also showed the presence of new functional groups, including oxygen-based and amine-based functional groups on the DES-functionalized Gr. Raman and XRD analyses ascertained surface modifications of Gr induced by DES functionalization with a maintained Gr's structural integrity. The restacking and exfoliation level of DES-functionalized Gr was greater than that of unfunctionalized Gr. In addition, BET result also revealed changes in the surface area of the Gr-structure following the oxidation and DES functionalization processes.

2. This study also demonstrated that the application of DESs as functionalizing agents was effective in reducing the cytotoxicity level of Grs, especially for the case of DESs ChCl:Ma, ChCl:G:W and ChCl:Gly:W. This effectiveness was due to several factors that resulted in surface modification, including morphology change, exfoliation and re-stacking effect, and the introduction of additional functional groups. The reduction in the cytotoxicity level of the DES-functionalized Gr was observed through cell viability, cell cycle progression, and ROS generation.

3. As for the drug loading capacity, GrMa and GrGW exhibited a significant increment in EE% and DL% for both TAM and DOX as compared to the unfunctionalized Gr. The GrMa resulted in the highest EE% and DL% of TAM with 42% and 21.34%, respectively, followed by GrGW with EE% 34.76% and DL% 17.38%. In contrast, in DOX loading, GrGW exhibited the highest EE% (56.57%) and DL% (28.28%), followed by GrMa (EE% 49.80% and DL% 27.83%).

4. The TAM- and DOX-loaded on the DES-functionalized Gr possessed higher toxicity level against MCF-7 and AGS cell lines in comparison to unloaded Gr samples. Especially for the case of DOX-GrF (IC_{50} 24.44) and DOX-GrG (IC_{50} 122.31) on MCF-7 and AGS cells, respectively. The TAM- and DOX-loaded DES-functionalized Gr also had destructive effects against cancerous cells through the generation of intracellular ROS (ROS generation > 90%) and cell cycle disruption (cell arrest at G₀/G₁ phase or at S and G₂/M phases) phenomena.

5. The cytotoxicity profile of TAM- and DOX-loaded Gr against cancerous cells was confirmed by real-time cell growth analysis. The result demonstrated that drug loading on DES-functionalized Gr more effectively inhibited cancer cell growth than did non-functionalized Gr, especially for the case of TAM-GrF, TAM-GrG, DOX-GrGW and DOX-GrFW. The untreated MCF-7 and AGS cells followed zero-order model ($R^2 > 0.95$) and 1st order model ($0.95 > R^2 > 0.71$). However, MCF-7 and AGS cells treated with drug-loaded Gr did not follow any of these kinetic models. This indicates the acute toxicity of drug-loaded Gr towards cancerous cells, which significantly disrupted the cell growth kinetic models. Across all tested cellular kinetic models, the most significant reduction in the growth rate constant of cancerous cells was obtained using graphene functionalized with DES ChCl:glucose:water (5:2:5) and ChCl:fructose:water (5:2:5), especially for DOX-GrGW and DOX-GrFW.

Overall, DES-functionalized graphene demonstrated improved anti-cancer activity compared to non-functionalized graphene. This study supports DESs as potential green functionalizing agents for nano drug carriers, owing to their lower cytotoxicity, higher drug loading capacity and better anti-cancer activity.

5.2 Novelties and implications of the study

Some novel findings and implications of this study are addressed as the following:

1. NADESs have successfully been applied as novel functionalizing agents for graphene. Some surface modifications and structural changes were observed in the DES-functionalized Gr. This finding is useful in any applications that require surface or structural modifications of graphene. This method of functionalization

can also be extended to other CNMs for numerous applications such as in electrochemical sensing and removal of toxic compounds in waste water treatment.

2. After DES functionalization, the cytotoxicity profile of DES-functionalized Gr was significantly reduced as compared to the PrGr and OxGr. This finding can be used to solve the problem of graphene's toxicity towards human health and environment which hinders its application. This is the first study on the cytotoxicity profile improvement of graphene using DESs as functionalizing agents, and its cellular biological behavior.
3. This study confirms that the DES-functionalized Gr possessed high drug loading capacity for both TAM and DOX. This serves as a useful reference for future studies in optimizing the yield of TAM/DOX loaded onto DES-functionalized Gr and also in extending the application to other types of drugs.
4. A significant increment in the anti-cancer activities (i.e., cell viability, reactive oxygen species generation, cell cycle, kinetic cell growth) of the TAM- and DOX-loaded Gr as compared to unloaded Gr. The significant toxicity for the drug-loaded Gr could be assigned to the anti-cancer attribute of the drugs, either via the efficient delivery of TAM/DOX or the synergistic cytotoxicity effect of TAM/DOX and graphene against cancerous cells.

5.3 Future recommendations

This thesis has provided some promising findings which also further proved that DESs can be used as effective functionalizing agents for CNMs, owing to their preparation simplicity and low-cost. Although the results are promising, these are still far from

clinical applications, with further investigation being needed prior to clinical use. Some further studies can be done by the following recommendations:

1. To investigate the nanoscopic properties of DES-functionalized graphene and its functionality relationship using molecular dynamics simulations.
2. Optimizing the yield of TAM/DOX loaded onto DES-functionalized Gr. This also can be extended to other anti-cancer drugs.
3. Controlling the kinetics of drug release from DES-functionalized Gr into cancerous cells.
4. To investigate the cellular uptake and localization of the dox-loaded functional Gr on cancerous cells.
5. To design specific-task DES-functionalized Gr able to target cancer cells.
6. To load more complex drugs, such as RNA, mRNA, DNA onto DES-functionalized Grs.
7. To evaluate the efficiency of drug-loaded DES-functionalized Gr in animal models.

REFERENCES

- Abbasalipourkibir, R., Salehzadeh, A., & Abdullah, R. (2012). Cytotoxicity of tamoxifen-loaded solid lipid nanoparticles. *The delivery of nanoparticles: IntechOpen*.
- Abbasalipourkibir, R., Salehzadeh, A., & Abdullah, R. (2016). Tamoxifen-loaded solid lipid nanoparticles-induced apoptosis in breast cancer cell lines. *Journal of Experimental Nanoscience*, 11(3), 161-174.
- Abbott, A. P., Boothby, D., Capper, G., Davies, D. L., & Rasheed, R. K. (2004). Deep eutectic solvents formed between choline chloride and carboxylic acids: Versatile alternatives to ionic liquids. *Journal of the American Chemical Society*, 126(29), 9142-9147.
- Abdul Hadi, N. m., Ng, M. H., Choo, Y. M., Hashim, M. A., & Jayakumar, N. S. (2015). Performance of choline-based deep eutectic solvents in the extraction of tocots from crude palm oil. *Journal of the American Oil Chemists' Society*, 92(11), 1709-1716.
- Abo-Hamad, A., Hayyan, M., AlSaadi, M. A., & Hashim, M. A. (2015). Potential applications of deep eutectic solvents in nanotechnology. *Chemical Engineering Journal*, 273, 551-567.
- Abo-Hamad, A., Hayyan, M., AlSaadi, M. A., Mirghani, M. E. S., & Hashim, M. A. (2017). Functionalization of carbon nanotubes using eutectic mixtures: A promising route for enhanced aqueous dispersibility and electrochemical activity. *Chemical Engineering Journal*, 311, 326-339.
- Abreu, C., Sanguinetti, M., Amillis, S., & Ramon, A. (2010). Urea, the major urea/h⁺ symporter in aspergillus nidulans. *Fungal Genetics and Biology*, 47(12), 1023-1033.
- Ahmadi, R., Hemmateenejad, B., Safavi, A., Shojaeifard, Z., Mohabbati, M., & Firuzi, O. (2018). Assessment of cytotoxicity of choline chloride-based natural deep eutectic solvents against human hek-293 cells: A qsar analysis. *Chemosphere*, 209, 831-838.
- Akhavan, O., & Ghaderi, E. (2010). Toxicity of graphene and graphene oxide nanowalls against bacteria. *ACS Nano*, 4(10), 5731-5736.

- Akhtar, M. J., Ahamed, M., & Alhadlaq, H. A. (2017). Therapeutic targets in the selective killing of cancer cells by nanomaterials. *Clinica Chimica Acta*, 469, 53-62.
- Al-Akayleh, F., Mohammed Ali, H. H., Ghareeb, M. M., & Al-Remawi, M. (2019). Therapeutic deep eutectic system of capric acid and menthol: Characterization and pharmaceutical application. *Journal of Drug Delivery Science and Technology*, 53, 101159.
- Aroso, I. M., Craveiro, R., Rocha, Â., Dionísio, M., Barreiros, S., Reis, R. L., . . . Duarte, A. R. C. (2015). Design of controlled release systems for thedes—therapeutic deep eutectic solvents, using supercritical fluid technology. *International Journal of Pharmaceutics*, 492(1), 73-79.
- Aroso, I. M., Silva, J. C., Mano, F., Ferreira, A. S., Dionísio, M., Sá-Nogueira, I., . . . Duarte, A. R. C. (2016). Dissolution enhancement of active pharmaceutical ingredients by therapeutic deep eutectic systems. *Eur. J. Pharm. Biopharm*, 98, 57-66.
- Ashley, C. E., Carnes, E. C., Phillips, G. K., Padilla, D., Durfee, P. N., Brown, P. A., . . . Brinker, C. J. (2011). The targeted delivery of multicomponent cargos to cancer cells by nanoporous particle-supported lipid bilayers. *Nature Materials*, 10, 389.
- Ashley, N., & Poulton, J. (2009). Mitochondrial DNA is a direct target of anti-cancer anthracycline drugs. *Biochemical and Biophysical Research Communications*, 378(3), 450-455.
- Azizullah, A., Nasir, A., Richter, P., Lebert, M., & Häder, D.-P. (2011). Evaluation of the adverse effects of two commonly used fertilizers, dap and urea, on motility and orientation of the green flagellate euglena gracilis. *Environmental and Experimental Botany*, 74(Supplement C), 140-150.
- Badisa, R. B., Darling-Reed, S. F., Joseph, P., Cooperwood, J. S., Latinwo, L. M., & Goodman, C. B. (2009). Selective cytotoxic activities of two novel synthetic drugs on human breast carcinoma mcf-7 cells. *Anticancer Research*, 29(8), 2993-2996.
- Bagheri, S., Bayat, Z., Mahdi Zadeh, S., & Taghizadeh, E. (2011). Molecular geometries of the doxorubicin-plga complex, based on theoretical study. *Journal of Chemical Pharmaceutical Research*, 3(4), 42-48.
- Bakirtzi, C., Triantafyllidou, K., & Makris, D. P. (2016). Novel lactic acid-based natural deep eutectic solvents: Efficiency in the ultrasound-assisted extraction of antioxidant polyphenols from common native greek medicinal plants. *Journal of Applied Research on Medicinal and Aromatic Plants*, 3(3), 120-127.

- Bao, H., Pan, Y., Ping, Y., Sahoo, N. G., Wu, T., Li, L., . . . Gan, L. H. (2011). Chitosan-functionalized graphene oxide as a nanocarrier for drug and gene delivery. *Small*, 7(11), 1569-1578.
- Becker, S., Soukup, J. M., Gilmour, M. I., & Devlin, R. B. (1996). Stimulation of human and rat alveolar macrophages by urban air particulates: Effects on oxidant radical generation and cytokine production. *Toxicology and Applied Pharmacology*, 141(2), 637-648.
- Benvenuti, L., Zielinski, A. A. F., & Ferreira, S. R. S. (2019). Which is the best food emerging solvent: Il, des or nades? *Trends in Food Science & Technology*, 90, 133-146.
- Bhatt, J., Mondal, D., Bhojani, G., Chatterjee, S., & Prasad, K. (2015). Preparation of bio-deep eutectic solvent triggered cephalopod shaped silver chloride-DNA hybrid material having antibacterial and bactericidal activity. *Materials Science and Engineering: C*, 56, 125-131.
- Bianco, A. (2013). Graphene: Safe or toxic? The two faces of the medal. *Angewandte Chemie International Edition*, 52(19), 4986-4997.
- Biswas, S., Dodwadkar, N. S., Deshpande, P. P., Parab, S., & Torchilin, V. P. (2013). Surface functionalization of doxorubicin-loaded liposomes with octa-arginine for enhanced anticancer activity. *European Journal of Pharmaceutics and Biopharmaceutics*, 84(3), 517-525.
- Bitounis, D., Ali-Boucetta, H., Hong, B. H., Min, D.-H., & Kostarelos, K. (2013). Prospects and challenges of graphene in biomedical applications. *Advanced Materials*, 25(16), 2258-2268.
- Bottari, G., Herranz, M. A., Wibmer, L., Volland, M., Rodriguez-Perez, L., Guldi, D. M., . . . Torres, T. (2017). Chemical functionalization and characterization of graphene-based materials. *Chemical Society Reviews*, 46(15), 4464-4500.
- Brigger, I., Chaminade, P., Marsaud, V., Appel, M., Besnard, M., Gurny, R., . . . Couvreur, P. (2001). Tamoxifen encapsulation within polyethylene glycol-coated nanospheres. A new antiestrogen formulation. *International Journal of Pharmaceutics*, 214(1), 37-42.
- Butler, M. (2004). *Animal cell culture and technology*: Taylor & Francis.

- Buzdar, A., Howell, A., Cuzick, J., Wale, C., Distler, W., Hocht-Boes, G., . . . Nabholz, J. M. (2006). Comprehensive side-effect profile of anastrozole and tamoxifen as adjuvant treatment for early-stage breast cancer: Long-term safety analysis of the atac trial. *Lancet Oncology*, 7(8), 633-643.
- Cao, J., Chen, L., Li, M., Cao, F., Zhao, L., & Su, E. (2018). Two-phase systems developed with hydrophilic and hydrophobic deep eutectic solvents for simultaneously extracting various bioactive compounds with different polarities. *Green Chemistry*, 20(8), 1879-1886.
- Cao, J., Yang, M., Cao, F., Wang, J., & Su, E. (2017a). Tailor-made hydrophobic deep eutectic solvents for cleaner extraction of polyprenyl acetates from ginkgo biloba leaves. *Journal of Cleaner Production*, 152, 399-405.
- Cao, J., Yang, M., Cao, F., Wang, J., & Su, E. (2017b). Well-designed hydrophobic deep eutectic solvents as green and efficient media for the extraction of artemisinin from artemisia annua leaves. *ACS Sustainable Chemistry & Engineering*, 5(4), 3270-3278.
- Cardellini, F., Germani, R., Cardinali, G., Corte, L., Roscini, L., Spreti, N., & Tiecco, M. (2015). Room temperature deep eutectic solvents of (1s)-(+)-10-camphorsulfonic acid and sulfobetaines: Hydrogen bond-based mixtures with low ionicity and structure-dependent toxicity. *RSC Advances*, 5(40), 31772-31786.
- Cardellini, F., Tiecco, M., Germani, R., Cardinali, G., Corte, L., Roscini, L., & Spreti, N. (2014). Novel zwitterionic deep eutectic solvents from trimethylglycine and carboxylic acids: Characterization of their properties and their toxicity. *RSC Advances*, 4(99), 55990-56002.
- Carriazo, D., Serrano, M. C., Gutierrez, M. C., Ferrer, M. L., & del Monte, F. (2012). Deep-eutectic solvents playing multiple roles in the synthesis of polymers and related materials. *Chemical Society Reviews*, 41(14), 4996-5014.
- Chakrabarti, M. H., Manan, N. S. A., Brandon, N. P., Maher, R. C., Mjalli, F. S., AlNashef, I. M., . . . Nir, D. (2015). One-pot electrochemical gram-scale synthesis of graphene using deep eutectic solvents and acetonitrile. *Chemical Engineering Journal*, 274, 213-223.
- Chang, Y., Yang, S. T., Liu, J. H., Dong, E., Wang, Y., Cao, A., . . . Wang, H. (2011). In vitro toxicity evaluation of graphene oxide on a549 cells. *Toxicology Letter*, 200(3), 201-210.

- Chanphai, P., Bekale, L., Sanyakamdhorn, S., Agudelo, D., Bérubé, G., Thomas, T., & Tajmir-Riahi, H. (2017). Pamam dendrimers in drug delivery: Loading efficacy and polymer morphology. *Canadian Journal of Chemistry*, 95(9), 891-896.
- Chatterjee, N., Eom, H.-J., & Choi, J. (2014). A systems toxicology approach to the surface functionality control of graphene–cell interactions. *Biomaterials*, 35(4), 1109-1127.
- Chen, J., Wang, Q., Liu, M., & Zhang, L. (2017). The effect of deep eutectic solvent on the pharmacokinetics of salvianolic acid b in rats and its acute toxicity test. *Journal of Chromatography B*, 1063, 60-66.
- Chen, K. H., Ling, Y. Z., Cao, C., Li, X. Y., Chen, X., & Wang, X. Y. (2016). Chitosan derivatives/reduced graphene oxide/alginate beads for small-molecule drug delivery. *Materials Science & Engineering C-Materials for Biological Applications*, 69, 1222-1228.
- Chen, M.-B., Shen, W.-X., Yang, Y., Wu, X.-Y., Gu, J.-H., & Lu, P.-H. (2011a). Activation of amp-activated protein kinase is involved in vincristine-induced cell apoptosis in b16 melanoma cell. *Journal of Cellular Physiology*, 226(7), 1915-1925.
- Chen, Y., Wan, Y., Wang, Y., Zhang, H., & Jiao, Z. (2011b). Anticancer efficacy enhancement and attenuation of side effects of doxorubicin with titanium dioxide nanoparticles. *International journal of nanomedicine*, 6, 2321.
- Cheng, C., Li, S., Thomas, A., Kotov, N. A., & Haag, R. (2017). Functional graphene nanomaterials based architectures: Biointeractions, fabrications, and emerging biological applications. *Chemical Reviews*.
- Childs, A. C., Phaneuf, S. L., Dirks, A. J., Phillips, T., & Leeuwenburgh, C. (2002). Doxorubicin treatment in vivo causes cytochrome release and cardiomyocyte apoptosis, as well as increased mitochondrial efficiency, superoxide dismutase activity, and bcl-2:Bax ratio. *Cancer research*, 62(16), 4592-4598.
- Chittasupho, C., Lirdprapamongkol, K., Kewsuwan, P., & Sarisuta, N. (2014). Targeted delivery of doxorubicin to a549 lung cancer cells by cxcr4 antagonist conjugated plga nanoparticles. *European Journal of Pharmaceutics and Biopharmaceutics*, 88(2), 529-538.
- Choi, Y. H. (2011). Are natural deep eutectic solvents the missing link in understanding cellular metabolism and physiology? *Plant Physiology*, 156(4).

- Chou, C. C., Yang, J. S., Lu, H. F., Ip, S. W., Lo, C., Wu, C. C., . . . Chen, D. R. (2010). Quercetin-mediated cell cycle arrest and apoptosis involving activation of a caspase cascade through the mitochondrial pathway in human breast cancer mcf-7 cells. *Archives of Pharmacal Research*, 33(8), 1181-1191.
- Cortés-Funes, H., & Coronado, C. (2007). Role of anthracyclines in the era of targeted therapy. *Cardiovascular Toxicology*, 7(2), 56-60.
- Cui, D., Tian, F., Ozkan, C. S., Wang, M., & Gao, H. (2005). Effect of single wall carbon nanotubes on human hek293 cells. *Toxicology Letter*, 155(1), 73-85.
- D'Agostino, C., Harris, R. C., Abbott, A. P., Gladden, L. F., & Mantle, M. D. (2011). Molecular motion and ion diffusion in choline chloride based deep eutectic solvents studied by 1h pulsed field gradient nmr spectroscopy. *Physical Chemistry Chemical Physics*, 13(48), 21383-21391.
- Dai, Y., Rozema, E., Verpoorte, R., & Choi, Y. H. (2016). Application of natural deep eutectic solvents to the extraction of anthocyanins from catharanthus roseus with high extractability and stability replacing conventional organic solvents. *Journal of Chromatography A*, 1434, 50-56.
- Dai, Y., van Spronsen, J., Witkamp, G.-J., Verpoorte, R., & Choi, Y. H. (2013a). Natural deep eutectic solvents as new potential media for green technology. *Analytica Chimica Acta*, 766, 61-68.
- Dai, Y., Witkamp, G.-J., Verpoorte, R., & Choi, Y. H. (2013b). Natural deep eutectic solvents as a new extraction media for phenolic metabolites in carthamus tinctorius l. *Analytical Chemistry*, 85(13), 6272-6278.
- Dai, Y., Witkamp, G.-J., Verpoorte, R., & Choi, Y. H. (2015). Tailoring properties of natural deep eutectic solvents with water to facilitate their applications. *Food Chemistry*, 187, 14-19.
- Dallavalle, M., Calvaresi, M., Bottoni, A., Melle-Franco, M., & Zerbetto, F. (2015). Graphene can wreak havoc with cell membranes. *ACS Applied Materials & Interfaces*, 7(7), 4406-4414.
- Das, S., Singh, S., Singh, V., Joung, D., Dowding, J. M., Reid, D., . . . Seal, S. (2013). Oxygenated functional group density on graphene oxide: Its effect on cell toxicity. *Particle & Particle Systems Characterization*, 30(2), 148-157.

- de Sousa, M., Visani de Luna, L. A., Fonseca, L. C., Giorgio, S., & Alves, O. L. (2018). Folic-acid-functionalized graphene oxide nanocarrier: Synthetic approaches, characterization, drug delivery study, and antitumor screening. *ACS Applied Nano Materials*, 1(2), 922-932.
- Deepa, K., Singha, S., & Panda, T. (2014). Doxorubicin nanoconjugates. *Journal of Nanoscience and Nanotechnology*, 14(1), 892-904.
- Depan, D., Shah, J., & Misra, R. D. K. (2011). Controlled release of drug from folate-decorated and graphene mediated drug delivery system: Synthesis, loading efficiency, and drug release response. *Materials Science and Engineering C*, 31(7), 1305-1312.
- Desoubzdanne, D., Marcourt, L., Raux, R., Chevalley, S., Dorin, D., Doerig, C., . . . Debitus, C. (2008). Alisiaquinones and alisiaquinol, dual inhibitors of plasmodium falciparum enzyme targets from a new caledonian deep water sponge. *Journal of Natural Product*, 71(7), 1189-1192.
- Dietze, E. C., Caldwell, L. E., Grupin, S. L., Mancini, M., & Seewaldt, V. L. (2001). Tamoxifen but not 4-hydroxytamoxifen initiates apoptosis in p53(-) normal human mammary epithelial cells by inducing mitochondrial depolarization. *Journal of Biological Chemistry*, 276(7), 5384-5394.
- DiPaola, R. S. (2002). To arrest or not to g2-m cell-cycle arrest: Commentary re: Ak tyagi et al., silibinin strongly synergizes human prostate carcinoma du145 cells to doxorubicin-induced growth inhibition, g2-m arrest, and apoptosis. *Clinical Cancer Research*, 8(11), 3311-3314.
- Dongil, A. B., Bachiller-Baeza, B., Guerrero-Ruiz, A., Rodríguez-Ramos, I., Martínez-Alonso, A., & Tascón, J. M. D. (2011). Surface chemical modifications induced on high surface area graphite and carbon nanofibers using different oxidation and functionalization treatments. *Journal of Colloid and Interface Science*, 355(1), 179-189.
- Doroshov, J. H., & Davies, K. J. (1986). Redox cycling of anthracyclines by cardiac mitochondria. Ii. Formation of superoxide anion, hydrogen peroxide, and hydroxyl radical. *Journal of Biological Chemistry*, 261(7), 3068-3074.
- Duarte, A. R. C., Ferreira, A. S. D., Barreiros, S., Cabrita, E., Reis, R. L., & Paiva, A. (2017). A comparison between pure active pharmaceutical ingredients and therapeutic deep eutectic solvents: Solubility and permeability studies. *European Journal of Pharmaceutics and Biopharmaceutics*, 114(Supplement C), 296-304.

- Duerr, S., Lyer, S., Mann, J., Janko, C., Tietze, R., Schreiber, E., . . . Alexiou, C. (2012). Real-time cell analysis of human cancer cell lines after chemotherapy with functionalized magnetic nanoparticles. *Anticancer Research*, 32(5), 1983-1989.
- Egorova, K. S., Gordeev, E. G., & Ananikov, V. P. (2017). Biological activity of ionic liquids and their application in pharmaceuticals and medicine. *Chemical Reviews*, 117(10), 7132-7189.
- El Achkar, T., Fourmentin, S., & Greige-Gerges, H. (2019). Deep eutectic solvents: An overview on their interactions with water and biochemical compounds. *Journal of Molecular Liquids*, 288, 111028.
- Faggian, M., Sut, S., Perissutti, B., Baldan, V., Grabnar, I., & Dall'Acqua, S. (2016). Natural deep eutectic solvents (nades) as a tool for bioavailability improvement: Pharmacokinetics of rutin dissolved in proline/glycine after oral administration in rats: Possible application in nutraceuticals. *Molecules*, 21(11), 1531.
- Faraj, F. L., Zahedifard, M., Paydar, M., Looi, C. Y., Abdul Majid, N., Ali, H. M., . . . Abdulla, M. A. (2014). Synthesis, characterization, and anticancer activity of new quinazoline derivatives against mcf-7 cells. *Scientific World Journal*, 2014, 15.
- Feng, L., Wu, L., & Qu, X. (2013). New horizons for diagnostics and therapeutic applications of graphene and graphene oxide. *Advanced Materials*, 25(2), 168-186.
- Ferlini, C., Scambia, G., Marone, M., Distefano, M., Gaggini, C., Ferrandina, G., . . . Mancuso, S. (1998). Tamoxifen induces oxidative stress and apoptosis in oestrogen receptor-negative human cancer cell lines. *British Journal of Cancer*, 79, 257.
- Ferlini, C., Scambia, G., Marone, M., Distefano, M., Gaggini, C., Ferrandina, G., . . . Mancuso, S. (1999). Tamoxifen induces oxidative stress and apoptosis in oestrogen receptor-negative human cancer cell lines. *British Journal of Cancer*, 79(2), 257-263.
- Ferrari, A. C., Meyer, J. C., Scardaci, V., Casiraghi, C., Lazzeri, M., Mauri, F., . . . Geim, A. K. (2006). Raman spectrum of graphene and graphene layers. *Physical Review Letters*, 97(18), 187401.
- Fiala, S., Jones, S. A., & Brown, M. B. (2010). A fundamental investigation into the effects of eutectic formation on transmembrane transport. *International Journal of Pharmaceutics*, 393(1), 68-73.

- Florindo, C., Oliveira, F. S., Rebelo, L. P. N., Fernandes, A. M., & Marrucho, I. M. (2014). Insights into the synthesis and properties of deep eutectic solvents based on cholinium chloride and carboxylic acids. *ACS Sustainable Chemistry & Engineering*, 2(10), 2416-2425.
- Fontana, G., Maniscalco, L., Schillaci, D., Cavallaro, G., & Giammona, G. (2005). Solid lipid nanoparticles containing tamoxifen characterization and in vitro antitumoral activity. *Drug Delivery*, 12(6), 385-392.
- Francisco, M., van den Bruinhorst, A., Zubeir, L. F., Peters, C. J., & Kroon, M. C. (2013). A new low transition temperature mixture (lttm) formed by choline chloride + lactic acid: Characterization as solvent for co2 capture. *Fluid Phase Equilibria*, 340, 77-84.
- Fu, P. P., Xia, Q., Hwang, H.-M., Ray, P. C., & Yu, H. (2014). Mechanisms of nanotoxicity: Generation of reactive oxygen species. *Journal of Food and Drug Analysis*, 22(1), 64-75.
- García, A., Rodríguez-Juan, E., Rodríguez-Gutiérrez, G., Rios, J. J., & Fernández-Bolaños, J. (2016). Extraction of phenolic compounds from virgin olive oil by deep eutectic solvents (dess). *Food Chemistry*, 197, Part A, 554-561.
- Georgakilas, V., Kordatos, K., Prato, M., Guldi, D. M., Holzinger, M., & Hirsch, A. (2002). Organic functionalization of carbon nanotubes. *Journal of the American Chemical Society*, 124(5), 760-761.
- Georgakilas, V., Otyepka, M., Bourlinos, A. B., Chandra, V., Kim, N., Kemp, K. C., . . . Kim, K. S. (2012). Functionalization of graphene: Covalent and non-covalent approaches, derivatives and applications. *Chemical Reviews*, 112(11), 6156-6214.
- Gertrudes, A., Craveiro, R., Eltayari, Z., Reis, R. L., Paiva, A., & Duarte, A. R. C. (2017). How do animals survive extreme temperature amplitudes? The role of natural deep eutectic solvents. *ACS Sustainable Chemistry & Engineering*, 5(11), 9542-9553.
- Goenka, S., Sant, V., & Sant, S. (2014). Graphene-based nanomaterials for drug delivery and tissue engineering. *Journal of Controlled Release*, 173, 75-88.
- Gonçalves, G., Vila, M., Portolés, M.-T., Vallet-Regi, M., Gracio, J., & Marques, P. A. A. P. (2013). Nano-graphene oxide: A potential multifunctional platform for cancer therapy. *Advanced Healthcare Materials*, 2(8), 1072-1090.

- Gorke, J., Srienc, F., & Kazlauskas, R. (2010). Toward advanced ionic liquids. Polar, enzyme-friendly solvents for biocatalysis. *Biotechnology and Bioprocess Engineering*, 15(1), 40-53.
- Gutiérrez, M. C., Ferrer, M. L., Mateo, C. R., & del Monte, F. (2009). Freeze-drying of aqueous solutions of deep eutectic solvents: A suitable approach to deep eutectic suspensions of self-assembled structures. *Langmuir*, 25(10), 5509-5515.
- Gutierrez, P. L. (2000). The role of nad(p)h oxidoreductase (dt-diaphorase) in the bioactivation of quinone-containing antitumor agents: A review. *Free Radical Biology and Medicine*, 29(3), 263-275.
- Hajrezaie, M., Paydar, M., Looi, C. Y., Moghadamtousi, S. Z., Hassandarvish, P., Salga, M. S., . . . Abdulla, M. A. (2015). Apoptotic effect of novel schiff based cdcl₂(c₁₄h₂₁n₃o₂) complex is mediated via activation of the mitochondrial pathway in colon cancer cells. *Scientific Reports*, 5, 9097.
- Hamwi, A., Alvergnat, H., Bonnamy, S., & Béguin, F. (1997). Fluorination of carbon nanotubes. *Carbon*, 35(6), 723-728.
- Haukvik, T., Bruzell, E., Kristensen, S., & Tønnesen, H. (2010). Photokilling of bacteria by curcumin in selected polyethylene glycol 400 (peg 400) preparations. Studies on curcumin and curcuminoids, xli. *Die Pharmazie-An International Journal of Pharmaceutical Sciences*, 65(8), 600-606.
- Hayes, J. E., Allen, P., Brunton, N., O'Grady, M. N., & Kerry, J. P. (2011). Phenolic composition and in vitro antioxidant capacity of four commercial phytochemical products: Olive leaf extract (*olea europaea* l.), lutein, sesamol and ellagic acid. *Food Chemistry*, 126(3), 948-955.
- Hayyan, A., Ali Hashim, M., Mjalli, F. S., Hayyan, M., & AlNashef, I. M. (2013a). A novel phosphonium-based deep eutectic catalyst for biodiesel production from industrial low grade crude palm oil. *Chemical Engineering Science*, 92, 81-88.
- Hayyan, A., Hashim, M. A., Hayyan, M., Mjalli, F. S., & AlNashef, I. M. (2014). A new processing route for cleaner production of biodiesel fuel using a choline chloride based deep eutectic solvent. *Journal of Cleaner Production*, 65, 246-251.
- Hayyan, M., Abo-Hamad, A., AlSaadi, M. A., & Hashim, M. A. (2015a). Functionalization of graphene using deep eutectic solvents. *Nanoscale Research Letter*, 10(1), 324.

- Hayyan, M., Hashim, M. A., Al-Saadi, M. A., Hayyan, A., AlNashef, I. M., & Mirghani, M. E. (2013b). Assessment of cytotoxicity and toxicity for phosphonium-based deep eutectic solvents. *Chemosphere*, *93*(2), 455-459.
- Hayyan, M., Hashim, M. A., & AlNashef, I. M. (2016a). Superoxide ion: Generation and chemical implications. *Chemical Reviews*, *116*(5), 3029-3085.
- Hayyan, M., Hashim, M. A., Hayyan, A., Al-Saadi, M. A., AlNashef, I. M., Mirghani, M. E. S., & Saheed, O. K. (2013c). Are deep eutectic solvents benign or toxic? *Chemosphere*, *90*(7), 2193-2195.
- Hayyan, M., Looi, C. Y., Hayyan, A., Wong, W. F., & Hashim, M. A. (2015b). In vitro and in vivo toxicity profiling of ammonium-based deep eutectic solvents. *PLoS One*, *10*(2), e0117934.
- Hayyan, M., Mbous, Y. P., Looi, C. Y., Wong, W. F., Hayyan, A., Salleh, Z., & Mohd-Ali, O. (2016b). Natural deep eutectic solvents: Cytotoxic profile. *SpringerPlus*, *5*(1), 1.
- He, W., Mullarkey, C. E., Duty, J. A., Moran, T. M., Palese, P., & Miller, M. S. (2015). Broadly neutralizing anti-influenza virus antibodies: Enhancement of neutralizing potency in polyclonal mixtures and iga backbones. *Journal of Virology*, *89*(7), 3610-3618.
- Hegab, H. M., ElMekawy, A., Zou, L., Mulcahy, D., Saint, C. P., & Ginic-Markovic, M. (2016). The controversial antibacterial activity of graphene-based materials. *Carbon*, *105*, 362-376.
- Hegge, A. B., Vukicevic, M., Bruzell, E., Kristensen, S., & Tønnesen, H. H. (2013). Solid dispersions for preparation of phototoxic supersaturated solutions for antimicrobial photodynamic therapy (apdt): Studies on curcumin and curcuminoides. *European Journal of Pharmaceutics and Biopharmaceutics*, *83*(1), 95-105.
- Hekmat, A., Saboury, A. A., & Divsalar, A. (2012). The effects of silver nanoparticles and doxorubicin combination on DNA structure and its antiproliferative effect against t47d and mcf7 cell lines. *Journal of Biomedical Nanotechnology*, *8*(6), 968-982.
- Hilmer, S. N., Cogger, V. C., Muller, M., & Le Couteur, D. G. (2004). The hepatic pharmacokinetics of doxorubicin and liposomal doxorubicin. *Drug metabolism and disposition*, *32*(8), 794-799.

- Horev-Azaria, L., Baldi, G., Beno, D., Bonacchi, D., Golla-Schindler, U., Kirkpatrick, J. C., . . . Korenstein, R. (2013). Predictive toxicology of cobalt ferrite nanoparticles: Comparative in-vitro study of different cellular models using methods of knowledge discovery from data. *Particle and Fibre Toxicology*, *10*(1), 32.
- Hou, X.-D., Liu, Q.-P., Smith, T. J., Li, N., & Zong, M.-H. (2013). Evaluation of toxicity and biodegradability of cholinium amino acids ionic liquids. *PLoS One*, *8*(3), e59145.
- How, C. W., Rasedee, A., Manickam, S., & Rosli, R. (2013). Tamoxifen-loaded nanostructured lipid carrier as a drug delivery system: Characterization, stability assessment and cytotoxicity. *Colloids and Surfaces B: Biointerfaces*, *112*, 393-399.
- Hussain, S., Boland, S., Baeza-Squiban, A., Hamel, R., Thomassen, L. C. J., Martens, J. A., . . . Marano, F. (2009). Oxidative stress and proinflammatory effects of carbon black and titanium dioxide nanoparticles: Role of particle surface area and internalized amount. *Toxicology*, *260*(1), 142-149.
- Janes, K. A., Fresneau, M. P., Marazuela, A., Fabra, A., & Alonso, M. a. J. (2001). Chitosan nanoparticles as delivery systems for doxorubicin. *Journal of Controlled Release*, *73*(2), 255-267.
- Jhong, H.-R., Wong, D. S.-H., Wan, C.-C., Wang, Y.-Y., & Wei, T.-C. (2009). A novel deep eutectic solvent-based ionic liquid used as electrolyte for dye-sensitized solar cells. *Electrochemistry Communications*, *11*(1), 209-211.
- Jin, W., Yang, Q., Huang, B., Bao, Z., Su, B., Ren, Q., . . . Xing, H. (2016). Enhanced solubilization and extraction of hydrophobic bioactive compounds using water/ionic liquid mixtures. *Green Chemistry*, *18*(12), 3549-3557.
- Jones, C. F., & Grainger, D. W. (2009). In vitro assessments of nanomaterial toxicity. *Advanced Drug Delivery Reviews*, *61*(6), 438-456.
- Jones, R. G., Plas, D. R., Kubek, S., Buzzai, M., Mu, J., Xu, Y., . . . Thompson, C. B. (2005). Amp-activated protein kinase induces a p53-dependent metabolic checkpoint. *Molecular Cell*, *18*(3), 283-293.
- Juneidi, I., Hayyan, M., & Hashim, M. A. (2015). Evaluation of toxicity and biodegradability for cholinium-based deep eutectic solvents. *RSC Advances*, *5*(102), 83636-83647.

- Juneidi, I., Hayyan, M., & Mohd Ali, O. (2016). Toxicity profile of choline chloride-based deep eutectic solvents for fungi and cyprinus carpio fish. *Environmental Science and Pollution Research*, 23(8), 7648-7659.
- Kataoka, K., Matsumoto, T., Yokoyama, M., Okano, T., Sakurai, Y., Fukushima, S., . . . Kwon, G. S. (2000). Doxorubicin-loaded poly(ethylene glycol)–poly(β -benzyl-l-aspartate) copolymer micelles: Their pharmaceutical characteristics and biological significance. *Journal of Controlled Release*, 64(1), 143-153.
- Keefe, D., Capizzi, R. L., & Rudnick, S. A. (1982). Methotrexate cytotoxicity for 15178y/asn-lymphoblasts: Relationship of dose and duration of exposure to tumor cell viability. *Cancer research*, 42(5), 1641-1645.
- Khuroo, T., Verma, D., Talegaonkar, S., Padhi, S., Panda, A. K., & Iqbal, Z. (2014). Topotecan–tamoxifen duple plga polymeric nanoparticles: Investigation of in vitro, in vivo and cellular uptake potential. *International Journal of Pharmaceutics*, 473(1), 384-394.
- Kim, S.-Y., Kim, S.-J., Kim, B.-J., Rah, S.-Y., Chung, S. M., Im, M.-J., & Kim, U.-H. (2006). Doxorubicin-induced reactive oxygen species generation and intracellular ca^{2+} increase are reciprocally modulated in rat cardiomyocytes. *Experimental & Molecular Medicine*, 38, 535.
- Kim, S., Choi, J. E., Choi, J., Chung, K.-H., Park, K., Yi, J., & Ryu, D.-Y. (2009). Oxidative stress-dependent toxicity of silver nanoparticles in human hepatoma cells. *Toxicology In Vitro*, 23(6), 1076-1084.
- Klasse, P. J., & Sattentau, Q. J. (2001). Mechanisms of virus neutralization by antibody. *Current Topics in Microbiology and Immunology*, 260, 87-108.
- Kudłak, B., Owczarek, K., & Namieśnik, J. (2015). Selected issues related to the toxicity of ionic liquids and deep eutectic solvents—a review. *Environmental Science and Pollution Research*, 22(16), 11975-11992.
- Kumar, B. N. P., Rajput, S., Dey, K. K., Parekh, A., Das, S., Mazumdar, A., & Mandal, M. (2013). Celecoxib alleviates tamoxifen-instigated angiogenic effects by ros-dependent vegf/vegfr2 autocrine signaling. *BMC Cancer*, 13(1), 273.
- Kurz, E. U., Douglas, P., & Lees-Miller, S. P. (2004). Doxorubicin activates atm-dependent phosphorylation of multiple downstream targets in part through the generation of reactive oxygen species. *Journal of Biological Chemistry*, 279(51), 53272-53281.

- Landeros-Martínez, L.-L., Chavez-Flores, D., Orrantia-Borunda, E., & Flores-Holguin, N. (2016). Construction of a nanodiamond–tamoxifen complex as a breast cancer drug delivery vehicle. *Journal of Nanomaterials*, 2016.
- Lannan, F. M., Mamajanov, I., & Hud, N. V. (2012). Human telomere sequence DNA in water-free and high-viscosity solvents: G-quadruplex folding governed by kramers rate theory. *Journal of American Chemical Society*, 134(37), 15324-15330.
- Lau, A. T., Wang, Y., & Chiu, J. F. (2008). Reactive oxygen species: Current knowledge and applications in cancer research and therapeutic. *Journal of Cellular Biochemistry*, 104(2), 657-667.
- Lee, Y. S., Kang, Y. S., Lee, S. H., & Kim, J. A. (2000). Role of nad(p)h oxidase in the tamoxifen-induced generation of reactive oxygen species and apoptosis in hepg2 human hepatoblastoma cells. *Cell Death And Differentiation*, 7, 925.
- Li, Q., Liang, J., You, X., Liu, X., Wu, H., Gao, W., . . . Zhang, F. (2017). A novel reactive oxygen species triggered polymeric nanoplatform for controlled drug delivery and cancer therapy. *Journal of Biomedical Nanotechnology*, 13(5), 513-521.
- Li, Y., He, H., Jia, X., Lu, W.-L., Lou, J., & Wei, Y. (2012). A dual-targeting nanocarrier based on poly(amidoamine) dendrimers conjugated with transferrin and tamoxifen for treating brain gliomas. *Biomaterials*, 33(15), 3899-3908.
- Li, Z., & Lee, P. I. (2016). Investigation on drug solubility enhancement using deep eutectic solvents and their derivatives. *International Journal of Pharmaceutics*, 505(1), 283-288.
- Lin, F., Du, F., Huang, J. Y., Chau, A., Zhou, Y. S., Duan, H. L., . . . Xiong, C. Y. (2016). Substrate effect modulates adhesion and proliferation of fibroblast on graphene layer. *Colloids and Surfaces B-Biointerfaces*, 146, 785-793.
- Lin, M., Zou, R., Shi, H., Yu, S., Li, X., Guo, R., . . . Dai, L. (2015). Ocular biocompatibility evaluation of hydroxyl-functionalized graphene. *Materials Science and Engineering C*, 50, 300-308.
- Ling, Y. H., el-Naggar, A. K., Priebe, W., & Perez-Soler, R. (1996). Cell cycle-dependent cytotoxicity, g2/m phase arrest, and disruption of p34cdc2/cyclin b1 activity induced by doxorubicin in synchronized p388 cells. *Molecular Pharmacology*, 49(5), 832-841.

- Liu, J., Cui, L., & Losic, D. (2013). Graphene and graphene oxide as new nanocarriers for drug delivery applications. *Acta Biomaterialia*, 9(12), 9243-9257.
- Liu, R.-L., Yu, P., Ge, X.-L., Bai, X.-F., Li, X.-Q., & Fu, Q. (2017). Establishment of an aqueous peg 200-based deep eutectic solvent extraction and enrichment method for pumpkin (*cucurbita moschata*) seed protein. *Food Analytical Methods*, 10(6), 1669-1680.
- Liu, Y., Friesen, J. B., McAlpine, J. B., Lankin, D. C., Chen, S.-N., & Pauli, G. F. (2018). Natural deep eutectic solvents: Properties, applications, and perspectives. *Journal of Natural Product*, 81(3), 679-690.
- Liu, Z., Robinson, J. T., Sun, X., & Dai, H. (2008). Pegylated nanographene oxide for delivery of water-insoluble cancer drugs. *Journal of the American Chemical Society*, 130(33), 10876-10877.
- Lobo, E. D., & Balthasar, J. P. (2002). Pharmacodynamic modeling of chemotherapeutic effects: Application of a transit compartment model to characterize methotrexate effects in vitro. *AAPS PharmSci*, 4(4), E42.
- Lodzki, M., Godin, B., Rakou, L., Mechoulam, R., Gallily, R., & Touitou, E. (2003). Cannabidiol—transdermal delivery and anti-inflammatory effect in a murine model. *Journal of Controlled Release*, 93(3), 377-387.
- Lu, C., Cao, J., Wang, N., & Su, E. (2016). Significantly improving the solubility of non-steroidal anti-inflammatory drugs in deep eutectic solvents for potential non-aqueous liquid administration. *MedChemComm*, 7(5), 955-959.
- Lv, Y., Tao, L., Annie Bligh, S. W., Yang, H., Pan, Q., & Zhu, L. (2016). Targeted delivery and controlled release of doxorubicin into cancer cells using a multifunctional graphene oxide. *Materials Science and Engineering: C*, 59, 652-660.
- Mahmoudi, M., Azadmanesh, K., Shokrgozar, M. A., Journeay, W. S., & Laurent, S. (2011). Effect of nanoparticles on the cell life cycle. *Chemical Reviews*, 111(5), 3407-3432.
- Mamajanov, I., Engelhart, A. E., Bean, H. D., & Hud, N. V. (2010). DNA and rna in anhydrous media: Duplex, triplex, and g-quadruplex secondary structures in a deep eutectic solvent. *Angewandte Chemie International Edition*, 49(36), 6310-6314.

- Mandel, B. (1984). Mechanisms of virus neutralization. In A. L. Notkins & M. B. A. Oldstone (Eds.), *Concepts in viral pathogenesis* (pp. 32-38). New York, NY: Springer New York.
- Mano, F., Martins, M., Sá-Nogueira, I., Barreiros, S., Borges, J. P., Reis, R. L., . . . Paiva, A. (2017). Production of electrospun fast-dissolving drug delivery systems with therapeutic eutectic systems encapsulated in gelatin. *AAPS PharmSciTech*, *18*(7), 2579-2585.
- Mao, J., Chen, L., Xu, B., Wang, L., Wang, W., Li, M., . . . Wang, L. (2009). Volume-activated chloride channels contribute to cell-cycle-dependent regulation of hela cell migration. *Biochemical Pharmacology*, *77*(2), 159-168.
- Markham, K. R., Gould, K. S., Winefield, C. S., Mitchell, K. A., Bloor, S. J., & Boase, M. R. (2000). Anthocyanic vacuolar inclusions — their nature and significance in flower colouration. *Phytochemistry*, *55*(4), 327-336.
- Martínez, M. T., Callejas, M. A., Benito, A. M., Cochet, M., Seeger, T., Anson, A., . . . Maser, W. K. (2003). Modifications of single-wall carbon nanotubes upon oxidative purification treatments. *Nanotechnology*, *14*(7), 691.
- Matés, J. M., & Sánchez-Jiménez, F. M. (2000). Role of reactive oxygen species in apoptosis: Implications for cancer therapy. *The International Journal of Biochemistry & Cell Biology*, *32*(2), 157-170.
- Matesanz, M.-C., Vila, M., Feito, M.-J., Linares, J., Gonçalves, G., Vallet-Regi, M., . . . Portolés, M.-T. (2013). The effects of graphene oxide nanosheets localized on f-actin filaments on cell-cycle alterations. *Biomaterials*, *34*(5), 1562-1569.
- Mayakrishnan, V., Abdullah, N., Abidin, M. H. Z., Fadzil, N. H. M., Johari, N. M. K., Aminudin, N., & Abidin, N. Z. (2013). Investigation of the antioxidative potential of various solvent fractions from fruiting bodies of schizophyllum commune (fr.) mushrooms and characterization of phytoconstituents. *Journal of Agricultural Science*, *5*(6), 58-69.
- Mbous, Y. P., Hayyan, M., Hayyan, A., Wong, W. F., Hashim, M. A., & Looi, C. Y. (2017a). Applications of deep eutectic solvents in biotechnology and bioengineering-promises and challenges. *Biotechnology Advances*, *35*(2), 105-134.
- Mbous, Y. P., Hayyan, M., Wong, W. F., Looi, C. Y., & Hashim, M. A. (2017b). Unraveling the cytotoxicity and metabolic pathways of binary natural deep eutectic solvent systems. *Scientific Reports*, *7*, 41257.

- McCallion, C., Burthem, J., Rees-Unwin, K., Golovanov, A., & Pluen, A. (2016). Graphene in therapeutics delivery: Problems, solutions and future opportunities. *European Journal of Pharmaceutics and Biopharmaceutics*, 104, 235-250.
- Miao, Z., & Scott Obach, R. (2010). Chapter 10 alcohols and phenols: Absorption, distribution, metabolism and excretion *Metabolism, pharmacokinetics and toxicity of functional groups: Impact of chemical building blocks on admet* (pp. 460-485): The Royal Society of Chemistry.
- Minotti, G., Menna, P., Salvatorelli, E., Cairo, G., & Gianni, L. (2004). Anthracyclines: Molecular advances and pharmacologic developments in antitumor activity and cardiotoxicity. *Pharmacological Reviews*, 56(2), 185-229.
- Mitra, S., Gaur, U., Ghosh, P. C., & Maitra, A. N. (2001). Tumour targeted delivery of encapsulated dextran–doxorubicin conjugate using chitosan nanoparticles as carrier. *Journal of Controlled Release*, 74(1), 317-323.
- Modica-Napolitano, J. S., & Aprile, J. R. (2001). Delocalized lipophilic cations selectively target the mitochondria of carcinoma cells. *Advanced Drug Delivery Reviews*, 49(1), 63-70.
- Moghimi, S. M., & Szebeni, J. (2003). Stealth liposomes and long circulating nanoparticles: Critical issues in pharmacokinetics, opsonization and protein-binding properties. *Progress in Lipid Research*, 42(6), 463-478.
- Mondal, D., Sharma, M., Mukesh, C., Gupta, V., & Prasad, K. (2013). Improved solubility of DNA in recyclable and reusable bio-based deep eutectic solvents with long-term structural and chemical stability. *Chemical Communications*, 49(83), 9606-9608.
- Mondal, D., Sharma, M., Wang, C.-H., Lin, Y.-C., Huang, H.-C., Saha, A., . . . Prasad, K. (2016). Deep eutectic solvent promoted one step sustainable conversion of fresh seaweed biomass to functionalized graphene as a potential electrocatalyst. *Green Chemistry*, 18(9), 2819-2826.
- Morrison, H. G., Sun, C. C., & Neervannan, S. (2009). Characterization of thermal behavior of deep eutectic solvents and their potential as drug solubilization vehicles. *International Journal of Pharmaceutics*, 378(1), 136-139.
- Mota-Morales, J. D., Gutiérrez, M. C., Ferrer, M. L., Sanchez, I. C., Elizalde-Peña, E. A., Pojman, J. A., . . . Luna-Bárcenas, G. (2013). Deep eutectic solvents as both active fillers and monomers for frontal polymerization. *Journal of Polymer Science Part A: Polymer Chemistry*, 51(8), 1767-1773.

- Nawara, K., Romiszewski, J., Kijewska, K., Szczytko, J., Twardowski, A., Mazur, M., & Krysinski, P. (2012). Adsorption of doxorubicin onto citrate-stabilized magnetic nanoparticles. *The Journal of Physical Chemistry C*, 116(9), 5598-5609.
- Nel, A., Xia, T., Mädler, L., & Li, N. (2006). Toxic potential of materials at the nanolevel. *Science*, 311(5761), 622-627.
- Ni, Z., Wang, Y., Yu, T., & Shen, Z. (2008). Raman spectroscopy and imaging of graphene. *Nano Research*, 1(4), 273-291.
- Nkuku, C. A., & LeSuer, R. J. (2007). Electrochemistry in deep eutectic solvents. *The Journal of Physical Chemistry B*, 111(46), 13271-13277.
- O'Shea, D., Law, J., Egli, A., Douglas, D., Lund, G., Forester, S., . . . Kneteman, N. (2016). Prevention of hepatitis c virus infection using a broad cross-neutralizing monoclonal antibody (ar4a) and epigallocatechin gallate. *Liver Transplantation*, 22(3), 324-332.
- Okoshi, R., Ozaki, T., Yamamoto, H., Ando, K., Koida, N., Ono, S., . . . Kizaki, H. (2008). Activation of amp-activated protein kinase induces p53-dependent apoptotic cell death in response to energetic stress. *Journal of Biological Chemistry*, 283(7), 3979-3987.
- Oktay, T., Pornsak, S., & R., D. C. (2013). Doxorubicin: An update on anticancer molecular action, toxicity and novel drug delivery systems. *Journal of Pharmacy and Pharmacology*, 65(2), 157-170.
- Orhan, I., & Üstün, O. (2011). Determination of total phenol content, antioxidant activity and acetylcholinesterase inhibition in selected mushrooms from turkey. *Journal of Food Composition and Analysis*, 24(3), 386-390.
- Ou, L., Song, B., Liang, H., Liu, J., Feng, X., Deng, B., . . . Shao, L. (2016). Toxicity of graphene-family nanoparticles: A general review of the origins and mechanisms. *Particle and Fibre Toxicology*, 13(1), 57.
- Panetta, J. C. (1997). A mathematical model of breast and ovarian cancer treated with paclitaxel. *Mathematical Biosciences*, 146(2), 89-113.
- Papadopoulou, C., Soulti, K., & Roussis, I. G. (2005). Potential antimicrobial activity of red and white wine phenolic extracts against strains of staphylococcus aureus, escherichia coli and candida albicans. *Food Technology and Biotechnology*, 43(1), 41-46.

- Park, J., Fong, P. M., Lu, J., Russell, K. S., Booth, C. J., Saltzman, W. M., & Fahmy, T. M. (2009). Pegylated plga nanoparticles for the improved delivery of doxorubicin. *Nanomedicine: Nanotechnology, Biology and Medicine*, 5(4), 410-418.
- Pedro, S. N., Freire, M. G., Freire, C. S. R., & Silvestre, A. J. D. (2019). Deep eutectic solvents comprising active pharmaceutical ingredients in the development of drug delivery systems. *Expert Opinion on Drug Delivery*, 16(5), 497-506.
- Pernak, J., & Chwała, P. (2003). Synthesis and anti-microbial activities of choline-like quaternary ammonium chlorides. *European Journal of Medicinal Chemistry*, 38(11), 1035-1042.
- Petkovic, M., Ferguson, J. L., Gunaratne, H. Q. N., Ferreira, R., Leitão, M. C., Seddon, K. R., . . . Pereira, C. S. (2010). Novel biocompatible cholinium-based ionic liquids—toxicity and biodegradability. *Green Chemistry*, 12(4), 643-649.
- Phaechamud, T., Tuntarawongsa, S., & Charoensuksai, P. (2016). Evaporation behavior and characterization of eutectic solvent and ibuprofen eutectic solution. *AAPS PharmSciTech*, 17(5), 1213-1220.
- Phan, C. W., David, P., Naidu, M., Wong, K. H., & Sabaratnam, V. (2015). Therapeutic potential of culinary-medicinal mushrooms for the management of neurodegenerative diseases: Diversity, metabolite, and mechanism. *Crit Rev Biotechnol*, 35(3), 355-368.
- Pifferi, V., Cappelletti, G., Di Bari, C., Meroni, D., Spadavecchia, F., & Falciola, L. (2014). Multi-walled carbon nanotubes (mwcnts) modified electrodes: Effect of purification and functionalization on the electroanalytical performances. *Electrochimica Acta*, 146, 403-410.
- Pisano, P. L., Espino, M., Fernández, M. d. l. Á., Silva, M. F., & Olivieri, A. C. (2018). Structural analysis of natural deep eutectic solvents. Theoretical and experimental study. *Microchemical Journal*, 143, 252-258.
- Potter, A. J., Gollahon, K. A., Palanca, B. J., Harbert, M. J., Choi, Y. M., Moskovitz, A. H., . . . Rabinovitch, P. S. (2002). Flow cytometric analysis of the cell cycle phase specificity of DNA damage induced by radiation, hydrogen peroxide and doxorubicin. *Carcinogenesis*, 23(3), 389-401.
- Proestos, C., Boziaris, I. S., Nychas, G. J. E., & Komaitis, M. (2006). Analysis of flavonoids and phenolic acids in greek aromatic plants: Investigation of their antioxidant capacity and antimicrobial activity. *Food Chemistry*, 95(4), 664-671.

- Prolongo, S. G., Jimenez-Suarez, A., Moriche, R., & Ureña, A. (2013). In situ processing of epoxy composites reinforced with graphene nanoplatelets. *Composites Science and Technology*, 86, 185-191.
- Radošević, K., Čanak, I., Panić, M., Markov, K., Bubalo, M. C., Frece, J., . . . Redovniković, I. R. (2018). Antimicrobial, cytotoxic and antioxidative evaluation of natural deep eutectic solvents. *Environmental Science and Pollution Research*.
- Radošević, K., Cvjetko Bubalo, M., Gaurina Srček, V., Grgas, D., Landeka Dragičević, T., & Radojčić Redovniković, I. (2015). Evaluation of toxicity and biodegradability of choline chloride based deep eutectic solvents. *Ecotoxicology and Environmental Safety*, 112, 46-53.
- Rahman, M. A., Abdullah, N., & Aminudin, N. (2016). Interpretation of mushroom as a common therapeutic agent for alzheimer's disease and cardiovascular diseases. *Crit Rev Biotechnol*, 36(6), 1131-1142.
- Ramirez, C., & Osendi, M. I. (2013). Characterization of graphene nanoplatelets-si3n4 composites by raman spectroscopy. *Journal of the European Ceramic Society*, 33(3), 471-477.
- Rana, V. K., Choi, M.-C., Kong, J.-Y., Kim, G. Y., Kim, M. J., Kim, S.-H., . . . Ha, C.-S. (2011). Synthesis and drug-delivery behavior of chitosan-functionalized graphene oxide hybrid nanosheets. *Macromolecular Materials and Engineering*, 296(2), 131-140.
- Ray, P. D., Huang, B.-W., & Tsuji, Y. (2012). Reactive oxygen species (ros) homeostasis and redox regulation in cellular signaling. *Cellular Signalling*, 24(5), 981-990.
- Ru, & Konig, B. (2012). Low melting mixtures in organic synthesis - an alternative to ionic liquids? *Green Chemistry*, 14(11), 2969-2982.
- Sánchez-Leija, R., Pojman, J., Luna-Bárcenas, G., & Mota-Morales, J. (2014). Controlled release of lidocaine hydrochloride from polymerized drug-based deep-eutectic solvents. *Journal of Materials Chemistry B*, 2(43), 7495-7501.
- Sanchez De Juan, B., Von Briesen, H., Gelperina, S. E., & Kreuter, J. (2006). Cytotoxicity of doxorubicin bound to poly(butyl cyanoacrylate) nanoparticles in rat glioma cell lines using different assays. *Journal of Drug Targeting*, 14(9), 614-622.

- Sanson, C., Schatz, C., Le Meins, J.-F., Soum, A., Thévenot, J., Garanger, E., & Lecommandoux, S. (2010). A simple method to achieve high doxorubicin loading in biodegradable polymersomes. *Journal of Controlled Release*, *147*(3), 428-435.
- Sasidharan, A., Panchakarla, L. S., Chandran, P., Menon, D., Nair, S., Rao, C. N. R., & Koyakutty, M. (2011). Differential nano-bio interactions and toxicity effects of pristine versus functionalized graphene. *Nanoscale*, *3*(6), 2461-2464.
- Sasidharan, A., Panchakarla, L. S., Sadanandan, A. R., Ashokan, A., Chandran, P., Girish, C. M., . . . Koyakutty, M. (2012). Hemocompatibility and macrophage response of pristine and functionalized graphene. *Small*, *8*(8), 1251-1263.
- Sato, H., Taguchi, G., Fukui, H., & Tabata, M. (1992). Role of malic acid in solubilizing excess berberine accumulating in vacuoles of *Coptis japonica*. *Phytochemistry*, *31*(10), 3451-3454.
- Sayes, C. M., Fortner, J. D., Guo, W., Lyon, D., Boyd, A. M., Ausman, K. D., . . . Colvin, V. L. (2004). The differential cytotoxicity of water-soluble fullerenes. *Nano Letters*, *4*(10), 1881-1887.
- Sayes, C. M., Liang, F., Hudson, J. L., Mendez, J., Guo, W., Beach, J. M., . . . Colvin, V. L. (2006). Functionalization density dependence of single-walled carbon nanotubes cytotoxicity in vitro. *Toxicology Letter*, *161*(2), 135-142.
- Serpe, L., Laurora, S., Pizzimenti, S., Ugazio, E., Ponti, R., Canaparo, R., . . . Bernengo, M. G. (2004). Cholesteryl butyrate solid lipid nanoparticles as a butyric acid pro-drug: Effects on cell proliferation, cell-cycle distribution and c-myc expression in human leukemic cells. *Anti-cancer Drugs*, *15*(5), 525-536.
- Serrano, M. C., Gutiérrez, M. C., Jiménez, R., Ferrer, M. L., & del Monte, F. (2012). Synthesis of novel lidocaine-releasing poly (diol-co-citrate) elastomers by using deep eutectic solvents. *Chemical Communications*, *48*(4), 579-581.
- Shadle, S. E., Bammel, B. P., Cusack, B. J., Knighton, R. A., Olson, S. J., Mushlin, P. S., & Ison, R. D. O. (2000). Daunorubicin cardiotoxicity: Evidence for the importance of the quinone moiety in a free-radical-independent mechanism. *Biochemical Pharmacology*, *60*(10), 1435-1444.
- Shekaari, H., Zafarani-Moattar, M. T., & Mokhtarpour, M. (2017). Solubility, volumetric and compressibility properties of acetaminophen in some aqueous solutions of choline based deep eutectic solvents at $t=(288.15 \text{ to } 318.15) \text{ K}$. *European Journal of Pharmaceutical Sciences*, *109*, 121-130.

- Shi, J., Kantoff, P. W., Wooster, R., & Farokhzad, O. C. (2016). Cancer nanomedicine: Progress, challenges and opportunities. *Nature Reviews Cancer*, 17, 20.
- Smith, E. L., Abbott, A. P., & Ryder, K. S. (2014). Deep eutectic solvents (dessa) and their applications. *Chemical Reviews*, 114(21), 11060-11082.
- Stankovich, S., Dikin, D. A., Piner, R. D., Kohlhaas, K. A., Kleinhammes, A., Jia, Y., . . . Ruoff, R. S. (2007). Synthesis of graphene-based nanosheets via chemical reduction of exfoliated graphite oxide. *Carbon*, 45(7), 1558-1565.
- Stankovich, S., Piner, R. D., Chen, X., Wu, N., Nguyen, S. T., & Ruoff, R. S. (2006). Stable aqueous dispersions of graphitic nanoplatelets via the reduction of exfoliated graphite oxide in the presence of poly(sodium 4-styrenesulfonate). *Journal of Materials Chemistry*, 16(2), 155-158.
- Stone, V., Shaw, J., Brown, D. M., MacNee, W., Faux, S. P., & Donaldson, K. (1998). The role of oxidative stress in the prolonged inhibitory effect of ultrafine carbon black on epithelial cell function. *Toxicology in Vitro*, 12(6), 649-659.
- Stott, P. W., Williams, A. C., & Barry, B. W. (1998). Transdermal delivery from eutectic systems: Enhanced permeation of a model drug, ibuprofen. *Journal of Controlled Release*, 50(1-3), 297-308.
- Subedi, R. K., Kang, K. W., & Choi, H.-K. (2009). Preparation and characterization of solid lipid nanoparticles loaded with doxorubicin. *European Journal of Pharmaceutical Sciences*, 37(3), 508-513.
- Sukumaran, S., Gadkar, K., Zhang, C., Bhakta, S., Liu, L., Xu, K., . . . Lin, K. (2015). Mechanism-based pharmacokinetic/pharmacodynamic model for thiomab™ drug conjugates. *Pharmaceutical Research*, 32(6), 1884-1893.
- Sultana, S., Khan, M. R., Kumar, M., Kumar, S., & Ali, M. (2013). Nanoparticles-mediated drug delivery approaches for cancer targeting: A review. *Journal of Drug Targeting*, 21(2), 107-125.
- Sun, J., Deng, Y., Li, J., Wang, G., He, P., Tian, S., . . . Xie, X. (2016). A new graphene derivative: Hydroxylated graphene with excellent biocompatibility. *ACS Applied Materials & Interfaces*, 8(16), 10226-10233.
- Sun, X., Liu, Z., Welsher, K., Robinson, J. T., Goodwin, A., Zaric, S., & Dai, H. (2008). Nano-graphene oxide for cellular imaging and drug delivery. *Nano Research*, 1(3), 203-212.

- Sut, S., Faggian, M., Baldan, V., Poloniato, G., Castagliuolo, I., Grabnar, I., . . . Dall'Acqua, S. (2017). Natural deep eutectic solvents (nades) to enhance berberine absorption: An in vivo pharmacokinetic study. *Molecules*, 22(11), 1921.
- Sutherland, R. L., Green, M. D., Hall, R. E., Reddel, R. R., & Taylor, I. W. (1983). Tamoxifen induces accumulation of mcf 7 human mammary carcinoma cells in the g₀/g₁ phase of the cell cycle. *European Journal of Cancer and Clinical Oncology*, 19(5), 615-621.
- Tagne, J.-B., Kakumanu, S., Ortiz, D., Shea, T., & Nicolosi, R. J. (2008). A nanoemulsion formulation of tamoxifen increases its efficacy in a breast cancer cell line. *Molecular Pharmaceutics*, 5(2), 280-286.
- Talaeemashhadi, S., Sansotera, M., Gambarotti, C., Famulari, A., Bianchi, C. L., Antonio Guarda, P., & Navarrini, W. (2013). Functionalization of multi-walled carbon nanotubes with perfluoropolyether peroxide to produce superhydrophobic properties. *Carbon*, 59, 150-159.
- Tang, B., Zhang, H., & Row, K. H. (2015). Application of deep eutectic solvents in the extraction and separation of target compounds from various samples. *Journal of Separation Science*, 38(6), 1053-1064.
- Tekin, G. I. M., & Ozturk, B. R. (2017). Effects of quercetin and hesperetin on mcf-7 cell proliferation by using real-time cell analyzer. *Journal of Basic and Clinical Pharmacy*, 8(3).
- Tønnesen, H. H. (2006). Solubility and stability of curcumin in solutions containing alginate and other viscosity modifying macromolecules. Studies of curcumin and curcuminoids. Xxx. *Pharmazie*, 61(8), 696-700.
- Tønnesen, H. H. (2002). Solubility, chemical and photochemical stability of curcumin in surfactant solutions. *Pharmazie*, 57(12), 820-824.
- Tønnesen, H. H., & Karlsen, J. (1985). Studies on curcumin and curcuminoids. *Zeitschrift für Lebensmittel-Untersuchung und Forschung*, 180(2), 132-134.
- Tønnesen, H. H., Karlsen, J., & van Henegouwen, G. B. (1986). Studies on curcumin and curcuminoids viii. Photochemical stability of curcumin. *Zeitschrift für Lebensmittel-Untersuchung und Forschung*, 183(2), 116-122.
- Tønnesen, H. H., Måsson, M., & Loftsson, T. (2002). Studies of curcumin and curcuminoids. Xxvii. Cyclodextrin complexation: Solubility, chemical and

photochemical stability. *International Journal of Pharmaceutics*, 244(1–2), 127-135.

Trzenschiok, H., Distaso, M., & Peukert, W. (2019). A new approach for the stabilization of amorphous drug nanoparticles during continuous antisolvent precipitation. *Chemical Engineering Journal*, 361, 428-438.

Tsang, W. P., Chau, S. P. Y., Kong, S. K., Fung, K. P., & Kwok, T. T. (2003). Reactive oxygen species mediate doxorubicin induced p53-independent apoptosis. *Life Sciences*, 73(16), 2047-2058.

Tu, Y., Lv, M., Xiu, P., Huynh, T., Zhang, M., Castelli, M., . . . Zhou, R. (2013). Destructive extraction of phospholipids from escherichia coli membranes by graphene nanosheets. *Nat Nanotechnol*, 8(8), 594-601.

Upadhyay, K. K., Bhatt, A. N., Mishra, A. K., Dwarakanath, B. S., Jain, S., Schatz, C., . . . Lecommandoux, S. (2010). The intracellular drug delivery and anti tumor activity of doxorubicin loaded poly(γ -benzyl l-glutamate)-b-hyaluronan polymersomes. *Biomaterials*, 31(10), 2882-2892.

Valentini, F., Calcaterra, A., Ruggiero, V., Di Giacobbe, M., Botta, M., & Talamo, M. (2018). Graphene as nanocarrier in drug delivery *JSM Nanotechnology & Nanomedicine*, 6(1), 1060.

van Osch, D. J. G. P., Zubeir, L. F., van den Bruinhorst, A., Rocha, M. A. A., & Kroon, M. C. (2015). Hydrophobic deep eutectic solvents as water-immiscible extractants. *Green Chemistry*, 17(9), 4518-4521.

Varadharajaperumal, P., Subramanian, B., & Santhanam, A. (2017). Biopolymer mediated nanoparticles synthesized from adenia hondala for enhanced tamoxifen drug delivery in breast cancer cell line. *Advances in Natural Sciences: Nanoscience and Nanotechnology*, 8(3), 035011.

Ventura, S. P. M., e Silva, F. A., Gonçalves, A. M. M., Pereira, J. L., Gonçalves, F., & Coutinho, J. A. P. (2014). Ecotoxicity analysis of cholinium-based ionic liquids to vibrio fischeri marine bacteria. *Ecotoxicology and Environmental Safety*, 102, 48-54.

Ventura, S. P. M., e Silva, F. A., Quental, M. V., Mondal, D., Freire, M. G., & Coutinho, J. A. P. (2017). Ionic-liquid-mediated extraction and separation processes for bioactive compounds: Past, present, and future trends. *Chemical Reviews*, 117(10), 6984–7052.

- Wang, G., Shen, X., Wang, B., Yao, J., & Park, J. (2009). Synthesis and characterisation of hydrophilic and organophilic graphene nanosheets. *Carbon*, 47(5), 1359-1364.
- Wang, M., Wang, J., Zhang, Y., Xia, Q., Bi, W., Yang, X., & Chen, D. D. Y. (2016a). Fast environment-friendly ball mill-assisted deep eutectic solvent-based extraction of natural products. *Journal of Chromatography A*, 1443, 262-266.
- Wang, Q., Dong, B., Zhao, Y., Huang, F., Xie, J., Cui, G., & Tang, B. (2018). Controllable green synthesis of crassula perforata-like tio₂ with high photocatalytic activity based on deep eutectic solvent (des). *Chemical Engineering Journal*, 348, 811-819.
- Wang, W., Cai, Y., Liu, Y., Zhao, Y., Feng, J., & Liu, C. (2016b). Microemulsions based on paeonol-menthol eutectic mixture for enhanced transdermal delivery: Formulation development and in vitro evaluation. *Artificial Cells, Nanomedicine, and Biotechnology*, 1-6.
- Wang, X., Xing, W., Song, L., Yu, B., Hu, Y., & Yeoh, G. H. (2013). Preparation of uv-curable functionalized graphene/polyurethane acrylate nanocomposite with enhanced thermal and mechanical behaviors. *Reactive and Functional Polymers*, 73(6), 854-858.
- Wang, Y., Li, Z., Wang, J., Li, J., & Lin, Y. (2011). Graphene and graphene oxide: Biofunctionalization and applications in biotechnology. *Trends in Biotechnology*, 29(5), 205-212.
- Wang, Y., Wei, X., Zhang, C., Zhang, F., & Liang, W. (2010). Nanoparticle delivery strategies to target doxorubicin to tumor cells and reduce side effects. *Therapeutic Delivery*, 1(2), 273-287.
- Wei, Z.-F., Wang, X.-Q., Peng, X., Wang, W., Zhao, C.-J., Zu, Y.-G., & Fu, Y.-J. (2015a). Fast and green extraction and separation of main bioactive flavonoids from radix scutellariae. *Industrial Crops and Products*, 63, 175-181.
- Wei, Z., Qi, X., Li, T., Luo, M., Wang, W., Zu, Y., & Fu, Y. (2015b). Application of natural deep eutectic solvents for extraction and determination of phenolics in cajanus cajan leaves by ultra performance liquid chromatography. *Separation and Purification Technology*, 149, 237-244.
- Wen, Q., Chen, J.-X., Tang, Y.-L., Wang, J., & Yang, Z. (2015). Assessing the toxicity and biodegradability of deep eutectic solvents. *Chemosphere*, 132, 63-69.

- Wikene, K. O., Bruzell, E., & Tønnesen, H. H. (2015). Characterization and antimicrobial phototoxicity of curcumin dissolved in natural deep eutectic solvents. *European Journal of Pharmaceutical Sciences*, 80, 26-32.
- Williams, H. D., Trevaskis, N. L., Charman, S. A., Shanker, R. M., Charman, W. N., Pouton, C. W., & Porter, C. J. H. (2013). Strategies to address low drug solubility in discovery and development. *Pharmacological Reviews*, 65(1), 315-499.
- Wiseman, H., & Halliwell, B. (1996). Damage to DNA by reactive oxygen and nitrogen species: Role in inflammatory disease and progression to cancer. *Biochemical Journal*, 313(Pt 1), 17-29.
- Woolfson, A., Malcolm, R., Campbell, K., Jones, D., & Russell, J. (2000). Rheological, mechanical and membrane penetration properties of novel dual drug systems for percutaneous delivery. *Journal of Controlled Release*, 67(2), 395-408.
- Wu, B., Zhang, Q., Shen, W., & Zhu, J. (2008). Anti-proliferative and chemosensitizing effects of luteolin on human gastric cancer ags cell line. *Molecular and Cellular Biochemistry*, 313(1), 125-132.
- Xavier, M. A., de Oliveira, M. T., Baranoski, A., & Mantovani, M. S. (2018). Effects of folic acid on the antiproliferative efficiency of doxorubicin, camptothecin and methyl methanesulfonate in mcf-7 cells by mrna endpoints. *Saudi Journal of Biological Sciences*, 25(8), 1568-1576.
- Xiang, X., Saha, A. K., Wen, R., Ruderman, N. B., & Luo, Z. (2004). Amp-activated protein kinase activators can inhibit the growth of prostate cancer cells by multiple mechanisms. *Biochemical and Biophysical Research Communications*, 321(1), 161-167.
- Xing, W., Xu, G., Dong, J., Han, R., & Ni, Y. (2018). Novel dihydrogen-bonding deep eutectic solvents: Pretreatment of rice straw for butanol fermentation featuring enzyme recycling and high solvent yield. *Chemical Engineering Journal*, 333, 712-720.
- Yaacob, N. S., Kamal, N., Wong, K. K., & Norazmi, M. N. (2015). Cell cycle modulation of mcf-7 and mda-mb-231 by a sub-fraction of strobilanthes crispus and its combination with tamoxifen. *Asian Pacific Journal of Cancer Prevention*, 16(18), 8135-8140.
- Yan, L., Lin, M., Zeng, C., Chen, Z., Zhang, S., Zhao, X., . . . Liu, Y. (2012a). Electroactive and biocompatible hydroxyl- functionalized graphene by ball milling. *Journal of Materials Chemistry*, 22(17), 8367-8371.

- Yan, L., Zheng, Y. B., Zhao, F., Li, S., Gao, X., Xu, B., . . . Zhao, Y. (2012b). Chemistry and physics of a single atomic layer: Strategies and challenges for functionalization of graphene and graphene-based materials. *Chemical Society Reviews*, 41(1), 97-114.
- Yang, K., Feng, L., Shi, X., & Liu, Z. (2013a). Nano-graphene in biomedicine: Theranostic applications. *Chemical Society Reviews*, 42(2), 530-547.
- Yang, K., Li, Y., Tan, X., Peng, R., & Liu, Z. (2013b). Behavior and toxicity of graphene and its functionalized derivatives in biological systems. *Small*, 9(9-10), 1492-1503.
- Yang, X., Zhang, X., Liu, Z., Ma, Y., Huang, Y., & Chen, Y. (2008). High-efficiency loading and controlled release of doxorubicin hydrochloride on graphene oxide. *Journal of Physical Chemistry C*, 112(45), 17554-17558.
- Yao, C., Hou, Y., Ren, S., Wu, W., Zhang, K., Ji, Y., & Liu, H. (2017). Efficient separation of phenol from model oils using environmentally benign quaternary ammonium-based zwitterions via forming deep eutectic solvents. *Chemical Engineering Journal*, 326, 620-626.
- Yazdani, M., Briggs, K., Jankovsky, C., & Hawi, A. (2004). The “high solubility” definition of the current fda guidance on biopharmaceutical classification system may be too strict for acidic drugs. *Pharmaceutical Research*, 21(2), 293-299.
- Yoo, H. S., Lee, K. H., Oh, J. E., & Park, T. G. (2000). In vitro and in vivo anti-tumor activities of nanoparticles based on doxorubicin-plga conjugates. *Journal of Controlled Release*, 68(3), 419-431.
- Yu, C., Zhou, M., Zhang, X., Wei, W., Chen, X., & Zhang, X. (2015). Smart doxorubicin nanoparticles with high drug payload for enhanced chemotherapy against drug resistance and cancer diagnosis. *Nanoscale*, 7(13), 5683-5690.
- Yuan, H., Miao, J., Du, Y.-Z., You, J., Hu, F.-Q., & Zeng, S. (2008). Cellular uptake of solid lipid nanoparticles and cytotoxicity of encapsulated paclitaxel in a549 cancer cells. *International Journal of Pharmaceutics*, 348(1), 137-145.
- Zahedifard, M., Lafta Faraj, F., Paydar, M., Yeng Looi, C., Hajrezaei, M., Hasanpourghadi, M., . . . Ameen Abdulla, M. (2015). Synthesis, characterization and apoptotic activity of quinazolinone schiff base derivatives toward mcf-7 cells via intrinsic and extrinsic apoptosis pathways. *Scientific Reports*, 5, 11544.

- Zakrewsky, M., Banerjee, A., Apte, S., Kern, T. L., Jones, M. R., Del Sesto, R. E., . . . Mitragotri, S. (2016). Choline and geranate deep eutectic solvent as a broad-spectrum antiseptic agent for preventive and therapeutic applications. *Advanced Healthcare Materials*, 5(11), 1282-1289.
- Zhang, K., Ren, S., Yang, X., Hou, Y., Wu, W., & Bao, Y. (2017). Efficient absorption of low-concentration so₂ in simulated flue gas by functional deep eutectic solvents based on imidazole and its derivatives. *Chemical Engineering Journal*, 327, 128-134.
- Zhang, L., & Wang, M. (2017). Optimization of deep eutectic solvent-based ultrasound-assisted extraction of polysaccharides from *dioscorea opposita* thunb. *International Journal of Biological Macromolecules*, 95, 675-681.
- Zhang, Q., De Oliveira Vigier, K., Royer, S., & Jerome, F. (2012a). Deep eutectic solvents: Syntheses, properties and applications. *Chemical Society Reviews*, 41(21), 7108-7146.
- Zhang, X., Hu, W., Li, J., Tao, L., & Wei, Y. (2012b). A comparative study of cellular uptake and cytotoxicity of multi-walled carbon nanotubes, graphene oxide, and nanodiamond. *Toxicology Research*, 1(1), 62-68.
- Zhang, Y., Ali, S. F., Dervishi, E., Xu, Y., Li, Z., Casciano, D., & Biris, A. S. (2010). Cytotoxicity effects of graphene and single-wall carbon nanotubes in neural phaeochromocytoma-derived pc12 cells. *ACS Nano*, 4(6), 3181-3186.
- Zhao, B.-Y., Xu, P., Yang, F.-X., Wu, H., Zong, M.-H., & Lou, W.-Y. (2015). Biocompatible deep eutectic solvents based on choline chloride: Characterization and application to the extraction of rutin from *sophora japonica*. *ACS Sustainable Chemistry & Engineering*, 3(11), 2746-2755.
- Zhao, N., Woodle, M. C., & Mixson, A. J. (2018). Advances in delivery systems for doxorubicin. *Journal of Nanomedicine & Nanotechnology*, 9(5), 519.
- Zhou, Q., Wu, X., Wen, C., Wang, H., Wang, H., Liu, H., & Peng, J. (2018). Toosendanin induces caspase-dependent apoptosis through the p38 mapk pathway in human gastric cancer cells. *Biochemical and Biophysical Research Communications*, 505(1), 261-266.
- Zhu, Y., Murali, S., Cai, W., Li, X., Suk, J. W., Potts, J. R., & Ruoff, R. S. (2010). Graphene and graphene oxide: Synthesis, properties, and applications. *Advanced Materials*, 22(35), 3906-3924.